Integrated Outcrop and Subsurface Studies of the Interwell Environment of Carbonate Reservoirs: Clear Fork (Leonardian-Age) Reservoirs, West Texas and New Mexico

Final Technical Report

October 1, 1998, to January 31, 2002

F. Jerry Lucia, Editor

January 2002

Prepared for U.S. Department of Energy
under Contract No. DE-AC26-98BC15105

The Semiannual Technical Report for the reporting period October 2001 to January 2002 is incorporated herein.

Bureau of Economic Geology
John A. and Katherine G. Jackson School of Geosciences
The University of Texas at Austin
Austin, Texas 78713-8924

DISCLAIMER

TABLE OF CONTENTS

INTEGRATED OUTCROP AND SUBSURFACE STUDIES OF THE INTERWELL ENVIRONMENT OF CARBONATE RESERVOIRS: CLEAR FORK (LEONARDIAN-AGE) RESERVOIRS, WEST TEXAS AND NEW MEXICO

Contract No. DE-AC26-98BC15105

Executive Summary

This is the final report of the project *Integrated Outcrop and Subsurface Studies of the Interwell Environment of Carbonate Reservoirs: Clear Fork (Leonardian-Age) Reservoirs, West Texas and New Mexico,* Department of Energy contract no. DE-AC26-98BC15105 and is the third in a series of similar projects funded jointly by the U.S. Department of Energy and The University of Texas at Austin, Bureau of Economic Geology, Reservoir Characterization Research Laboratory for Carbonates. All three projects focus on the integration of outcrop and subsurface data for the purpose of developing improved methods for modeling petrophysical properties in the interwell environment. The first project, funded by contract no. DE-AC22-89BC14470, was a study of San Andres outcrops in the Algerita Escarpment, Guadalupe Mountains, Texas and New Mexico, and the Seminole San Andres reservoir, Permian Basin. This study established the basic concepts for constructing a reservoir model using sequence-stratigraphic principles and rock-fabric, petrophysical relationships. The second project, funded by contract no. DE-AC22-93BC14895, was a study of Grayburg outcrops in the Brokeoff Mountains, New Mexico, and the South Cowden Grayburg reservoir, Permian Basin. This study developed a sequence-stratigraphic succession for the Grayburg and improved methods for locating remaining hydrocarbons in carbonate ramp reservoirs.

The current study is of the Clear Fork Group in Apache Canyon, Sierra Diablo Mountains, West Texas, and the South Wasson Clear Fork reservoir, Permian Basin. The focus was on scales of heterogeneity, imaging high- and low-permeability layers, and the impact of fractures on reservoir performance. In this study (1) the Clear Fork cycle stratigraphy is defined, (2) important scales of petrophysical variability are confirmed, (3) a unique rock-fabric, petrophysical relationship is defined, (4) a porosity method for correlating high-frequency cycles and defining rock-fabric flow layers is described, (5) Clear Fork fractures are described and geomechanical modeling of fractures is investigated, and (6) most importantly, new statistical

methods are developed for scaleup of petrophysical properties from the core to the layer scale and for retaining stratigraphic layering in simulation models.

The outcrop study defined two high-frequency sequences in the lower Clear Fork and three high-frequency sequences in the upper Clear Fork. Unfortunately, much of the upper Clear Fork is eroded at this location. Importantly, the Clear Fork was found to be highly cyclic with both subtidal mud-to-grain cycles and well-developed tidal-flat-capped cycles. The cycles formed layers that are continuous across as much as 2,000 ft of outcrop. This finding contrasts with the prevailing concept that the Clear Fork is highly discontinuous. Characterizing the Clear Fork as composed of continuous high-frequency cycles was important for the construction of the subsurface model. Petrophysical studies of the outcrop demonstrated a gradual lateral change in porosity and permeability from tidal-flat facies to subtidal facies. As has been observed in all three outcrop studies, the petrophysical properties are highly variable and poorly correlated at the inch to foot scale, but a longer range pattern does appear to have spatial correlation. The concepts of the spatial distribution of petrophysical properties developed using this outcrop data together with previous data have a major impact on methods for building carbonate reservoir models.

A sequence-stratigraphic model was built for the South Wasson Clear Fork field using the outcrop sequence model, vertical succession of facies from core descriptions, and seismic data. The two high-frequency sequences defined in the lower Clear Fork in outcrop were also identified in the subsurface. High-frequency sequences were more difficult to define in the upper Clear Fork because of poor log resolution and incomplete coverage of the reservoir interval by outcrop section. Nevertheless, three longer range sequences were defined, one of which coincides with the reservoir top. Core descriptions show cyclicity at a scale similar to that of the outcrop.

A surprising result of the rock-fabric, petrophysical study was that the South Wasson Clear Fork reservoir can be characterized by a single porosity-permeability transform and a single saturation, porosity, and reservoir-height equation despite the presence of a robust variety of rock fabrics. This allowed porosity models to be converted to permeability directly without having to integrate a rock-fabric number. However, this made it difficult to identify cycles from wireline logs. Carbonate cycles could not be identified using the gamma-ray log because of the large amount of diagenetic uranium in the Clear Fork, and cross plots of porosity and water saturation are of little use because the fabrics group into one petrophysical class. A statistical study of

porosity and rock fabrics shows the mud-dominated fabrics have lower porosity than the grain-dominated fabrics do on the average. Therefore, vertical increases in porosity were interpreted to mean a change from mud-dominated to grain-dominated fabrics.

There are two reservoirs in the South Wasson Clear Fork field: a lower and a middle Clear Fork reservoir. The seal for the lower Clear Fork is the Tubb sandstone, and the seal for the middle Clear Fork is at a sequence boundary within the upper Clear Fork. Using porosity as a surrogate for rock fabric, 21 cycles were mapped in the middle Clear Fork and 21 cycles in the lower Clear Fork. To maintain high and low permeability in the flow model, each high-frequency cycle was divided into a lower, low-permeability mud-dominated layer and an upper, high-permeability grain-dominated packstone layer. The layers, which are referred to as rock-fabric flow layers, are the basic elements in the construction of a flow model.

Integrating outcrop and subsurface data shows that petrophysical heterogeneity in the South Wasson Clear Fork reservoir is composed of a large-scale stratigraphically controlled component and a small-scale poorly correlated component. Scaleup from core-plug scale to reservoir-layer scale results in effective permeability increasing by a factor of 2. The large-scale variability exists as a flow-unit-scale petrophysical layering that is laterally persistent at interwell scales and produces highly stratified reservoir behavior. Modeling these large-scale heterogeneities as trends using moving averages within a high-resolution sequence-stratigraphic framework reduced the requirement for arbitrary k_v/k_h adjustments to inhibit cross-flow in waterflood simulations. Carefully controlled power-averaging effectively captured the rate-enhancing effect of the small-scale variability. A comparison with traditional models shows models constructed using the methods presented in this study better capture the geologic/petrophysical layering and give more realistic results.

A portion of this project was dedicated to a study of inputting fracture permeability into a matrix reservoir model. Fracture aperture, length, and spacing were measured along six scan lines in the Clear Fork outcrop, and fracture width and length were measured in cores using thin sections and scanning-electron-microscope cathodoluminescence images. Fracture aperture-length relationships are power law, although correlation coefficients for these relationships are low. Most of the fractures were partially or completely filled with dolomite and anhydrite. The dolomite is thought to be synkinematic (formed during fracture growth), whereas anhydrite is thought to be postkinematic. The timing and distribution of different phases of dolomite and

anhydrite precipitation with respect to fracturing are needed to predict the distribution of open fractures. However, this factor is not yet understood.

Fractures were modeled using a geomechanical approach where a physical understanding of the fracture process is used to predict fracture characteristics. Key inputs into this model are subcritical crack growth index, strain, bed thickness, and fracture fill. Subcritical crack growth parameters were measured from representative rock samples of the South Wasson Clear Fork reservoir. These measurements, along with other inferred parameters such as the strain and Young's modulus, were used with a geomechanical crack growth simulator to generate fracture patterns at a series of increasing strain levels. The resulting fracture patterns exhibited total fracture lengths, mean fracture lengths, and cluster spacing dependent on strain level, bed height, and subcritical crack index. Fluid-flow simulations were conducted to estimate effective permeability in the simulated fracture patterns. The ratio of effective permeability to matrix permeability, R_k, was found to increase with strain level, total fracture length, and mean fracture length. For a given strain level, R_k depended on the subcritical crack index and bed height. Fracture aperture, however, did not have a strong effect on R_k. The experiments with fracture fills indicated a large reduction in effective permeability occurred with filling of fractures with diagenetic cements.

We were unable to include the results of the fracture study in the reservoir model because not all the necessary variables could be quantified. However, the model study shows that the effective grid permeability due to the presence of fractures is enhanced by a factor of between 2 and 10. A number of important research questions resulting from this work need to be answered before a realistic matrix-fracture flow model can be constructed.

The most valuable result of these three projects is the development of a new approach to the construction of the carbonate reservoir model, an approach that truly integrates geologic descriptions, petrophysics, and flow simulation. In particular, the San Andres project produced characterization methods that formed the basis for a new reservoir model that the operator, Amerada Hess, completed in the year 2001. The model will be used to improve recovery from Amerada's CO_2 flood. The Grayburg project convinced Unocal, the operator, to redesign its waterflood and forego a planned infill program that it was too risky, thereby saving Unocal $24 million that can be invested elsewhere. The current Clear Fork project provided basic information that Oxy Permian (previously Altura) has used as a basis for a new simulation study

to justify investing in an expanded CO_2 flood in the South Wasson Clear Fork field, a flow simulation that, for the first time in the long history of this field, provides a history match sufficiently accurate to be used for performance prediction. Although specific reservoir additions cannot be attributed to any of these three projects, they impacted major operational decisions in three major reservoirs in the Permian Basin.

INTEGRATED GEOLOGICAL AND PETROPHYSICAL STUDIES OF CLEAR FORK RESERVOIR ANALOG OUTCROPS: SIERRA DIABLO MOUNTAINS, TEXAS

Stephen C. Ruppel, W. Bruce Ward,[1] Eduardo Ariza,[2]
and James W. Jennings, Jr.

Bureau of Economic Geology
John A. and Katherine G. Jackson School of Geosciences
The University of Texas at Austin

Current addresses: [1] Earthworks, P.O. Box 297, West Redding, CT 06896-0297
[2] Ecopetrol, Calle 37 No. 8-43, Piso 12, Gerencia de Yacimientos, Bogota, Colombia

TABLE OF CONTENTS

FIGURES

TABLE

ABSTRACT

Clear Fork Group reservoirs exhibit recovery efficiencies that are the lowest among carbonate reservoirs in the Permian Basin. It is widely assumed that the key factor contributing to these poor efficiencies is heterogeneity. However, the exact nature of this heterogeneity is poorly known. The superb outcrops of reservoir-equivalent Clear Fork rocks in the Sierra Diablo of West Texas offer an excellent opportunity to examine the stratigraphic and petrophysical heterogeneity that exists in these rocks and to develop improved models for interpreting subsurface reservoir successions.

The best outcrops of reservoir-equivalent Clear Fork strata are exposed in outcrops extending more than 2 mi (3.2 km) along the south wall of Apache Canyon. Lower Clear Fork rocks document two low-accommodation transgressive events: a lower symmetrical high-frequency sequence (HFS 2.1) composed of basal and capping tidal flats separated by intervening maximum flooding subtidal deposits. The upper sequence (HFS 2.2) contains a similar transgressive succession but no highstand regressive section because of forced regression at the end of lower Clear Fork Leonardian sequence 3 deposition.

The upper Clear Fork section comprises three HFS that document Leonardian sequence 3 transgression. The lower succession (HFS 3.1), whose base is made up of transgressive Tubb silt-rich carbonates, displays all of the major facies tracts and styles of cyclicity encountered in Clear Fork reservoirs: transgressive ramp, outer ramp, ramp crest, inner ramp, and tidal flat. The overlying sequence (HFS 3.2), which exhibits similar architecture, demonstrates important differences in cyclicity and facies development in higher accommodation settings.

The spatial statistics of porosity and permeability in the interwell environment were examined by collecting closely space data from two horizontal traverses and one vertical traverse. The porosity and permeability data are similar to data from the South Wasson Clear Fork field. Horizontal variogram statistics demonstrate that permeability in the interwell environment is near randomly distributed at the small scale and has a spatial structure at a range of 180 ft. The horizontal data also show that the low permeability in tidal-flat facies changes gradually over 100 ft to higher permeability in subtidal facies.

Clear Fork sequence architecture and facies in Apache Canyon are consistent with data from subsurface Clear Fork reservoirs in the Permian Basin, indicating these outcrops are directly analogous. The concepts and interpretations derived from these excellent outcrop successions are fundamental tools that can be applied to subsurface reservoir successions to produce better models for more efficient exploitation of this important hydrocarbon play.

INTRODUCTION

The Leonardian Series in the Permian Basin contains a thick (as much as 2,500 ft; 800 m) sequence of carbonate rocks that accumulated on shallow-water platforms and shelves in West Texas and New Mexico during the middle Permian (fig. 1). Reservoirs developed in Leonardian carbonates are typical of a large class of carbonate reservoirs that Tyler and others (1984) referred to as "restricted platform systems." These reservoirs (1) are dolomitized, (2) are associated with evaporites, (3) exhibit low permeability and porosity values, and (4) display low recovery efficiencies (fig. 2). As a group, restricted platform carbonate reservoirs have accounted for nearly 70 percent of the cumulative production from the Permian Basin, although they contain only about half of the original oil in place (OOIP) (Tyler and Banta, 1989).

Leonardian reservoirs account for a substantial percentage of the hydrocarbon resources in the Permian Basin. Estimates of OOIP indicate that Leonardian reservoirs contained more than 14.5 billion barrels of oil at discovery, or 15 percent of the total resource in the Permian Basin (fig. 3). Recovery of this substantial resource, however, has proven difficult; as of January 1990, only 2.8 billion barrels of the total oil resource had been produced (fig. 4). Leonardian carbonate reservoirs currently exhibit a recovery efficiency of 20 percent, which is considerably below the 32-percent average for carbonate reservoirs in the Permian Basin (Tyler and Banta, 1989; Holtz and Garrett, 1990). Shallow-water-platform reservoirs of the Clear Fork Group have recovered an even lower 18 percent of OOIP (Holtz and others, 1992).

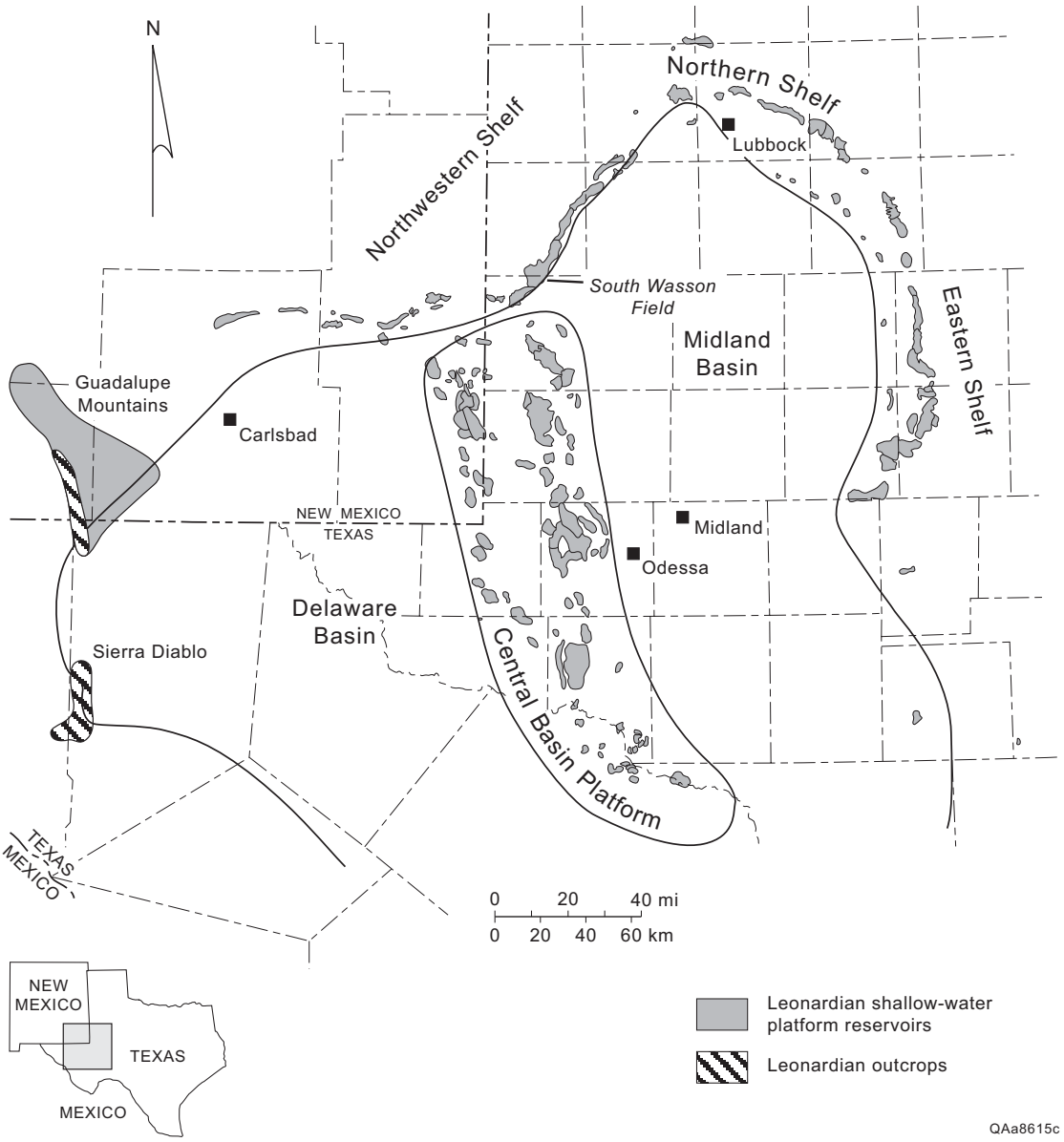

Figure 1. Map of the Permian Basin showing Leonardian paleotopography and the location of the current study area in the Sierra Diablo.

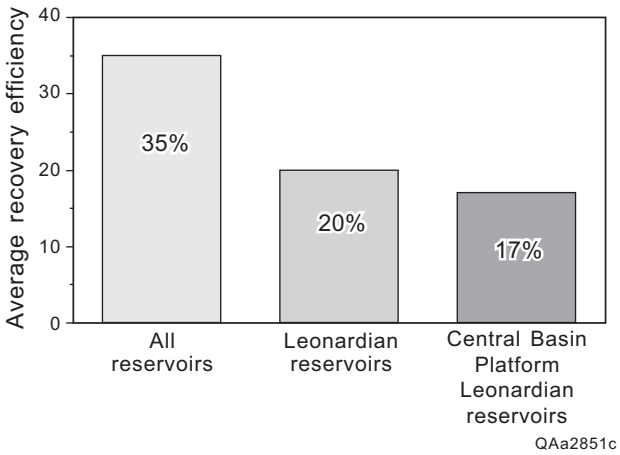

Figure 2. Recovery efficiencies of Leonardian reservoirs in the Permian Basin.

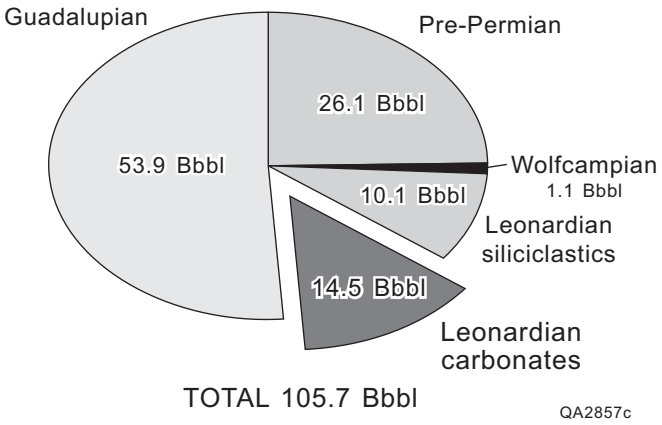

Figure 3. Distribution, by age, of original oil in place in the Permian Basin.

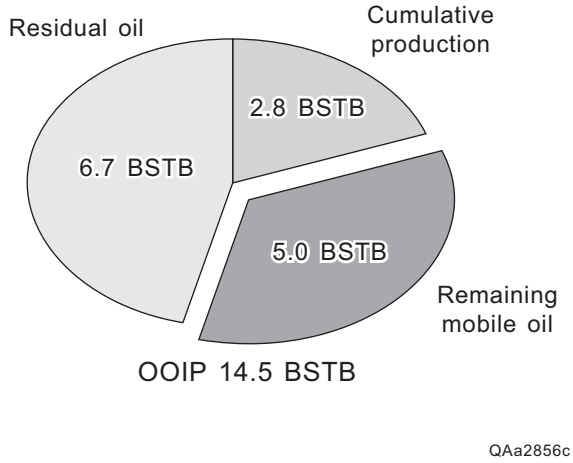

Figure 4. Volumetrics of Leonardian reservoirs in the Permian Basin.

Several authors have recognized that the abnormally low recovery efficiencies in Leonardian reservoirs are the result of extreme lithologic heterogeneity (for example, Tyler and others, 1984; Holtz and others, 1992). Ruppel (1992) and Atchley and others (1999) described styles of cyclicity in the Clear Fork and the effects of overprinting diagenesis on the basis of subsurface core and wireline log data. However, important details of Leonardian facies and stratal architecture remain equivocal.

The purpose of this study is to develop improved concepts and models of the Leonard platform carbonate succession on the basis of examination of well-exposed Leonardian outcrops in the Sierra Diablo. The lateral continuity of these exposures provides a much better understanding of the sequence and cycle architecture of these rocks, which will facilitate better prediction and mapping of reservoir architecture and flow unit geometries in this important class of reservoirs.

SETTING

Most outcrops of reservoir-equivalent, Leonardian carbonate platform successions in the Texas and New Mexico area are poorly exposed or inaccessible. Striking exceptions to this are outcrops in the Sierra Diablo in Hudspeth and Culberson Counties, Texas. Here, the Leonardian is well exposed and readily accessible in the area of Apache Canyon on the Figure 2 and Puett ranches (fig. 5).

The Sierra Diablo is situated on the western edge of the Delaware Basin along a major structural high. Basal Permian (Wolfcampian) deposits unconformably overlie folded Devonian to Precambrian strata throughout the region (fig. 6). Both the Hueco Group (Wolfcampian) and the overlying Victorio Peak and Bone Spring Formations (Leonardian) are exposed in the Beach, Baylor, and Sierra Diablo Mountains (fig. 6). The best exposures are in the Sierra Diablo, where at least 1,200 ft (360 m) of the Hueco Group, 1,200 ft (360 m) of the Victorio Peak Formation, and 3,000 ft (900 m) of the Bone Spring Formation are exposed (King, 1942, 1965).

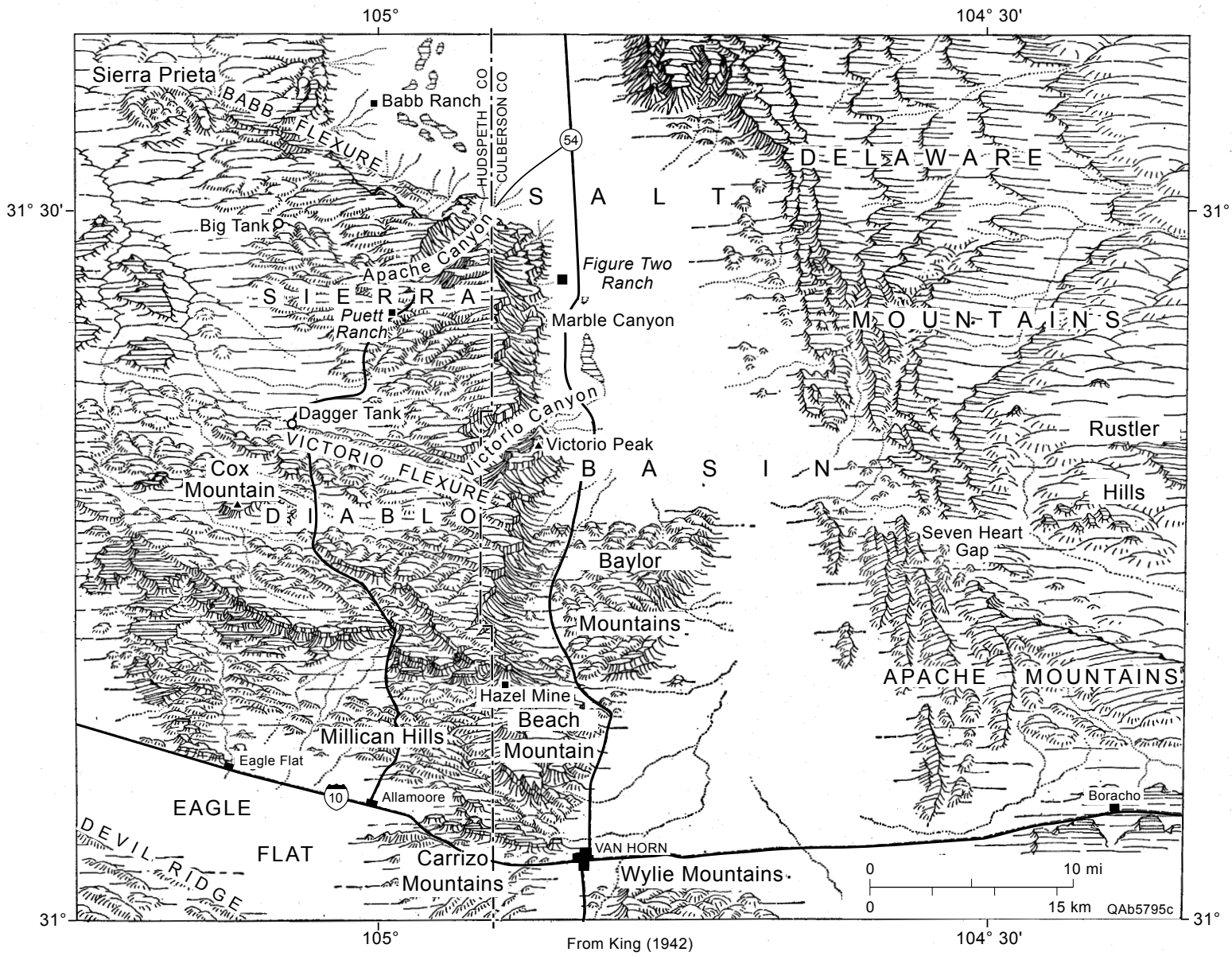

Figure 5. Map of Sierra Diablo area showing major topographic features and field trip route from Van Horn, Texas, to the Puett Ranch and Apache Canyon. From King (1942).

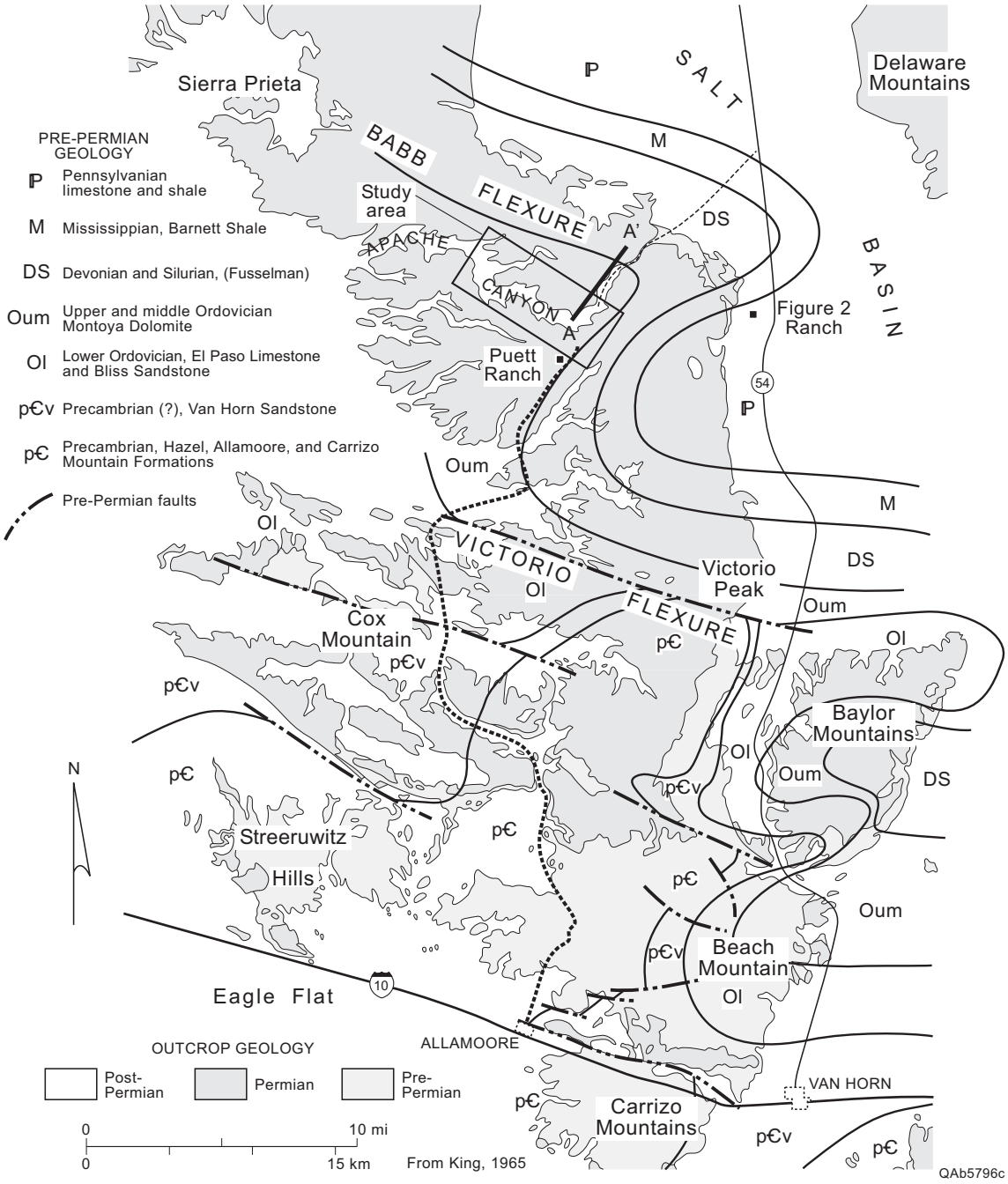

Figure 6. Geologic map of the Sierra Diablo showing the distribution outcrops and the pre-Permian subcrop geology. Note major pre-Permian folds of the Babb and Victorio flexures.

PREVIOUS WORK

The basic Permian stratigraphy of the Sierra Diablo was worked out by P. B. King in a classic study undertaken in the 1930's and published in 1942 and 1965 (King, 1942, 1965). This work still stands today as the fundamental resource of geologic information on the area. Until recently, very little additional work had been done. Recent work has focused on the sequence architecture of the Wolfcampian Hueco Group and Leonardian Victorio Peak and Bone Spring Formations in the Apache Canyon area. This work (Fitchen and others, 1995) established a basic framework for further studies in the area and provides an initial basis for relating outcrop studies of the Leonardian to coeval subsurface producing reservoirs of the Clear Fork and Wichita Groups (fig. 7). It further establishes the Sierra Diablo as a fundamental research venue for characterization of Leonardian sequence stratigraphy and architecture.

The original outcrop definitions of the Victorio Peak and Bone Spring Formations employed by King (1942, 1965) and other workers are very generalized relative to equivalent subsurface stratigraphic subdivisions (fig. 7). The Victorio Peak Formation consists of a wide variety of facies, mineralogy, and depositional settings. In Apache Canyon, this includes mixed shallow-water-platform dolostone and limestone assignable to the subsurface Abo, shallow-water-platform dolostone assignable to the subsurface lower Clear Fork, silty dolostone assignable to the subsurface Tubb, and mixed shallow-water-platform and platform-margin dolostone and limestone assignable to the subsurface upper Clear Fork. The Bone Spring constitutes outer platform to basin lime mudstone. For purposes of this paper, we will refer to subsurface stratigraphic nomenclature, which has more specific stratigraphic, depositional, and reservoir significance.

Fitchen and others (1995) recognized six sequences within the Leonardian Victorio Peak on the basis of well-exposed stratal relationships in Apache Canyon (fig. 8). These relationships suggest the Leonardian exposed in Apache Canyon constitutes a longer duration transgressive-regressive succession, marked by backstepping at the base and progradation at the top. Sequence boundaries within this long-term succession are best defined along the Leonardian platform margin. Significant aspects of the Leonardian sequence architecture visible at the platform

SERIES	STAGE	SUBSURFACE						OUTCROP		
		CENTRAL BASIN PLATFORM				NORTHERN SHELF		GUADALUPE MOUNTAINS/ SIERRA DIABLO		
		NEW MEXICO		TEXAS				PLATFORM	MARGIN	SEQUENCE
Lower Permian	LEONARDIAN	San Andres		San Andres		San Andres		San Andres	Cutoff	Guad 1
									Victorio Peak	Leo 7-8
		Glorieta		Glorieta		Glorieta		Glorieta		Leo 6
		Yeso	Paddock	upper Clear Fork	Clear Fork Group	upper Clear Fork	Clear Fork Group	Victorio Peak		Leo 5
			Blinebry			middle Clear Fork				Leo 4
			Tubb	Tubb		Tubb				Leo 3
			Drinkard	lower Clear Fork		lower Clear Fork				Leo 2
		Abo		Abo	Wichita Group	Abo	Wichita Group		Bone Spring	Leo 1
		Wolfcamp		Wolfcamp		Wolfcamp		Hueco	Hueco	Wolf 3

Figure 7. Correlation of outcrop and subsurface stratigraphy.

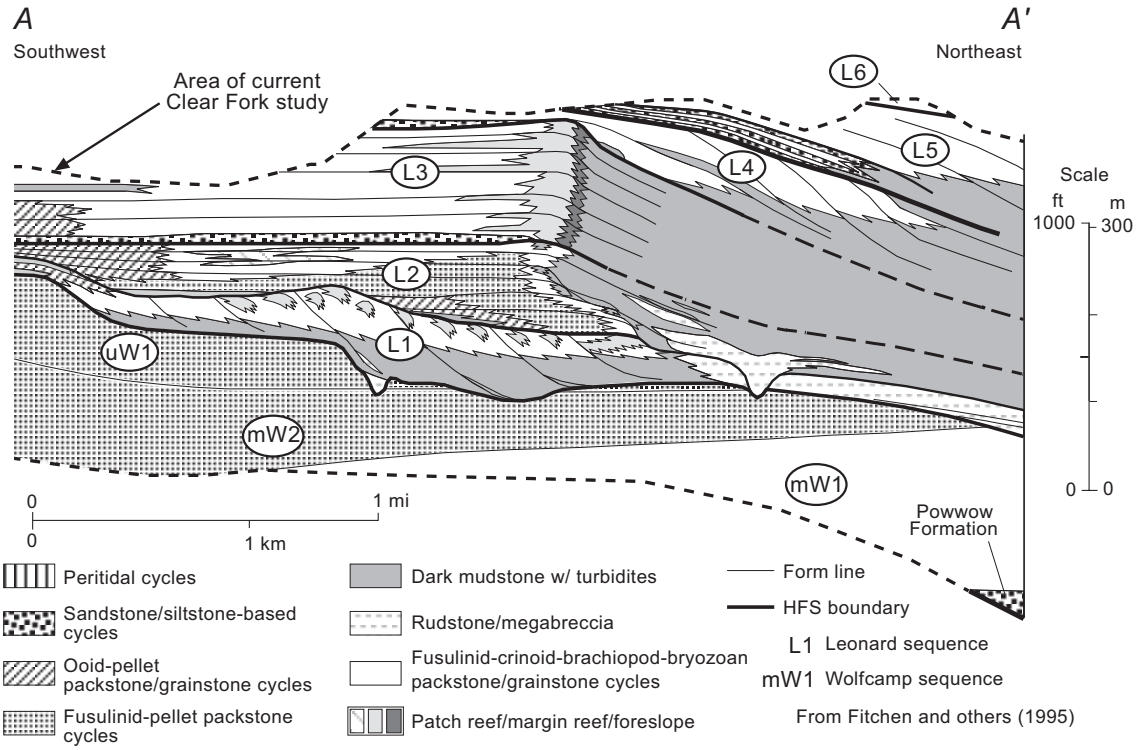

Figure 8. Sequence stratigraphic relationships in the Wolfcampian and Leonardian in Apache Canyon along approximate depositional dip. This section from Fitchen and others (1995) displays the stratal architecture along the northwest wall of Apache Canyon. Line of section (A–A′) is shown in figure 6.

margin are (1) the generally transgressive or backstepping nature of sequences L1 and L2, (2) major erosion and downcutting at the base of both of these sequences, (3) the variable backstepping to vertically aggradational character of sequence L3, and (4) the dominantly prograding geometries of sequences L4, L5, and L6 (fig. 8).

Although the work of Fitchen and others (1995) established the overall sequence architecture of the Leonardian, the stratal architecture of the updip, platform interior Leonardian facies is less well known. It is these deposits, which are the temporal and depositional equivalents of productive Clear Fork reservoir successions on the Northern Shelf, Eastern Shelf, and Central Basin Platform of the Permian Basin, that are the focus of this study.

CURRENT STUDIES

During the past 4 years, Bureau of Economic Geology studies of the Leonardian in the Sierra Diablo have focused on the sequence and cycle stratigraphy of Abo and Clear Fork reservoir-equivalent outcrops. Abo studies have been reported by Kerans and others (2000). Preliminary results of studies of Clear Fork outcrop studies were reported in Ruppel and others (2000); final results are reported here.

Although parts of all six Leonardian sequences are exposed in Apache Canyon (fig. 8), detailed reservoir analog studies have focused on only the lower part of the Clear Fork Group (Leonardian sequences 2 and 3). Only this part of Leonardian succession in Apache Canyon displays continuous high-quality exposures of reservoir-equivalent platform-top facies necessary for high-resolution 2-D reservoir characterization and modeling. Basal upper Clear Fork rocks (sequence 3) are particularly well exposed on the southern wall of Apache Canyon along approximately 2 mi (3 km) of section. Sixteen major sections (fig. 9) and numerous shorter sections have been described and measured along this wall to (1) define the basic elements of the cycle and sequence stratigraphy of the Clear Fork and (2) assess the value of these outcrops as analogs for subsurface reservoirs productive from the Clear Fork in the Permian Basin. Research has focused on defining the cycle- and sequence-scale architecture of the Clear Fork succession and collecting basic petrophysical data on representative facies in vertical and horizontal traverses.

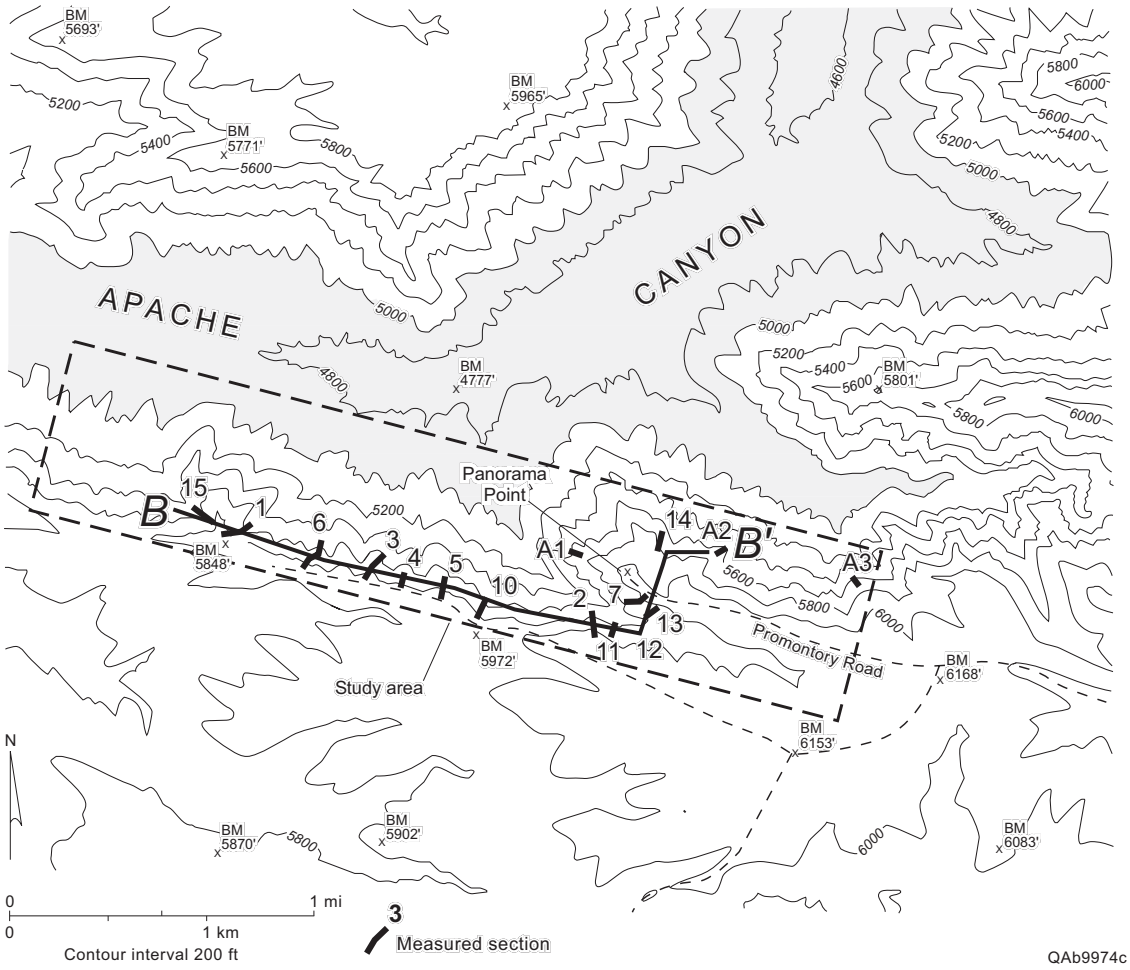

Figure 9. Topographic map of part of Apache Canyon showing the location of the study area and line of section shown in figure 10.

The Clear Fork equivalent succession along the south wall of Apache Canyon, which includes all of the lower Clear Fork, the Tubb, and part of the lower upper Clear Fork, measures as much as 400 ft (130 m) thick. This section includes about 160 ft (50 m) of lower Clear Fork, 40 ft (13 m) of Tubb, and 200 ft (65 m) of upper Clear Fork (fig. 10). Upper Clear Fork rocks are extremely well exposed along more than 2 mi (3 km) of outcrop, thus affording an opportunity to examine interwell-scale changes in facies, cyclicity, and petrophysics that cannot be observed in reservoir successions. Although lower Clear Fork rocks are less well exposed, they are nevertheless sufficient to serve as a direct analog to subsurface reservoirs (Ariza, 1998). Specific goals of outcrop studies are (1) to develop cycle models derived from Apache Canyon outcrops for application in Clear Fork reservoirs in the Permian Basin and (2) to analyze and interpret petrophysical relationships in well-constrained outcrops to provide an improved basis for interpreting subsurface data.

METHODS

Lower and upper Clear Fork–equivalent strata were studied along an approximately 2-mi continuous outcrop on the south wall of Apache Canyon (fig. 9). Sixteen primary sections were measured and described on a foot-by-foot basis. Average thickness of the sections was 300 ft. Sections were tied into photomosaic panels that were prepared by digitizing outcrop photos. Correlations were established by walking out cycle contacts between sections wherever possible and tracing them onto photomosaics. Twelve supplementary sections located between primary sections were described to constrain lateral facies and cycle relationships. Thin sections were collected in three of the primary sections to check facies identifications.

Porosity and permeability were measured in both vertical and horizontal sections along the south wall. Samples were obtained by drilling 1-inch-diameter core plugs in representative facies in two vertical sections (111 measurements). Plugs were also drilled along horizontal transects in two individual cycles in the upper Clear Fork to characterize lateral variations in porosity and permeability: 660 plugs were collected and analyzed along a 2,800-ft-long cycle transect, and 344 plugs were analyzed along a second, 1,795-ft-long cycle transect.

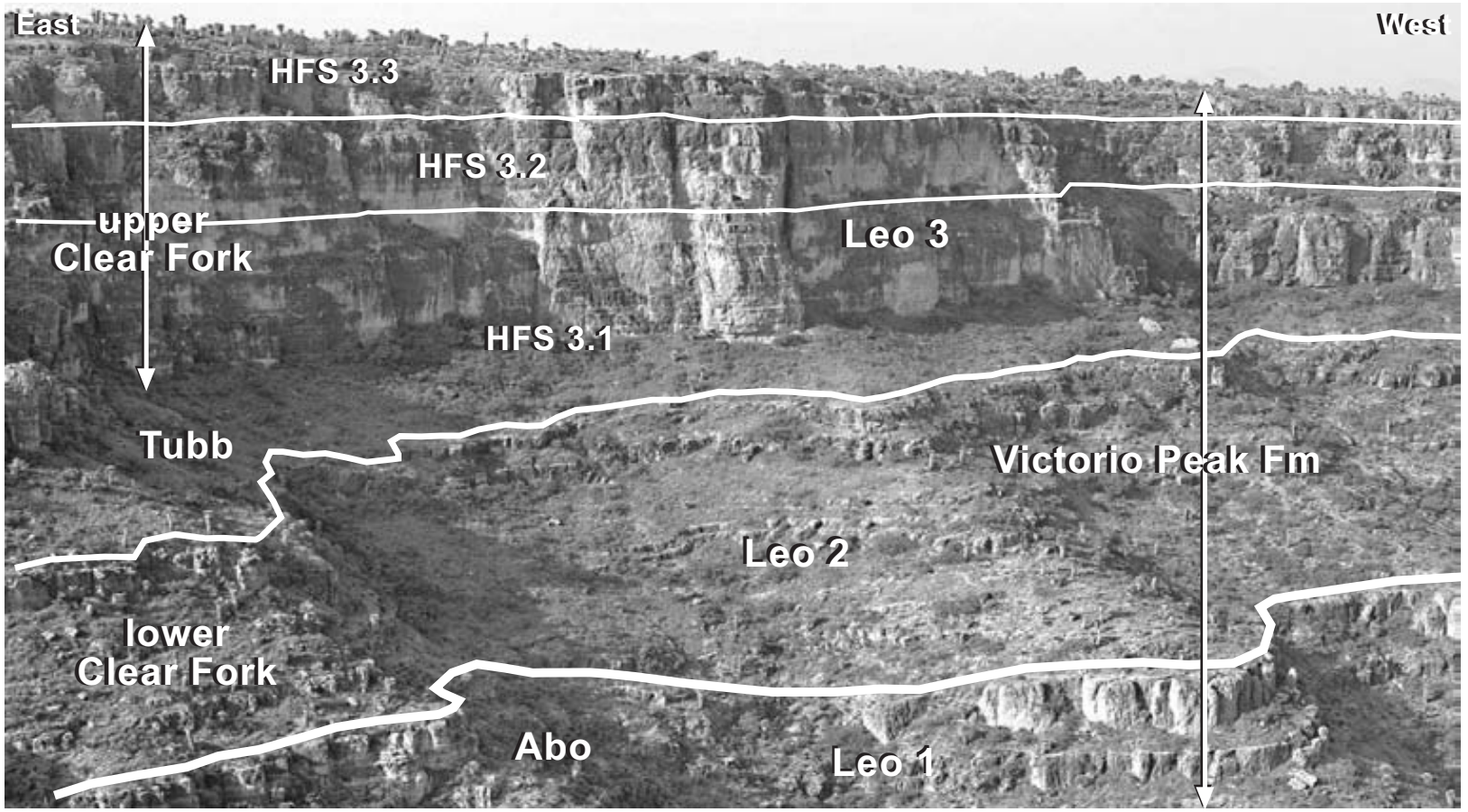

Figure 10. Photomosaic of south wall of Apache Canyon showing major sequence and formation boundaries.

CLEAR FORK FACIES IN APACHE CANYON

Clear Fork–equivalent outcrops in Apache Canyon contain eight major depositional facies: (1) ooid grain-dominated packstone/grainstone, (2) peloid grain-dominated packstone, (3) crinoid/peloid grain-dominated packstone, (4) peloid wackestone/packstone, (5) skeletal/peloid wackestone/packstone, (6) fusulinid wackestone/packstone, (7) tidal flat, and (8) silty mudstone/wackestone. Each of these facies is interpreted to represent distinctive depositional conditions of wave energy and accommodation and platform setting.

Facies

Ooid Grain-dominated Packstone/Grainstone

The term *grainstone* is used for those rocks that are grain supported, contain little or no mud, exhibit interparticle pore space (either unfilled or filled), and display visible crossbedding. Rocks that possess these properties but display no crossbedding are termed *grain-dominated packstones*. Because dolomitization commonly obscures bedding as well as subtle textural details, these rocks are not rigorously distinguishable.

The ooid grain-dominated packstone/grainstone facies is composed of abundant, well-sorted peloids, many of which are definable as ooids (fig. 11a). Grain size ranges from 150 to 350 μm. Where dolomitization obscures texture, ooids are distinguished by their larger grain size (fecal pellets are generally smaller than 150 μm). Most of these rocks in Apache Canyon display horizontal stratification or low-angle cross-stratification. Skeletal grains are locally common; crinoids and fusulinids are common in basinward deposits, whereas bivalves and gastropods are found in more platformward settings. Modern ooids are formed in platform-margin settings where relatively high wave energies are common (Ball, 1967; Harris, 1979). The presence of ooids, good sorting, crossbedding and the near absence of mud indicate that the ooid grain-dominated packstone/grainstone facies was deposited in relatively high wave-energy conditions. Where interparticle pores are not occluded by cement or sediment, these rocks display high porosity and permeability.

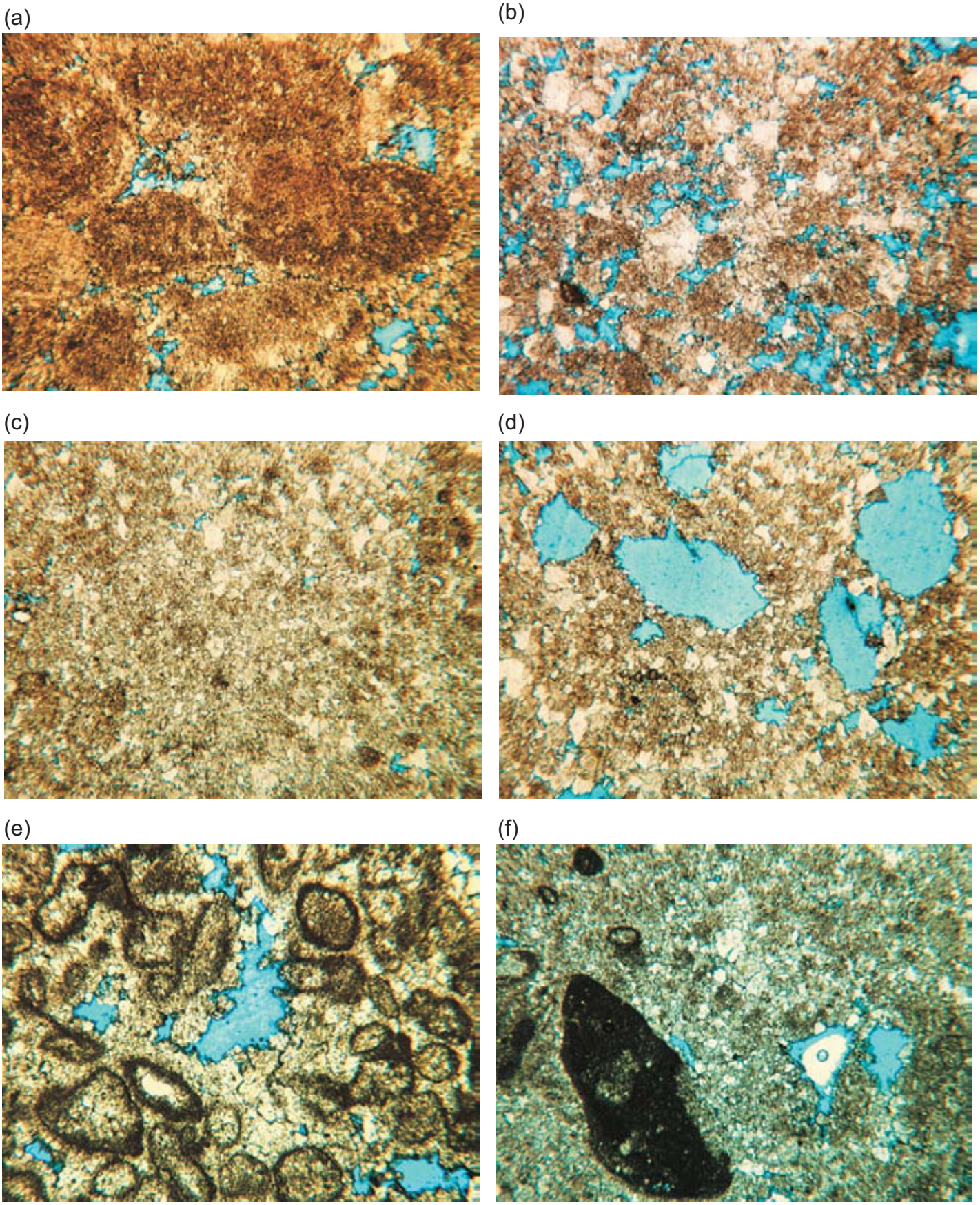

Figure 11. Thin-section photomicrographs of representative Clear Fork facies. (a) Ooid grain-dominated packstone/grainstone. Porosity: 7.3 percent; permeability: 7.5 md. Petrophysical traverse 1: 725 ft. Field of view 3.1 mm wide. (b) Peloid grain-dominated packstone. Porosity: 16.0 percent; permeability: 100.8 md. Petrophysical traverse 1. 1,800 ft. Field of view 3.1 mm wide.(c) Peloid wackestone/packstone. Porosity: 3.1 percent; permeability: 0.01 md. Petrophysical traverse 1, 1,300 ft. Field of view 3.1 mm wide. (d) Fusulinid wackestone/packstone. Porosity: 8.6 percent; permeability: 0.001 md. Petrophysical traverse 2, 715 ft. Field of view 3.1 mm wide. (e) Tidal-flat pisolite/coated grain packstone with fenestral pores. Porosity: 4.6 percent; permeability: 0.01 md. Petrophysical traverse 1, 35 ft. Field of view 3.1 mm wide. (f) Tidal flat peloidal wackestone with fenestral pores. Porosity: 6.3 percent; permeability: 0.02 md. Petrophysical traverse 1, 190 ft. Field of view 3.1 mm wide.

Peloid Grain-dominated Packstone

These are well-sorted, grain-supported rocks that contain visible carbonate mud and like grainstones exhibit interparticle pore space (either unfilled or filled). They grade into wackestone/packstone as mud content increases. Peloids comprise subspherical pellets that exhibit no discernible internal structure and most commonly range in size from 80 to 120 μm (fig. 11b). Ooids and skeletal debris are minor accessory grains in this facies. Most peloids are probably fecal pellets produced by infaunal sediment-feeding organisms. However, some grains may be small ooids, eroded clasts of mudstone, or rounded skeletal fragments. Peloid grain-dominated packstone grades into skeletal grain-dominated packstone with increasing skeletal content.

The fecal pellets that dominate this facies are produced by burrowing organisms in shallow-marine mud-rich, generally low energy, inner platform settings. In the modern Bahamas, for example, pelleted muds occupy broad expanses of the interior, wave-restricted platform of Andros Island (Purdy, 1963; Multer, 1977). Most of the pellets in these sediments, however, are poorly indurated and have little preservation potential during burial, their ancient rock equivalents being mudstones and pelleted mudstones (Milliman, 1974) rather than the packstones of this facies. Some pelleted muds in these low-energy settings, however, undergo early lithification and can be preserved (Shinn and Robbin, 1983). It is these deposits that are the precursors to the pellet grain-dominated packstone facies. Thus peloid grain-dominated packstones owe their origins more to early diagenesis than to deposition in wave-agitated environments, as is the case with conventional packstones (Dunham, 1961). The excellent sorting observed in these rocks, which is a key to their good permeability in reservoir settings, is a function of the sizes of the organisms that produced them rather than hydraulic processes. The causes of the early lithification of these pellets that is the key to their preservation as "packstones" are not well understood. However, Beales (1965) suggested cementation of such sediments is favored during sea-level-fall events.

Crinoid/Peloid Grain-dominated Packstone

This minor facies is composed dominantly of subspherical peloids and crinoids. Peloids range from about 100 to 350 μm in size. The size of these peloids suggests that they are poorly

preserved ooids, as does their association with crinoids. Crinoids are representative of normal-marine platform- and platform-top settings in Paleozoic rocks. They are relatively rare in Permian carbonate platform rocks in the Permian Basin, and this is especially true in the exposed Clear Fork succession in Apache Canyon and in the subsurface of the Permian Basin. Crinoid/peloid grain-dominated packstones are most abundant in the uppermost and easternmost of the outcrops in Apache Canyon, areas that are interpreted to represent the most seaward of the platform deposits at Apache Canyon on the basis of their crinoid content and other paleobathymetric indicators. They are also typically associated with ooid grain-dominated packstone/grainstone, supporting the interpretation that these peloids are ooids.

Peloid Wackestone/Packstone

These rocks are more mud-rich equivalents of peloid grain-dominated packstones (fig. 11c). Discernible peloids (which comprise both pellets and unidentifiable grains) are less abundant and commonly smaller, ranging from 120 μm to as small as 60 μm. Skeletal debris is locally present, most commonly consisting of mollusks. Pellets are generally well sorted. However, the abundance of mud indicates that this not the result of wave action but rather a function of the burrowing infauna. These rocks are found throughout the lower and upper Clear Fork successions in Apache Canyon but are most common in more landward (western end of the south wall) settings. They probably were formed in very low energy burrowed mud flats much like those developed in the interior of Andros Island mud flats (Purdy, 1963; Multer, 1977).

Skeletal/Peloid Wackestone/Packstone

These rocks are similar to and are intergradational to peloid wackestone/packstones but contain substantially higher volumes of skeletal debris. More open-marine faunas (fusulinids and crinoids) are dominant in the eastern parts of the south wall, whereas restricted faunas (mollusks) are common to the west. Like the more skeletal-poor peloid wackestone/packstones, these rocks represent low-energy deposition across the platform.

Fusulinid Wackestone/Packstone

The fusulinid wackestone/packstone facies typically comprises abundant fusulinids and peloids (fig. 11d). Fusulinids generally average 2 to 3 mm in diameter and range in length from 5

to 20 mm. Their abundance ranges from about 10 percent to as much as 40 percent. Peloids are primarily fecal pellets produced by burrowing, as attested by their size and sorting. Fusulinid-bearing rocks are most abundant in the upper Clear Fork at the eastern end of the south wall of Apache Canyon. Studies of other Permian successions in the Permian Basin demonstrate that fusulinids are most common in relatively open marine waters on the outer part of the carbonate platform in water depths of approximately 30 m (Sonnenfeld, 1991). As such, fusulinid wackestone/packstone deposits represent the deepest water facies in most middle Permian successions. Accordingly, like the tidal-flat facies, which records the shallowest water setting, this facies is a key indicator facies of sea-level-rise/fall history.

Tidal Flat

These rocks contain perhaps the most complex assemblage of textures, fabrics, and structures of all Clear Fork facies. Textures range from mudstone to grainstone, although wackestone and packstone are dominant. Allochems include intraclasts, peloids, skeletal debris (dominantly mollusks), coated grains, peloids, and pisolites (figs. 11e, 11f). Structures include fenestral pores (birdseyes), keystone vugs, stromatolitic laminations, mudcracks, and burrows. The most common lithologies are stromatolitic mudstone, pisolite packstone, and fenestral mudstone. These grade laterally and vertically into an array of intermediate intermixtures of these sediments and other lithologies including featureless mudstone, lithoclast breccia, and peloidal wackestone. Common to all of these deposits is direct evidence of or association with subaerial exposure. Because of this association with exposure and the wide diversity of sediment types, these rocks are grouped as a single facies: tidal flat. Although modern tidal flats contain subtidal, intertidal, and supratidal sediments (Shinn, 1983; Hardie and Shinn, 1986), only intertidal and supratidal sediments contain features that permit them to be reliably identified as belonging to the tidal flat. Accordingly, Clear Fork tidal-flat rocks exclude subtidal rocks, although such rocks may actually have been part of the tidal-flat complex. Because these rocks document exposure of the carbonate platform, this facies is a key indicator of platform accommodation and water depth. As such, it is a critical facies for defining patterns of sea-level rise and fall.

Silty Mudstone/Wackestone

These rocks are characterized in outcrop by yellowish to pinkish color and the presence of common small burrows (average 2 to 3 mm diameter). Silt content is highly variable, commonly accounting for only 10 to 20 percent of the rock. Allochems are generally rare, although skeletal debris (chiefly mollusks) and peloids are locally present. These deposits are essentially restricted to the interval designated as the equivalent of the subsurface Tubb. Because of their silt content and muddy nature, these rocks do not crop out well. Their generally covered outcrop expression as well as their lithologic character forms a readily definable break between the platform carbonate successions of the lower and upper Clear Fork.

Depositional Setting and Accommodation

Clear Fork–equivalent facies in Apache Canyon are much like those documented for younger (Guadalupian-age) Permian successions (for example, San Andres and Grayburg Formations) in the subsurface and in outcrops of the Permian Basin (Bebout and others, 1987; Sonnenfeld, 1991; Ruppel and Cander, 1988a, 1988b; Kerans and others, 1994; Kerans and Fitchen, 1995). Kerans and Ruppel (1994) and Ruppel and others (1995) used established interrelationships among these facies to construct a depositional model that relates facies to platform geography and accommodation (fig. 12). This model provides a basis for understanding the spatial distribution of facies and facies tracts on the platform.

Four major platform facies tracts are represented in the model. The innermost platform is dominated by tidal-flat facies (such as fenestral mudstones, stromatolitic mudstones, and pisolite wackestone/packstones) that show evidence of frequent exposure and thus minimum platform accommodation. The middle platform is characterized by mud-dominated facies (such as skeletal and peloidal wackestones) because of low accommodation (water depth) and low wave energy. Wave restriction is a function of distance from the open platform or position shoreward of the ramp crest. The ramp crest forms at the impingement point of open-marine wave trains and thus occupies a high-energy setting. Ramp-crest facies are dominated by ooid grainstones and grain-dominated packstones. Parts of the ramp crest commonly aggrade to sea level, and capping tidal-flat deposits are locally common. In many cases, evidence of exposure and tidal-flat deposition is apparent at the top of ramp crest successions. The outer platform marks the transition from

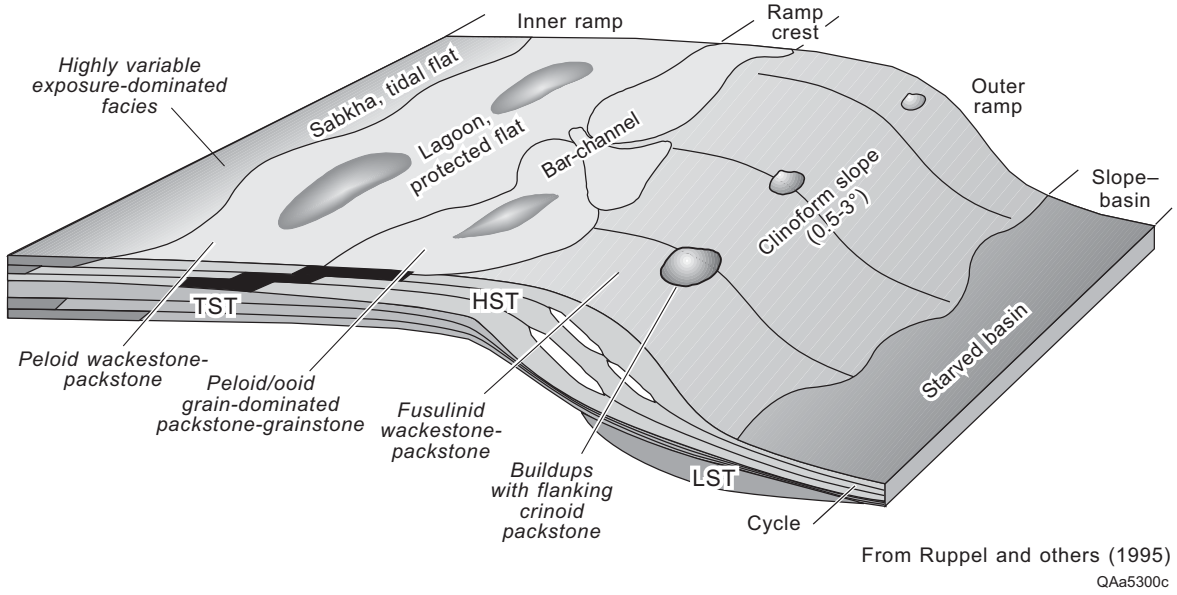

Figure 12. Depositional model for Permian shallow-water carbonate platforms in the Permian Basin. From Ruppel and others (1995).

shallow to deeper water conditions. This setting is dominated by fusulinid wackestone/packstones and locally by buildups with associated crinoid wackestone/packstones.

It should be pointed out that the model is a composite of Permian platform facies tracts, not all of which are developed on the platform at all times. Ramp crests, for example, are best developed in high-accommodation early highstand settings (Kerans and Fitchen, 1995); they are generally greatly reduced or absent in transgressive settings. Thus, this model is not designed to portray the detailed paleogeography at any discrete point in time. Instead, the model displays the accommodation-based distribution of major facies types. As such, it provides a basis for understanding and interpreting accommodation-driven facies stacking patterns and cyclicity. For example, since most platform cycles are asymmetrical, upward-shallowing cycles (parasequences of some authors), cycle boundaries are defined by the superposition of deeper water (higher accommodation) facies over shallower water (lower accommodation) facies. For example, inner platform cycles are defined by the superposition any subtidal facies over tidal-flat facies (which reflect minimum accommodation). Fusulinid-bearing rocks define deepening and cycle bases in any succession of platform rocks (because they represent minimum platform accommodation) wherever they overlie other platform facies.

DIAGENESIS

All rocks in the lower and upper Clear Fork successions in the study area have been dolomitized. As such, they are analogous to Clear Fork rocks that comprise subsurface reservoirs in the Permian Basin. Although truly definitive studies of the diagenesis of Leonardian carbonates have not been completed, work to date suggests that most Clear Fork dolomites were formed relatively early, by at least Guadalupian time (Saller and Henderson, 1998; Ye and Mazzullo, 1993; Ruppel, 1992; in press). Calcite is locally present in small amounts in the dolomites from the south wall of Apache Canyon, but both the distribution and character of these calcites suggest that they are due to late diagenesis. Some calcite is in the form of partial rims around open vugs. The optical character of these calcites and their occurrence suggest that they are due to partial replacement of anhydrite nodules. Other minor volumes of calcite cement encountered in these rocks may be the result of the precipitation of meteoric calcite during the Tertiary uplift of the Leonardian section.

The Clear Fork succession in Apache Canyon differs principally from its subsurface counterpart in the absence of anhydrite. Calcium sulfate, mostly in the form of anhydrite, is abundant in most occurrences of Clear Fork rocks in the subsurface. The absence of sulfate in outcrop probably attests to late dissolution and removal of anhydrite by meteoric waters. The presence of vugs in Apache Canyon outcrops, commonly the size of sulfate nodules observed in Clear Fork reservoirs, further supports this theory.

SEQUENCE STRATIGRAPHY

Outcrop studies demonstrate that the Clear Fork section in Apache Canyon consists of proximal outer ramp to ramp-crest to inner platform facies successions very much like the productive subsurface reservoir sections in the Permian Basin. The lower Clear Fork section (Leonardian sequence 2) can be subdivided into two high-frequency sequences (HFS), whereas the exposed upper Clear Fork section (part of Leonardian sequence 3) contains three HFS based on facies stacking patterns and lateral facies offsets (fig. 13). The Tubb siltstone interval forms the base of HFS 3.1, the basal HFS in Leonardian sequence 3 (fig. 13).

Leonardian 2: Lower Clear Fork Sequence Architecture

As in the subsurface, the lower Clear Fork section in Apache Canyon is underlain by the Abo. As described by Kerans and others (2000), the Abo is locally karsted and the overlying lower Clear Fork displays local variations in thickness and facies controlled by Abo paleotopography. Where karsting and associated thickness variations are developed, largely in platform marginal settings, the contact between the Abo and lower Clear Fork is a relatively sharp and undulating, unconformable surface. Updip throughout most of the south wall study area, however, no karsting is apparent and the contact is less pronounced. For the most part, however, the base of the lower Clear Fork is characterized by thin-bedded, light-colored tidal-flat deposits that are readily discernible from the more massive subtidal facies of the underlying Abo.

The lower Clear Fork comprises a single sequence that consists of a lower symmetrical high-frequency sequence (HFS 2.1) and an upper asymmetrical high-frequency sequence (HFS 2.2). HFS 2.1 is characterized by (1) a basal transgressive leg composed of tidal-flat and tidal-

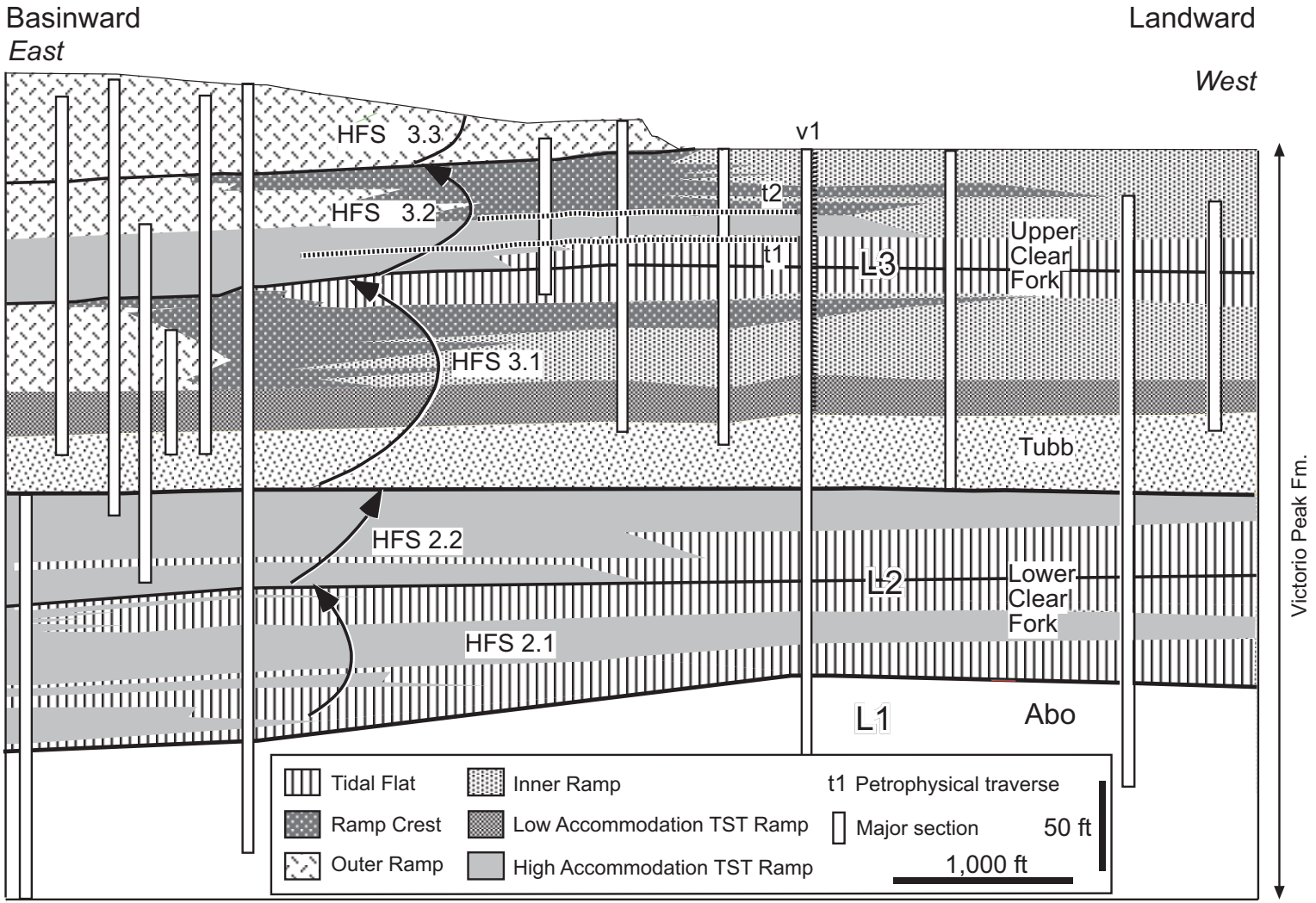

Figure 13. Cross section depicting the sequence architecture of Clear Fork equivalents along the southern wall of Apache Canyon.

flat-capped cycles, (2) a middle maximum flooding leg composed of subtidal cycles (high-accommodation transgressive systems tract (TST) ramp of fig. 13), and (3) an upper highstand leg of tidal-flat and tidal-flat-capped cycles (fig. 13). These three high-frequency sequence legs display reciprocal thickness and facies changes associated with decreasing accommodation to the west (landward). The middle subtidal leg, which is composed of open-ramp subtidal cycles having peloid-ooid packstone caps in distal sections, thins and grades into more restricted facies successions to the west (fig. 13).

HFS 2.2 is marked by a backstepping of subtidal cycles composed of skeletal wackestones (mollusks) and peloid-ooid packstones over the highstand tidal-flat deposits at the top of 2.1. This basal L2.1 transgression is readily definable in the more distal sections but more cryptic updip where these subtidal rocks grade into tidal-flat deposits, again reflecting the east-to-west decrease in accommodation (fig. 13). The actual HFS boundary may lie within the tidal-flat succession but is placed at the base of the subtidal rocks for convenience. Up section, HFS 2.2 is characterized by continued transgression and backstepping, which is demonstrated by progressively more open marine deposits upward. Unlike 2.1, HFS 2.2 displays no highstand turnaround to shallow-water deposition. It appears, on the basis of relationships in Apache Canyon and in the subsurface of the Permian Basin, that the absence of HFS 2.2 highstand deposits is the result of forced regression caused by rapid sea-level fall at the end of Leonard sequence 2 deposition, which left no depositional record, and/or subsequent erosion of the L2.1 highstand deposits.

Characterization of internal cycle architecture in the lower Clear Fork is compromised by variable-quality exposures in Apache Canyon. In tidal-flat-capped successions and less commonly in subtidal successions, 3- to 6-ft-thick (1- to 2-m-thick) cycles are definable in vertical sections but are generally not correlatable. However, subtidal cycle bundles, which average 15 to 30 ft (5 to 9 m) in thickness, can be correlated at typical interwell distances. These bundles typically consist of upward-shallowing successions that have skeletal wackestones at their bases and peloid-ooid packstones at their tops (fig. 13).

The quality of lower Clear Fork–equivalent outcrops in Apache Canyon is generally poorer than that of the underlying Abo or the overlying upper Clear Fork deposits. The difference is largely a result of the dominance of tidal-flat and other mud-rich inner ramp facies in the lower Clear Fork. This limits the resolution of cycle-scale facies stacking patterns. Nevertheless,

critical sequence stratigraphic relationships are clearly definable. Most significant of these are the accommodation-driven facies stacking patterns in L2 HFS (L2.1 and L2.2). These relationships (a symmetrical, shallow to maximum flooding to shallow facies succession for L2.1 and an asymmetrical shallow to deepening facies succession for L2.2) provide a basic model for interpreting and modeling subsurface reservoirs in the Permian Basin.

Leonardian 3: Upper Clear Fork Architecture

Only the lower part of the Leonardian 3 reservoir equivalent platform succession is exposed in Apache Canyon. However, these outcrops give a detailed picture of high-frequency sequence architecture that (1) is not apparent in more basinward successions and (2) is directly relevant to subsurface reservoir architecture characterization.

On the basis of outcrop relationships, we place the contact between Leonardian sequence 2 and Leonardian sequence 3 at the base of the Tubb silty interval (fig. 13). In most outcrop sections, this contact is poorly exposed and somewhat equivocal. However, locally there is evidence of truncation and possible karsting below this surface (Fitchen and others, 1995; Kerans, personal communication, 1998). In addition, there is a relatively sharp contrast in facies between the open-marine fusulinid wackestones and peloid-ooid packstones at the top of Leonardian 2 and the silt-rich shallow-water mudstones, wackestones, and tidal-flat rocks of the Tubb succession at the base of Leonardian 3. The placement of the Tubb at the base of a major sequence is also consistent with clastic sediment distribution patterns observed throughout the Permian in the Permian Basin. In the Grayburg Formation, for example, silt-rich sediments are most common at or near sequence and/or high-frequency sequence bases (Barnaby and Ward, 1994; Ruppel and Bebout, 1996).

Parts of three high-frequency sequences (HFS) are definable within Leonardian 3 in outcrops along the south wall of Apache Canyon (fig. 13). The lower two HFS (3.1 and 3.2) have well-defined transgressive bases and highstand tops; the third (3.3) contains only a transgressive base, the top having been removed by modern erosion. Patterns of facies- and sequence-offsets in the exposed Leonardian 3 section on the south wall of Apache Canyon indicate that all three HFS are part of the transgressive, or backstepping, leg of Leonardian 3.

HFS 3.1

The basal HFS of Leonardian 3, which reaches a maximum thickness of about 130 ft (40 m), documents the initial transgression of the Clear Fork platform following sea-level fall at the end of Leonardian 2. The basal third of the HFS is composed of the Tubb, which because of its high silt content is generally poorly exposed in outcrop (fig. 10).

Although the Tubb is largely covered, scattered exposures of the Tubb indicate that it consists of approximately 35 to 40 ft (8 to 13 m) of siltstone-based cycles, the lowermost of which possess peritidal caps. These high-frequency, exposure-capped cycles document gradual low-accommodation transgression associated with Leonardian 3 sea-level rise. Cycles in the upper Tubb contain more normal marine peloidal and skeletal packstone. Fitchen and others (1995) demonstrated that downdip, the Tubb clastic-rich interval passes into deposits of siltstone and sandstone that are demonstrably subaqueous. The Tubb is readily correlatable throughout most of the platform-top areas of Apache Canyon by its recessive weathering profile at the base of the much more resistant, cliff-forming outcrops of the overlying Clear Fork section.

Above the siliciclastic-rich Tubb interval is a succession of transgressive, fusulinid wackestone-based and grain-dominated, peloid packstone-capped high-frequency cycles of the siliciclastic-free, upper transgressive systems tract (TST). These rocks, which represent the basal upper Clear Fork, are low-accommodation sediments that accumulated during slow transgression in a relatively low energy setting. These deposits are isopachous and continuous over broad expanses of the platform.

Transgressive systems tract deposits are overlain by progressively higher energy, coarser grained, ooid-peloid grain-dominated packstones and grainstones of the HFS 3.1 highstand systems tract. To the east and possibly at least obliquely down depositional dip, these deposits pass into a thick amalgamated succession of ooid grainstones of the ramp-crest development. Farther northeast and more clearly downdip, high-energy ramp-crest deposits are replaced by fusulinid-based cycles typical of the outer ramp (fig. 13).

In contrast to the continuity of low-accommodation TST deposits of the basal HFS 3.1, there is considerable lateral variability in the overlying maximum flooding and highstand legs. Three distinct facies tracts are apparent: an updip or landward inner ramp succession, a downdip or basinward outer ramp succession, and an intermediate ramp-crest succession (fig. 13). The inner ramp is characterized by weakly cyclic mud-rich peloid packstones and wackestones, the

ramp crest by amalgamated peloid-ooid packstones and grain-dominated packstones, and the outer ramp by fusulinid-based and peloid packstone-capped cycles. An extensive tidal-flat succession forms the top of the inner ramp and ramp-crest successions.

The top of HFS 3.1 is best defined in the ramp-crest area. In this area, renewed sea-level rise is documented by the superposition of outer ramp fusulinid-bearing cycles over ramp-crest grainstone with incipient fenestral fabric and a thin peritidal cap. The sequence boundary is much more cryptic both updip and downdip. Outcrop tracing of the boundary shows that in the inner ramp area the top of HFS 3.1 lies in a thick section of tidal-flat deposits (fig. 13). It is apparent that tidal flats developed during late 3.1 highstand and during the early transgression of the overlying 3.2. Without 2-D control and traceable outcrops, the contact would mistakenly be placed at the top of the tidal-flat succession.

In the outer ramp, recognition of the HFS boundary is similarly difficult. There, peloid-ooid packstone-grainstone-capped cycles of the 3.1 highstand outer ramp succession are overlain by somewhat muddier and finer grained but similar peloidal packstones of the basal HFS 3.2.

In summary, HFS 3.1 comprises six distinct facies tracts or systems tracts: (1) a basal transgressive, low-accommodation silt-rich TST, (2) an overlying low-accommodation carbonate TST, (3) a maximum flooding to early HST outer platform, (4) a middle platform, maximum flooding to early HST ramp crest, (5) a maximum flooding to early HST inner platform, and (6) a sequence-capping, low-accommodation, late HST exposed platform top.

HFS 3.2

The internal sequence architecture of HFS 3.2 is similar to that of 3.1, having a basal transgressive ramp succession overlain by accommodation-controlled outer ramp, ramp-crest, and inner ramp facies tracts. The primary differences in the two HFS is the lack of siliciclastics at the base of 3.2 and the absence of a well-developed tidal-flat succession at the top. However, there are also differences in the transgressive legs of the two sequences that probably reflect inherited accommodation patterns on the platform. Unlike HFS 3.1, HFS 3.2 transgressive deposits are clearly differentiated into facies tracts: a high-accommodation transgressive systems tract (TST) ramp downdip and a tidal flat updip (fig. 13). Facies tract differentiation during 3.2 transgression probably reflects platform accommodation trends inherited from sedimentation patterns during HFS 3.1. The presence of thicker and more continuous fusulinid deposits in the

transgressive leg of HFS 3.2 (compared with 3.1) indicates higher accommodation flooding and deposition, which were probably a result of continued longer term (sequence-scale) sea-level rise.

The base of HFS 3.2 is defined by facies offset along the 2-D dip section; this is particularly easy to recognize above the 3.1 ramp crest, where high-energy ooid/peloid packstones and grainstones are overlain by lower energy skeletal (fusulinid/mollusks) wackestones representative of renewed flooding and sea-level rise. As described above, the HFS contact is much more difficult to define in more landward tidal-flat areas. For the most part, however, highstand exposure facies at the top of HFS 3.1 comprise pisolitic grain-dominated packstones and other diagenetically overprinted subtidal deposits. By contrast, basal transgressive HFS 3.2 deposits more commonly contain laminated, fenestral, mud-dominated tidal-flat facies. This contrasts with the findings of Kerans and Fowler (1995), who found that the tepee-pisolite complexes were more common in the transgressive legs of Grayburg Formation sequences. Further work is clearly needed to determine whether tidal-flat facies development in these Permian carbonate successions is systematic or random.

Although 2-D relationships demonstrate that the HFS 3.1–3.2 boundary lies well below the top of the tidal-flat succession (see fig. 13) , there is a sharp erosional contact at the top of the tidal-flat deposits that would probably be selected as the sequence boundary in 1-D or limited 2-D sections. This surface, which displays erosional truncation of underlying beds and the development of small solution pits, is a marine flooding surface that separates underlying exposed tidal-flat rocks from overlying subtidal fusulinid-bearing wackestone-packstone. The presence of this sharp contact above the true sequence boundary demonstrates the care that must be taken to accurately define the sequence stratigraphy of carbonate platform successions.

Inner and outer ramp facies tracts in HFS 3.2 are similar in facies composition and cyclicity to those of HFS 3.1. The 3.2 ramp-crest facies tract, however, differs from that of 3.1 in being more ooid rich. The greater abundance of ooids in 3.2 is consistent with an upward increase in accommodation and energy associated with continuing transgression through Leonardian 3.

The top of HFS 3.2 is similar to the top of 3.1. The contact with HFS 3.3 is best defined in the ramp-crest area where ramp-crest ooid-peloid grainstones and packstones are overlain by outer ramp fusulinid wackestones. Like the marine flooding surface near the base of 3.2, this surface displays erosional truncation and solution pitting of the underlying rocks. In the inner and

outer ramp areas, the contact is again more cryptic. There is no HFS-capping tidal flat at the top of HFS 3.2; nor is there a basal tidal-flat succession at the base of HFS 3.3. However, this pattern probably reflects the progressive westward (landward) flooding of the platform. HFS capping and basal tidal-flat deposits would probably be encountered farther east if these deposits had not been removed by modern erosion.

HFS 3.3

HFS 3.3 is truncated by modern erosion along the south wall of Apache Canyon. The transgressive leg of the HFS is exposed, but only in the eastern, more basinward, parts of the canyon (fig. 13). As discussed above, the base of the sequence is indicated by a sharp erosional contact between the ooid grainstone and grain-dominated packstone cycles of the upper HFS 3.2 and overlying basal fusulinid-dominated cycles of HFS 3.3. This surface, which is very similar in nature to the marine flooding surface in the lower TST of HFS 3, displays development of karst pits and as much as 3 ft (1 m) of relief. Although the contact between HFS 3.2 and 3.3 is less dramatic basinward, an obvious floodback is definable by the presence of abundant fusulinids at the base of HFS 3.3. Eastward, these outer ramp cycles become increasingly dominated by crinoids and brachiopods.

CYCLICITY AND CYCLE STACKING PATTERNS

Clear Fork–equivalent outcrops in Apache Canyon offer important insights into cycle composition and cycle stacking patterns that are useful in describing and interpreting subsurface Clear Fork reservoir successions. From studies of these outcrops it is apparent that cyclicity, facies stacking patterns, and cycle continuity vary among facies tracts. Within facies tracts, accommodation is perhaps the major control on cycle development.

Transgressive Systems Tract Cyclicity

Facies stacking patterns in Clear Fork transgressive systems tracts vary depending on accommodation. High-accommodation TST cycles (fig. 14) are typical of outer platform settings. In Apache Canyon, these cycles are well developed in distal parts of HFS 3.2 and 3.3 (in the

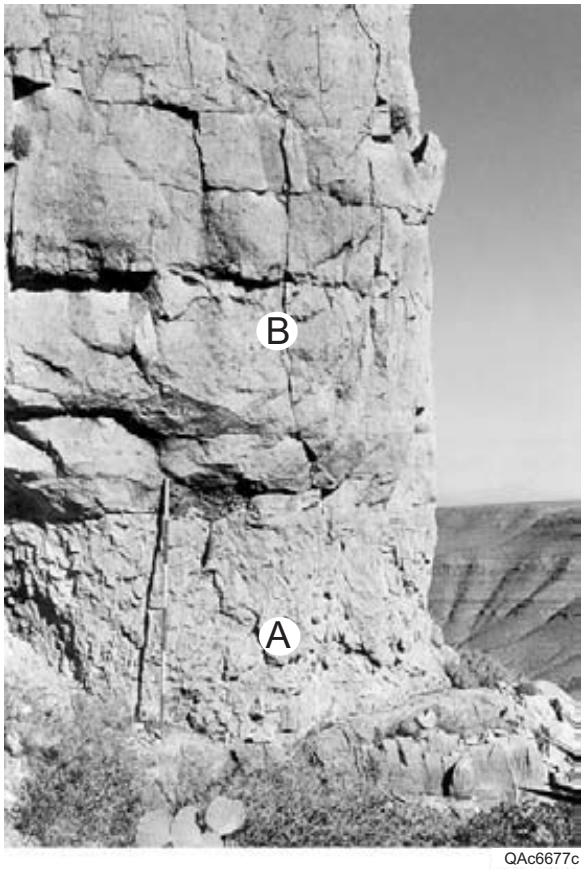

Figure 14. Outcrop photograph of typical high-accommodation transgressive cycle. Cycle base (A) is composed of burrowed fusulinid-rich wackestone; top (B) is peloid-skeletal packstone. Staff, which is 6 ft long, rests on cycle base. HFS 3.2.

eastern part of the canyon). These cycles have fusulinid wackestone-packstone bases and ooid-peloid grain-dominated packstone tops (fig. 15a). Commonly, cycle tops are strongly burrowed, making precise delineation of cycle boundaries difficult because of admixing of sediments from the overlying cycle into cycle-top deposits. In more proximal settings, especially in or near the ramp crest, cycle tops may comprise high-energy grainstones containing mixtures of ooids, peloids, and skeletal debris; cycle bases are typically finer grained peloid packstones with scattered skeletal debris (fig. 15b). In some instances, ramp-crest cycles are amalgamated, although this is most common in highstand successions.

Low-accommodation TST cycles differ from the above principally in being more mud rich and finer grained. These deposits are characteristically developed in more proximal platform settings during early transgression. Low-accommodation subtidal cycles are lower energy, updip equivalents of the high-accommodation cycles of the outer ramp discussed above. These cycles, which are best developed in the transgressive leg of HFS 3.1 (basal upper Clear Fork), are characterized by skeletal-rich bases and peloidal tops (fig. 16). Cycle boundaries are gradational and symmetrical: typical for subtidal transgressive cycles. The continuity of these cycles is among the highest in the Clear Fork. Individual cycles can be traced for more than 1.5 mi (2.5 km) along the outcrop. Textural contrast between cycle base and top is small, however. Accordingly, these cycles may not express systematic petrophysical differences in subsurface reservoirs.

More updip low-accommodation TST cycles are dominated by tidal-flat successions. These cycles typically comprise peloidal mudstone-wackestone bases and exposure caps (fig. 17a). Such cycles characterize basal deposits of HFS 2.1 and 2.2 (lower Clear Fork) in Apache Canyon. These cycles are commonly difficult to distinguish from exposure cycles found in highstand settings, for example, at the top of HFS L3.1 (figs. 13 and 17b).

Highstand Systems Tract Cyclicity

Typical highstand systems tracts (HST) are poorly developed in low-accommodation HFS at Apache Canyon (HFS 2.1 and 2.2 are low-accommodation HFS at least in the study area). However, they are well represented in the upper legs of Leonardian HFS 3.1 and 3.2 (fig. 13). Two types of HST cycles are dominant (fig. 18). Cycles in distal or open ramp settings contain

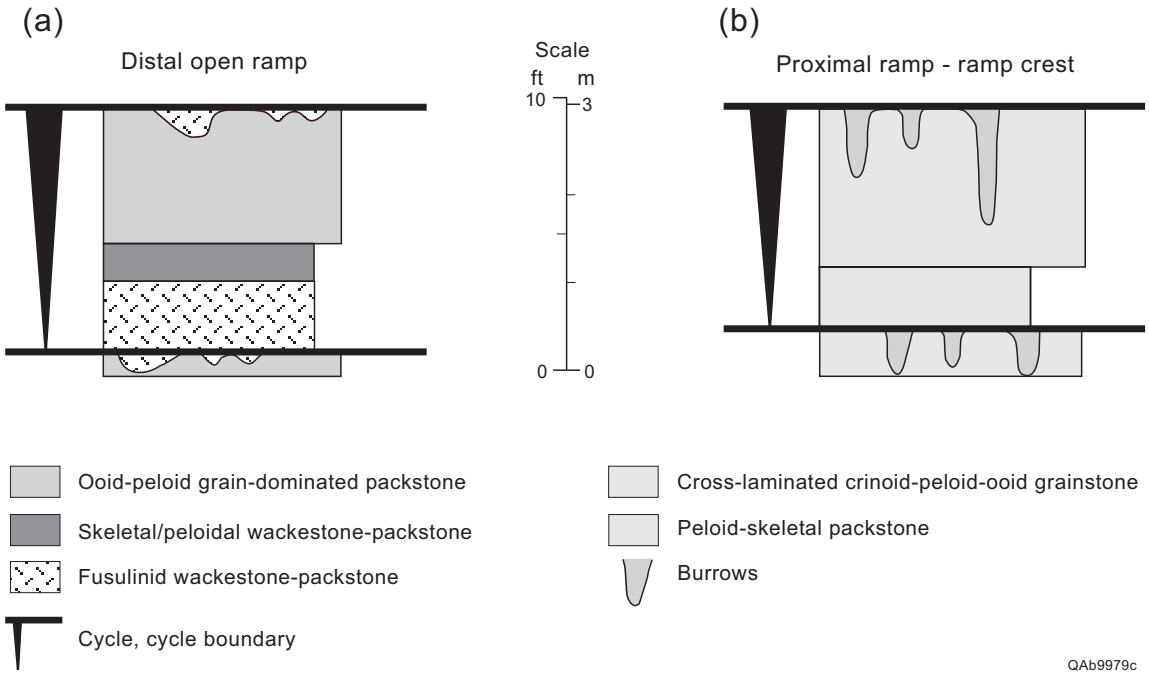

Figure 15. Characteristic facies stacking patterns in high-accommodation, transgressive systems tract cycles.

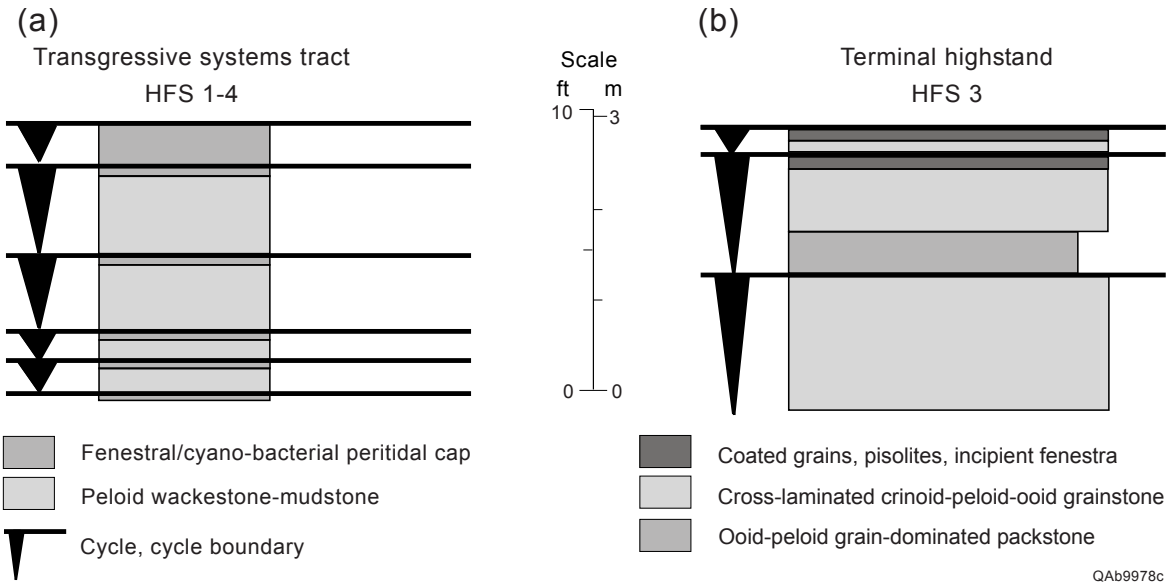

Figure 16. Outcrop expression of cyclicity in low-accommodation transgressive systems tract cycles. HFS 3.1.

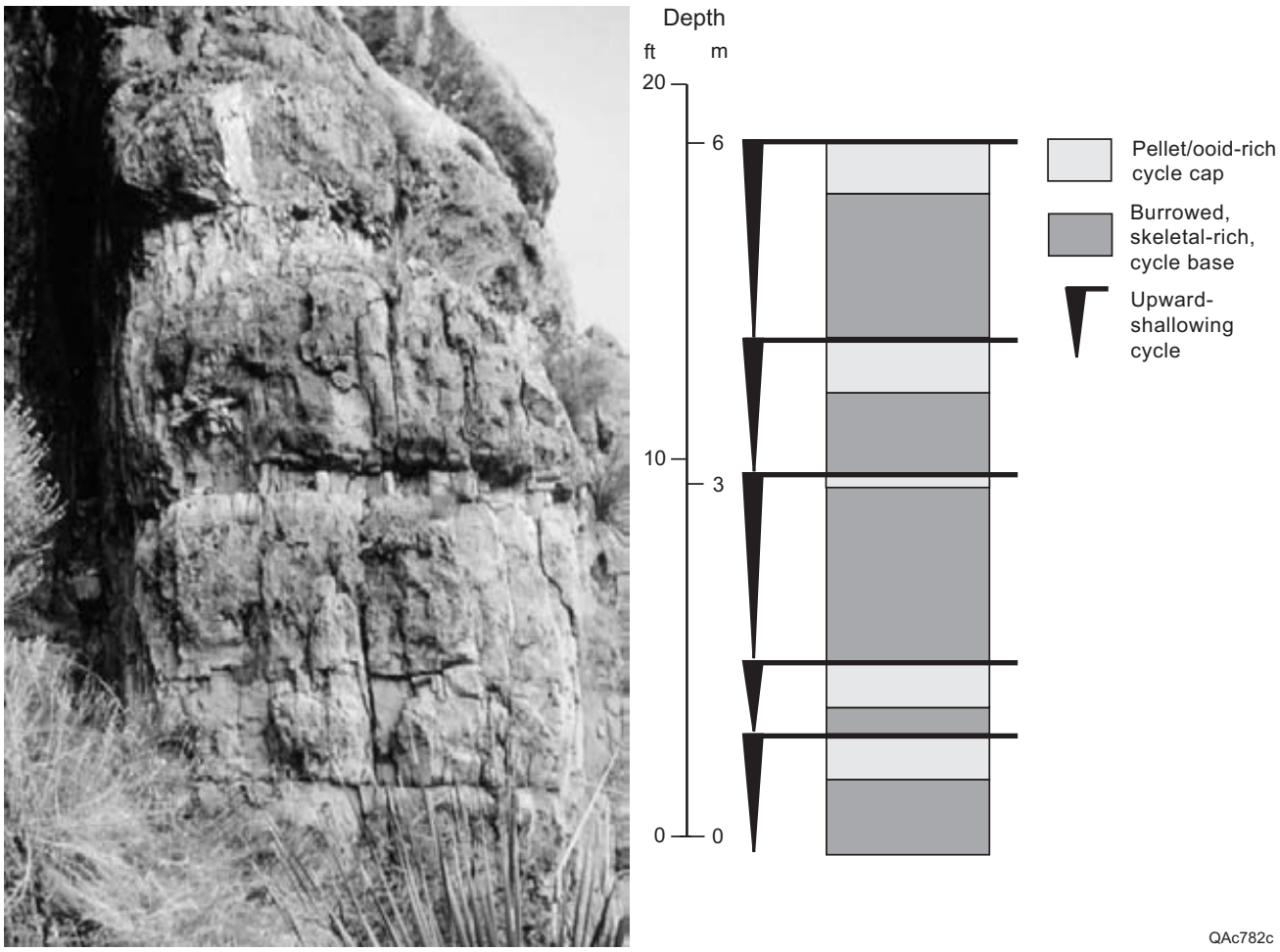

Figure 17. Styles of exposure-capped cycle development in the Clear Fork of Apache Canyon.

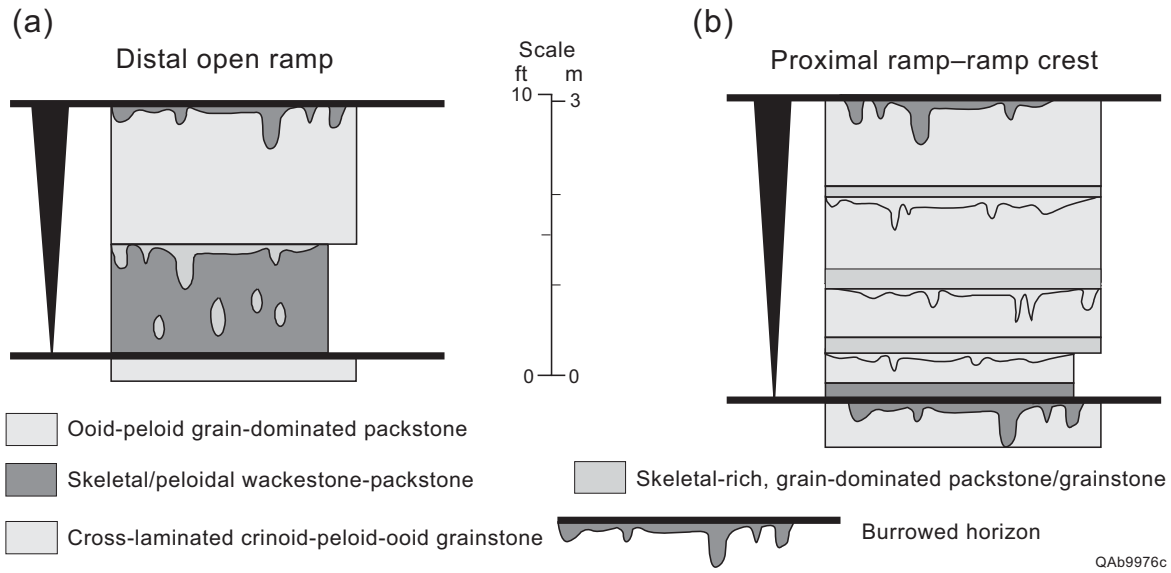

Figure 18. Styles of cyclicity in Clear Fork highstand systems tracts.

peloidal-skeletal packstone-grain-dominated packstone bases and ooid-peloid grain-dominated packstone tops (fig. 18a). Although similar to distal ramp TST cycles (fig. 15a) these cycles differ in containing only rare fusulinids. Instead they contain a mixed skeletal complement of mollusks, brachiopods, and crinoids. Cycle-base facies are typically highly burrowed and weather to rough irregular surfaces.

Proximal HST cycles reflect higher energy conditions of the ramp crest. They typically comprise amalgamated grain-dominated packstone to grainstone successions (fig. 18b). Cycle boundaries are commonly difficult to define, although locally they are marked by vertical burrows that contain skeletal sediment fill (fig. 18b). These cycles are common in the highstand ramp crests of HFS 3.1 and 3.2 (fig. 13).

Terminal HST cycles display the effects of overprinting early diagenesis related to exposure during late highstand and ensuing sea-level fall. These cycles, which are common in the top of HFS 3.1 in Apache Canyon overlying and landward of the ramp crest (fig. 13), are locally difficult to distinguish from tidal-flat deposits. Most, however, are composed of ooid-peloid grain-dominated packstones to grainstones that display pisolite formation and the development of keystone vugs in exposed, high-energy ramp-crest deposits (fig. 17b).

Cycle and Facies Continuity

Facies continuity is greatest in Leonardian TST successions. This is especially apparent in basal cycles of HFS 3.1 and HFS 3.2. In both, basal transgressive cycles and component facies can be traced for more than 1 mi (1.6 km) along the south wall of Apache Canyon. Although facies undergo minor changes in allochem content (principally a basinward increase in cycle-base fusulinid content), cycles are correlative throughout this distance (fig. 19). In the case of HFS 3.1, cycle continuity is consistent with flooding a relatively flat topped platform. This is supported by the character and continuity of the siliciclastic-rich cycles of the underlying Tubb succession. The character of these low-accommodation transgressive cycles is displayed in figure 19. Weathering patterns (fig. 16) permit these cycles to be traced along the entire length of the outcrop.

Cycle continuity is also excellent in the transgressive leg of HFS 3.2. This is perhaps somewhat surprising considering the depositional relief developed during HFS 3.1 highstand

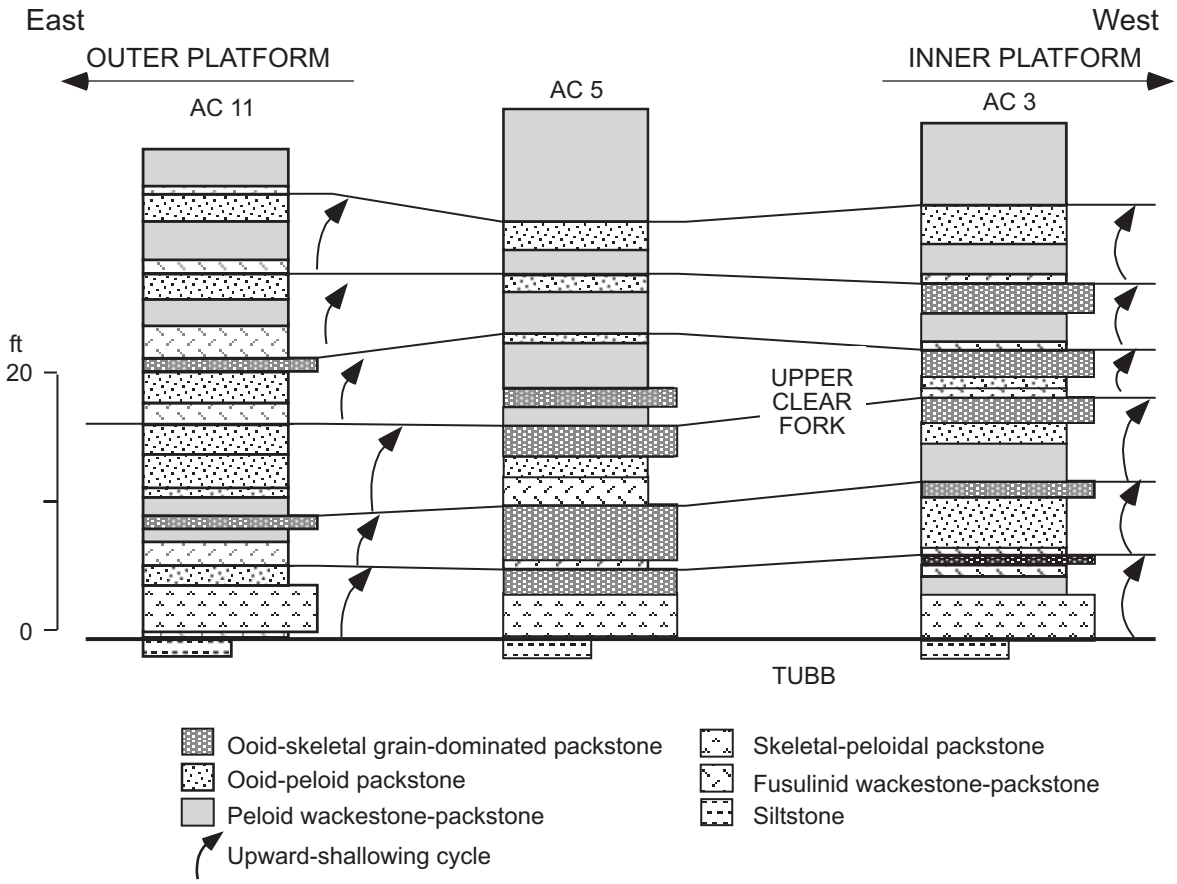

Figure 19. Correlation of highly continuous transgressive cycles in HFS 3.1.

indicated by the change from exposure overprinted ramp-crest to outer ramp deposits (fig. 13). Good continuity in TST deposits suggests that this relief was filled by early TST deposition along the outer ramp before highly continuous TST cycles were deposited. Figure 20 depicts cycle development and continuity in the HFS 3.2 transgressive deposits and in the overlying ramp crest at the turnaround from TST to highstand. The basal cycle of this set of cycles (part of the TST) displays nearly constant facies stacking relationships along more than 1 mi (1.6 km) of outcrop exposure. The overlying early highstand cycles, however, display less lateral continuity because of amalgamation of cycles and facies in ramp-crest areas.

Cycle Definition and Correlation

Facies relationships expressed in the Leonardian in Apache Canyon offer important insights and caveats to recognizing and defining cycles in subsurface Clear Fork Group reservoirs. It is significant that the styles of cyclicity and internal facies stacking patterns exhibited here are consistent with and similar to styles documented from outcrop studies of Guadalupian reservoir successions (Sonnenfeld, 1991; Barnaby and Ward, 1994; Kerans and others, 1994; Kerans and Fitchen, 1995). This is perhaps somewhat surprising considering how difficult cycle recognition and correlation have proven to be in many Clear Fork reservoirs. Nevertheless, basic facies stacking patterns are consistent with models of Permian depositional environments and paleogeography developed from studies of Guadalupian outcrops and reservoirs (fig. 12). Complications to standard Permian cycle styles are apparent in the Leonardian of Apache Canyon, however, that make cycle definition and recognition difficult.

In contrast to Guadalupian cycles, Clear Fork cycles appear to be dominated by lower energy deposition. This is supported by the rarity of ooid-rich grainstones and the dominance of peloidal wackestones and packstones. Because of the prevalence of lower energy conditions, cycle boundaries are commonly gradational and more difficult to define. Throughout most of the Clear Fork succession in Apache Canyon, cycles are best defined by contrasts in skeletal and nonskeletal allochems. In general, subtidal cycles are composed of poorly sorted, skeletal-rich, burrowed, muddier bases and well-sorted, skeletal-poor, peloid- to ooid-rich tops. Examples are shown in figures 12, 13, and 15. Key indicators of cycle definition are thus sorting, skeletal distribution, burrowing, and grain size.

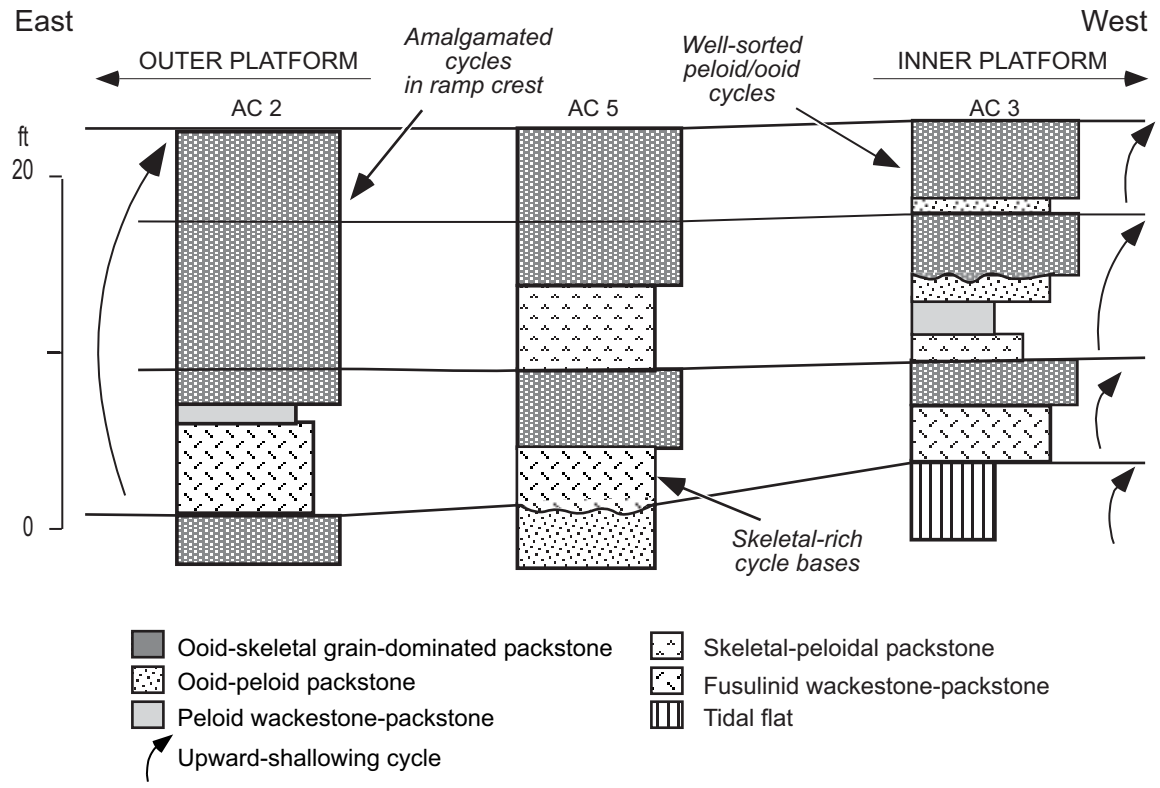

Figure 20. Correlation of late transgressive cycles and early highstand cycles in the ramp crest to inner ramp area (HFS 3.2).

Infaunal burrowers have contributed significantly to Leonardian depositional processes, as is evident from the abundant pellets in these shallow-water-platform sediments. Although much of the burrowing is associated with slower rates of sedimentation in cycle-base facies, burrows are also very common at cycle and bed contacts. The presence of abundant burrows in cycle bases enhances their outcrop recognition by creating distinctive weathering styles (figs. 14 and 16). Vertical burrowing at cycle and bed tops, however, produces intermixtures of textures and sediment types that make positioning of cycle boundaries difficult. For example, in many cases, fusulinids and other skeletal debris are admixed into cycle-top facies (fig. 15). This means that cycle tops may contain common to abundant skeletal material due to postcycle burrowing.

Cycle and Facies Tract Dimensions

Styles of cycle development vary systematically among facies tracts. Aspects of these variations that have potential significance in defining reservoir flow properties include facies tract width, cycle continuity, cycle thickness, and textural contrast. Each of these can be measured in the L3 (upper Clear Fork) succession of continuous outcrops along the south wall of Apache Canyon (table 1).

Table 1. Properties of Clear Fork cycles and facies tracts.

Facies tract	Tract width	Cycle continuity	Cycle thickness	Textural contrast
Low-accommodation TST platform	Thousands of feet (>5,000)	Width of facies tract	5–10 ft (2–3 m)	Subtle
High-accommodation TST platform	Thousands of feet (>5,000)	Width of facies tract	10 ft (3 m)	Marked
Outer platform HST	Thousands of feet (>2,000)	Width of facies tract	5–10 ft (2–3 m)	Marked
Low-energy inner platform HST	Thousands of feet (>3,000)	Variable (<2,000 ft)	10–20 ft (3–6 m)	Variable
Ramp crest	Narrow (<2,000)	Variable	Variable 10–20 ft (3–6 m)	Variable
Tidal-flat TST, HST	Thousands of feet (>5,000)	Very limited	2–6 ft (1–2 m)	Variable

Because facies tracts have relatively consistent styles of cycle development and continuity, a knowledge of the extent of both cycles and facies tracts can be important in developing models for reservoir flow. The outcrops along the south wall probably extend in a direction that is somewhat oblique to depositional dip; thus dip-versus-strike dimensions are not certain. A measure of facies tract width and cycle extent (continuity) from the Apache Canyon outcrops is nevertheless valuable because, in most cases, depositional strike and dip are also poorly known in the subsurface. A knowledge of cycle thicknesses and textural contrast is important for developing a basis for defining cycles and component facies and interpreting and modeling vertical permeability. As used here, textural contrast refers to the textural contrast at cycle boundaries. If great, this contrast can be the basis of marked vertical changes in permeability.

Both low-and high-accommodation TST tracts have large lateral extents. This is explained by the flat character of the antecedent platform and the resulting widespread similarity of accommodation conditions across the platform during transgression. In Apache Canyon these facies tracts can be traced for at least 5,000 ft, the length of the studied outcrop. It is possible that their true extent is even greater. Individual cycles can be traced for the full extent of these TST facies tracts. It is, in fact, the cycle continuity (demonstrated by actual tracing of cycles on photomosaics) that defines the extent of the facies tract. Cycle thicknesses are similar in both TST tracts, although, not surprisingly, cycles appear to be slightly thicker in the higher accommodation TST. The textural contrast between component facies (at cycle boundaries and within cycles) is substantially greater in the high-accommodation TST (figs. 13 and 14; table 1). This is a result of the higher energy conditions associated with higher accommodation settings even in basal HFS TST tracts. These differences in contrast mean that high-accommodation TST cycles may result in a cyclic vertical permeability structure, whereas the low-contrast cycles of the low-accommodation TST (fig. 16) may not.

Highstand Clear Fork facies tracts display generally shorter dimensions and possess more variable properties of cycle continuity, thickness, and textural contrast (fig. 18; table 1). This reflects the partitioning of the platform during highstand by wave- and energy-related carbonate deposition. In terms of facies tract dimensions, the Clear Fork ramp crest is especially noteworthy in that it displays a dip dimension of as short as 2,000 ft or less (fig. 13). This is particularly significant when it is considered that the facies of the ramp crest (ooid/peloid grain-

dominated packstones and grainstones) are potentially the most porous and permeable in the succession. The outer and inner platform tracts have significantly greater extents, being limited by the platform margin and updip strandline, respectively. Cycle continuity and textural contrast in the outer platform HST are similar to that found in the high-accommodation TST; this is due to the similarity in cycle composition and facies stacking between the two tracts. By contrast, these properties vary substantially in the ramp crest and inner platform. In the case of the former, this is a result of local cycle amalgamation. On the updip and downdip margins of the ramp crest, cycles display good continuity and strong textural contrast at cycle boundaries. In the high-energy center of the ramp crest, however, some muddier subtidal bases are absent, resulting in reduced textural contrast at cycle boundaries and an apparent thickening of cycles. In the inner platform, cycle continuity is difficult to define because of the low contrast in dominantly muddy facies.

Late HST and early TST tidal-flat tracts also exhibit rather extensive facies tract development (table 1). In Apache Canyon, HST tidal-flat facies extend updip beyond the study area (at least 5,000 ft). Cycles in the tidal-flat tract are thinner than in other tracts (fig. 17; table 1), and continuity is the lowest in the Clear Fork outcrop succession. Accordingly, textural contrast across cycle boundaries is highly variable and unpredictable. This reflects the widely varying conditions on the tidal flat and the resulting heterogeneous array of sediment types.

POROSITY AND PERMEABILITY

Porosity and permeability data were collected using 1-inch plugs drilled from upper Clear Fork outcrops on the south wall of Apache Canyon in both vertical and horizontal traverses. Samples were collected at 111 locations on vertical measured sections to obtain facies-specific petrophysical data. These data demonstrate a close similarity between facies and rock fabrics in the Clear Fork outcrops of Apache Canyon and Clear Fork reservoir data sets in terms of both porosity distribution and porosity/permeability relationships.

Petrophysical data collected from plugs in the vertical section (fig. 13) are representative of the overall facies assemblage in the upper Clear Fork in Apache Canyon and are similar to those encountered in most subsurface reservoir successions. Porosity varies directly with depositional texture (fig. 21): grain-dominated rocks exhibit the highest average porosity of 10 percent (fig. 21a), packstones have 7 percent, and wackestones have 5 percent (fig. 21b, c).

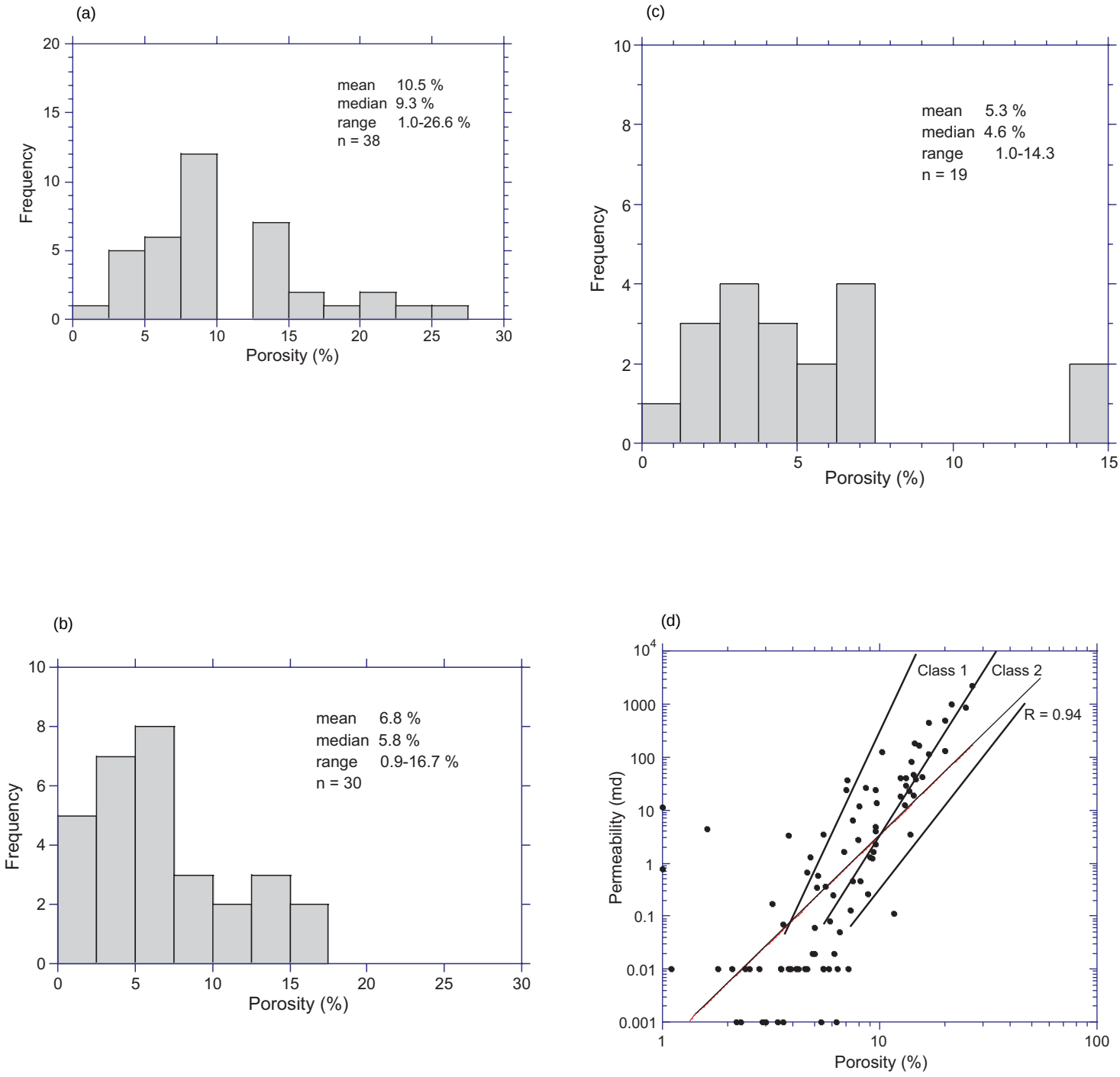

Figure 21. Petrophysical data from vertical measured sections in the upper Clear Fork section at Apache Canyon. (a) Histogram of porosity distribution in mud-dominated rocks (wackestones and packstones). (b) Histogram of porosity distribution in packstones). (c) Histogram of porosity distribution in grain-dominated rocks (packstones and grainstones). (d) Cross plot of permeability and porosity for all rocks (dominantly subtidal) in the L3 sequence at Apache Canyon.

Permeability displays a good fit to porosity in these samples of dominantly subtidal Clear Fork facies and plot in the petrophysical class 1 field of Lucia (1995) (fig. 21d).

Petrophysical plug data were also collected along horizontal traverses within two individual cycles, both in the transgressive leg of HFS 3.2 (fig. 13). The first traverse lies within a basal transgressive cycle that grades from fenestral and pisolitic tidal-flat deposits at the west end (updip) to grain-dominated packstone (downdip). The purpose of sampling this cycle was to examine lateral changes in petrophysical attributes along a continuous horizontal transect at the interwell scale across a facies transition from tidal flat to subtidal and within a rock-fabric layer. Porosity and permeability data were obtained from 414 samples drilled along a 2,740-ft horizontal traverse at 5-ft spacing, and thin sections were made from every fourth sample.

The samples were cut into 696 plugs, the longer samples being cut into multiple 1-inch plugs. Sample examination found that 218 samples had fractures and 44 have large vugs. Statistical analyses were performed on the complete data set and on groups having fractures and vugs. Porosity and permeability statistics of the fractured and unfractured groups are similar: all differences can be explained by sampling variability at the 5-percent significance level. The vuggy group has means and variance of both porosity and permeability larger than those of the other groups.

As expected, comparison of porosity and permeability data from this transect shows distinct differences between tidal-flat facies and subtidal facies. Tidal-flat rocks are characteristically low porosity (average: 5.3 percent; maximum 11 percent; fig. 22a) and low permeability and display a poor relationship between porosity and permeability (fig. 22b). Subtidal rocks, which along much of the traverse consist of medium crystalline mud-dominated dolopackstone and ooid/peloid grain-dominated packstone, display much higher porosity (average: 8.9 percent; maximum 28.7 percent; fig. 22c) and permeability and a good relationship between the two (fig. 22d). The data plot within the petrophysical class 1 field, although the rock-fabric descriptions are typical class 2 fabrics. This characteristic is also found in the South Wasson Clear Fork field.

Petrophysical data from a second cycle traverse are similar. This cycle, which is at the top of the HFS 3.2 TST (fig. 13), is composed of basal burrowed skeletal wackestone and capping skeletal-peloid grain-dominated packstone (fig. 14). Petrophysical sampling was confined to the

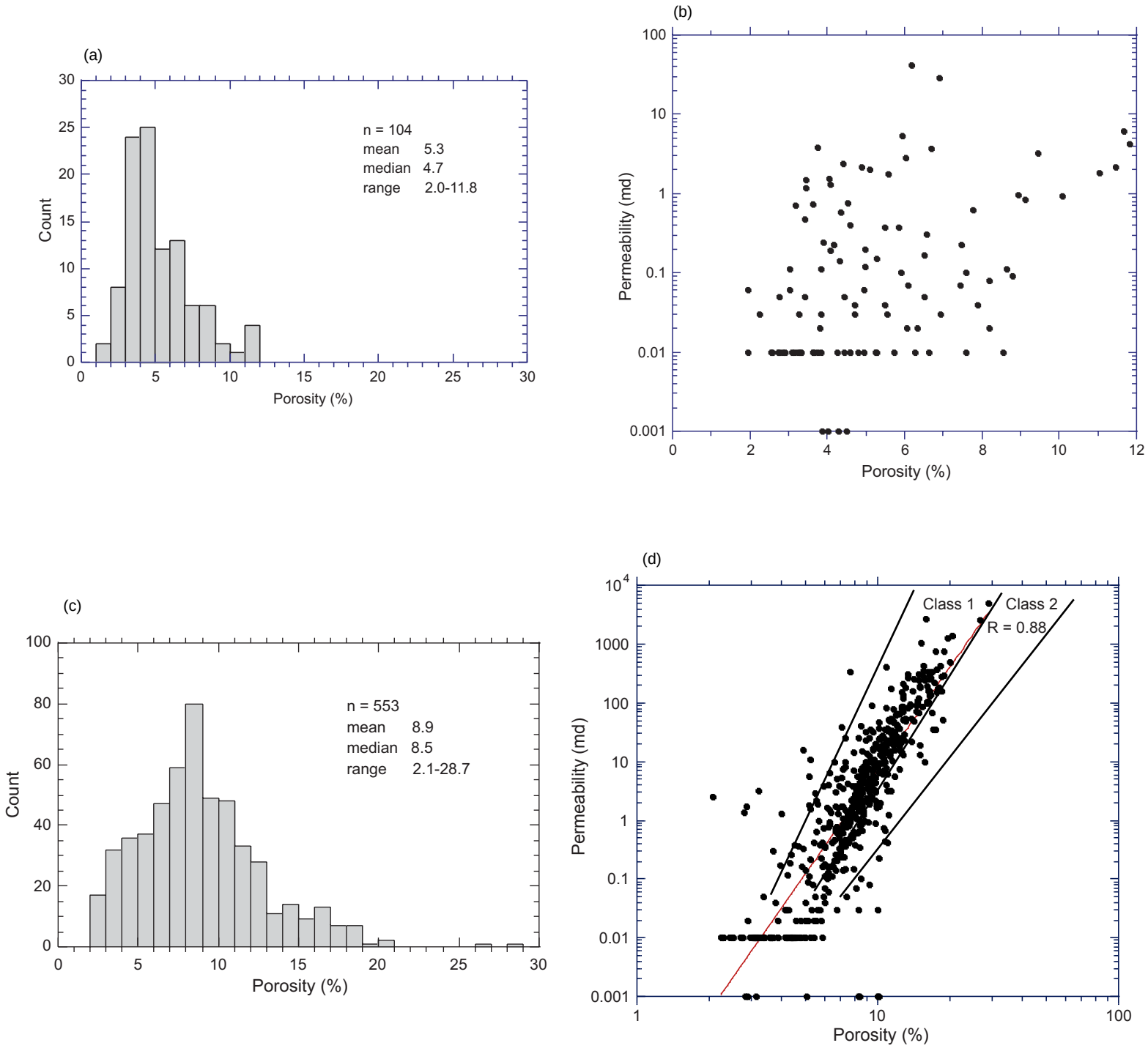

Figure 22. Petrophysical data from 2,800-ft horizontal traverse in a single cycle (L3 TST) of the upper Clear Fork at Apache Canyon. (a) Histogram of porosity distribution in tidal-flat rocks. (b) Crossplot of porosity and permeability in tidal-flat rocks. Note that there is no apparent relationship between porosity and permeability. (c) Histogram of porosity distribution in grain-dominated packstone subtidal rocks. (d) Crossplot of porosity and permeability in grain-dominated subtidal rocks (ooid/peloid packstones) illustrating that the data fall within petrophysical class 1. Line is power-law fit.

cycle top, which displays generally consistent facies along the entire south wall. Average porosity from this cycle is 12 percent, slightly higher than measured in the cycle capping ooid-peloid grain-dominated packstone of traverse 1 (fig. 23a), whereas permeability is somewhat lower and plots in the class 2 field (fig. 23b). Thin-section study shows that the packstones of this cycle contain more moldic porosity than do the ooid/peloid grain-dominated packstone of traverse 1.

The spatial statistics of these data have been discussed by Jennings in two publications (Jennings, 2000, and Jennings and others, 2000). Both porosity and permeability data from cycle traverse 1 display high spatial variability similar to that which we have observed elsewhere and have come to expect from dolomitized carbonate outcrops (fig. 24). Longer range features include a general increase in permeability with distance from the start of the traverse, two average-porosity and --permeability contrasts at about 400 and 1,200 ft, and a 180-ft wavelength periodicity. The general permeability increase is in a direction corresponding to increasing wave energy and may be related to a decrease in mud content or an increase in grain size and sorting. The two average-permeability contrasts have gradational transitions over a distance of several hundred feet, not abrupt jumps. The contrast at 400 ft corresponds to a facies transition from tidal-flat to subtidal rocks. The similar contrast at 1,200 ft is, however, contained entirely within the subtidal facies. The 180-ft periodicity exists in both porosity and permeability with and without the fractured and vuggy samples. It does not correspond to changes in facies, texture, or rock fabric from either outcrop observations or examination of 122 thin sections.

The semivariogram computed from all the data has power-law behavior, with a slope of about 0.14 in the 5- to 100-ft range (fig. 25) The semivariogram computed from only the unfractured and nonvuggy plugs is noisier because of the fewer data: otherwise it is similar. A single semivariogram point at 1-inch separation computed from multiple plugs at many sample locations indicates a steeper semivariogram slope at scales smaller than 5 ft. The relatively coherent 180-ft-wavelength periodicity produces at least five semivariogram oscillations that are more distinct in a smoothed semivariogram computed with a lag tolerance five times greater than the lag spacing. A J-Bessel model with a β near -0.5 can be fit to the semivariogram.

Preliminary examination of the data from traverse 2, however, does not reveal such fluctuations. However, the inability to recognize the oscillations in this data set may be the result of the shorter sample length and fewer sample points. The causes and significance of these petrophysical fluctuations are the subject of continuing research.

(a)

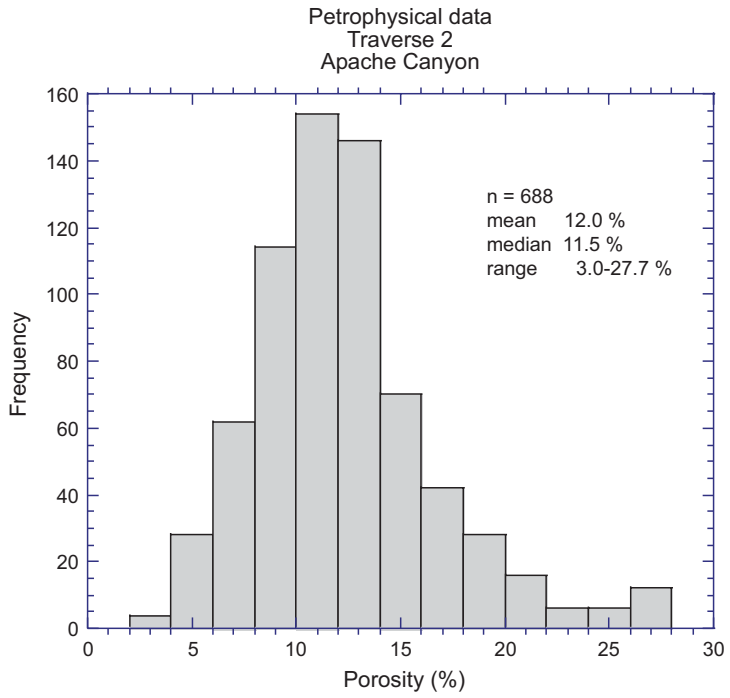

(b)

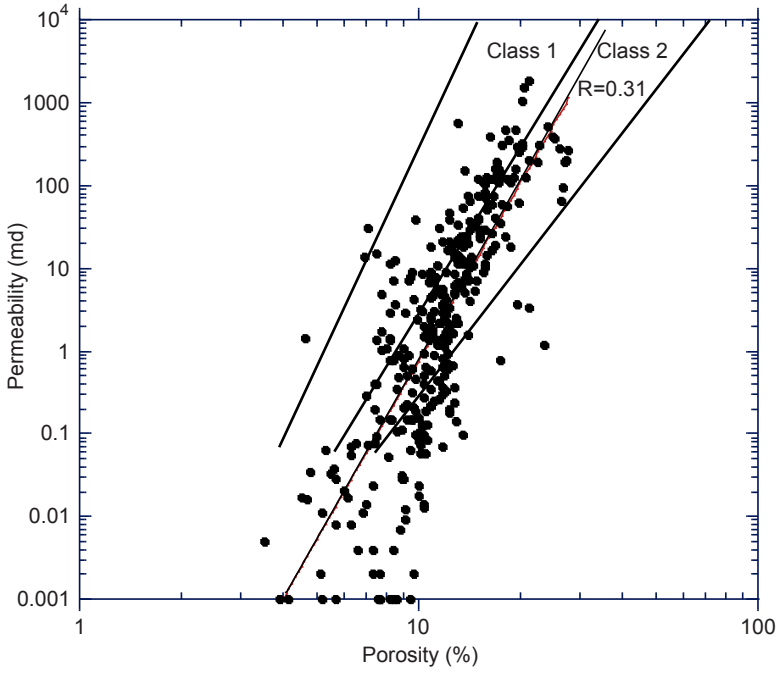

Figure 23. Petrophysical data from 1,795-ft horizontal traverse in a single subtidal cycle (L3 TST) of the upper Clear Fork at Apache Canyon. (a) Histogram of porosity distribution in dominantly skeletal/peloidal packstones of the cycle top. (b) Crossplot of porosity and permeability in same rocks illustrating that the data fall within petrophysical class 2. Line is power-law fit.

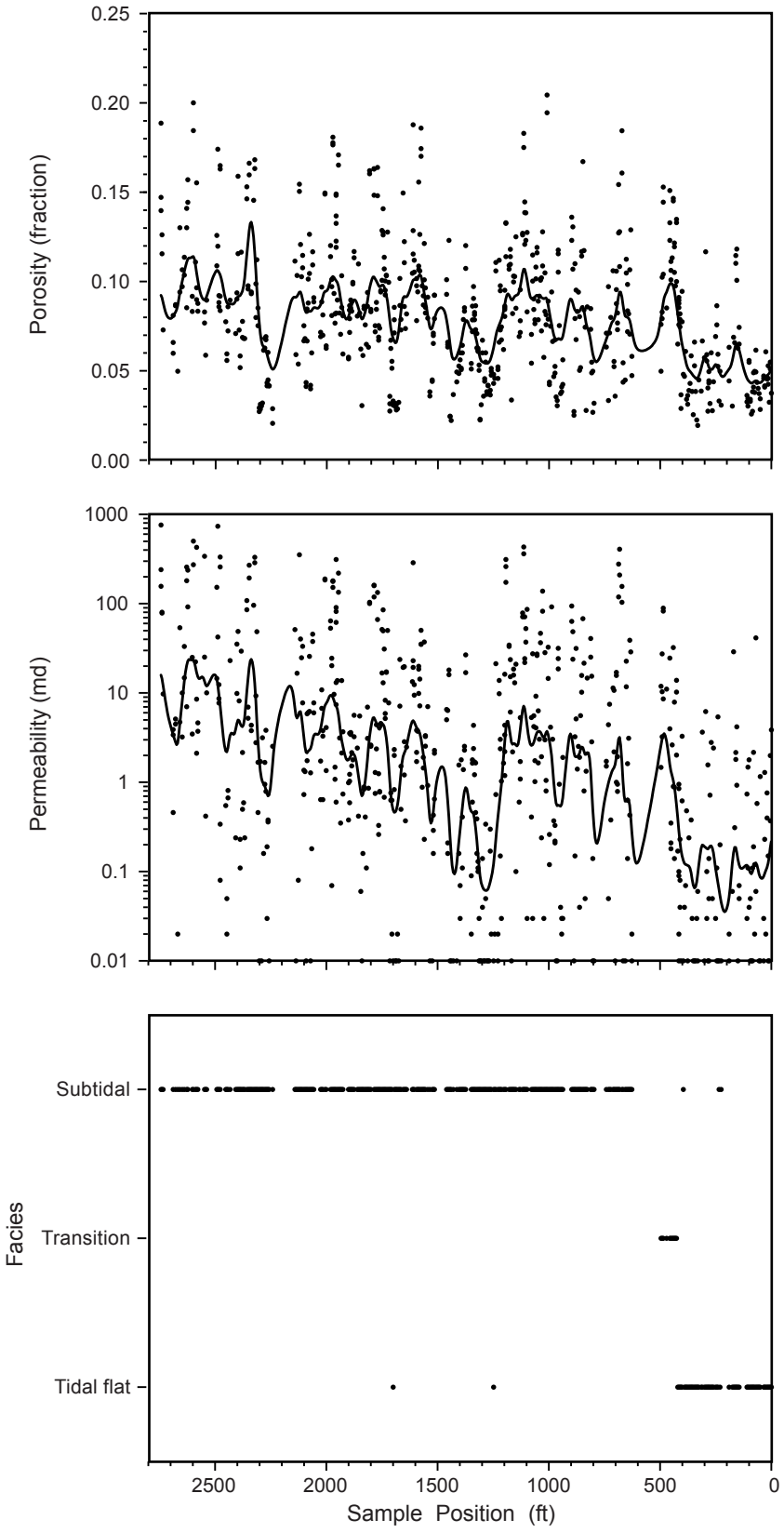

Figure 24. Variations in porosity and permeability along petrophysical traverse 1. See figure 13 for location of traverse. Sample number 0 is at the west (depositional updip) end of the traverse.

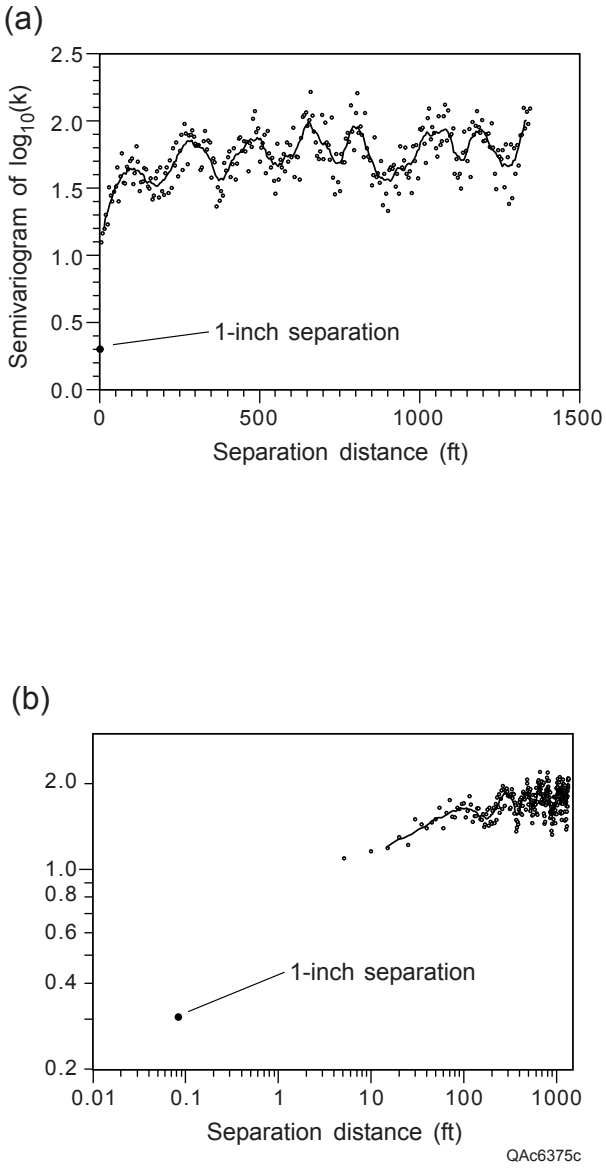

Figure 25. Spatial statistics for petrophysical traverse 1. Apache Canyon horizontal-permeability semivariogram, (a) Cartesian coordinates. (b) Logarithmic coordinates, estimated semivariogram (points), and smoothed semivariogram (curves).

CONCLUSIONS

Clear Fork reservoir-equivalent outcrops in Apache Canyon of the Sierra Diablo are critical guides to an improved understanding of the styles and character of heterogeneity found in Clear Fork reservoirs. The sequence architectures defined for the lower and upper Clear Fork serve as a fundamental basis for interpreting reservoir flow unit geometry and distribution. The styles of facies and cycle stacking observed within architectural elements provide a template for interpreting and describing vertical facies successions in subsurface cores. The spatial statistics of permeability data from horizontal traverses in this outcrop and others provide a basis for understanding the scale of variability of petrophysical properties in the interwell environment. Together, these outcrop models form a critical starting point from which more accurate characterization of subsurface Clear Fork reservoirs can proceed.

ACKNOWLEDGMENTS

This research was funded by the U.S. Department of Energy under contract no. DE-AC26-98BC15105 and by the sponsors of the Reservoir Characterization Research Laboratory: Altura, Amerada Hess, Anadarko, Aramco, ARCO, BP International, Chevron, Elf Aquitaine, ExxonMobil, Great Western Drilling, Japan National Oil Corporation, Kinder Morgan, Marathon, Oxy, Pan Canadian, Pennzoil, Petroleum Development Oman, Shell International, Statoil, South Western Energy, Texaco, and TOTAL. The Bureau of Economic Geology, The University of Texas at Austin, acknowledges support of this research by Landmark Graphics Corporation via the Landmark University Grant Program. Bill Fitchen introduced us to the excellent outcrops in Apache Canyon. Field assistance was provided by Jubal Grubb, Greg Ramirez, and Neil Tabor. We are indebted to Mr. Nelson Puett, owner of the Puett Ranch, for permitting us access to these world-class exposures. Editing was by Susann Doenges, and design and layout were by Scarlett Hurt. Figures were prepared by the Bureau of Economic Geology graphics department under the direction of Joel L. Lardon.

REFERENCES

Ariza, E. E., 1998, High-resolution sequence stratigraphy of the Leonardian lower Clear Fork Group in the Permian Basin, West Texas: The University of Texas at Austin, unpublished Master's thesis, 128 p.

Atchley, S. C., Kozar, M. G., and Yose, L. A., 1999, A predictive model for reservoir characterization in the Permian (Leonardian) Clear Fork and Glorieta Formations, Robertson field area, West Texas: American Association of Petroleum Geologists Bulletin, v. 83, p. 1031–1056.

Ball, M. M., 1967, Carbonate sand bodies of Florida and the Bahamas: Journal of Sedimentary Petrology, v. 37, no. 2, p. 556–591.

Barnaby, R. J., and Ward, W. B., 1994, Sequence stratigraphic framework, high-frequency cyclicity and 3-dimensional heterogeneity: Grayburg Formation, Brokeoff Mountains, New Mexico, *in* Pause, P. H., and Candelaria, M. P., eds., Carbonate facies and sequence stratigraphy: practical applications of carbonate models: PBS-SEPM Publication 95-36, p. 37–50.

Beales, F. W., 1965, Diagenesis in pelleted limestones, *in* Pray, L. C., and Murray, R. C., eds., Dolomitization and limestone diagenesis—a symposium, SEPM Special Publication no. 13, p. 49–70.

Bebout, D. G., Lucia, F. J., Hocott, C. R., Fogg, G. E, and Vander Stoep, G. W., 1987, Characterization of the Grayburg reservoir, University Lands Dune field, Crane County, Texas: The University of Texas at Austin, Bureau of Economic Geology Report of Investigations No. 168, 98 p.

Dunham, R. J., 1961, Classification of carbonate rocks according to depositional texture, *in* Ham, W. E., ed., Classification of carbonate rocks: American Association of Petroleum Geologists Memoir 1, p. 108–121.

Fitchen, W. M., Starcher, M. A., Buffler, R. T., and Wilde, G. L., 1995, Sequence stratigraphic framework and facies models of the early Permian platform margins, Sierra Diablo, West Texas, *in* Garber, R. A., and Lindsay, R. F., eds., Wolfcampian-Leonardian shelf margin facies of the Sierra Diablo—seismic scale models for subsurface exploration: West Texas Geological Society Publication 95-97, p. 23–66.

Hardie, L. A., and Shinn, E. A., 1986, Carbonate depositional environments, modern and ancient, Part 3: Tidal flats: Colorado School of Mines Quarterly, v. 81, no. 1, 74 p.

Harris, P. M., 1979, Facies anatomy and diagenesis of a Bahamanian ooid shoal: Comparative Sedimentology Laboratory, University of Miami, Miami, Florida, 163 p.

Holtz, M. H., and Garrett, C. M., 1990, Geologic and engineering characterization of Leonardian carbonate oil reservoirs: a framework for strategic recovery practices in four oil plays, *in* Flis, J. E., and Price, R. C., eds., Permian Basin oil and gas fields: innovative ideas in exploration and development: West Texas Geological Society Publication No. 90-87, p. 76.

Holtz, M. H., Ruppel, S. C., and Hocott, C. R., 1992, Integrated geologic and engineering determination of oil-reserve-growth potential in carbonate reservoirs: Journal of Petroleum Technology, November, p. 1250–1258.

Jennings, J. W., Jr., 2000, Spatial statistics of permeability data from carbonate outcrops of West Texas and New Mexico: implications for improved reservoir modeling: The University of Texas at Austin, Bureau of Economic Geology Report of Investigations No. 258, 50 p.

Jennings, J. W., Jr., Ruppel, S. C., and Ward, W. B., 2000, Geostatistical analysis of permeability data and modeling of fluid flow effects in carbonate outcrops: Society of Petroleum Engineers Reservoir Evaluation and Engineering, v. 3, no. 4, p. 292–304.

Kerans, Charles, and Fitchen, W. M., 1995, Sequence hierarchy and facies architecture of a carbonate ramp system: San Andres Formation of Algerita Escarpment and western Guadalupe Mountains, West Texas and New Mexico: The University of Texas at Austin, Bureau of Economic Geology Report of Investigations No. 235, 86 p.

Kerans, C., and Fowler, D., 1995, Role of high-frequency cycles in analysis of ancient facies: an example from shelf-crest tepee-pisolite facies of the Guadalupian section, Guadalupe Mountains and subsurface of the Central Basin Platform, West Texas (abs.): American Association of Petroleum Geologists Annual Convention Program, p. 49A.

Kerans, Charles, Kempter, K., Rush, J., and Fisher, W. L., 2000, *in* Lindsay, R., Trentham, R., Ward, R. F., and Smith, A. H., eds., Classic Permian geology of West Texas and Southeastern New Mexico, 75 years of Permian Basin oil & gas exploration & development: West Texas Geological Society Publication 00-108, p. 55–82.

Kerans, Charles, Lucia, F. J., and Senger, R. K., 1994, Integrated characterization of carbonate ramp reservoirs using Permian San Andres Formation outcrop analogs: American Association of Petroleum Geologists Bulletin, v. 78, no. 2, p. 181–216.

Kerans, C., and Ruppel, S. C., 1994, San Andres sequence framework, Guadalupe Mountains: implications for San Andres type section and subsurface reservoirs: *in* Garber R. A., and Keller, D. R., eds., Field guide to the Paleozoic section of the San Andres Mountains: Permian Basin Section SEPM Publication 94-35, p. 105–116.

King, P. B., 1942, Permian of West Texas and southeastern New Mexico: American Association of Petroleum Geologists Bulletin, v. 26, no. 4, p. 535–763.

King, P. B., 1965, Geology of the Sierra Diablo region, Texas: U.S. Geological Survey Professional Paper 480, 185 p.

Lucia, F. J, 1995, Rock-fabric/petrophysical classification of carbonate pore space for reservoir characterization: American Association of Petroleum Geologists Bulletin, v. 79, no. 9, 1275–1300.

Milliman, J. D., 1974, Marine carbonates: New York, Springer-Verlag, 375 p.

Multer, H. G., 1977, Field guide to some carbonate rock environments, Florida Keys ands western Bahamas: Dubuque, Iowa, Kendall/Hunt, 415 p.

Purdy, E. G., 1963, Recent calcium carbonate facies of the great Bahama Bank. 2. Sedimentary facies: Journal of Geology, v. 71, p. 472–497.

Ruppel, S. C., 1992, Styles of deposition and diagenesis in Leonardian carbonate reservoirs in West Texas: implications for improved reservoir characterization: Society of Petroleum Engineers Annual Exhibition and Technical Conference, 24691, p. 313–320.

Ruppel, S. C., in press, Geological controls on Leonardian reservoir development, Monahans Clear Fork field, West Texas: The University of Texas at Austin, Bureau of Economic Geology Report of Investigations.

Ruppel, S. C., and Bebout, D. G., 1996, Effects of stratal architecture and diagenesis on reservoir development in the Grayburg Formation: South Cowden field, Ector County, Texas: Fossil Energy, DOE/BC 14895-10, 80 p.

Ruppel, S. C., and Cander, H. S., 1988a, Effects of facies and diagenesis on reservoir heterogeneity: Emma San Andres field, West Texas: The University of Texas at Austin, Bureau of Economic Geology Report of Investigations No. 178, 67 p.

Ruppel, S. C., and Cander, H. S., 1988b, Dolomitization of shallow-water platform carbonates by sea water and seawater-derived brines: San Andres Formation (Guadalupian), West Texas, *in* Sedimentology and geochemistry of dolostones: Society of Economic Paleontologists and Mineralogists, Special Publication No. 43, p. 245–262.

Ruppel, S. C., Kerans, Charles, Major, R. P., and Holtz, M. H., 1995, Controls on reservoir heterogeneity in Permian Basin shallow-water platform carbonate reservoirs, Permian Basin: implications for secondary recovery: The University of Texas at Austin, Bureau of Economic Geology Geological Circular 95-2, 30 p.

Ruppel, S. C., Ward, W. B., Ariza, E. E., and Jennings, J. W., Jr., 2000, Cycle and sequence stratigraphy of Clear Fork reservoir-equivalent outcrops: Victorio Peak Formation, Sierra Diablo, Texas, *in* Lindsay, R., Trentham, R., Ward, R. F., and Smith A. H., eds., Classic Permian geology of West Texas and southeastern New Mexico, 75 years of Permian Basin oil & gas exploration & development: West Texas Geological Society Publication 00-108, p. 109–130.

Saller, A. H., and Henderson, N., 1998, Distribution of porosity and permeability in platform dolomites: insights from the Permian of West Texas: American Association of Petroleum Geologists Bulletin, v. 82, no. 8, p. 1528–1550.

Shinn, E. A., 1983, Tidal flat, *in* Scholle, P. A., Bebout, D. G., and Moore, C. H., eds., Carbonate depositional environments: American Association of Petroleum Geologists Memoir 33, p. 171–210.

Shinn, E. A., and Robbin, D. M.,1983, Mechanical and chemical compaction in fine-grained shallow-water limestones: Journal of Sedimentary Petrology, v. 53 no. 2, p. 595–618.

Sonnenfeld, M. D., 1991, High-frequency cyclicity within shelf-margin and slope strata of the upper San Andres sequence, Last Chance Canyon, *in* Meader-Roberts, Sally, Candelaria, M. P., and Moore, G. E., eds., Sequence stratigraphy, facies and reservoir geometries of the San Andres, Grayburg, and Queen Formations, Guadalupe Mountains, New Mexico and Texas: Permian Basin Section, Society of Economic Paleontologists and Mineralogists Publication 91-32, p. 11–51.

Tyler, Noel, and Banta, N. J., 1989, Oil and gas resources remaining in the Permian Basin: targets for additional hydrocarbon recovery: The University of Texas at Austin, Bureau of Economic Geology Geological Circular 89-4, 20 p.

Tyler, Noel, Galloway, W. E., Garrett, C. M., Jr., and Ewing, T. E., 1984, Oil accumulation, production characteristics, and targets for additional recovery in major oil reservoirs of Texas: The University of Texas at Austin, Bureau of Economic Geology Geological Circular 84-2, 31 p.

Ye, Qiucheng, and Mazzullo, S. J. , 1993, Dolomitization of lower Permian platform facies, Wichita Formation, north platform, Midland Basin, Texas: Carbonates and Evaporites v. 8, no. 1, p. 55–70.

CYCLE AND SEQUENCE STRATIGRAPHY OF THE CLEAR FORK RESERVOIR AT SOUTH WASSON FIELD: GAINES COUNTY, TEXAS

Stephen C. Ruppel and Eduardo Ariza[1]

Bureau of Economic Geology
John A. and Katherine G. Jackson School of Geosciences
The University of Texas at Austin

Current address: [1] Ecopetrol, Calle 37 No. 8-43, Piso 12, Gerencia de Yacimientos, Bogota, Colombia

TABLE OF CONTENTS

LIST OF FIGURES

ABSTRACT

Despite more than 50 years of production, Leonard shallow-water platform carbonate reservoirs contain a sizeable volume of remaining oil. This remaining resource constitutes a significant target for improved methods of characterization and recovery. The Clear Fork reservoir at South Wasson field is typical of the fields that contain this remaining oil resource. Analysis of data from subsurface cores, 2-D and 3-D seismic, and wireline logs combined with models derived from study of analogous outcrops provides important insights into the geological controls on heterogeneity and reservoir architecture that are key to better recovery.

The lower Clear Fork reservoir succession at South Wasson comprises a single stratigraphic sequence, which can be subdivided into two high-frequency sequences (HFS): a symmetrical, transgressive-regressive-transgressive lower HFS, and an upper asymmetrical, transgressive sequence. Although the two HFS have some common facies, they display important differences in facies and facies tract architecture that have reservoir significance. High-frequency cycles, averaging 6 ft in thickness, and cycle sets, averaging 50 ft in thickness, are definable in both.

The upper Clear Fork succession is thicker, consisting of parts of three stratigraphic sequences. Although HFS are usually not readily definable within these sequences from existing data, each sequence displays significantly differently architecture and facies tracts that make their distinction important. Like the lower Clear Fork, high-frequency cycles (average 7 ft thick) and cycle sets (average 60 ft) are definable throughout the upper Clear Fork. Cycles in both the lower and upper Clear Fork are capped by grain-rich packstones (peloid-rich in the lower Clear Fork and crinoid- and peloid-rich in the upper Clear Fork); cycle bases are typically composed of peloid/skeletal wackestones. Porosity is best developed in cycle-top, grain-dominated packstones and is commonly low in cycle bases.

Core-based correlations document that cycles are continuous across the field area. However, correlation of cycle and cycle sets is limited using gamma-ray logs because of highly variable uranium distribution. Nevertheless, correlation of the cycle-controlled porosity distribution is an important key to developing an accurate reservoir model of the reservoir.

INTRODUCTION

The middle Permian (Leonardian) Clear Fork Group is one of the major oil-producing reservoir successions in the Permian Basin. With a cumulative production of more than 3 billion barrels, these rocks are second only to the San Andres Formation (Guadalupian) in terms of total original and remaining oil resource volume (fig. 1). Estimates of original oil in place indicate that Leonardian reservoirs contained more than 14.5 billion barrels of oil at discovery (Holtz and others (1992), or 15 percent of the total resource in the Permian Basin. Recovery of this substantial resource has proven difficult, however; as of January 2000, only 3.1 billion barrels of the total oil resource had been produced. Leonardian carbonate reservoirs currently exhibit an average recovery efficiency of 20 percent, which is considerably below the 32 percent average for all carbonate reservoirs in the Permian Basin (Tyler and Banta, 1989; Holtz and Garrett, 1990). Holtz and others (1992) estimated that these rocks contain 6.5 billion barrels of remaining mobile. This is a huge target for development of improved technologies for characterizing, modeling, and recovery processes.

Tyler and others (1984) attributed the abnormally low recovery efficiencies in Leonardian reservoirs to extreme lithologic heterogeneity. The purpose of this study is to characterize this heterogeneity in the Clear Fork and propose geological models that can serve as a basis for interpretation and modeling of petrophysical attributes, reservoir architecture, and flow-unit geometries in this important class of reservoirs. South Wasson Clear Fork reservoir (fig. 2) was selected for detailed study because (1) it is representative of Clear Fork reservoirs having a large resource base and low recovery efficiency, (2) it contains an extensive, good-quality set of wireline, core, and geophysical data, (3) it is operated by a progressive company (Oxy Permian) that is dedicated to implementing improved technologies for advanced recovery.

This chapter characterizes the geology of the upper and lower Clear Fork reservoirs at South Wasson field and describes the important roles geological processes play in reservoir development. A key element of this study is the application of concepts and models developed from detailed study of analogous outcrops in the Sierra Diablo Mountains of West Texas (Ruppel and others, this volume).

SETTING

The Leonardian Series in the Permian Basin contains a thick (as much as 2,500 ft) succession of carbonate rocks that accumulated on shallow-water ramps and shelves in West

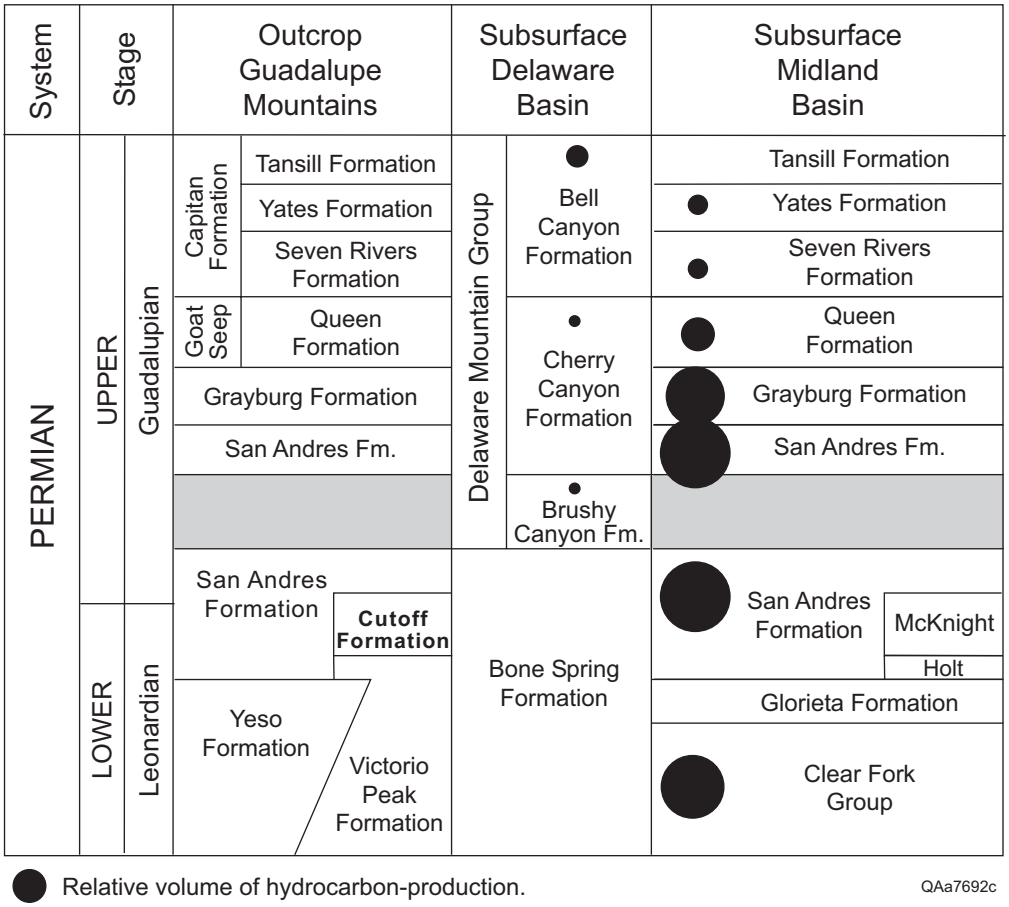

Figure 1. Stratigraphic nomenclature of major formations in outcrops and the subsurface of the Permian Basin and their relative ranking in cumulative oil production.

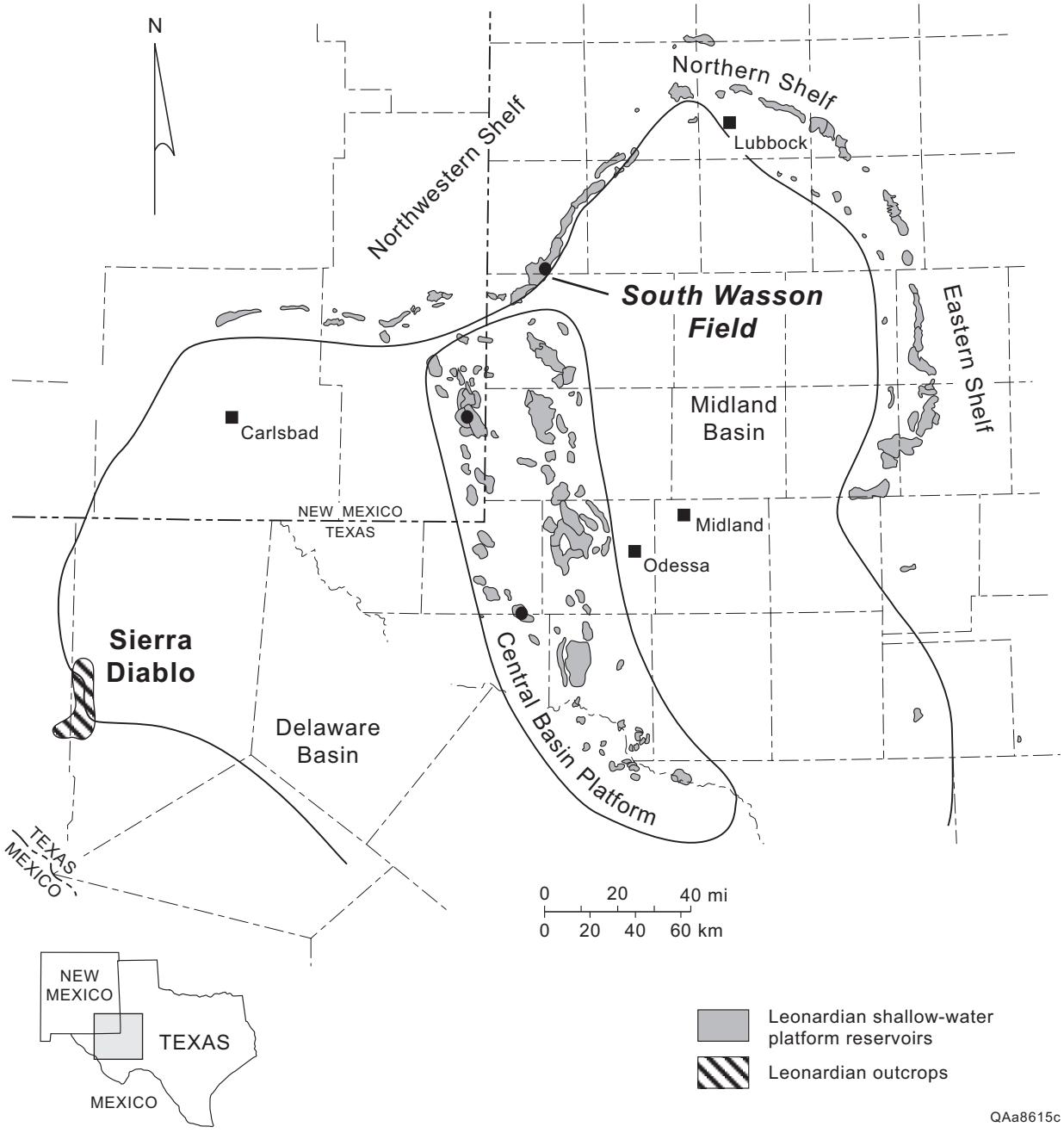

Figure 2. Map of the Permian Basin showing Leonardian paleotopography and the location of the South Wasson Clear Fork field.

Texas and New Mexico during the middle Permian (fig. 1). Reservoirs developed in Leonardian carbonates are typical of a large class of carbonate reservoirs that Tyler and others (1984) referred to as "restricted platform systems." These reservoirs (1) are dolomitized, (2) are associated with evaporites, (3) exhibit low permeability and porosity values, and (4) display low recovery efficiencies. As a group, restricted platform carbonate reservoirs have accounted for nearly 70 percent of the cumulative production from the Permian Basin, although they contain only about half of the original oil in place (Tyler and Banta, 1989).

The South Wasson Clear Fork field is one of several fields developed in the Clear Fork (Glorieta, upper Clear Fork, and lower Clear Fork) and Wichita/Albany/Abo along the eastern margin of the northern shelf (fig. 1). Cumulative production from the Wasson field alone (of which South Wasson Unit is a part) totals more than 138 million barrels, the majority of it coming from the upper and lower Clear Fork. Like most Leonardian platform carbonates, recovery efficiency from these rocks is low.

Most of the production from the South Wasson Clear Fork reservoir comes from the middle part of the upper Clear Fork and the lower Clear Fork (fig. 3). Minor production comes from the underlying Wichita/Albany or Abo Formation. Structurally, the field is part of a northeast-striking, southeast-dipping monocline that extends from Russell field to the southwest to Prentice field to the northeast (fig. 2). A small dome within the field provides local closure in the middle of the field (fig. 4). The updip seal is formed by evaporite-rich carbonates; the top seal is created by similar carbonates at the top of the Clear Fork and Glorieta and the overlying low-permeability San Andres.

METHODS

Interpretations presented in this study are primarily based on detailed examination of 13 cores totaling approximately 5,000 ft. Major cored wells are shown in figure 4. Description of cores was supplemented by examination of 550 thin sections. Conventional core analysis data were available for all cores. A 3-D seismic data volume covers most of the productive field (fig. 4). These data were used to guide wireline log correlations through the field.

PREVIOUS WORK

Previous studies of Leonardian-age carbonates in West Texas are few. Mazzullo (1982) and Mazzullo and Reid (1989) presented overviews of lower Leonard stratigraphy and

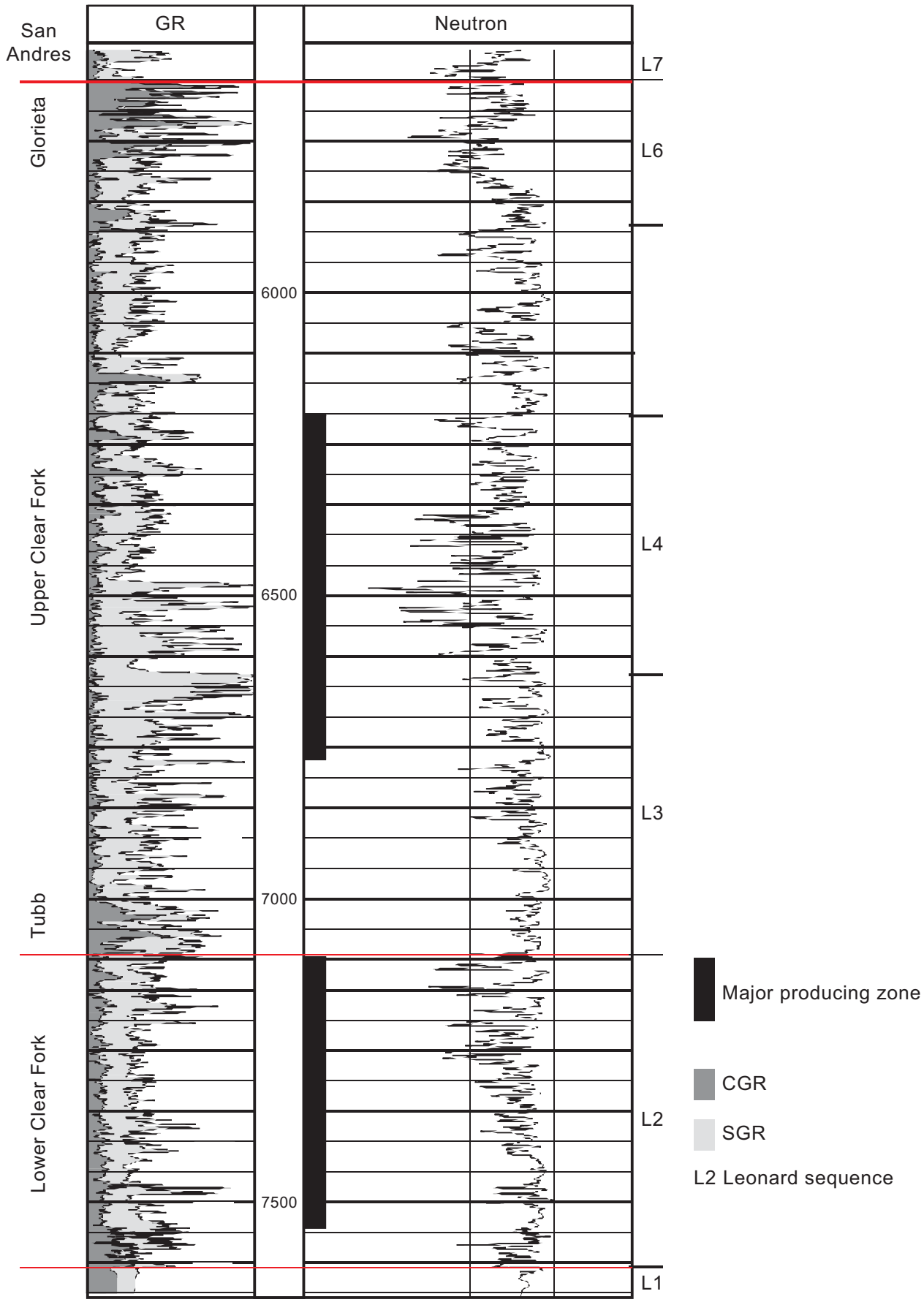

Figure 3. Type log for Clear Fork reservoir succession at South Wasson field.

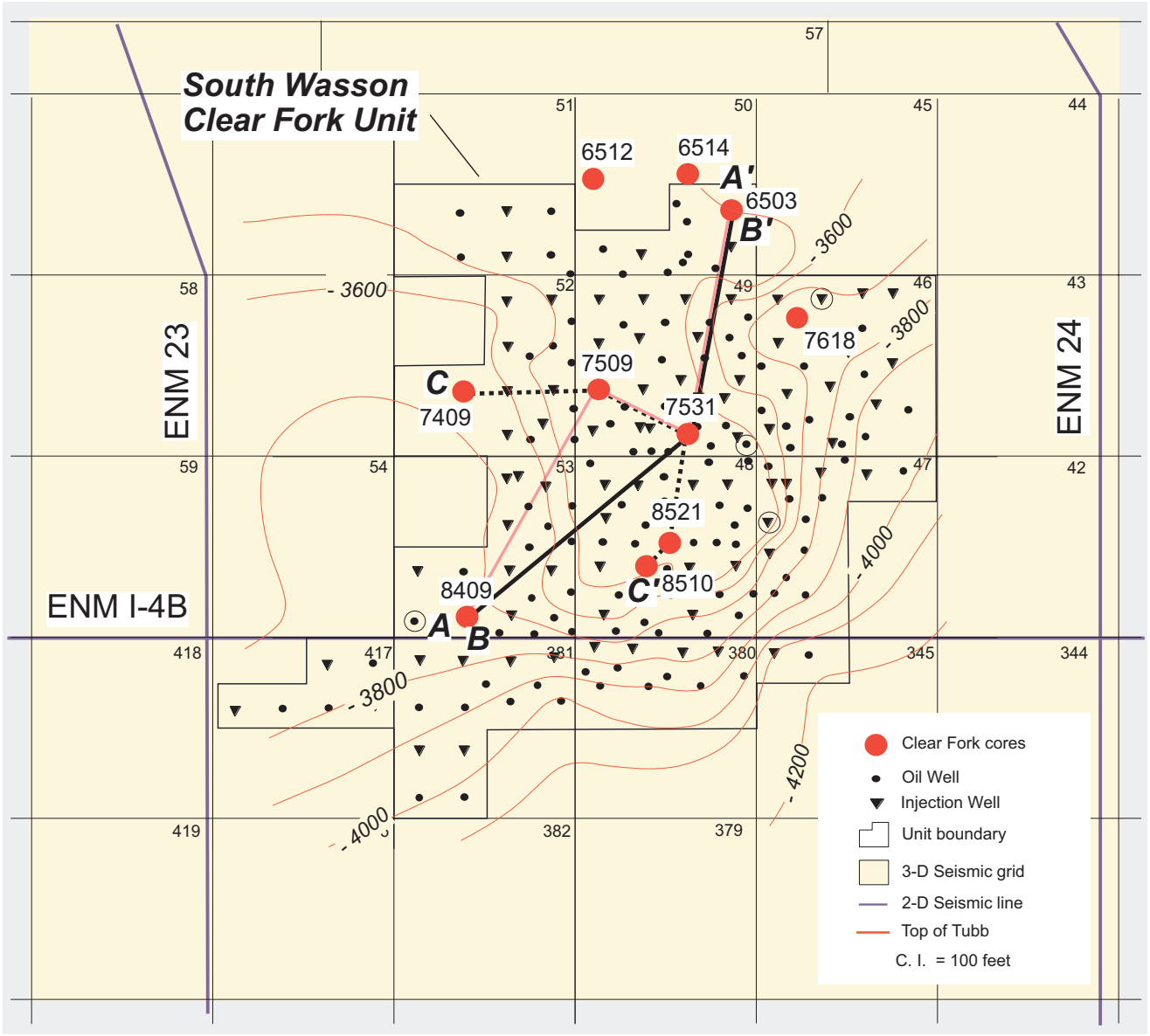

Figure 4. Map of the South Wasson Clear Fork field, Andrews County, Texas, showing reservoir structure as mapped on the top of the Tubb.

depositional systems in the Midland Basin. Presley (1982) documented the highly cyclic, predominantly evaporitic facies of the upper Leonard Glorieta and upper Clear Fork units in the Texas Panhandle. Ruppel (1992; in press) described the facies, cyclicity, and diagenesis in the Monahans Clear Fork field on the Central Basin Platform and postulated that reservoir development was a function of episodic sea-level rise and fall. Atchley and others (1999) described the facies in the Clear Fork reservoir at Robertson field at the north end of the Central Basin Platform and proposed a similar model for structural control over facies deposition and reservoir development.

GENERAL LEONARDIAN STRATIGRAPHY AT SOUTH WASSON FIELD

The general stratigraphy of the South Wasson Clear Fork reservoir is displayed in figure 3. Although locally productive in the field, the Abo or Wichita was not examined as part of this study. Limited cores from the field, however, indicate that the Abo at South Wasson, like its counterparts in Apache Canyon outcrops, consists of dolomitized open-marine carbonates that are locally karsted. The top of the Abo is clearly defined in outcrop and in the subsurface by this karsting, which developed following a major sea-level-fall event at the end of Abo time (Kerans and others, 2000).

Lower Clear Fork comprises dolomitized shallow-water carbonates, again similar to those observed in outcrops (Ruppel and others, this volume). The high-CGR (potassium/thorium) gamma-ray signature of the lower part of the lower Clear Fork (fig. 3) correlates with tidal-flat deposits that contain small volumes of clay and silt. These tidal-flat deposits are well developed in Apache Canyon outcrops and vary widely in thickness. Although the base of the lower Clear Fork is difficult to rigorously define at South Wasson with existing data, it appears that the unit averages as much 500 ft in thickness. This is substantially thicker than observed in equivalent lower Clear Fork outcrops in Apache Canyon where thicknesses range from 100 to 300 ft (Ruppel and others, this volume) and apparently reflects differences in local accommodation.

It is apparent from limited core control and wireline logs that the Tubb at South Wasson is composed of interbedded silt-rich intervals and cleaner carbonates much like the equivalent section in outcrop. These intervals are well defined by the CGR gamma ray (fig. 3). Like the lower Clear Fork, the subsurface Tubb, is two to three times thicker than its outcrop equivalent (Ruppel and others, this volume), again reflecting regional differences in accommodation. Outcrop studies (Kerans and others, 2000, Ruppel and others, 2000; Ruppel and others, this

volume), indicate that the Tubb constitutes the base of a major Leonard sequence (L3). The abundant siliciclastics in the Tubb probably accumulated as windblown sediments during post–lower Clear Fork sea-level lowstand and were subsequently reworked during the ensuing sea-level rise and transgression.

Like the lower Clear Fork, the upper Clear Fork is composed dominantly of relatively shallow water, dolomitized carbonates. Regional outcrop and subsurface studies suggest that this part of the Leonard section correlates with three major sequences: L3, L4, and L5. Recognition of these boundaries with seismic data and wireline logs, however, is commonly problematical.

The upper Leonard Glorieta is not part of the productive reservoir section at South Wasson. However, previous studies of the Glorieta section in other reservoirs (Ruppel, 1992; in press) indicate that the high CGR and total gamma-ray response in the Glorieta reflect clay- and silt-rich tidal-flat facies like those of the basal lower Clear Fork. The contact of the Glorieta with the overlying San Andres is a readily definable marker on wireline logs and on seismic due to the striking contrast between the siliciclastic-rich dolomites of the Glorieta and the sometimes limestone-rich clean carbonates of the overlying San Andres.

CLEAR FORK FACIES IN SOUTH WASSON RESERVOIR

Clear Fork rocks in the South Wasson field contain very similar facies to those encountered in equivalent outcrops in Apache Canyon. Primary reservoir facies include (1) peloid grain-dominated packstone, (2) crinoid/peloid grain-dominated packstone, (3) peloid wackestone/packstone, (4) skeletal/peloid wackestone/packstone, (5) fusulinid wackestone/packstone, (6) tidal flat, (7) silty mudstone/wackestone/siltstone, and (8) skeletal buildup. South Wasson Clear Fork rocks differ from outcrop rocks in two principal respects. First, no grainstone facies are defined in the subsurface. Rather than reflecting a difference in depositional settings, this probably reflects the difficulty of observing cross laminations (the basis for a grainstone definition) in cores. Second, the Clear Fork at South Wasson field contains short intervals of skeletal buildup. These rocks, which are skeletal wackestones that display evidence of organic binding and trapping, are essentially absent from outcrop exposures in Apache Canyon.

DIAGENESIS

As is the case with outcrop equivalents in Apache Canyon, all rocks in the lower and upper Clear Fork successions in the South Wasson Clear Fork reservoir have been dolomitized. No detailed research was undertaken in this study to determine the diagenetic history of these rocks. Previous studies of Clear Fork dolomites in the Permian Basin suggest that most were formed relatively early, by at least Guadalupian time (Saller and Henderson, 1998; Ye and Mazzullo, 1993; Ruppel, 1992; in press). Ruppel (1992; in press) presented evidence, based on studies of regional Clear Fork reservoir data, that Clear Fork dolomites are the result of at least two dolomitization events: an early event in which dolomite formed at cycle tops during sea-level fall/rise cycles, and a later massive reflux event that resulted in the complete dolomitization of the section.

The Clear Fork succession in the South Wasson field differs principally from its outcrop equivalents in Apache Canyon in the presence of anhydrite. Calcium sulfate, mostly in the form of anhydrite, is abundant throughout the subsurface section. In cores, this anhydrite is most obviously present in the form of nodules that range in size from 1 to 10 cm in diameter. These anhydrite nodules are almost entirely restricted to subtidal rocks. More cryptic in cores, but readily apparent in thin sections, is poikilotopic anhydrite, which is present as irregularly distributed intercrystalline networks. Poikilotopic anhydrite is present in all facies and is a significant contributor to the fabric and petrophysics of the entire Clear Fork section.

SEQUENCE STRATIGRAPHY

The development of a sequence-stratigraphic framework for the South Wasson Clear Fork reservoir is based on examination of facies stacking succession in available cores combined with an appreciation of sequence-stratigraphic relationships established in outcrops. Previous integrated studies of outcrops and regional subsurface data indicate that the Leonardian comprises eight sequences (fig. 5; Fitchen and others, 1995; Kerans and others, 2000, Ruppel and others, 2000). The basal and upper parts of the Leonard succession are well worked out. The basal Abo or Wichita/Albany corresponds to sequence L1 (Fitchen and others, 1995; Kerans and others, 2000), the lower Clear Fork comprises L2 (Kerans and others, 2000, Ruppel and others, 2000), and the uppermost Leonard lower San Andres Formation comprises L7 and L8 Kerans and others, 1994, 1995). However, the middle Leonard section, which includes the Clear Fork Group and Glorieta Formation, is less clearly defined.

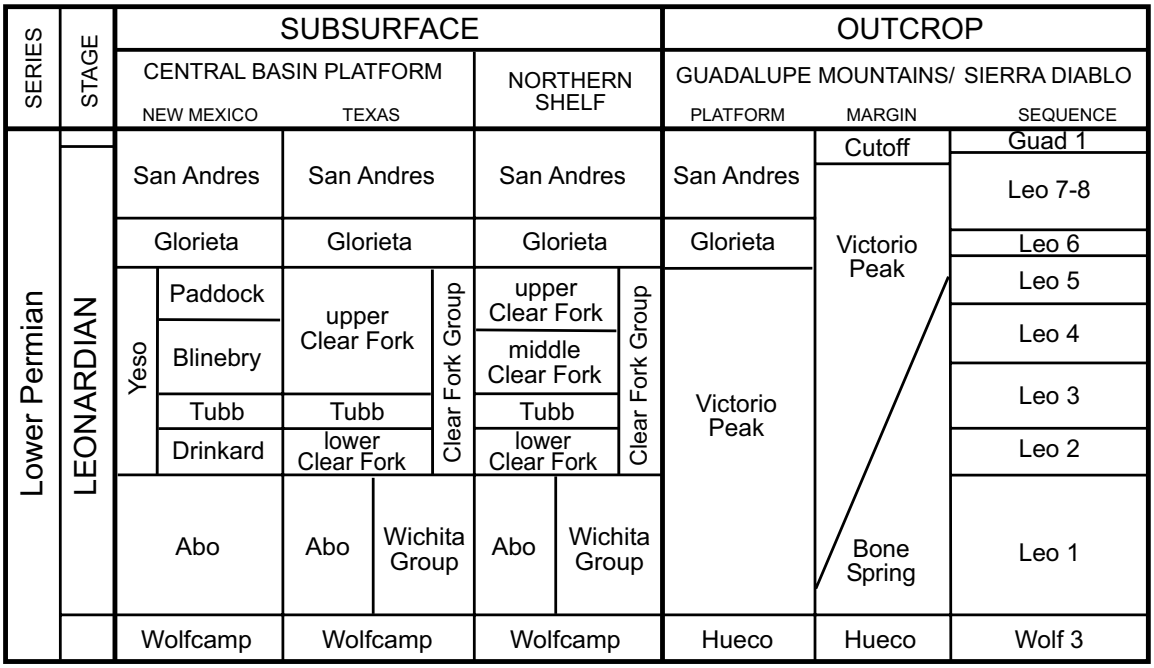

Figure 5. Relationship of standard Leonardian stratigraphic units to sequence stratigraphy.

Examination of 2-D seismic data in the Wasson field area supports the previously proposed sequence architecture of the Leonard (Fitchen and others, 1995; Kerans and others, 2000). Figure 6 displays part of an east-trending 2-D line that is 2 mi north of the South Wasson Clear Fork Unit. These data reveal that the Leonard comprises six seismically definable sequences on the platform in the Wasson field area. Comparison of these data with integrated studies of 3-D seismic data and wireline log data in Wasson field for this study confirms ties between the L1 sequence and the Abo, the L2 and the lower Clear Fork, the L6 and the Glorieta, and the L7 and the lower San Andres (Ariza, 1998). At the platform margin between the Northern Shelf and the Midland Basin, the 2-D seismic data document a major sea-level-fall event during the middle part of the upper Clear Fork succession. The L4 sequence, as currently defined, comprises a platform succession and a series of basinward-stepping prograding wedges (fig. 6) that were deposited during this sea-level-fall event. Sequences L5 and L6 record subsequent sea-level rise and renewed deposition (largely aggradation) on the platform.

Although the major fall in sea level during L4 is well defined on the 2-D seismic data at the platform margin, correlation of this event into the Wasson reservoir succession is problematic because of the relatively low resolution of the data. Similarly, characterization of higher frequency sea-level rise/fall events and the resulting architecture is not possible from seismic data but requires careful analysis of core and wireline data.

Lower Clear Fork (L2) Sequence Architecture

Although only four cores through the lower Clear Fork reservoir at South Wasson field were available, they are sufficient to characterize the sequence-scale architecture of most of the sequence. The facies stacking patterns in these cores indicate the presence of two distinct high-frequency sequences (HFS) in the lower Clear Fork (fig. 7). The lower sequence, L2.1, consists of a basal tidal-flat succession overlain by an interval of cyclic, fusulinid-rich facies, and capped by an uppermost succession of cyclic, peloidal grain-rich facies. The basal tidal-flat succession represents slow transgression and backstepping across the platform during sea-level rise. The middle leg of HFS L2.1 documents the development of relatively deep water, outer platform conditions during maximum flooding of the platform (fig. 7). The top of L2.1 is characterized by the development of relatively high energy depositional conditions across the platform, as reflected by the presence of peloidal and ooid grain-dominated packstones. Locally (at the northern end of the field), tidal-flat deposits at the top of L2.1 document exposure. The presence

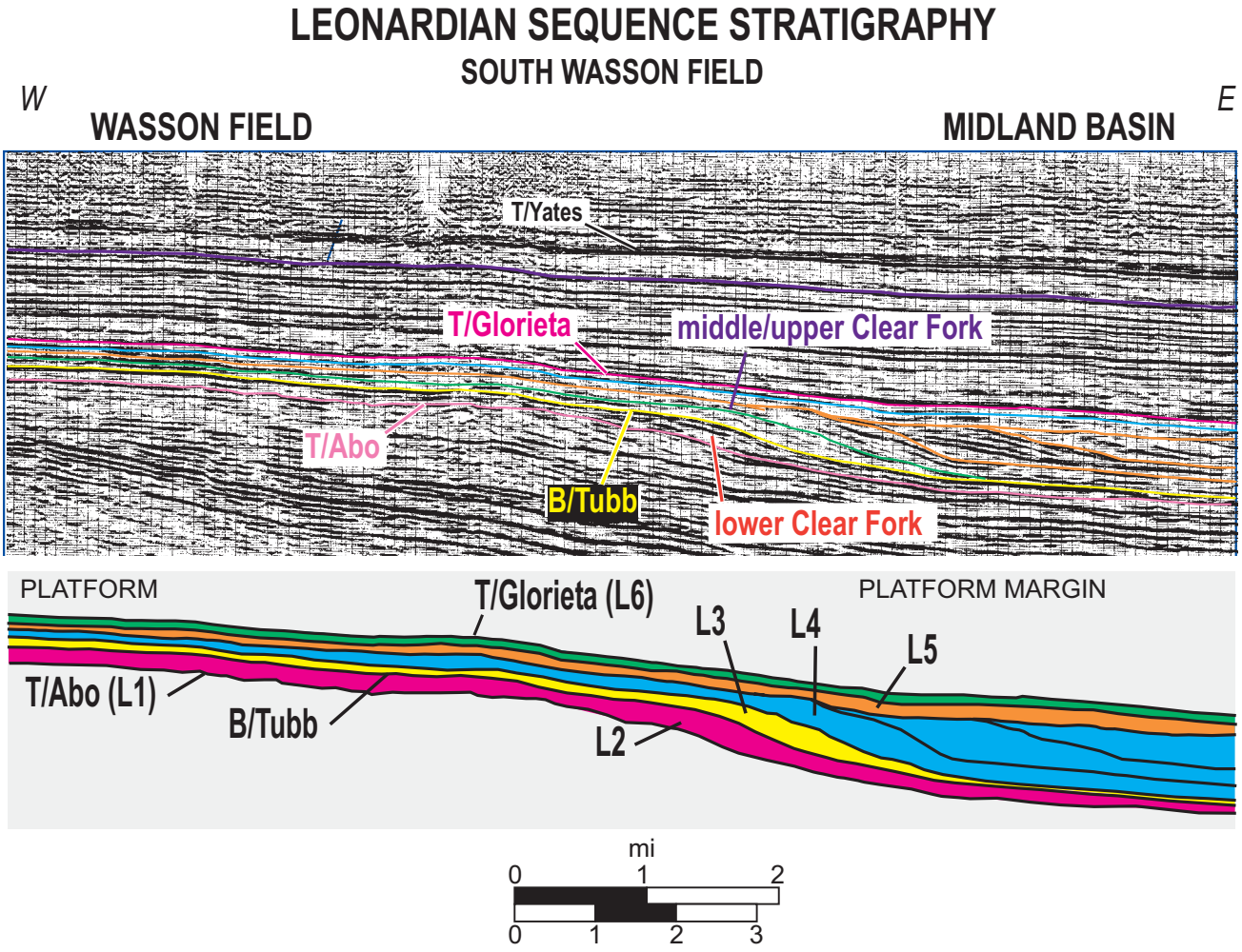

Figure 6. Regional sequence stratigraphy in the South Wasson field area. 2-D seismic line trends eastward along depositional dip from the Wasson field situated on the carbonate platform of the Northern Shelf into the Midland Basin.

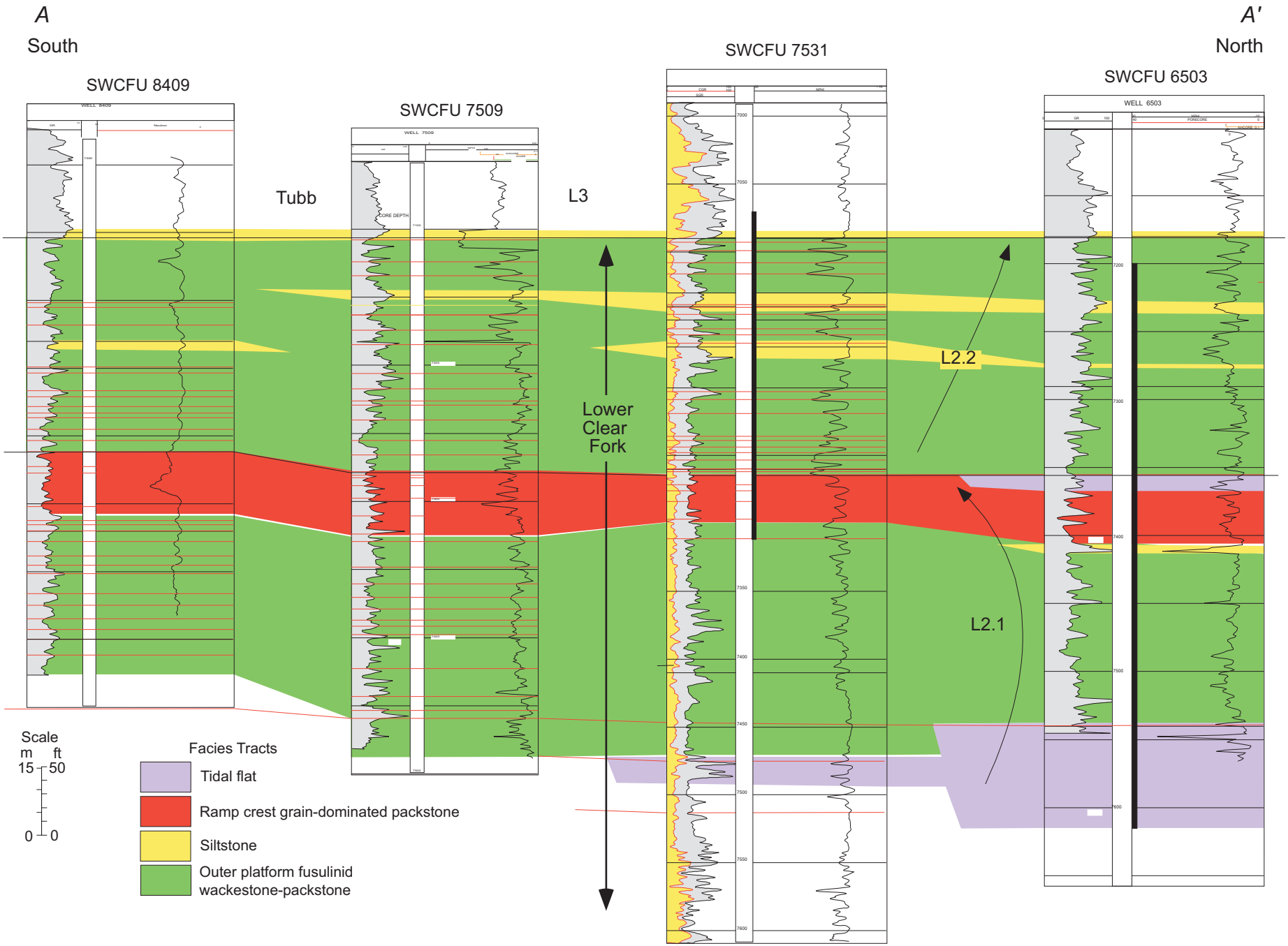

Figure 7. Cross section (A–A′) showing high-frequency sequence stratigraphy and distribution of facies tracts in the lower Clear Fork.

of tidal-flat facies at the base and top of L2.1 defines a symmetrical HFS that documents transgression and backstepping, maximum flooding of the platform, aggradation and shallowing, and finally, platform exposure (at least across part of the field). This succession of facies tracts closely resembles the L2.1 succession defined in outcrops (Ruppel and others, this volume) in terms of accommodation history, suggesting that it is the result of basinwide changes in relative sea level.

The lower Clear Fork HFS 2.2 is dominated by fusulinid-rich wackestones and packstones typical of outer platform depositional conditions (fig. 7). These rocks document renewed sea-level rise and flooding of the platform. They differ slightly from the outer platform succession of L2.1 in containing discontinuous intervals of silty wackestone and siltstone (fig. 7). The top of L2.2 is marked by a sharp contact with the Tubb Formation, which outcrop studies suggest represents the base of sequence L3 (Kerans and others, 2000; Ruppel and others, this volume). HFS 2.2 thus displays none of the symmetry apparent in 2.1. The top of 2.2, for example, shows no evidence of aggradation or shallowing like that characteristic of the top of 2.2. This apparent absence of the upper shallow water leg of the HFS 2.2 depositional cycle is consistent with the outcrop record of this succession where the top of the lower Clear Fork appears to missing owing to rapid sea-level fall by forced regression (Kerans and others, 2000, Ruppel and others, 2000).

Thickness and facies relationships suggest that the lower Clear Fork at South Wasson field was deposited in a deeper water, higher accommodation setting than the equivalent outcrops in Apache Canyon. In South Wasson field, HFS 2.2 averages about 170 ft and is composed of outer platform fusulinid facies (fig. 7). In outcrop, where HFS 2.2 comprises shallow-water subtidal and tidal-flat facies, its thickness averages only about 50 ft (Ruppel and others, this volume). HFS 2.1 displays an even greater difference in thickness between outcrop and subsurface, averaging about 100 ft in outcrop and as much as 330 ft at South Wasson field (fig. 7).

Upper Clear Fork Sequence Architecture

The interval that includes the Tubb, upper Clear Fork, and Glorieta averages about 1,300 ft at South Wasson field (fig. 8). Within this section, four Leonard sequences (L3–L6) can be defined from combined subsurface core data, 2-D and 3-D seismic data, and outcrop analog studies. As predicted from seismic data (fig. 6), these sequences are largely isopachous and flat

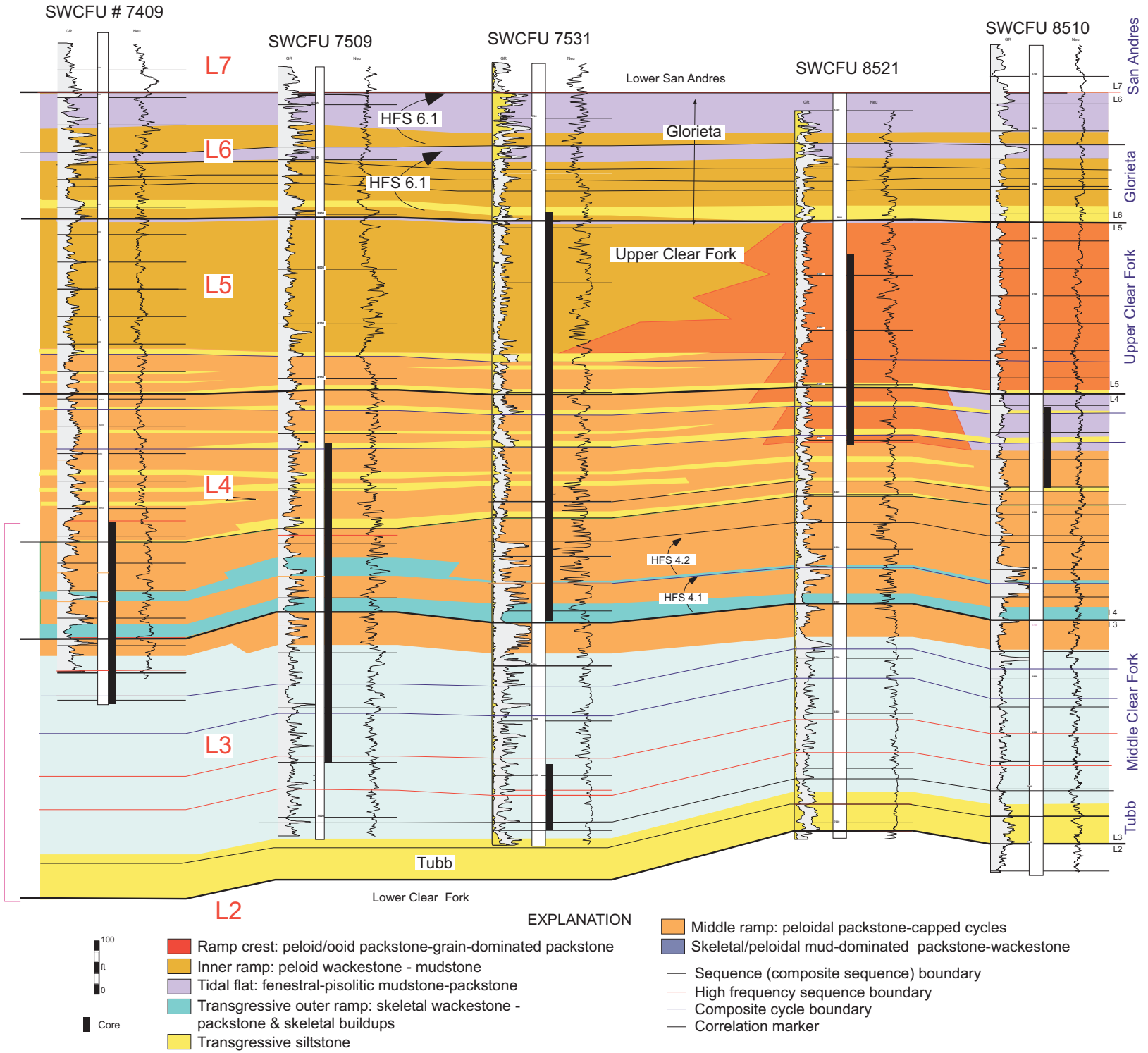

Figure 8. Cross section (B–B´) showing sequence stratigraphy and distribution of facies tracts in the upper Clear Fork and Glorieta. Note that although this section runs perpendicular to structural dip, facies and thickness relationships indicate that the most basinward end of the section was probably relatively higher than surrounding parts of the platform because of decreased subsidence rates over an underlying structure.

across the Wasson field area. Where facies stacking relationships can be adequately defined from cores (part of L4) or from wireline logs (L6), some sequences can be further subdivided into component high-frequency sequences.

Leonardian 3

The Leonardian 3 sequence averages about 400 ft and comprises the Tubb and the lower part of the upper Clear Fork (fig. 8). The Tubb forms an isopachous blanket of cyclically interbedded siltstone to silty carbonate wackestones and shallow-water carbonates that extends across the South Wasson field area and beyond. In the South Wasson area, it averages about 70 ft in thickness. The silty nature of the Tubb reflects its origin as a basal transgressive unit formed by submarine reworking of eolian silts that accumulated on the exposed lower Clear Fork platform during sea-level fall (Kerans and others, 2000, Ruppel and others, 2000). Although vertical core and log successions across the Tubb/lower Clear Fork contact are not always sharp, outcrop studies clearly establish the base of the Tubb as a major sequence boundary.

Overlying the Tubb, L3 consists of siliciclastic-free, dominantly mud-rich, cyclic shallow-water carbonates (fig. 8). Most of the section comprises skeletal-peloidal wackestones and muddy packstones. The top of the sequence is marked by a 60-ft-thick interval of grain-rich peloidal packstones. Outcrop studies show that L3 consists of high-frequency sequences averaging 50 to 100 ft in thickness. Core control is insufficient, however, to define any of these HFS in the L3 at South Wasson. The lack of core control in this part of the section reflects the fact that most of the L3 section is below the major oil-saturated reservoir interval in this field (fig. 3).

Leonardian 4

As revealed by 2-D seismic data, the Leonard 4 sequence records a time of initial aggradation on the platform followed by marked sea-level fall and basinward progradation (fig. 6). Reflecting this history, the Leonard 4 sequence on the platform in South Wasson is composed of lower and upper parts that contain significantly different facies and facies-stacking patterns (fig. 8). The lower L4 succession consists of siliciclastic-free carbonate facies that document a marked sea-level-rise event across the platform following L3 deposition, the transgression then aggradation of the platform. At the base of the Leonard 4 sequence are successions of alternating skeletal wackestones/organic buildups and overlying peloidal packstones to grain-dominated

grainstones that define this sea-level-rise event. These facies successions, which average 60 to 80 ft in thickness, may represent HFS. Note that both successions display progressive lateral changes in facies from organic buildup facies to peloidal packstones, suggesting accommodation-related facies development (fig. 8). Wells 8521 and 8510, for example, are located in basinward positions but display relatively shallower water facies development in both L4 and younger sequences. This suggests that this area of the platform was relatively positive compared with surrounding parts of the platform.

The upper part of L4 differs principally from the lower part in having abundant siltstone and silty carbonates (fig. 8). These silt-rich intervals are cyclically interbedded with shallow-water peloidal packstones, grain-dominated packstones, and skeletal wackestones. These deposits document decreasing accommodation on the platform and progradation basinward during late L4 time. Silt was probably carried onto the platform during periodic sea-level-fall events and then reworked by the ensuing transgressions. The top of L4 is marked by local exposure and the development of tidal flats and associated flanking high-energy ramp-crest facies on high parts of the platform (fig. 8).

Leonardian 5

Seismic data demonstrate the major sea-level fall that occurred during L4 deposition (fig. 6). Although the magnitude and duration of this fall are unclear, it seems certain that the platform including the Wasson field area was emergent for a considerable length of time. Nevertheless, the evidence of this major hiatus is lacking in all but one of the available cores. In all but the 8521 well, where the contact is marked by the superposition of high-energy subtidal ramp-crest deposits over the exposed tidal flats at the top of L4, there is no obvious break in the vertical facies succession (fig. 8). The base of L5 in platformward cores, for example, consists of siltstone and silty carbonate-based cycles like those in L4. The base of the sequence in the more basinward 8521 well contains cycles of peloid grain-dominated packstone also virtually identical to those in the underlying L4.

Except for the base, however, L5 is very different from L4 and other underlying sequences in terms of facies and facies tract differentiation. L5 consists of two well-defined and very different facies tracts: a ramp-crest succession and a landward inner platform succession (fig. 8). The ramp-crest facies tract is developed in the eastern part of the field and is especially well developed on the structural high (fig. 8). Like most ramp crests in the Permian of the

Permian Basin, which are typically developed as high-energy carbonate sands at the windward platform margin (fig. 9), ramp-crest facies at South Wasson field comprise peloid and ooid grain-dominated packstones and packstones (fig. 8). Because of the dominance of grain-rich facies, ramp-crest facies tracts are commonly the site of best reservoir development in Permian reservoirs.

In striking contrast, rocks landward of the ramp crest are dominated by mud-rich facies, primarily peloidal and skeletal wackestones and mudstones of the inner platform (fig. 8). Inner platform rocks are typically mud rich because of their protected position behind the ramp crest where wave energy is greatly reduced (fig. 9). These rocks are typically very poor reservoir rocks, as is the case at South Wasson field.

Although there are limited core data to document it, L5 clearly contains a third, more basinward facies tract. Regional outcrop and subsurface of the Leonard and younger Permian successions demonstrate that an outer platform facies tract is invariably developed basinward of the ramp crest (fig. 9). At South Wasson field, this facies tract is developed at the eastern edge of the field (fig. 10).

In contrast to the highly progradational nature of L4, both seismic and core data indicate that L5 is dominantly aggradational. This is consistent with the transgressive nature of L5. This sequence documents renewed sea-level rise and platform flooding following major sea-level fall at the end of L4. The top of L5 is marked across the field by a thin succession of tidal-flat facies (fig. 8). This demonstrates that the magnitude of the post-L4 sea-level rise was less than earlier Leonard rises.

Leonardian 6

Regional studies show that L6 represents the late highstand leg of a major sea-level rise/fall cycle (Kerans and others, 1994; Fitchen and others, 1995; Ruppel and others, 2000). The boundary between L5 and the overlying L6 sequence at South Wasson field is readily defined by the tidal-flat deposits at the top of L5 and the presence of an extensive siltstone at the base of L6 (fig. 8). No core data are available to define facies in L6. However, previous studies of this part of the Leonard suggest that this section is characterized by cycles of alternating inner platform facies and tidal-flat facies. Ruppel (1992; in press) showed that tidal-flat facies can be identified by high-CGR gamma-ray signatures because of the presence of clay and silt. These high-GR signatures are commonly used to define the Glorieta Formation. Two apparent high-frequency

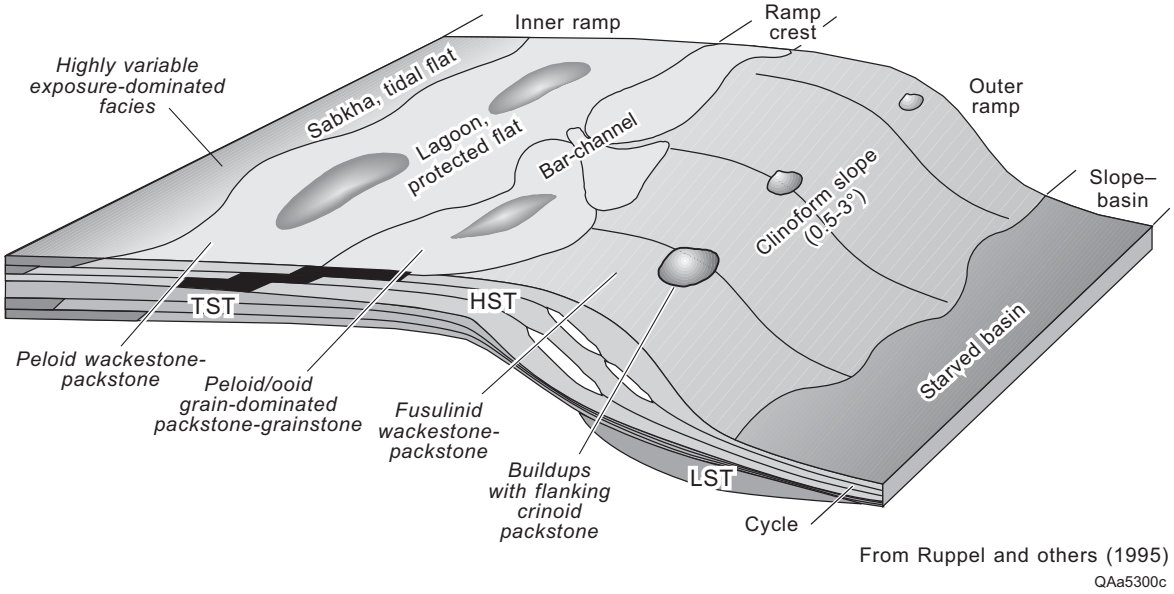

Figure 9. Depositional model for Permian shallow-water carbonate platforms in the Permian Basin. From Ruppel and others (1995).

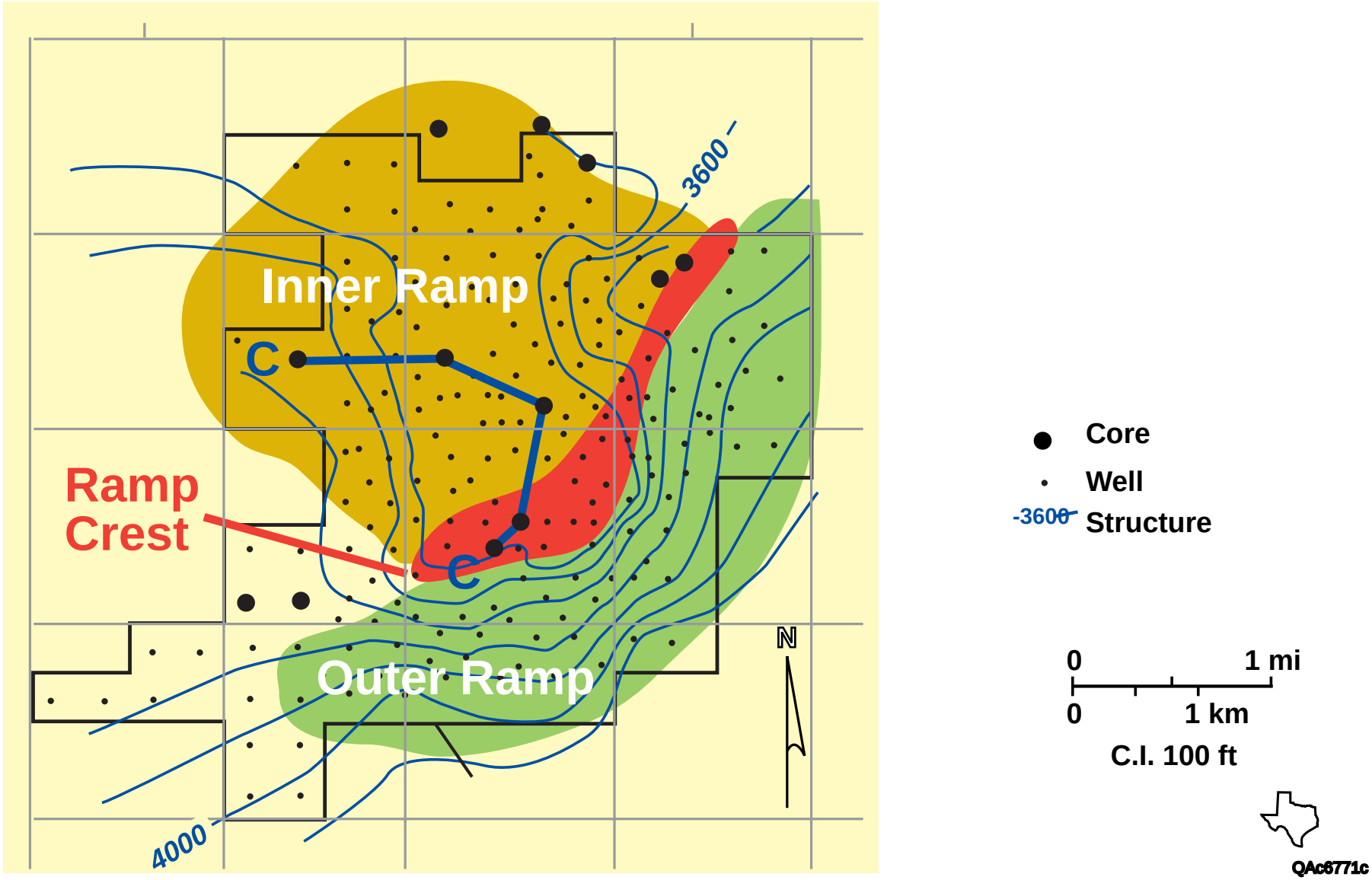

Figure 10. Paleogeographic map of South Wasson field showing development of major facies tracts during L5 time. The ramp-crest facies tract that is especially well developed over the structural high is the center of the field that was active during Clear Fork deposition.

sequences can be defined from these log patterns, each characterized by subtidal carbonate bases and tidal-flat carbonate tops (fig. 8). Although productive in some fields in the Wasson field, the Glorieta does not contribute to production at South Wasson field.

CYCLE DEFINITION AND CORRELATION

Cycles defined in the Clear Fork at South Wasson field are based on vertical facies stacking patterns observed in cores. Two assumptions are key to cycle definition: (1) most carbonate facies stacking patterns are dominantly the result of the creation then filling of accommodation or space, and (2) each facies can be associated with a specific water depth, energy, or accommodation setting. Accommodation can be created by subsidence, by sea-level rise, or by a combination of the two. On most stable carbonate platforms, carbonate production is relatively continuous and filling of accommodation begins almost as soon as it is created. Vertical facies successions reflect changes in water depth (generally decreasing upward), wave energy (usually increasing then decreasing upward), and biotic content as accommodation is filled. The depositional conditions under which facies are deposited can be inferred from studies of modern carbonate environments and by application to ancient systems. Identification of subsurface Clear Fork cycles in this study is based on the development of an accommodation model of depositional facies derived from studies of Permian carbonate outcrop successions (fig. 9). Because carbonate sedimentation proceeds to fill accommodation, cycles typically consist of upward-shallowing successions (fig. 11). Cycle boundaries are defined where upward-shallowing successions are overlain by relatively deeper water, or more basinward facies indicting that sea level has risen and deeper water or more basinward conditions have moved landward across the platform. Because fusulinids are deposited in rocks that typically form on the outer platform of Permian platforms (fig. 9), fusulinid-bearing facies are perhaps the most important indicator of sea-level change and, thus, cycle boundaries in the Permian.

Lower Clear Fork Cyclicity

Vertical facies stacking patterns observed in Clear Fork cores at South Wasson field define two scales of apparent cyclicity (fig. 12). High-frequency cycles range from 2 to 15 ft in thickness and average about 6 ft. Subtidal cycles are dominantly two types: outer platform (deeper water) cycles are composed of fusulinid wackestone-packstone bases and peloid packstone tops; shallow platform cycles contain peloid-skeletal wackestone bases and peloid

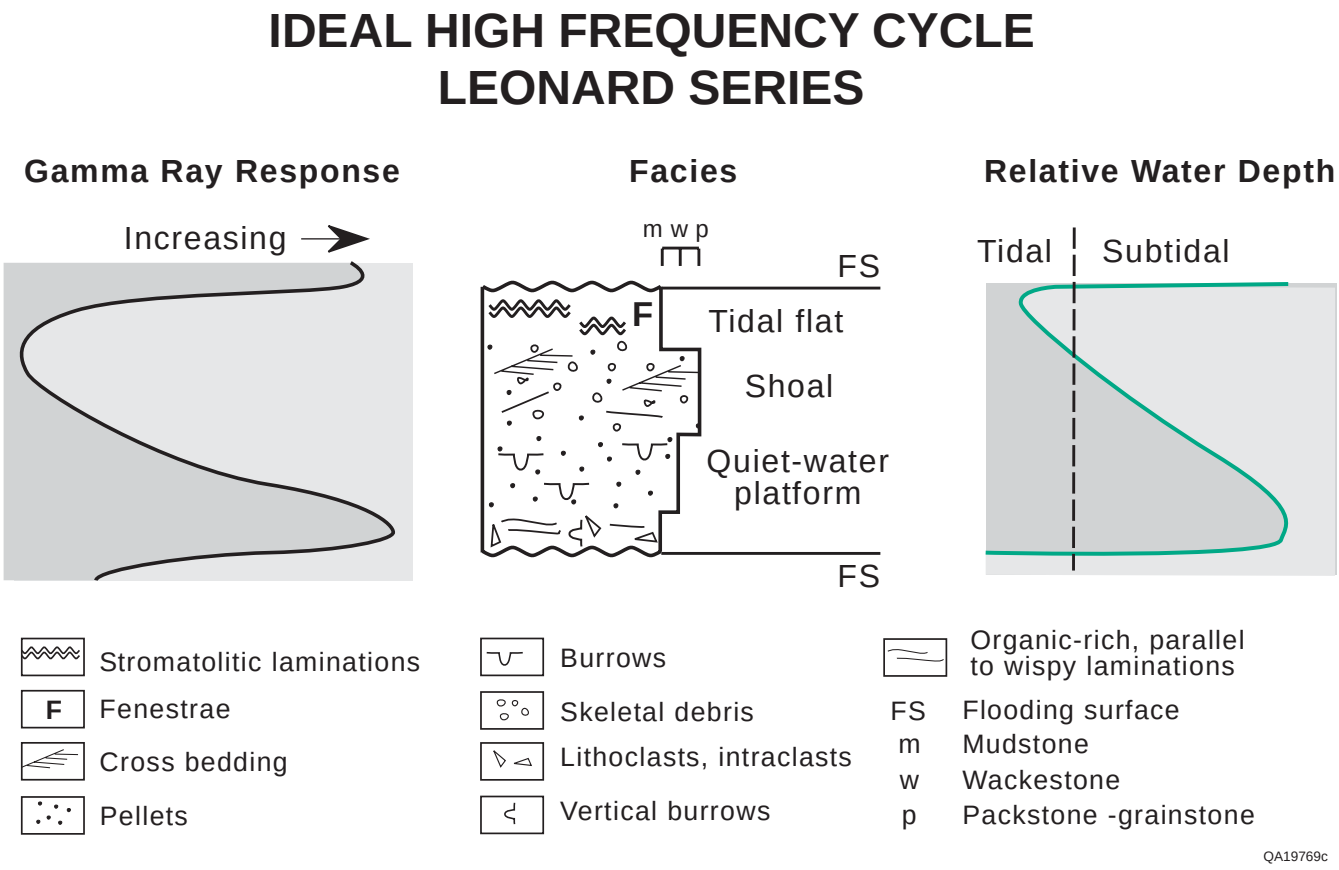

Figure 11. Facies succession and log signature in an ideal shallow-water platform carbonate cycle.

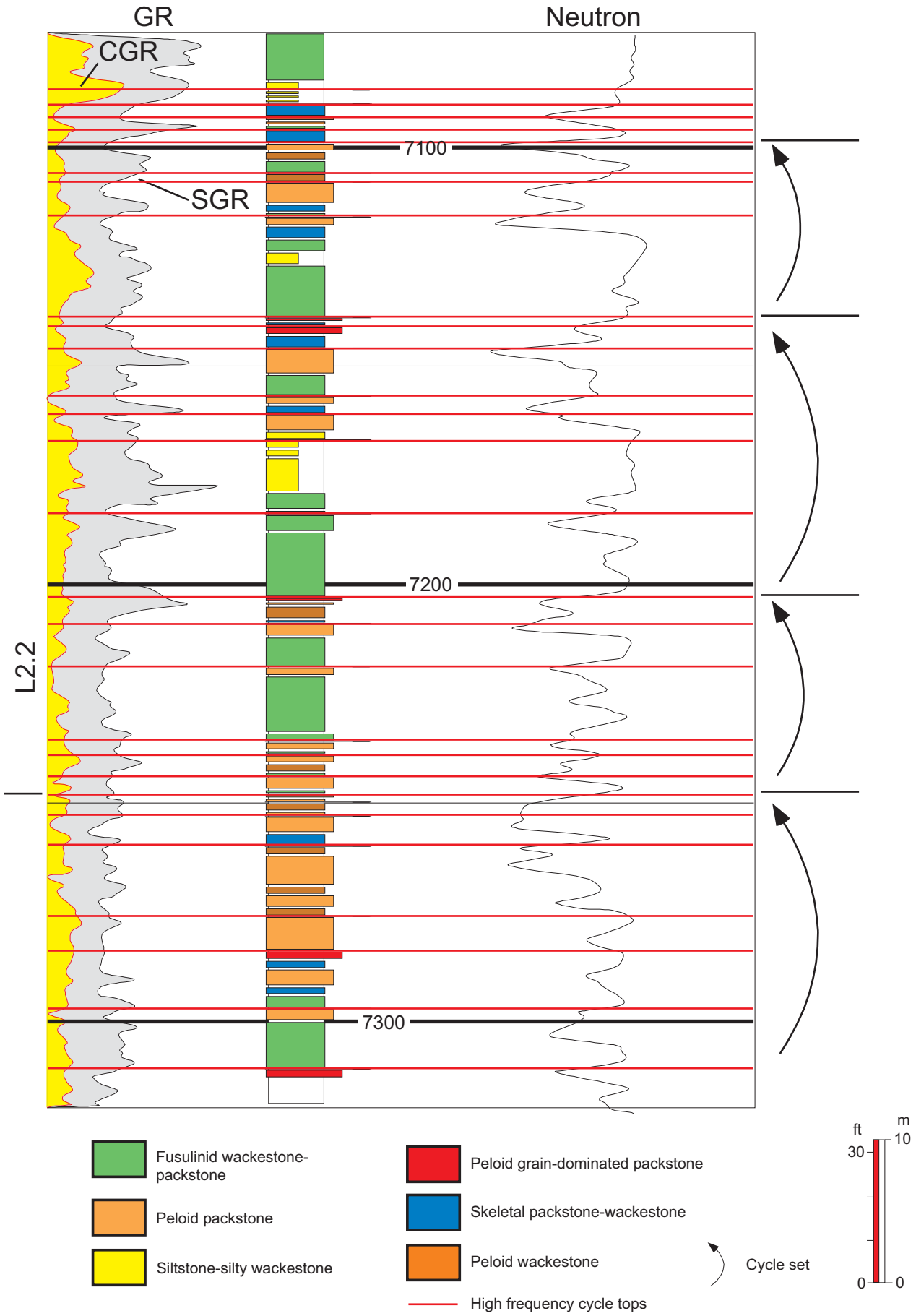

Figure 12. Styles of cyclicity in the lower Clear Fork at South Wasson field.

packstone to grain-dominated packstone tops (fig. 12). Cycle stacking patterns suggest the presence of thicker cycles or cycle sets, averaging about 50 ft in thickness. These cycles sets are composed of fusulinid-bearing high-frequency cycles at their bases and fusulinid-free peloid-rich cycles at their tops (fig. 12).

Porosity is generally better developed in the peloid-dominated cycle tops of the lower Clear Fork high-frequency cycles than in the fusulinid-rich bases (fig. 12). Because cycle sets contain dominantly peloidal cycles, their tops also display higher porosity than their bases. Thus, porosity in these rocks is cyclic, at two different scales.

Upper Clear Fork Cyclicity

Two scales of cyclicity are also apparent in the upper Clear Fork succession at South Wasson field. High-frequency cycles and cycle sets are similar in thickness facies stacking patterns to those in the lower Clear Fork: high-frequency cycles range from 2 to 15 ft in thickness and average about 7 ft; cycle sets average about 60 ft (fig. 13). Component facies in both cycles and cycle sets vary depending on accommodation. L3 and L4 transgressive systems tract (TST) cycles commonly contain skeletal wackestone bases and peloid packstone tops. L3 and L4 highstand systems tract (HST) cycle bases are mostly composed of peloid wackestone bases and peloid grain-dominated packstone-packstone tops. L3 and L4 cycle sets are typically defined by stacked skeletal-peloid-rich cycles at their bases and peloid-rich cycles at their tops (fig. 13). Siltstone and silty wackestone facies are common in the bases and middle legs of cycle sets (fig. 13).

L5 cycles do not display any systematic vertical changes in facies stacking that would define TST and HST. Basinward L5 ramp-crest facies tract cycles are characterized by peloid mud-rich bases and peloid grain-rich tops (fig. 13). Inner platform L5 cycles are mud rich, composed of peloid or skeletal wackestone bases and mudstone (possibly incipient tidal-flat exposure facies) caps (fig. 13).

As with lower Clear Fork cycles, peloid grain-rich cycle tops in the upper Clear Fork (L3, L4, and L5) generally contain higher porosity than typically mud-rich peloid/skeletal wackestone (figs. 8 and 13).

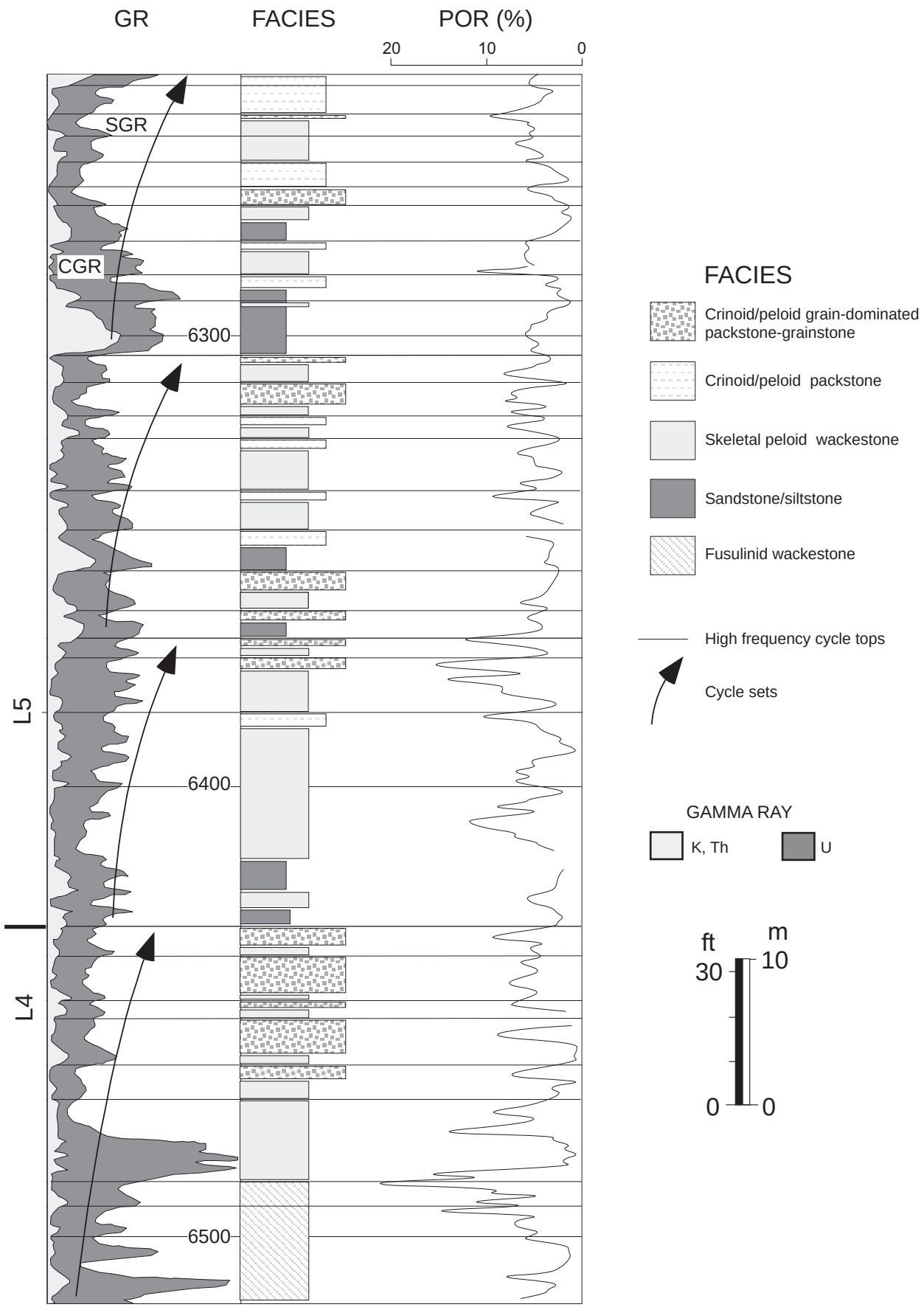

Figure 13. Cross section depicting the sequence architecture and facies tracts in the upper Clear Fork succession at South Wasson field.

Cycle Correlation

Both high-frequency cycles and cycle sets are of sufficient thickness to be potentially correlatable across the South Wasson field area. Correlation cycles in cored wells show that even high-frequency cycles are correlative across the field (fig. 14). However, where cores are absent, correlations are difficult. In many carbonate successions, gamma-ray curves can be used to correlate cycles (fig. 11). In these cases, gamma-ray response is due to systematic variations in uranium or potassium. Uranium, for example, can be preferentially associated with cycle bases because they were deposited slowly and contain organic-rich muds that attract uranium. Cycle tops, conversely, contain low uranium levels because they contain less mud. Many Clear Fork cycles at mud-rich cycle bases in the South Wasson Clear Fork reservoir display high gamma-ray bases and low gamma-ray tops; however, many do not (figs. 12 and 13). Because uranium content varies widely in the Clear Fork carbonate rocks at South Wasson field, gamma logs are not generally reliable for correlation. Spectral gamma-ray logs are locally useful for correlation in the field, especially in the silt-rich rocks of the L4 and lower L5 sequences. The CGR gamma-ray log can, in some cases, separate the potassium/thorium response of these silty rocks from the variable uranium content in the carbonates (fig. 13). However, these logs are few. In their absence, the acoustic log is a better correlation tool for silty intervals.

CONCLUSIONS

The Clear Fork reservoir at South Wasson field is typical of many Clear Fork reservoirs in the Permian Basin in terms of both oil production efficiency and geological attributes. Perhaps more importantly, it also displays marked similarity to Clear Fork outcrop equivalents in the Apache Mountains of West Texas. These similarities make it possible to utilize outcrop data along with subsurface data to construct an accurate geological model.

The lower Clear Fork sequence architecture at South Wasson field is virtually identical to that defined in outcrop, suggesting that this architecture is representative of lower Clear Fork succession across the Permian Basin. Although outcrops provide only partial analogs of the upper Clear Fork succession, they do contribute important insights into facies tract development and architecture that can be critical in interpreting subsurface data.

As observed in the outcrop by Ruppel and others (this report) and as shown by Lucia and Jennings for the subsurface (this report), porosity in both upper and lower Clear Fork reservoir

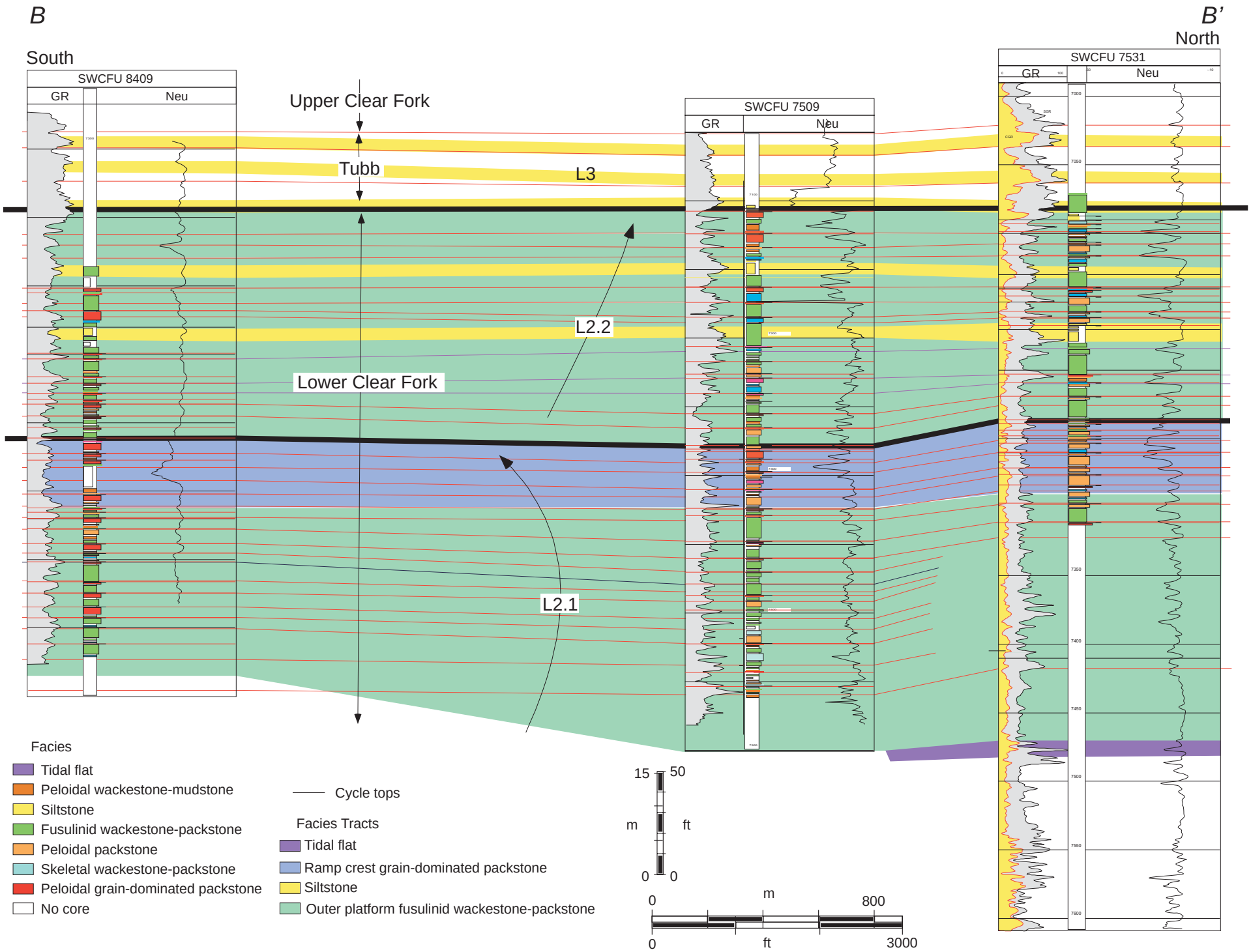

Figure 14. Cross section depicting the sequence architecture and facies tracts in the lower Clear Fork succession at South Wasson field

intervals is concentrated in cycle-top peloid grain-dominated packstones. Typically mud-rich cycle bases generally form lower porosity and permeability baffles. Because of the cycle-based segregation of porosity and permeability in these rocks, cycle correlation is key to the development of a robust model of the reservoir architecture. Construction of such a model is fundamental to the development of effective techniques for recovery of remaining mobile oil in the South Wasson Clear Fork reservoir and other similar reservoirs in the Permian Basin.

ACKNOWLEDGMENTS

This research was funded by the U.S. Department of Energy under contract no. DE-AC26-98BC15105 and by the sponsors of the Reservoir Characterization Research Laboratory: Altura, Amerada Hess, Anadarko, Aramco, ARCO, BP International, Chevron, Elf Aquitaine, ExxonMobil, Great Western Drilling, Japan National Oil Corporation, Kinder Morgan, Marathon, Oxy, Pan Canadian, Pennzoil, Petroleum Development Oman, Shell International, Statoil, South Western Energy, Texaco, and TOTAL. The Bureau of Economic Geology, The University of Texas at Austin, acknowledges support of this research by Landmark Graphics Corporation via the Landmark University Grant Program. Bill Fitchen introduced us to the excellent outcrops in Apache Canyon. Field assistance was provided by Jubal Grubb, Greg Ramirez, and Neil Tabor. We are indebted to Mr. Nelson Puett, owner of the Puett Ranch, for permitting us access to these world-class exposures. Editing was by Susann Doenges, and design and layout were by Scarlett Hurt. Figures were prepared by the Bureau of Economic Geology graphics department under the direction of Joel L. Lardon.

REFERENCES

Ariza, E. E., 1998, High resolution sequence stratigraphy of the Leonardian lower Clear Fork Group in the Permian Basin, West Texas: The University of Texas at Austin, unpublished Master's thesis, 128 p.

Atchley, S. C., Kozar, M. G., and Yose, L. A., 1999, A predictive model for reservoir characterization in the Permian (Leonardian) Clear Fork and Glorieta Formations, Robertson field area, West Texas: American Association of Petroleum Geologists Bulletin, v. 83, p. 1031–1056.

Fitchen, W. M., Starcher, M. A., Buffler, R. T., and Wilde, G. L., 1995, Sequence stratigraphic framework and facies models of the early Permian platform margins, Sierra Diablo, West Texas, *in* Garber, R. A., and Lindsay, R. F., eds., Wolfcampian-Leonardian shelf margin facies of the Sierra Diablo— seismic scale models for subsurface exploration: West Texas Geological Society Publication 95-97, p. 23–66.

Holtz, M. H., and Garrett, C. M., 1990, Geologic and engineering characterization of Leonardian carbonate oil reservoirs: a framework for strategic recovery practices in four oil plays, *in* Flis, J. E., and Price, R. C., eds., Permian Basin oil and gas fields: innovative ideas in exploration and development: West Texas Geological Society Publication No. 90-87, p. 76.

Holtz, M. H., Ruppel, S. C., and Hocott, C. R., 1992, Integrated geologic and engineering determination of oil-reserve-growth potential in carbonate reservoirs: Journal of Petroleum Technology, November, p. 1250–1258.

Kerans, Charles, Lucia, F. J., and Senger, R. K., 1994, Integrated characterization of carbonate ramp reservoirs using Permian San Andres Formation outcrop analogs: American Association of Petroleum Geologists Bulletin, v. 78, no. 2, p. 181–216.

Kerans, Charles, Kempter, K., Rush, J., and Fisher, W. L., 2000, Facies and Stratigraphic Controls on a Coastal Paleokarst, Lower Permian, Apache Canyon, West Texas, *in* Lindsay, R., Trentham, R., Ward, R. F., and Smith, A. H., eds., Classic Permian geology of West Texas and southeastern New Mexico, 75 years of Permian Basin oil & gas exploration & development: West Texas Geological Society Publication 00-108, p 55–82.

Kerans, Charles, and Fitchen, W. M., 1995, Sequence hierarchy and facies architecture of a carbonate ramp system: San Andres Formation of Algerita Escarpment and western Guadalupe Mountains, West Texas and New Mexico: The University of Texas at Austin, Bureau of Economic Geology Report of Investigations No. 235, 86 p.

Mazzullo, S. J., 1982, Stratigraphy and depositional mosaics of lower Clear Fork and Wichita groups (Permian), northern Midland Basin, Texas: American Association of Petroleum Geologists Bulletin, v. 66, p. 210–227.

Mazzullo, S. J. and Reid, A. 1989, Lower Permian platform and basin depositional systems, northern Midland Basin, *in* Controls on carbonate platform and basin development: SEPM Special Publication no. 44, p. 303–320.

Presley, M. W., 1982, Evolution of Permian evaporite basin in the Texas Panhandle: American Association of Petroleum Geologists Bulletin, v. 71, p. 167-190.

Ruppel, S. C., in press, Geological controls on Leonardian reservoir development, Monahans Clear Fork field, West Texas: The University of Texas at Austin, Bureau of Economic Geology Report of Investigations.

Ruppel, S. C. , 1992, Styles of deposition and diagenesis in Leonardian carbonate reservoirs in West Texas: implications for improved reservoir characterization: Society of Petroleum Engineers Annual Exhibition and Technical Conference, 24691, p. 313–320.

Ruppel, S. C. , Kerans, Charles, Major, R. P., and Holtz, M. H., 1995, Controls on reservoir heterogeneity in Permian Basin shallow-water platform carbonate reservoirs, Permian Basin: implications for secondary recovery: The University of Texas at Austin, Bureau of Economic Geology Geological Circular 95-2, 30 p.

Ruppel, S. C., Ward, W. B., Ariza, E. E., and Jennings, J. W., Jr., 2000, Cycle and sequence stratigraphy of Clear Fork reservoir-equivalent outcrops: Victorio Peak Formation, Sierra Diablo, Texas, *in* Lindsay, R., Trentham, R., Ward, R. F., and Smith, A. H., eds., Classic Permian geology of West Texas and southeastern New Mexico, 75 years of Permian Basin oil & gas exploration & development: West Texas Geological Society Publication 00-108, p. 109–130.

Saller, A. H., and Henderson, N., 1998, Distribution of porosity and permeability in platform dolomites: insights from the Permian of West Texas: American Association of Petroleum Geologists Bulletin, v. 82, no. 8, p. 1528–1550.

Shinn, E. A., 1983, Tidal flat, *in* Scholle, P. A., Bebout, D. G., and Moore, C. H., eds., Carbonate depositional environments: American Association of Petroleum Geologists Memoir 33, p. 171–210.

Tyler, Noel, Galloway, W. E., Garrett, C. M., Jr., and Ewing, T. E., 1984, Oil accumulation, production characteristics, and targets for additional recovery in major oil reservoirs of Texas: The University of Texas at Austin, Bureau of Economic Geology Geological Circular 84-2, 31 p.

Tyler, Noel, and Banta, N. J., 1989, Oil and gas resources remaining in the Permian Basin: targets for additional hydrocarbon recovery: The University of Texas at Austin, Bureau of Economic Geology Geological Circular 89-4, 20 p.

Ye, Qiucheng, and Mazzullo, S. J. , 1993, Dolomitization of lower Permian platform facies, Wichita Formation, north platform, Midland Basin, Texas: Carbonates and Evaporites v. 8, no. 1, p. 55–70.

CALCULATION AND DISTRIBUTION OF PETROPHYSICAL PROPERTIES IN THE SOUTH WASSON CLEAR FORK FIELD

F. Jerry Lucia and James W. Jennings, Jr.

Bureau of Economic Geology
John A. and Katherine G. Jackson School of Geosciences
The University of Texas at Austin

TABLE OF CONTENTS

LIST OF FIGURES

ABSTRACT

The South Wasson Clear Fork reservoir can be characterized by a single porosity-permeability transform and a single saturation, porosity, and reservoir-height equation despite the presence of a robust variety of rock fabrics. Rock fabrics include large and medium crystalline grain-dominated dolopackstones and medium crystalline mud-dominated dolostone of class 1 and 2. Cross plots of porosity and permeability demonstrate that all the fabrics tend to plot in the petrophysical class 1 field, whether classified as class 1 or class 2. It is suggested that the class 2 fabrics shift into the class 1 field as a result of the presence of unusually large volumes of poikilotopic and pore-filling anhydrite. The anhydrite patches have no porosity and occupy an average of 20 percent of the rock, creating a nonuniform patchwork of porous and dense rock. Adding the patches of anhydrite reduces the porosity, but the pore sizes remain constant. This results in samples moving laterally from a higher petrophysical class to a lower class instead of moving within a petrophysical class. The capillary pressure curves are also of the petrophysical class 1 type.

Core descriptions show two types of high-frequency cycles (HFC's) in this reservoir: silt-based cycles that are capped by grain-dominated dolopackstone and carbonate cycles that typically have bases composed of mud-dominated fabrics and caps of grain-dominated dolopackstone. The acoustic and porosity logs were used to identify silt beds and silt-based cycles. Carbonate cycles could not be identified using the gamma-ray log because of the large amount of diagenetic uranium in the Clear Fork, and cross plots of porosity and water saturation are of little use because the fabrics group into one petrophysical class. A statistical study of porosity and rock fabrics shows the mud-dominated fabrics have lower porosity than the grain-dominated fabrics do on the average. Therefore, vertical increases in porosity were interpreted to mean a change from mud-dominated to grain-dominated fabrics. This approach was used to pick and map HFC's.

In order to maintain high and low permeability in the flow model, each HFC was divided into a lower, low-permeability mud-dominated layer and an upper, high-permeability grain-dominated packstone layer. The layers, which are referred to as rock-fabric flow layers, are the basic elements in the construction of a flow model.

INTRODUCTION

The principal objective of this subsurface study is to construct a 3-D model of petrophysical properties of porosity, permeability, and water saturation suitable for developing a flow simulation model in a 1-mi^2 area of the South Wasson Clear Fork (SWCF) field, Gaines County, Texas (fig. 1). Production data and Archie water saturation calculations indicate that the Clear Fork reservoir is divided into lower and middle Clear Fork reservoirs (fig. 2). Although there is some oil saturation in the upper Clear Fork and Glorieta Formation, on the basis of production history the oil appears to be at residual saturation, suggesting that oil in this reservoir has remigrated. The reservoir study is focused on the lower and middle Clear Fork reservoirs.

The Tubb sandstone is the seal for the lower Clear Fork reservoir, and a dense interval between the middle and upper Clear Fork is the seal for the middle Clear Fork reservoir (fig. 2). The seal for the upper Clear Fork reservoir that contains residual oil is most likely at the top of the Glorieta Formation. In Clear Fork reservoirs it is common for the Tubb Formation to seal the lower Clear Fork reservoir and the Glorieta Formation to seal the upper Clear Fork and Glorieta reservoirs. These seals conform to well-known sequence boundaries L2 and L6 (fig. 2, Ruppel, this report). The seal for the middle Clear Fork is less well known. However, this seal coincides with a prominent sequence boundary observed on regional seismic lines and labeled L4 (see Ruppel and Ariza, this report). Sequence boundaries L1, L3, and L5 do not appear to be reservoir seals.

A key activity in building a realistic reservoir model suitable for flow simulation is quantifying the geologic model in terms of porosity, permeability, and oil saturation. There are currently two basic approaches used in this activity. The most common is referred to as rock typing, defining rock types having similar petrophysical properties and relating these rock types to geologic facies (Kerans and Tinker, 1997; Neo and others, 1998; Grotsch and Mercadier, 1999; Martin and others, 1999). The rock-type method emphasizes collecting rocks into petrophysical groups using cluster analysis, fuzzy logic, and similar statistical methods, and then relating the rock types to geology. The second method, and the one used in this study, is referred to as the rock-fabric method, which depends upon developing relationships between rock fabrics and petrophysical properties. The rock-fabric method integrates geologic descriptions with petrophysical properties by emphasizing the relationship between pore-size distribution, rock fabrics, and petrophysical properties.

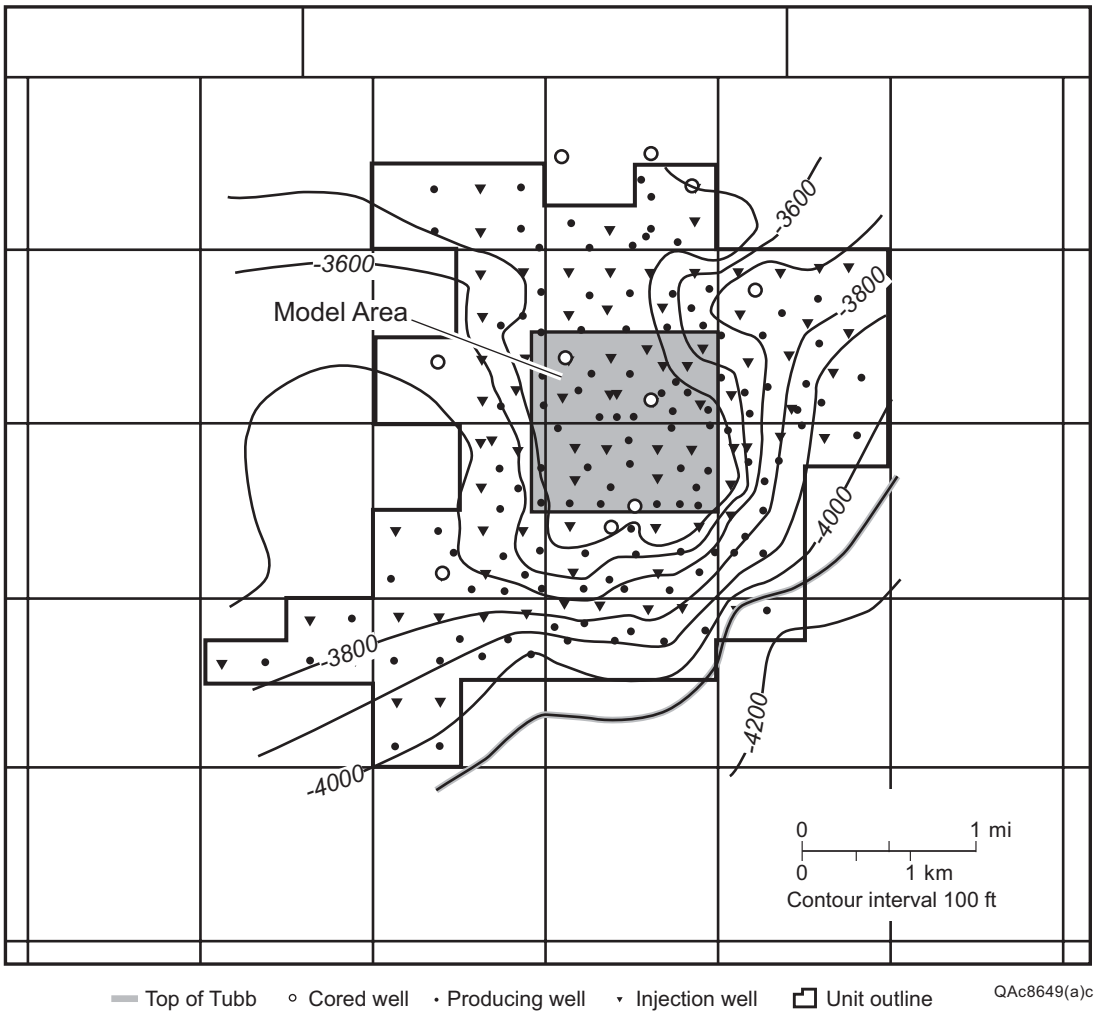

Figure 1. Location map showing structure and study area.

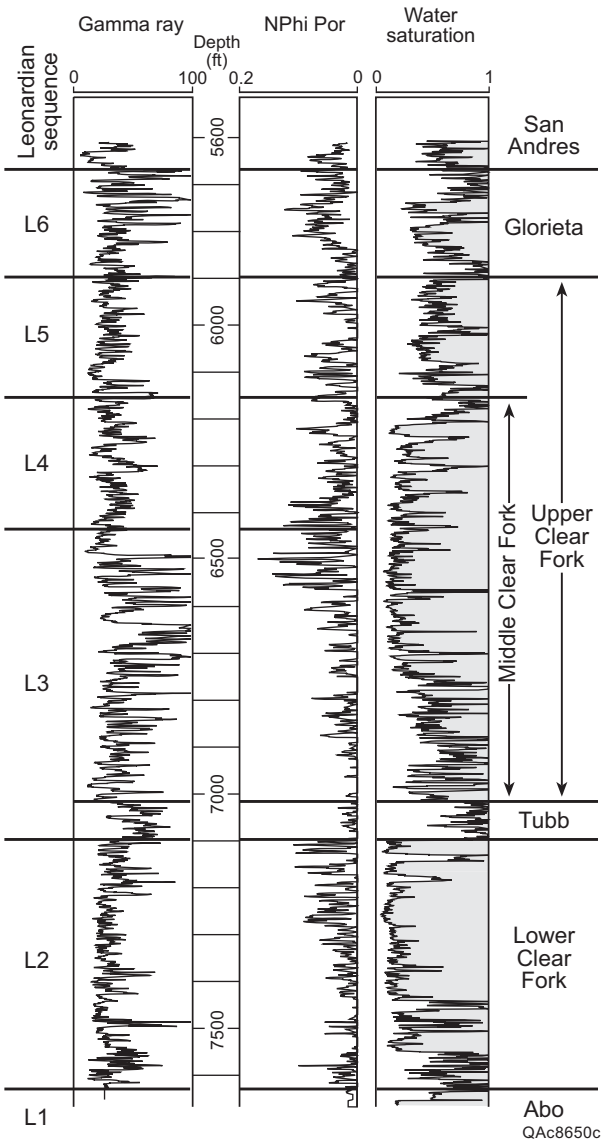

Figure 2. Type log from well 7531 showing Leonardian sequences and formation names.

METHODS

The first activity in the rock-fabric method is developing relationships between rock fabrics and porosity, permeability, and capillary properties. Thin sections are made from the ends of permeability plugs and described using the classification of Lucia (1995). Visible interparticle porosity, separate-vug porosity, and mineral percentages are determined by point-counting 300 points per thin section. Total porosity is determined from core analysis, and interparticle porosity by subtracting visible separate-vug porosity from total porosity. Average dolomite crystal size and grain size are estimated using a micrometer. Cross plots of various rock fabrics are made using total porosity, interparticle porosity, and permeability, from which rock-fabric-specific porosity-permeability transforms are developed. Capillary pressure data are grouped by rock-fabric and porosity. A multivariant analysis approach is used to create a model relating water saturation to porosity and rock fabric.

The second activity is to calibrate wireline log responses with rock fabrics and interparticle porosity. Interparticle porosity is usually calibrated to acoustic log response. Rock fabric can be calibrated to porosity, gamma-ray logs, and relationships between saturation, reservoir height, and porosity. An important aspect of this activity is the vertical stacking of rock fabrics into HFC's. Typically, HFC's are vertical successions of increasing grain content, from mud-dominated to grain-dominated fabrics. The cycles are first identified in cores using the vertical succession of facies. Detail facies descriptions are combined into rock-fabric facies and then calibrated with wireline logs to develop criteria for identifying HFC's from logs. Once the logs are calibrated, HFC's and rock-fabric units are defined in every well.

The third activity is to correlate the HFC's between wells. Once the HFC framework has been established the vertical succession of rock fabrics is used to define flow layers, layers having the same rock-fabric, petrophysical relationships. The 3-D model of flow layers provides the basic framework to be populated with porosity from wireline logs, permeability from rock-fabric-specific porosity-permeability transforms, and saturation from rock-fabric-specific relationships between porosity, saturation, and reservoir height.

ROCK-FABRIC PETROPHYSICAL RELATIONSHIPS (ZERO-DIMENSIONAL ANALYSIS)

The rock-fabric method has been described by Lucia (1995, 1999) and Jennings and Lucia (2001). Porosity is divided into three basic types, interparticle, separate vug, and touching vug. Interparticle porosity is characterized by the amount of interparticle porosity, grain size and sorting, and dolomite crystal size. Crystal size is important for characterizing dolomitized mud-dominated fabrics. Separate-vug porosity is characterized by amount and type. Touching-vug porosity is characterized by type only because the amount does not relate to pore size.

A general relationship between these basic pore types, rock fabrics, and petrophysical properties of porosity, permeability, and water saturation has been presented by Lucia (1995). Interparticle porosity is the most common interconnected pore type and provides most of the permeability in many reservoirs. It is divided into three basic petrophysical classes. Class 1, the most permeable, includes grainstone, dolograinstone, and large crystalline dolostone. Class 2, the next most permeable, includes grain-dominated packstone and fine –to medium crystalline grain-dominated dolopackstone and medium crystalline mud-dominated dolostone. Class 3, the least permeable, includes mud-dominated limestones and fine crystalline mud-dominated dolostones. Separate-vug porosity is generally characterized as providing storage volume for hydrocarbons but contributing little to fluid flow. Touching vugs form a connected pore system that is independent of interparticle porosity and is generally characterized as a low-porosity, high-permeability pore system.

The rock fabrics described from the South Wasson Clear Fork field are anhydritic dolostones and sandstones. Dolostones include class 1 large crystalline dolostones, dolograinstones, and large-grain grain-dominated dolopackstones (fig. 3). Large-grain grain-dominated packstones have been recently added to petrophysical class 1 on the basis of a study of the Ghawar field (Lucia and others, 2001). Included in class 2 are medium crystalline grain-dominated dolopackstones, mud-dominated dolopackstones, and dolowackestones (fig. 4). Only a few class 3 fine crystalline mud-dominated dolopackstones and dolowackestones have been described from the SWCF field. Separate-vug porosity is rare because most of the intrafossil and moldic pore space has been filled with anhydrite. Only a few samples have more than 3 percent moldic porosity. Some touching-vug porosity is present in the form of microfractures, but most

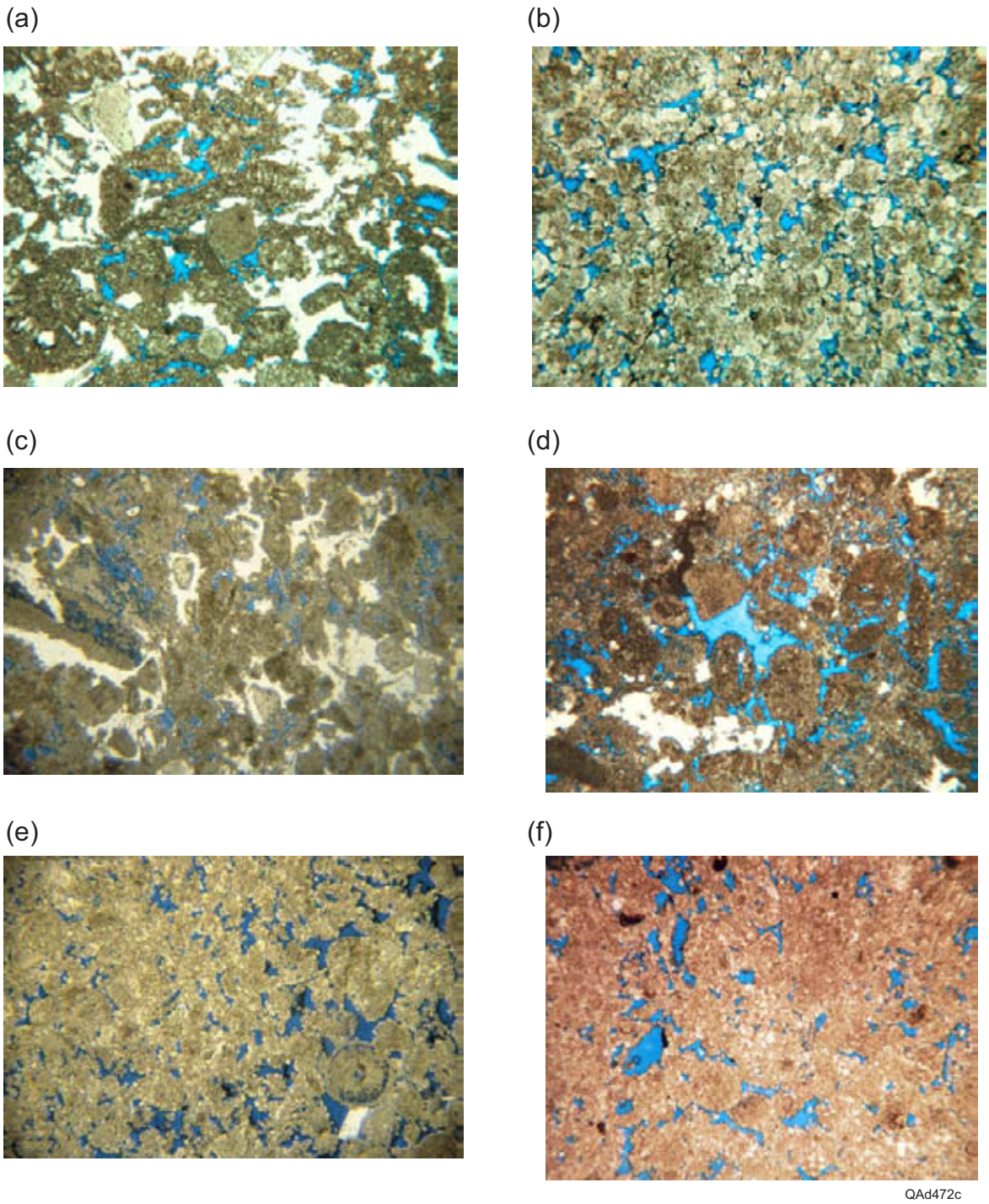

Figure 3. Photomicrographs of petrophysical class 1 fabrics. Light color is anhydrite, and blue is pore space. (a) Dolograinstone, ϕ = 7.1%, k = 1.6 md. (b) Large crystalline grain-dominated dolopackstone, ϕ = 8.2%, k = 7.8 md. (c) Large-grain grain-dominated dolopackstone, ϕ = 8.1%, k = 11 md. (d) Large-grain grain-dominated dolopackstone, ϕ = 9.9%, k = 14 md. (e) Large-grain grain-dominated dolopackstone, ϕ = 8.1%, k = 13 md. (f) Large-grain grain-dominated dolopackstone, ϕ = 10.3%, k = 60 md.

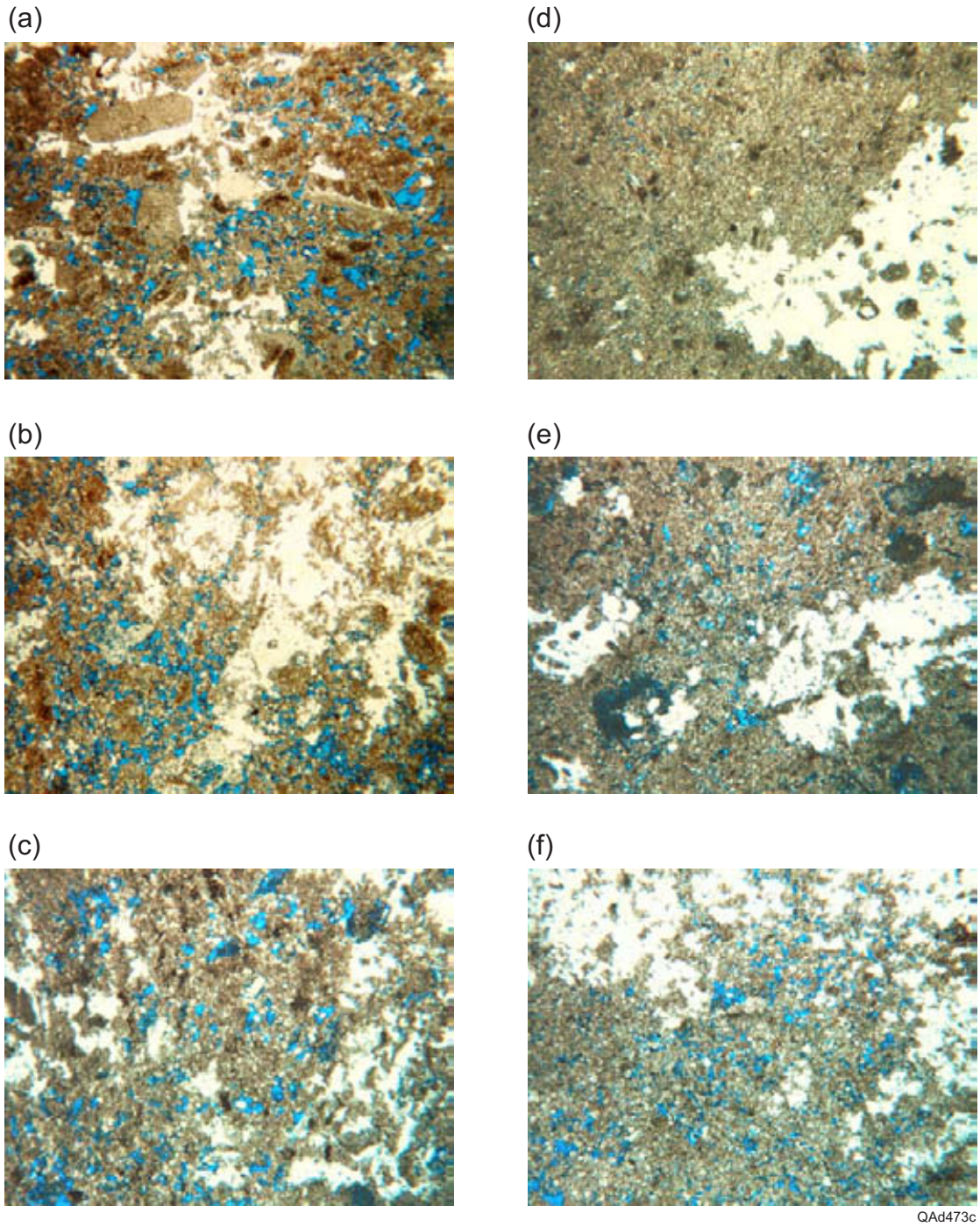

Figure 4. Photomicrographs of petrophysical class 2 fabrics. Light color is anhydrite, and blue is pore space. (a–c) Medium crystalline grain-dominated dolopackstones. (d–f) Medium crystalline dolowackestones. Petrophysical properties: (a) ϕ = 6.4%, k = 0.66 md, (b) ϕ = 13.5%, k = 11 md, (c) ϕ = 9.4%, k = 5.8 md, (d) ϕ = 7.7%, k = 0.47 md, (e) ϕ = 12.6%, k = 4.8 md, (f) ϕ = 6.2%, k = 0.41 md.

of the fractures have been filled with anhydrite. Fractures are described in detail by Gale and Laubach in this report. Sandstones are composed of silt-sized quartz and rare feldspar grains mixed with dolomite, usually fine crystalline. The sandstones have less than 0.1 md permeability and form flow barriers in this reservoir.

Anhydrite is present as pore-filling, poikilotopic, and nodular anhydrite. Nodular anhydrite is scattered throughout the reservoir but occupies an insignificant volume. In those rare instances where it is present in a core plug, however, the petrophysical measurements are biased and must therefore be removed from the data set as unrepresentative. The average amount of pore-filling and poikilotopic anhydrite in the thin sections is 20 percent and ranges from 0 to 60 percent of the thin section. The large volume of anhydrite has a major effect on the relationship between rock fabric, porosity, permeability, and capillary properties, as will be discussed later.

Porosity-Permeability Transform

Porosity-permeability cross plots for the middle and upper Clear Fork reservoirs are similar in the 1-mi study area (fig. 5a). The plots show a relatively good grouping of data greater than 1 md. Below 1 md the data are more scattered because of the presence of numerous samples that have low porosity and measurable permeability. It is judged that these data are biased owing to measurement error, poor sample preparation, and flow through stylolites or induced fractures. Careful measurements made by Westport Laboratory in Houston as part of this study on 41 new core plugs show a good grouping of data including the samples having less than 1 md of permeability (fig. 5b). This grouping supports the contention that the scatter below 1 md in the routine core data is biased and should not be considered when developing a porosity-permeability transform.

Porosity-permeability cross plots for samples having thin sections are similar to plots of all the data, indicating that the thin sections are a good sampling of the reservoir (figs. 6a, 6b). Rock fabrics, as described from thin sections, are plotted on porosity-permeability cross plots in an attempt to develop rock-fabric-specific porosity-permeability transforms. Only three samples are dolograinstone, and only one is permeability, which plots in the class 1 field as expected (fig. 6a). Most of the permeable samples are grain-dominated dolopackstones. Many grain-dominated dolopackstones have large grains ranging from 500 to >1,000 μm in diameter, and these samples

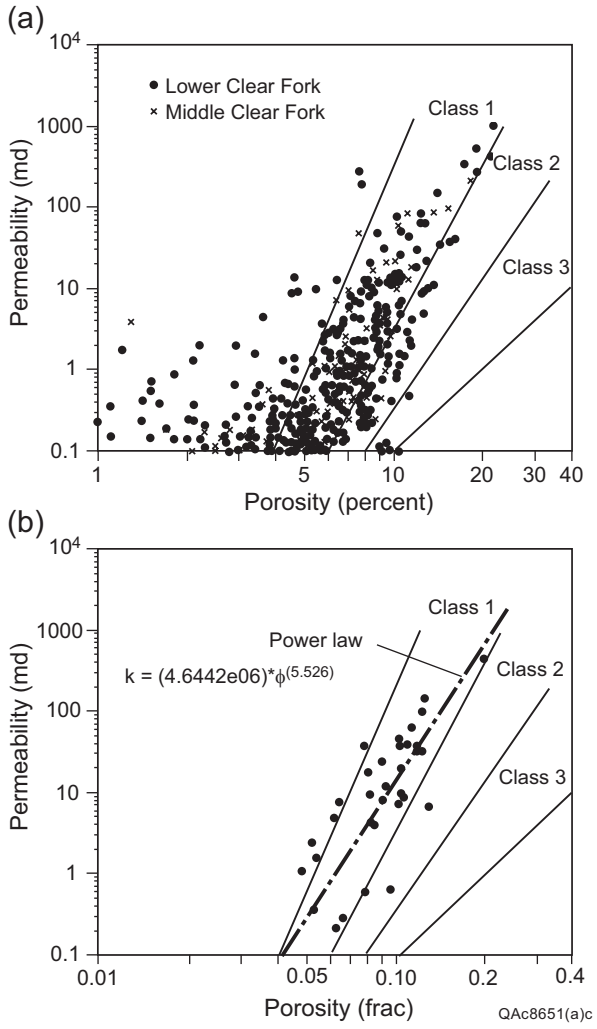

Figure 5. Porosity-permeability cross plots. (a) Cross plot of all middle and lower Clear Fork data from well 7531, illustrating that most of the data fall within petrophysical class 1 field. (b) Cross plot of new data from well 7531 from the middle Clear Fork, showing a power-law transform and the lack of data to the left of the class 1 field.

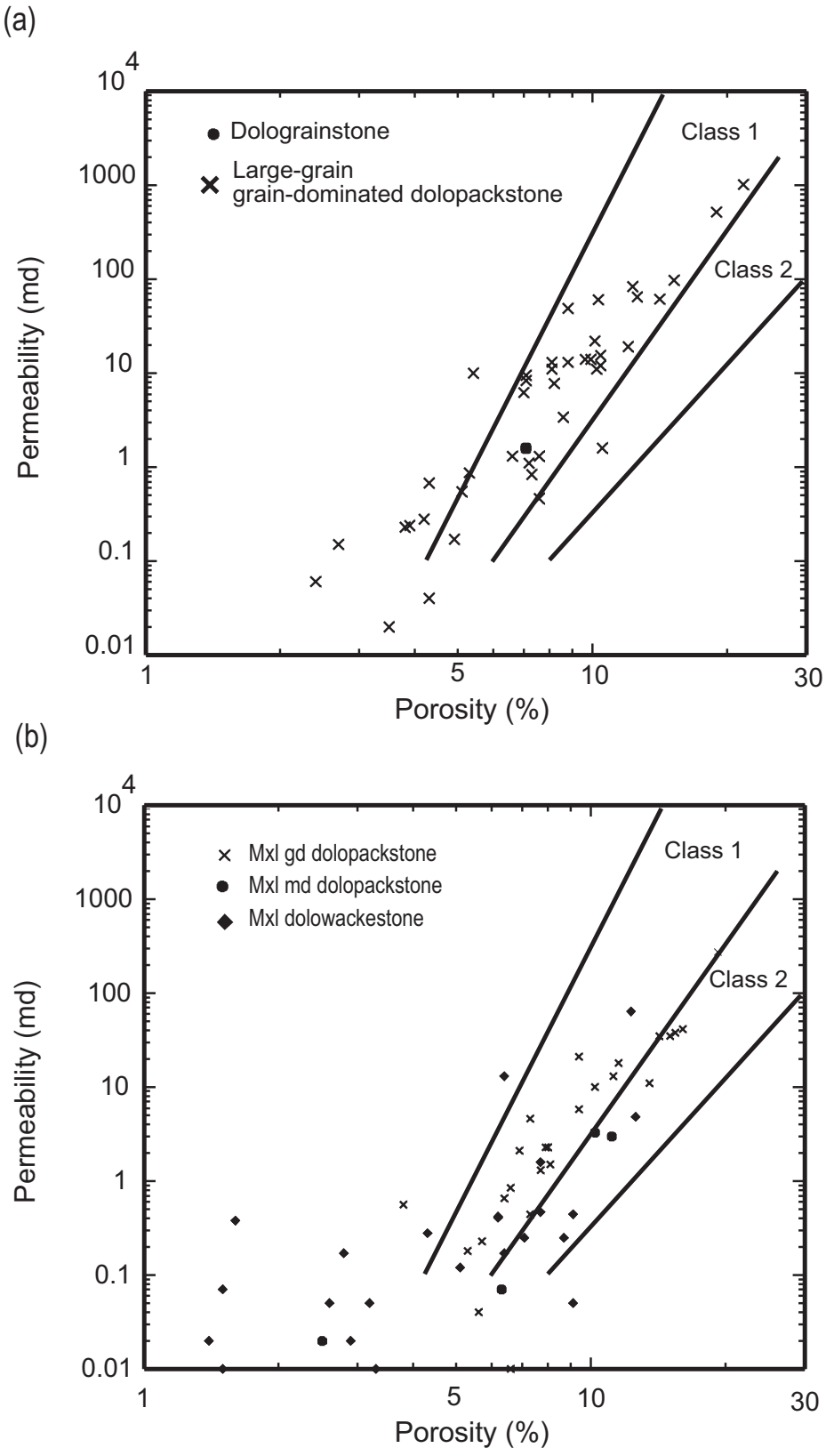

Figure 6. Porosity-permeability cross plots. (a) Cross plot of class 1 rock fabrics showing that the data fall within the class 1 field as predicted. (b) Cross plot of class 2 rock fabrics showing that most of the data fall within the class 1 field also rather than within the class 2 field.

also plot in the class 1 field (fig. 6a). It has been shown (Lucia and others, 2001) that large-grain grain-dominated packstones characteristically plot in the class 1 field. Some grain-dominated dolopackstones and mud-dominated dolostones have dolomite crystal sizes larger than 100 μm, and they plot in the class 1 field as predicted. However, most of the medium crystalline grain-dominated dolopackstones and mud-dominated dolostones that belong to petrophysical class 2 also plot in the class 1 field (fig. 6b), which was not predicted by Lucia (1995).

An explanation for this unpredicted behavior can be developed by exploring the fundamental controls of rock fabrics on petrophysical properties and pore-size distribution. When developing rock-fabric-specific porosity-permeability transforms the basic assumption is that pore sizes are evenly distributed throughout the sample. The geologic model for this assumption is that the initial pore-size distribution is controlled by sediment grain size and sorting and that the pore sizes are reduced uniformly throughout the sediment by carbonate cementation and compaction. Dolostone fabrics mimic the precursor limestone, and pore size is further reduced by a uniform introduction of dolomite cement.

In nature pore sizes are not uniformly distributed, which may account for much of the scatter in well-constrained rock-fabric-specific porosity-permeability transforms. The large volume of poikilotopic anhydrite in these samples, however, presents a special case (figs 3, 4). The average volume of anhydrite in the thin sections is 20 percent but varies widely from 0 to 60 percent with no distinction between tight and permeable samples. Much of the variation is probably due to the fact that the thin sections represent a very small sample of the core plug. The variability would most likely be greatly reduced if the volume of anhydrite in the whole sample could be determined. The anhydrite patches have no porosity and create a nonuniform patchwork of porous and dense rock. Conceptually, adding the patches of anhydrite reduces porosity but does not affect the pore sizes. The pore-size distribution is changed radically but not the actual pore sizes, and the pore sizes control permeability.

Pore-size distribution cannot be measured, but a statistical distribution of pore-throat sizes can be measured using the mercury porosimeter. A relationship between pore-throat size, total porosity, and permeability for siliciclastic rocks has been developed by Pittman (1992) and a similar relationship by Winland (see Kolodzie, 1980). In these equations, pore size is equal to a specific pore-throat size determined by converting a capillary-pressure equivalent to 35 percent mercury saturation into a pore-throat radius using this well-known equation:

$$r_c = (2\sigma^*\cos\theta/Pc) * 0.145 \quad (1)$$

Because these relationships are developed from siliciclastic rocks that have only intergrain porosity, they may not apply to vuggy carbonates. However, a similar relationship can be shown to exist in nonvuggy carbonate reservoir rocks. Pore-throat sizes at 35 percent mercury saturation were calculated for a collection of capillary pressure data that includes a variety of carbonate rock fabrics from various reservoirs, and the data were plotted on a porosity-permeability cross plot (fig. 7). Although data are insufficient to define a relationship between interparticle porosity, permeability, and pore-throat size, there is a clear trend of increasing permeability with increasing pore-throat size.

Lines of equal pore-throat size cut across rock-fabric petrophysical-class fields because pore-throat size (or pore-size distribution) changes with changes in interparticle porosity within a rock-fabric class (fig. 7). If it is assumed that a large volume of anhydrite is added in patches to a carbonate having a relatively uniform pore-throat size, the porosity will be reduced but the pore-throat size will remain constant. The result will be that as porosity is reduced, the sample will shift along the line of equal pore-throat size rather than along the rock-fabric transform (fig. 8). As the porosity is reduced, the sample will shift from a higher petrophysical class into a lower class. This model explains why the petrophysical class 2 samples containing large volumes of anhydrite have shifted from the class 2 field into the class 1 field.

As a result of the lateral shift into the class 1 field, a single porosity-permeability transform characterizes the middle and lower Clear Fork reservoirs in the study area. The transform given below has a correlation coefficient of 0.95 and is based on recent data from Westport Laboratory in Houston (fig. 5). Most of the data from samples having thin sections also group within the class 1 field, with the exception of a small number that plot to the left of the class 1 field (figs. 6a, 6b). The porosity-permeability transform for these data, excluding the outlying group, is similar to the one based on the more recent data. Therefore, the following single porosity-permeability transform is used to calculate permeability from porosity logs for the carbonates in this reservoir:

$$k(md) = (4.6442*10^{6}) * \varphi_f^{\,5.526} \; r = 0.95, \quad (2)$$

where k = permeability in millidarcys and φ_f = porosity in fractions.

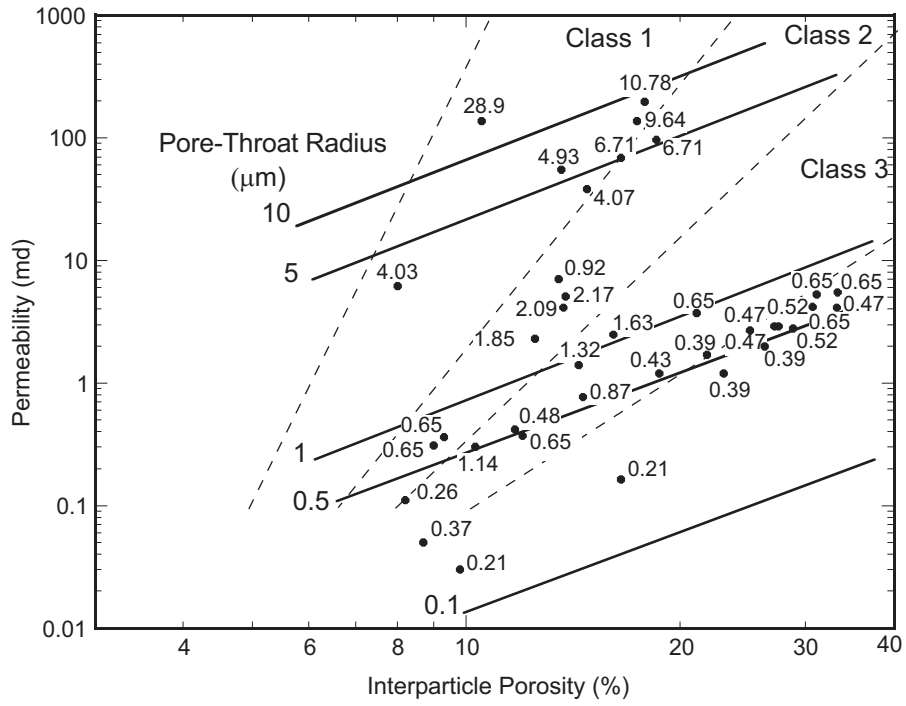

Figure 7. Zee plot of pore-throat radius (r_c) from capillary pressure measurements on a porosity-permeability cross plot. Note (1) that r_c increases systematically with increasing permeability and (2) that lines of equal r_c cut across the petrophysical class fields.

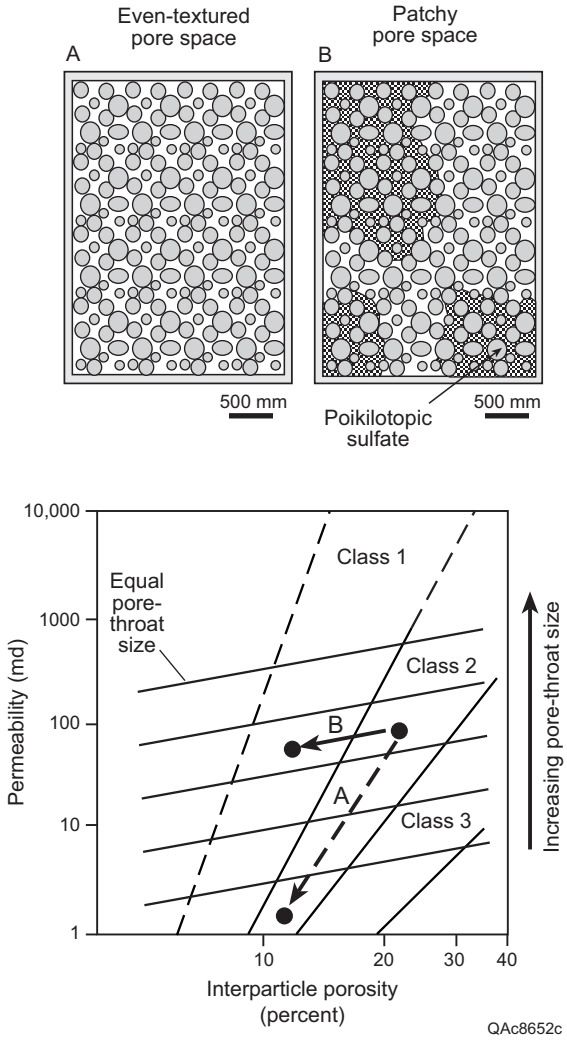

Figure 8. Cartoon showing (1) even-textured pore space and uneven-textured (patchy) pore space resulting from emplacement of patches of poikilotopic anhydrite and (2) porosity-permeability plot showing rock-fabric fields and lines of equal pore-throat size. Changes in porosity by cementation and compaction of the even-textured fabric result in changes in pore-throat size and permeability, according to the rock-fabric fields (A). Changes in porosity by patchy poikilotopic anhydrite result in no change in pore size and a change in permeability, according to the line of equal pore-throat size (B).

Calculated permeability is compared with core permeability in a depth plot illustrated in figure 9. Accurate porosity values are critical because of the transform's steep slope. A difference of one porosity unit changes permeability by a factor of about 1.4. The difference between calculated and core permeability in figure 9 is explained by the differences in core and calculated porosity. Overall, however, the single transform does a good job of characterizing the vertical permeability profile of the well.

The class 1 porosity-permeability transform for SWCF is unique for Permian reservoirs. A porosity cutoff of 4 percent is indicated by this transform, assuming a permeability of 0.1 md for the lower limit required for oil to move. San Andres and Grayburg reservoirs typically have cutoff porosities of 6 to 8 percent, similar rock fabrics, but much less sulfate in permeable intervals (Bebout and others, 1987; Lucia and others, 1995; Lucia, 2000). The steep slope of the transform results in a rapid increase in permeability with increasing porosity. The transform calculates a permeability of 2 md at 7 percent porosity and 14 md at 10 percent porosity. Therefore, although the average porosity of the SWCF reservoir is lower than that of typical San Andres and Grayburg reservoirs, the average permeability is similar because of the large amounts and patchy distribution of anhydrite in the permeable intervals.

Saturation Model

Data from 19 available capillary pressure curves were grouped into 5 porosity bins. All but three capillary pressure curves have class 1 characteristics when compared with the saturation models presented by Lucia (1995), which is consistent with the class 1 characteristics of the porosity-permeability relationship discussed above. The 0 to 3 percent porosity group is illustrated in figure 10a and is typical of low-permeability carbonates. The 3 to 6 percent group (fig. 10b) has characteristics of productive carbonates and supports the 4-percent porosity cutoff. The groups in the porosity range of 6 to 8 percent (fig. 10c) and 8 to 10 percent (fig. 10d) have increasing better saturation characteristics. Only one sample has porosity greater than 10 percent, and the curve is shown in figure 10e. Figure 10f illustrates curves for three samples in the 3 to 6 percent porosity range that have capillary pressure curves more typical of class 2 carbonates than class 1 when compared with generic saturation models (Lucia, 1995). Porosity and permeability

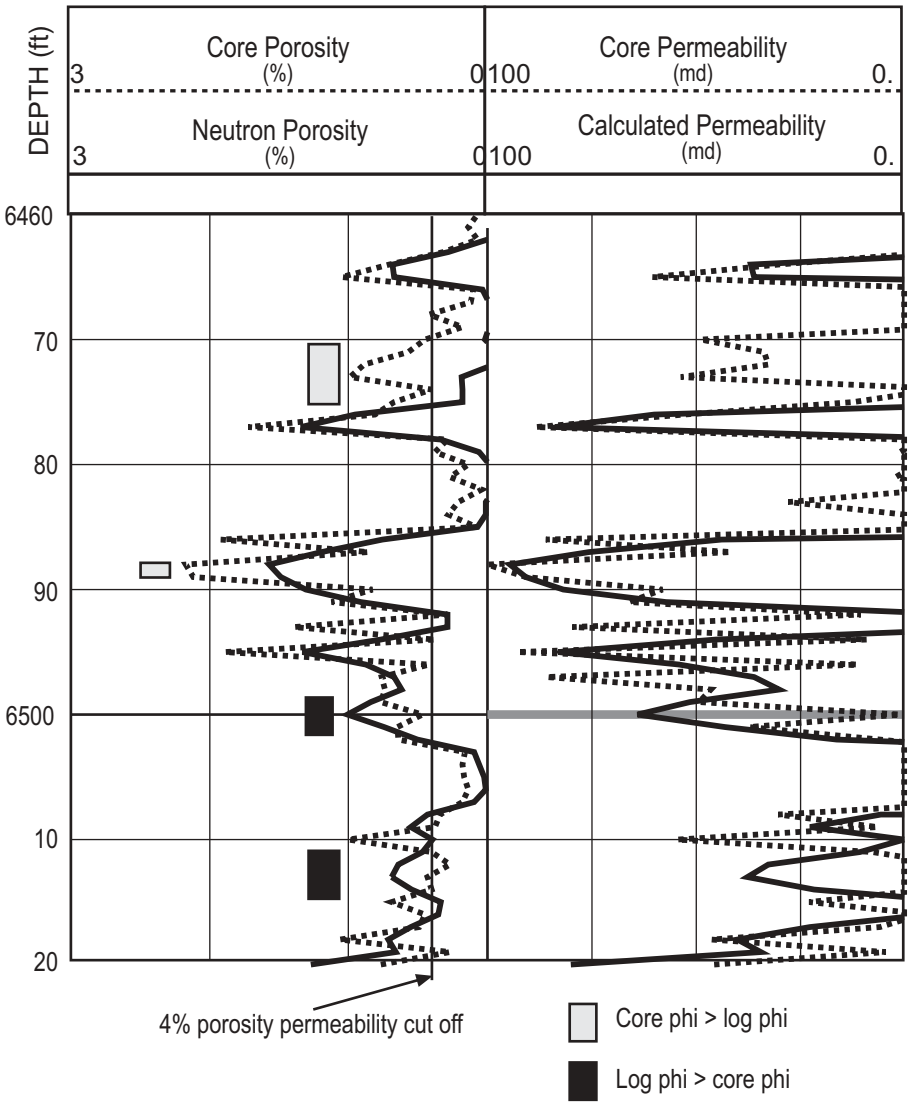

Figure 9. Comparison of core porosity and permeability with log calculations of porosity and permeability from well 7531. Note that where calculated permeability deviates from core permeability calculated and core porosity also deviate.

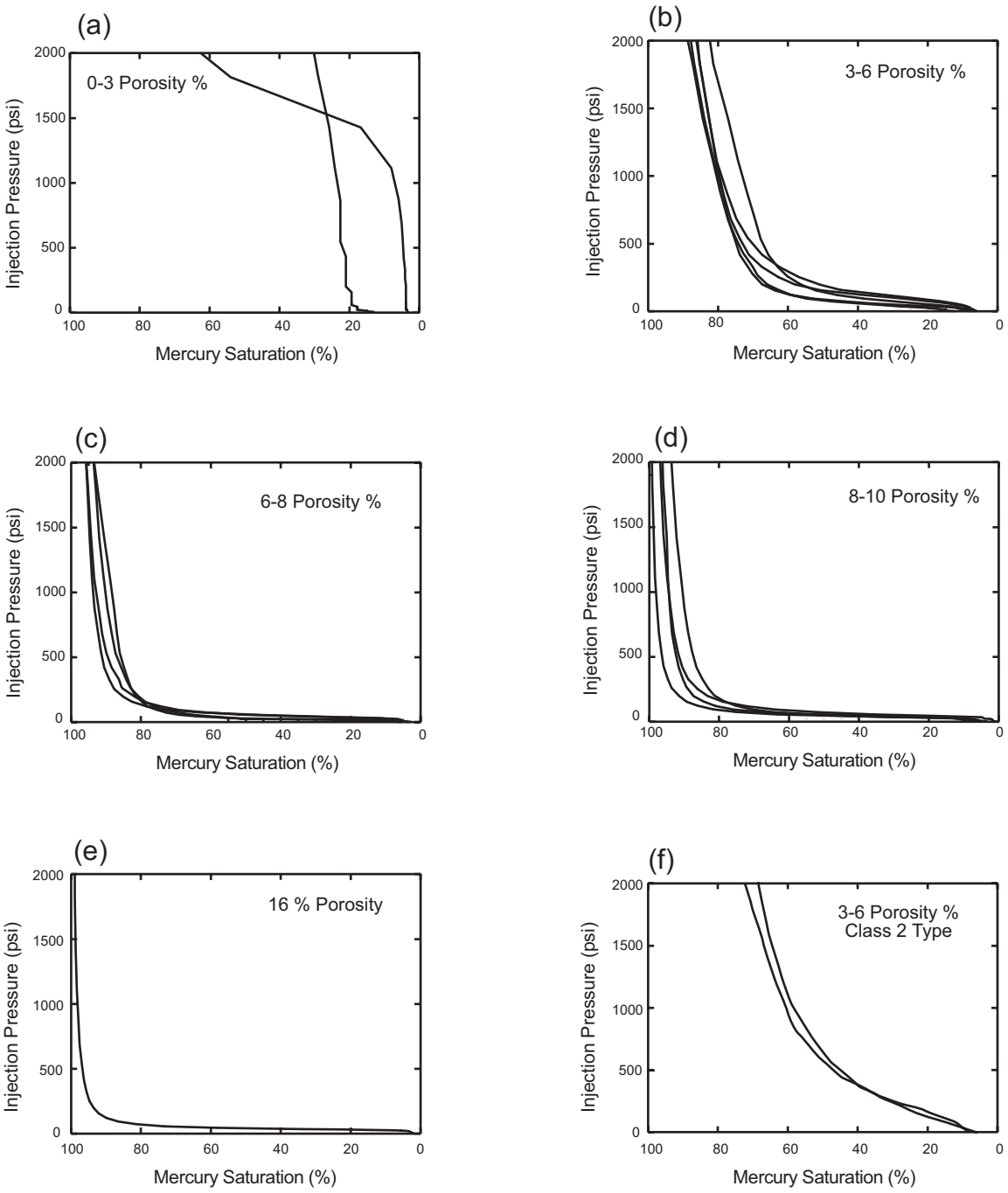

Figure 10. An illustration of capillary pressure curves grouped by porosity.

data from these samples plot in the class 2 porosity-permeability field and are described as class 3 fine crystalline dolowackestones.

An average porosity value and capillary pressure curve were calculated for each group. The results presented in figure 11a show a systematic change in the capillary pressure curves with change in porosity and little change in entry pressure.

A saturation model that relates water saturation to porosity and capillary pressure was developed using all the capillary pressure data and multivariate analysis methods. The resulting model is presented below in equation 3. A comparison of the average capillary pressure curves and model curves is presented in figure 11b and shows that the calculated curves do not match the average measured curves exactly but are a reasonably good representation.

$$Sw = [1 - A*\ln(B/Pc)]^{\wedge} (-\lambda/A) \quad (3)$$

where,

Pc = Capillary pressure, and

λLambda = $C*(D + \ln\phi)$.

Constants are given as

$A = 0.98$

$B = 22.7$

$C = 0.91$

$D = 4.2$

Model saturations are compared with Archie saturations from the middle Clear Fork reservoir in figure 12. Archie water saturation values were calculated from porosity and resistivity logs using $m = 2$, $n = 2$, and $R_w = 0.05$. Model saturations were calculated using porosity from wireline logs and capillary pressure determined by converting reservoir height into capillary pressure using equation 4. Reservoir height is defined as the distance from a zero-capillary-pressure level to any point in the reservoir. The zero-capillary-pressure level in the middle Clear Fork is assumed to be at a subsea depth of –3,400 ft (personal communication from Oxy Permian).

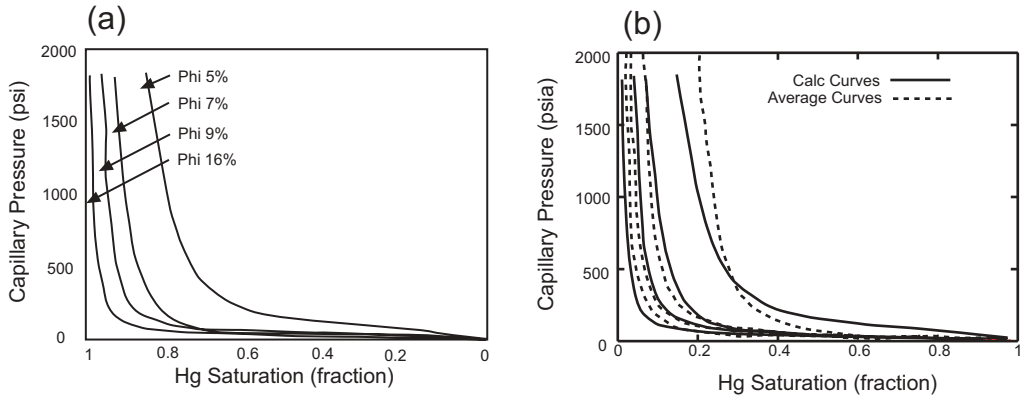

Figure 11. An illustration of (a) averaged capillary pressure curves and (b) a comparison of averaged capillary pressure curves and capillary pressure curves calculated from the saturation model.

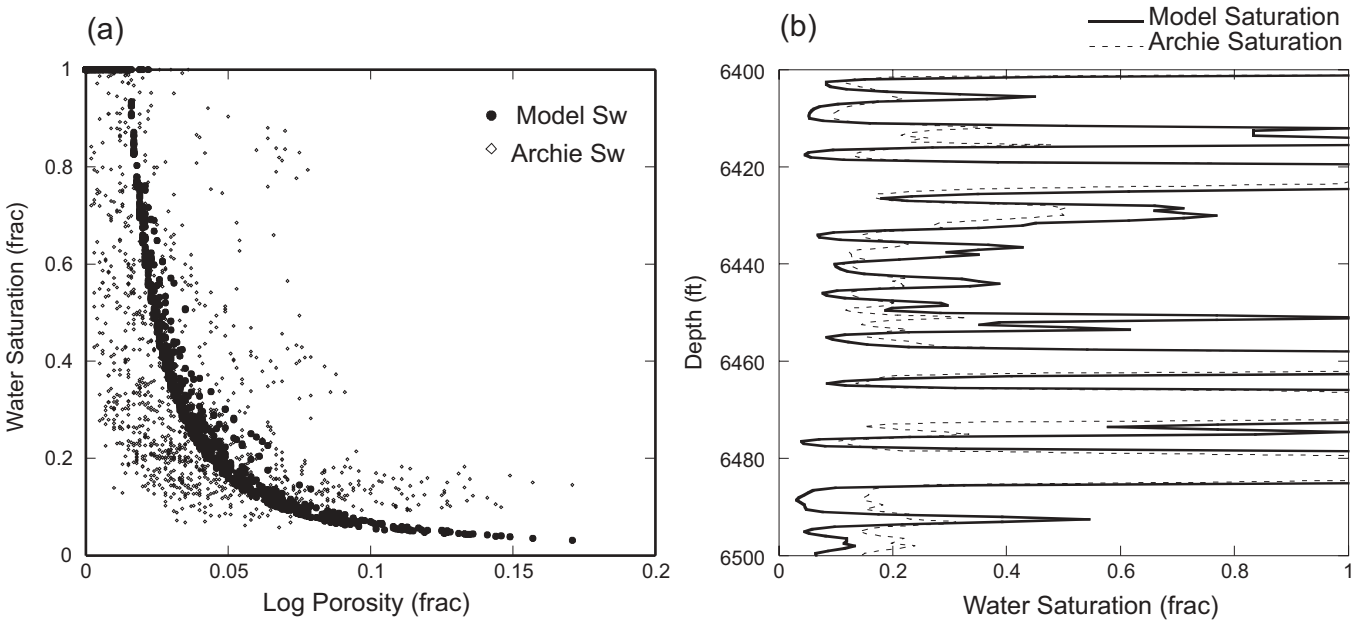

Figure 12. Comparison of Archie water saturations and model saturations from well 7531. (a) Cross plot of Archie and model saturation versus porosity showing that Archie saturations do not decrease with increasing porosity as do the model saturations and that Archie saturations are higher than model saturations in the low porosity range. (b) Depth plot of Archie and model saturation.

$$Pc = H_r \times \frac{(\sigma\cos\theta)_{a/hg}}{(\sigma\cos\theta)_{o/w}} \times 0.434(\rho. \quad - \rho o) \qquad (4)$$

where,

H_r = Reservoir height

σ = Surface tension

θ = Contact angle

a/hg = Air/mercury system

o/w = Oil/water system

ρ_w = Density of water

ρ_o = Density of oil

Compared with Archie saturations, model saturations are high in the low porosity range and lower in the high porosity range (fig. 12). The Archie equation typically underestimates water saturation in low-porosity carbonates, which accounts for the disparity in the low porosity range. As a rule, saturation should decrease with increasing porosity. An exception to this rule occurs when there is a change in rock fabric from a lower petrophysical class to a higher class. This exception does not apply here, however, because the fabrics all group into class 1. Instead of decreasing with increasing porosity, there is a tendency in the SWCF field for saturations to increase with increasing porosity. The most likely cause for this observation is invasion of mud filtrate into the more porous and permeable fabrics. Therefore, the model water saturation values are concluded to be more accurate than the Archie saturations.

DEFINING HIGH-FREQUENCY CYCLES (1-D ANALYSIS)

Vertical permeability and saturation profiles in the SWCF field can be calculated from porosity logs by using a single porosity-permeability transform and a single saturation, porosity, capillary-pressure model. Lateral correlation of vertical porosity, permeability, and saturation profiles, however, presents a major challenge in reservoir modeling. Our approach is to map rock-fabric flow layers within HFC's and distribute petrophysical properties within this stratigraphic framework. Outcrop studies in Apache Canyon (Ruppel and others, this report)

have shown that the Clear Fork can be characterized by HFC's composed of a vertical succession of mud-dominated fabrics grading upward to grain-dominated fabrics (usually grain-dominated packstones) and occasionally capped by tidal-flat facies (fig. 13).

In the SWCF field, core descriptions demonstrate that the HFC's typically do not have tidal-flat caps. Two groups of HFC's are present: (1) silt-based HFC's grading upward into mud-dominated fabrics and capped by grain-dominated fabrics and (2) carbonate-based HFC's grading upward from mud-dominated to grain-dominated fabrics. Silt-based HFC's are easily identified from logs because the basal silt beds are readily apparent from overlaying sonic and porosity logs and from water saturation profiles (fig. 14). Gamma-ray logs are useful to a limited extent because of the presence of diagenetic uranium in the dolomite. In figure 14, the tops of cycles B and D are defined by the gamma-ray log but not cycles C and A. Interestingly, the acoustic-porosity cross plot for dolostone does not match the Wyllie time-average curve but has a slope that is characteristic of vuggy porosity in other reservoirs (Lucia, 1999, 2000)(fig. 15). This deviation from the Wyllie time-average curve is most likely related to the patchy distribution of porosity.

Defining carbonate-based HFC's is more difficult for two principal reasons. First, the gamma-ray log is of little value because the Clear Fork contains large amounts of diagenetic uranium. The gamma-ray activity from the uranium masks the depositional signature from potassium and thorium, making it nearly impossible to use the gamma-ray log to identify HFC's. Second, cross plots of Archie water-saturation values and total porosity do not define rock fabrics in this reservoir because all the fabrics group in petrophysical class 1. Saturation-porosity cross plots have been used successfully in other reservoirs where a variety of rock-fabric petrophysical classes are present (Lucia and others, 1995), but the combining of all fabrics into one petrophysical class renders this approach of little value.

Examination of rock fabric and porosity data, however, suggests that grain-dominated packstones tend to have higher porosity than do mud-dominated fabrics. This observation was tested by using thin-section descriptions and core porosity data from both the upper and middle Clear Fork (fig. 16). In the middle Clear Fork, dolowackestones have an average porosity of 4.5 percent and make up 70 percent of the samples having <5 percent porosity. Mud-dominated dolopackstones have an average porosity of 7 percent, and grain-dominated dolopackstones an

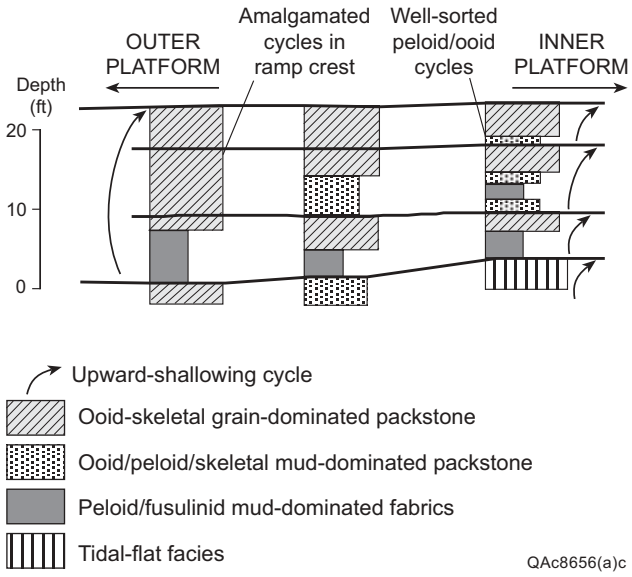

Figure 13. Example of high-frequency cycles from Leonardian sequence 3, Apache Canyon, Sierra Diablo Mountains, West Texas. The cycles are defined by a lower mud-dominated fabric and an upper grain-dominated fabric. Cycles may become amalgamated in the high-energy ramp-crest environment.

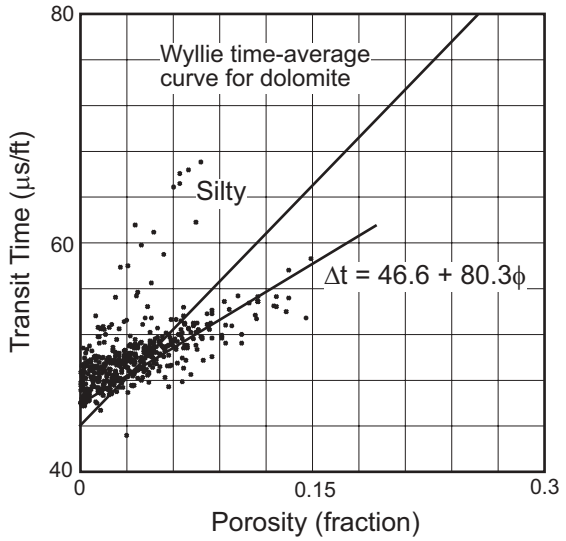

Figure 14. Depth plot of the gamma-ray log, water saturation, and an overlay of the sonic log on the porosity log showing that the sonic-porosity overlay and the water saturation clearly identify silt beds, whereas the gamma-ray log only identifies beds D and B.

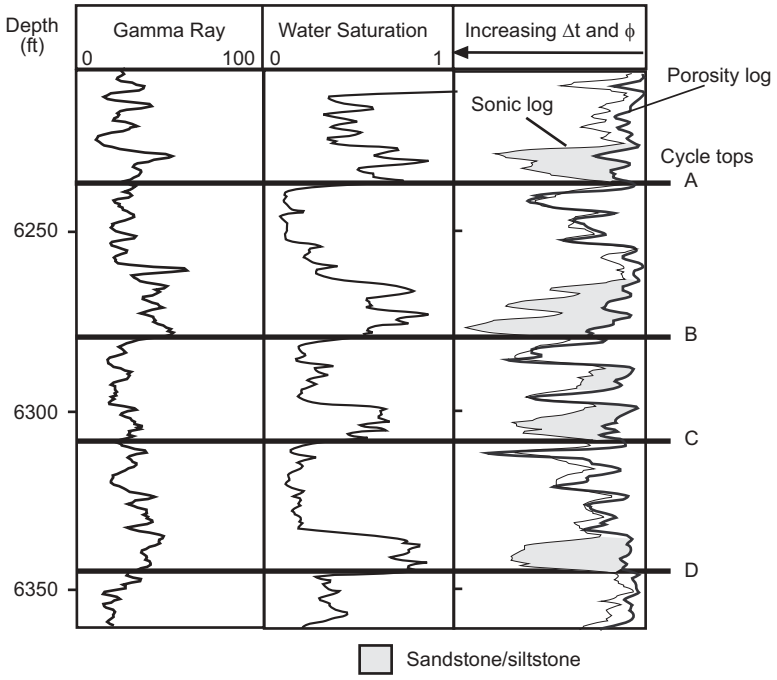

Figure 15. Cross plot of acoustic travel time and porosity showing a reduced major axis (RMA) correlation that does not match the Wyllie time-average line.

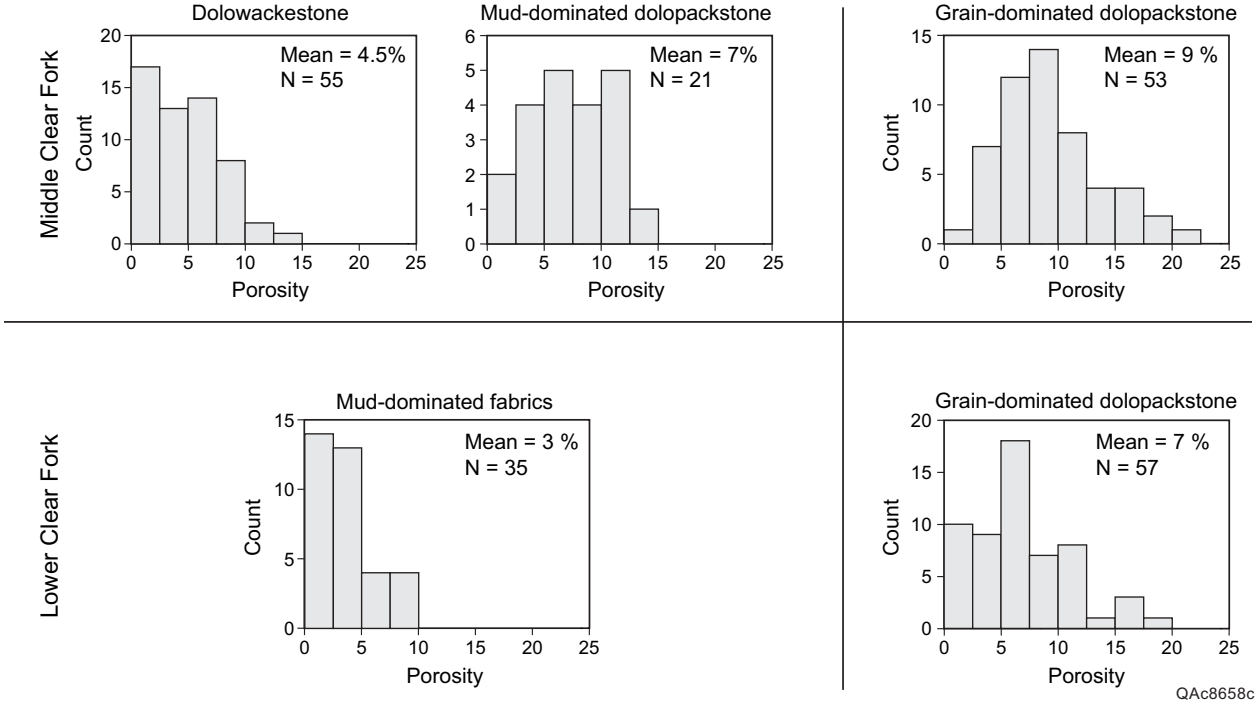

Figure 16. Statistical comparison of porosity and rock fabrics in the middle and upper Clear Fork reservoirs. Grain-dominated fabrics tend to have more porosity than mud-dominated fabrics.

average porosity of 9 percent. Together, dolopackstones make up 70 percent of the samples having >5 percent porosity, and grain-dominated dolopackstones make up 70 percent of the samples having >10 percent porosity. A similar result was found in the lower Clear Fork, where the average porosity of the mud-dominated dolostones is 3 percent, and the grain-dominated dolopackstone 7 percent. Here, only 60 percent of the samples having <5 percent porosity are mud-dominated fabrics, whereas 80 percent of the samples having >5 percent porosity are grain-dominated packstone.

Therefore, in the middle Clear Fork, an interval having >10 percent porosity is most likely to be grain-dominated packstone. An interval having <5 percent porosity is most likely to be composed of mud-dominated fabrics. In the lower Clear Fork, an interval having >5 percent porosity can reasonably be concluded to be grain-dominated packstone, but lower porosity intervals can be either mud- or grain-dominated fabrics.

This relationship appears to be carried over from the precursor limestone during dolomitization. In limestone fields, mud-dominated packstones, wackestones, and mudstones are typically lower in porosity that the grain-dominated packstones and grainstones. Two examples of this are presented in figure 17. In the Tubarao Cretaceous field, offshore Brazil (Cruz, 1997) the mud-dominated fabrics average about 2 percent porosity, whereas the grain-dominated packstones average 9 percent and the grainstones 17 percent. In the Jurassic limestones of the Ghawar field, Saudi Arabia, porosity gradually decreases from grainstone and grain-dominated packstones having about 16 percent porosity to mudstones having an average of 7 percent. Interestingly, porosity in the mud-dominated packstones is bimodal. The high peak is in the range of the grain-dominated fabrics, and the low peak is in the range of the mud-dominated fabrics. This pattern suggests that the distinction between mud- and grain-dominated packstone is not clearly defined in this data set.

Rock fabrics in the Seminole San Andres Unit have been described in detail (Lucia, 1995). Statistical analysis of porosity values shows a similar trend with dolomitized rock fabrics (fig. 17). Dolograinstones have an average porosity of 12 percent, similar to an average of 13 percent in grain-dominated dolopackstones. The average porosity in the mud-dominated fabrics decreases from 10 percent in the mud-dominated dolopackstones to 6 percent in the dolomudstones. The reduction in porosity with increasing mud content is similar to that observed

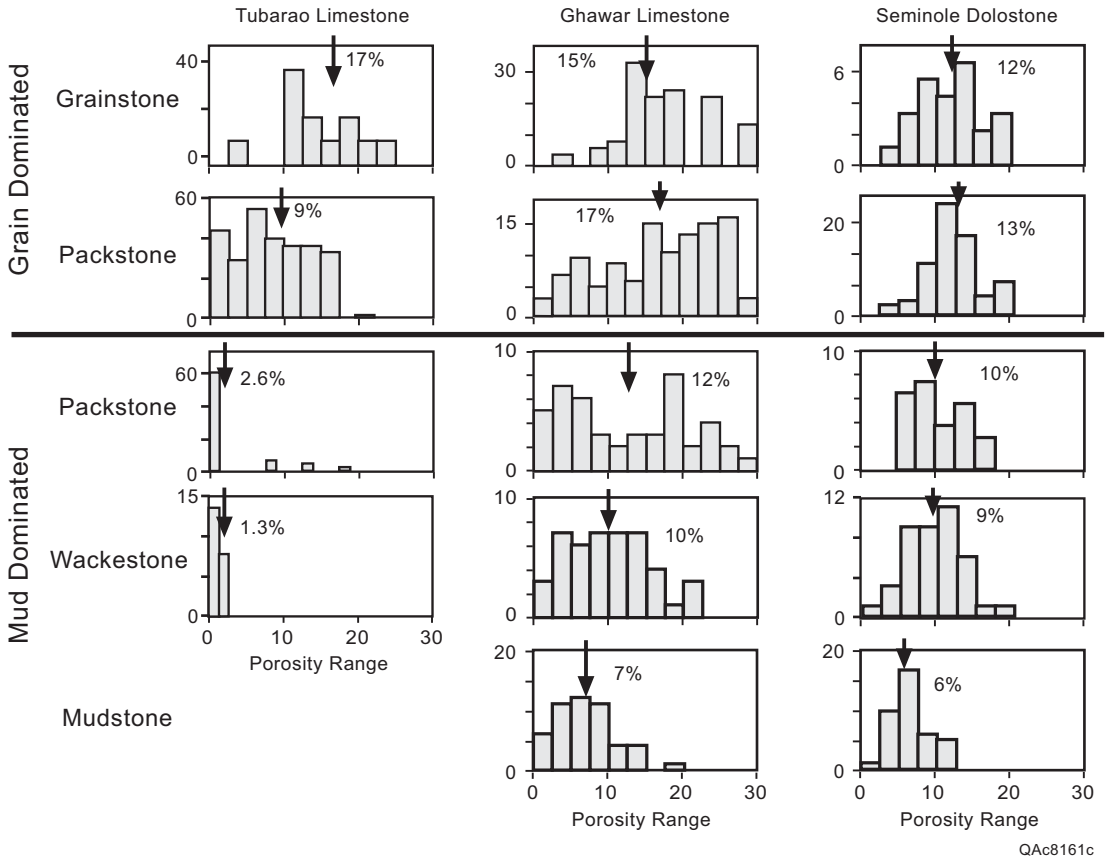

Figure 17. Statistical comparison of porosity and rock fabrics from two limestone reservoirs and on dolostone reservoir. Grain-dominated fabrics tend to have more porosity than mud-dominated fabrics in both limestone and dolostone reservoirs. The Tubarao reservoir is of Cretaceous age from offshore Brazil, the Ghawar reservoir is of Jurassic age from Saudi Arabia, and the Seminole dolostone is of Permian (Guadalupian) age from West Texas, USA.

in limestones and supports the contention that the porosity profile is inherited from the precursor limestone.

These observations suggest that vertical porosity profiles can be used to define the mud- and grain-dominated portions of subtidal carbonate-based HFC's in the middle and lower Clear Fork reservoirs. There is too much overlap in porosity values to use a linear relationship between rock fabric and porosity, or to use a single porosity value to separate mud- from grain-dominated fabrics. Instead vertical porosity trends together with a working knowledge of cycle thickness and scales of porosity variability from descriptions of Permian outcrops are used to define carbonate-based HFC's. In the Apache Canyon outcrop, Clear Fork HFC's vary in thickness from 5 to 20 ft (Ruppel and others, this report). Much of the variability in porosity and permeability values occurs at a scale of inches to feet and is near randomly distributed. It is important to recognize the spatially correlated, longer range vertical porosity patterns to identify HFC's (Jennings and others, 2000).

The method of using porosity profiles as a surrogate for rock fabric was tested using core and log data from the lower and middle Clear Fork of well 7531. It was not tested in well 7509 because the core is from a twinned well and the logs are from the original well. The middle Clear Fork core from well 8521 is too short to be useful. Detailed geologic descriptions were made of the core slabs with careful attention to fabric, grain type, and depositional structures (Ruppel and Ariza, this report). This information was the basis for the sequence stratigraphic framework and defined a number of cycles. However, rock fabrics are not clearly defined from core slab examination. Fabric descriptions commonly include terms such as packstone or grain-dominated packstone/grainstone. Thin sections were made of core plugs used in making core measurements for a more definitive rock-fabric description. Unfortunately, some thin sections were made from the core slabs because many core plugs were not available. Detailed rock-fabric descriptions were made from thin sections with special attention to dolomite crystal size, lithology, and separate and touching vugs. The distinction between dolograinstone, grain-dominated dolopackstone, and mud-dominated dolopackstone is more accurate using thin sections than core slabs. Grain type and depositional structures, however, are not prime descriptors in this method. As a result, the vertical succession of rock fabrics described from thin sections is commonly simpler than that described from core slabs. In some instances, cycles picked from core descriptions were simplified on the basis of rock-fabric descriptions. The resulting succession of rock fabrics and HFC's is compared with HFC's interpreted from the porosity log assuming that

vertical trends of increasing porosity represent a vertical stacking of mud-dominated to grain-dominated dolostones.

Figure 18 illustrates the result from a middle Clear Fork core. Cycles 6, 5, 4, and 2 clearly show upward-increasing porosity and correlate with cycle tops identified by core descriptions. Cycle 3 top is highly interpretive. Cycle 7 does not have a well-defined high-porosity top in this well but does in offsetting wells. A cycle top labeled 4a identified in core descriptions is not clearly defined by the porosity log because thin sections show that anhydrite and dolomite cement fill the pore space in the capping grain-dominated dolopackstone. Therefore, this approach clearly identified five out of seven tops using the porosity log. Cycle 3 and 7 tops are carried in from offsetting wells, and their exact location is not critical to the flow model because the cycles in this well are dense. Therefore, seven tops are properly located in this example, including tops carried through dense intervals based on offsetting wells. Cycle 4a, however, was missed entirely and is combined with cycle 3.

The difference between the computed gamma-ray (CGR) and the spectral gamma-ray (SGR) logs relates to the amount of diagenetic uranium in the dolomite (fig. 18). The CGR has little character and is not useful for picking cycle tops. The SGR, which includes the uranium response, identifies the top of cycles 5 and 4 but fails to respond to cycles 7, 6, 3, and 2. For this reason the gamma-ray log was not used to pick cycles.

Figure 19 illustrates the results from the lower Clear Fork core. The approach was the same as outlined for the middle Clear Fork core described in the previous paragraph. The cycles are about half the thickness of the middle Clear Fork cycles. From core descriptions, 17 HFC's are identified, and 17 are defined from the porosity log. Allowing for minor depth adjustment between core and log depth, 13 cycles match and 4 cycles do not (fig. 19). Cycle LC5 combines one thin core cycle with a thicker one. Cycle LC7 has no porosity expression in this well but is identified from offsetting wells and carried through this well for completeness. Below cycle LC11, the tie between porosity and HFC becomes weaker and at least two porosity cycles do not tie with core cycles. It appears that the porosity approach is viable in the upper 150 ft of the lower Clear Fork but deteriorates below 150 ft.

The gamma-ray, CGR, and SGR logs were useful for picking the upper four cycles (fig. 19). The base of these cycles has a higher gamma-ray response than the cycle tops, which is the

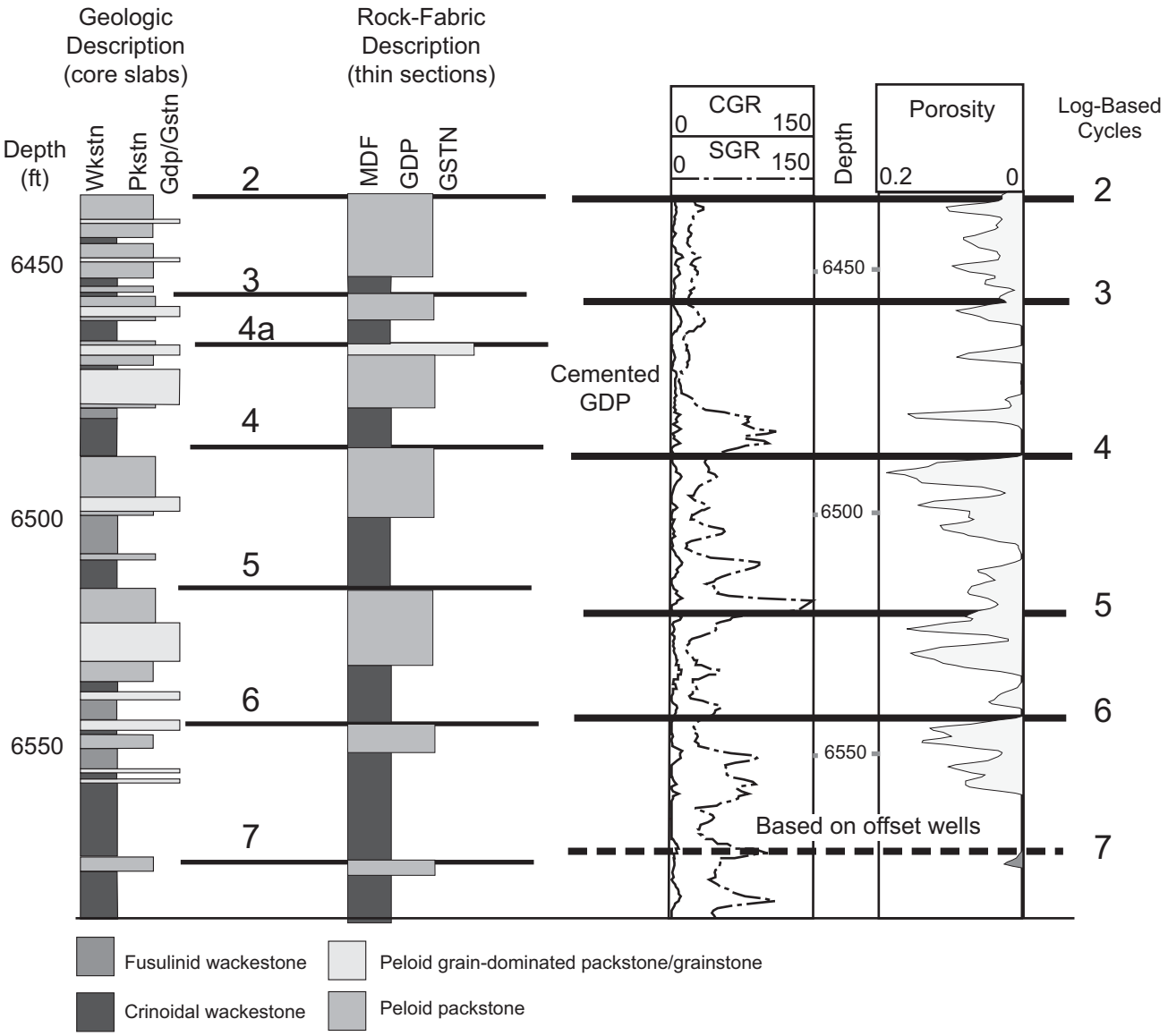

Figure 18. Comparison of middle Clear Fork cycles based on core and rock-fabric description with cycles based on the porosity log in well 7531. Note that the gamma-ray log only defines cycles 4 and 5.

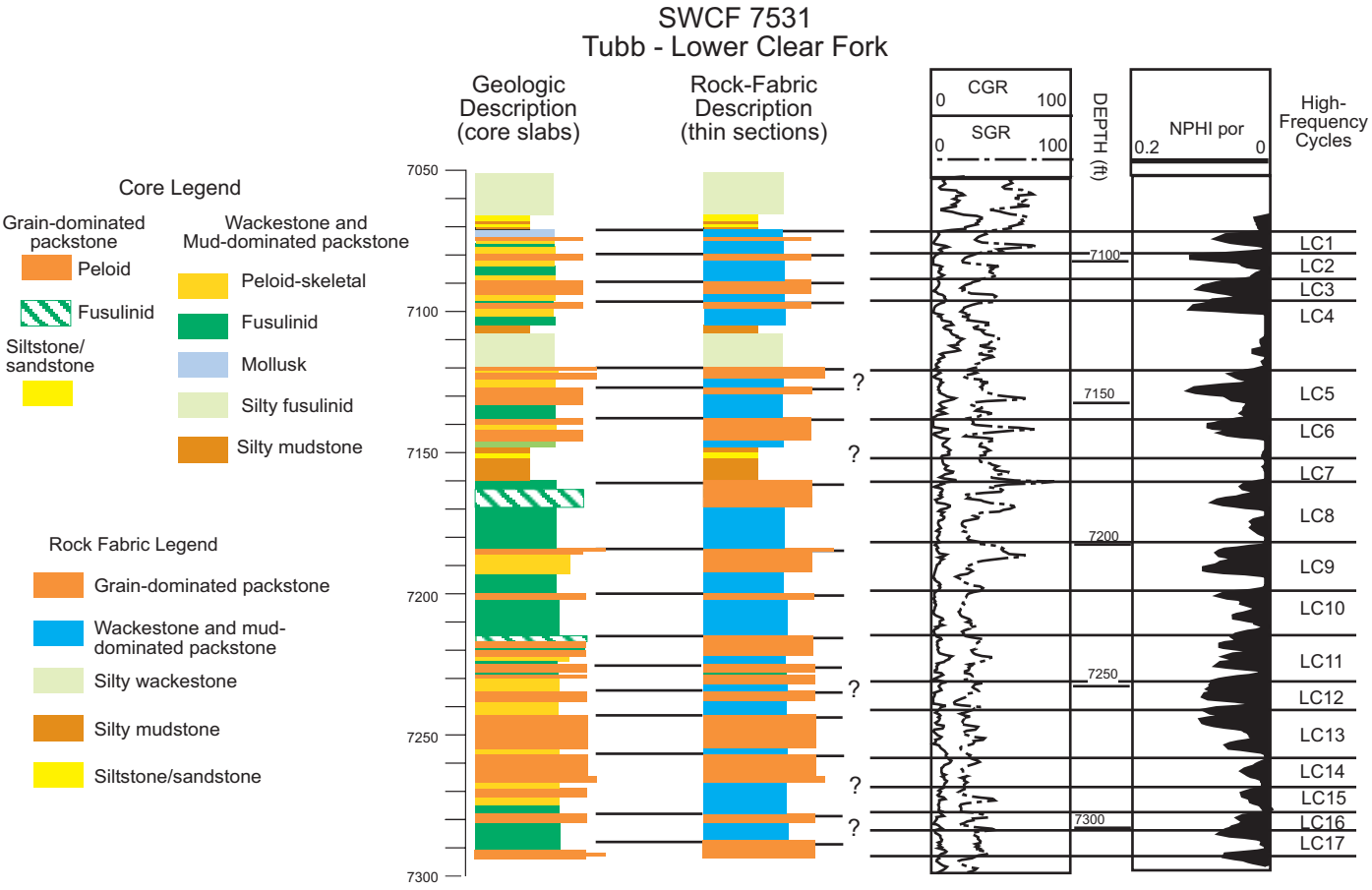

Figure 19. Comparison of lower Clear Fork cycles based on core and rock-fabric description with cycles based on the porosity log in well 7531. Note that the gamma-ray log does not define cycles.

predicted response from depositional energy considerations. The CGR response over the silty dolomite in cycle LC4 is predictably high. Below cycles LC4, however, there is little correspondence between the CGR or the SGR and cycle tops, and the gamma-ray log was of little use.

MODEL CONSTRUCTION (3-D ANALYSIS)

High-frequency cycles were picked in the 48 wells having calibrated porosity logs using porosity as a surrogate for rock fabric (fig. 20). Seismic data showed no evidence of offlap or onlap in the study area, and the cycles were correlated assuming a middle-ramp to ramp-crest paleotopography. In many instances the cycles are not porous, and cycles tops are correlated through these wells on the basis of offsetting wells. The exact location of the cycle top in a dense well is not important to the construction of the flow model. The final number of cycles was determined after all the wells were correlated and those cycle tops that were most continuous were selected.

A segment of the resulting cycle stratigraphy in the middle Clear Fork is shown in figure 21a. Considerable judgment is always exercised in picking the tops of the HFC's. Well 7531 is a cored well, and the HFC tops and core description are shown in figure 18. In well 7538 the vertical increase in porosity within each HFC is apparent except for HFC 2, where the basal mud-dominated fabric is very thin or nonexistent. In well 7531, no grain-dominated cap is indicated to HFC 7 by porosity, most likely because it is cemented. HFC 7 is extended through this interval from neighboring wells. A vertical increase in porosity is apparent in all the cycles in well 8542. The mud-dominated base of HFC 6 thickens greatly in well 8542, and the correctness of this correlation must be judged by examination of nearby wells.

An example of correlation in the lower Clear Fork is shown in figure 22a. Again, well 7531 is a cored well, and the core calibration is illustrated in figure 19. Cycles 1 through 3 correlate well and show porosity increasing upward. Cycle 4 has a thin porous top and also correlates well. The base is porous in some wells. Cycles 5 and 6 correlate well between wells 7538 and 7531. However, in well 8542 the base of cycle 5 is poorly defined and cycle 6 is dense. Porosity increases upward in well 8542, cycle 7, but cycle 7 is dense in the other two wells. Cycle 8 is dense in well 7538, and the porosity increases upward in the other two wells.

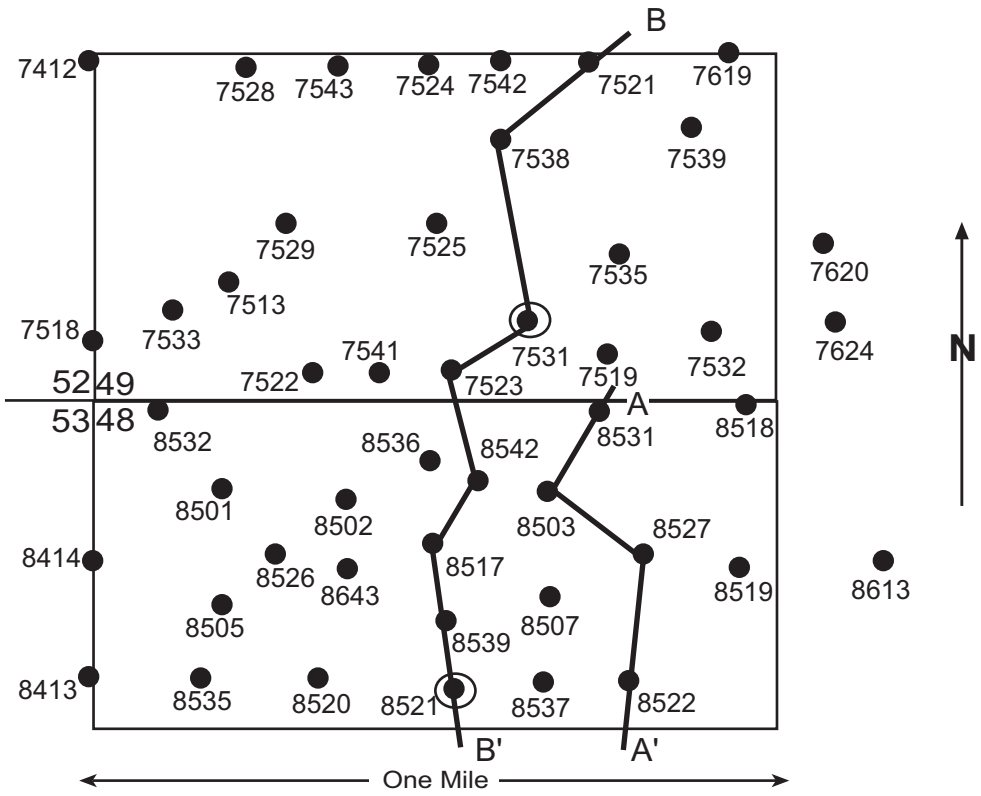

Figure 20. Map of study area showing wells used in construction of the reservoir model and the location of cross sections A–A´ and B–B´.

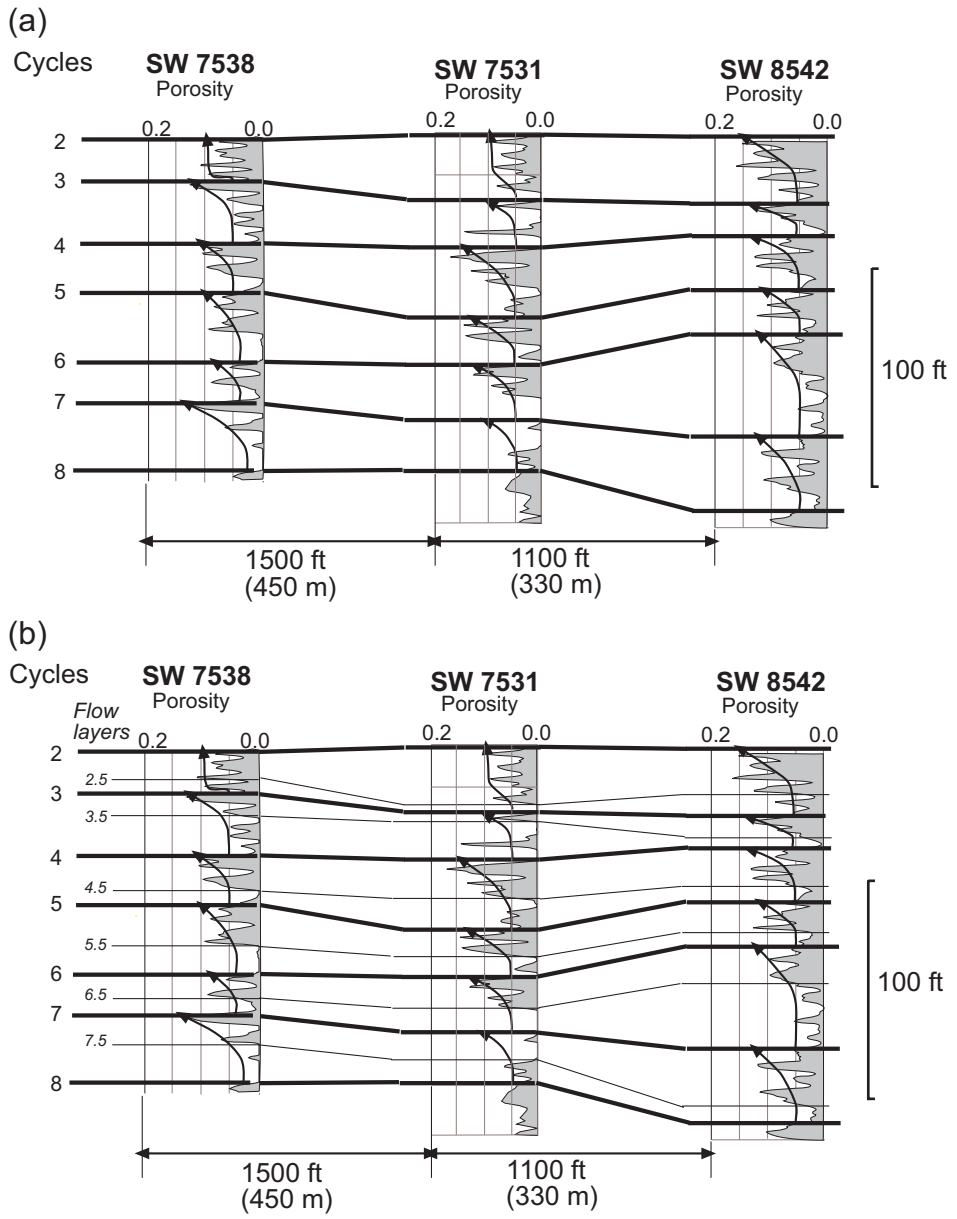

Figure 21. Cross section from the middle Clear Fork showing (a) correlation of HFC's based on porosity logs and (b) rock-fabric flow layers also based on porosity logs.

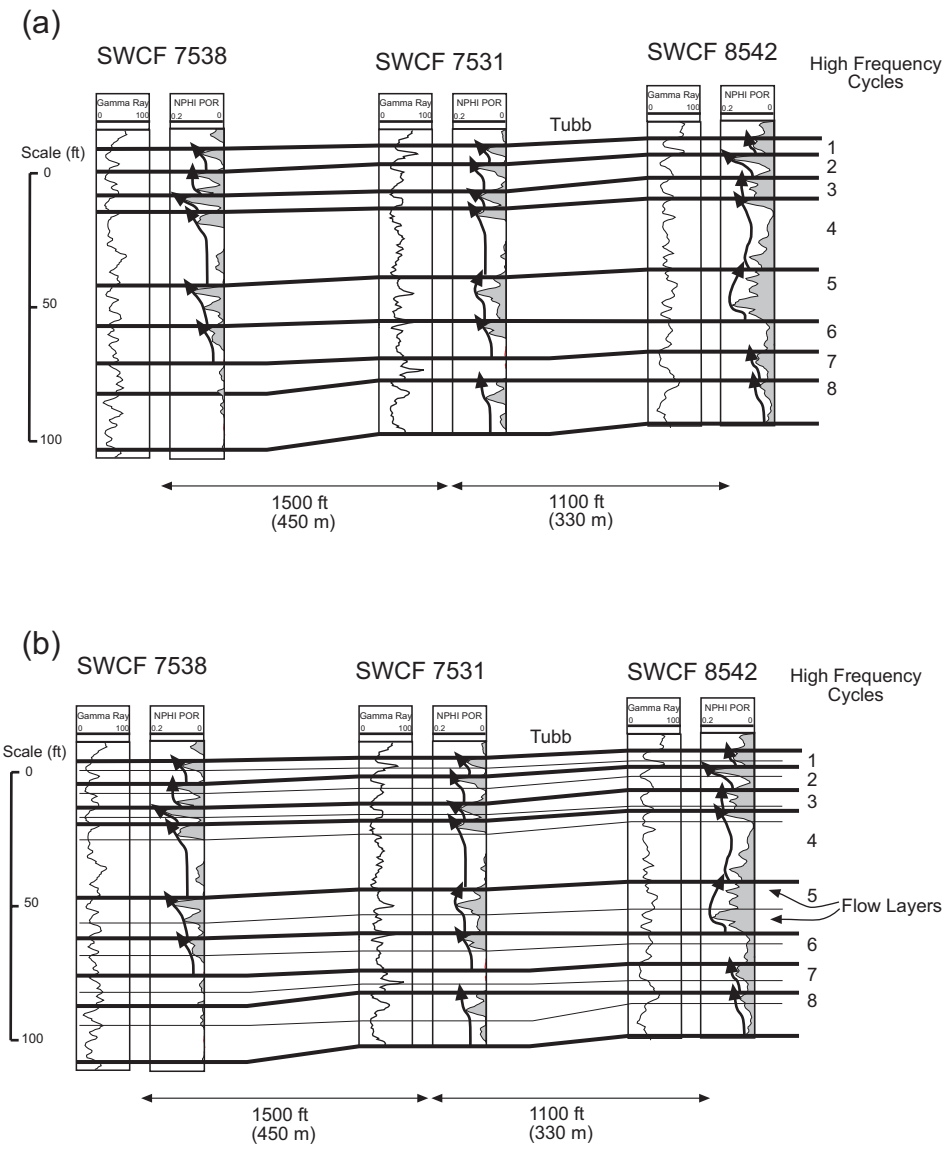

Figure 22. Cross section from the lower Clear Fork showing (a) correlation of HFC's based on porosity logs and (b) rock-fabric flow layers also based on porosity logs.

A key requirement in construction of a reservoir model is that high and low permeabilities be maintained. High permeability controls the time of water breakthrough, and low permeability controls cross flow. To accomplish this control, each HFC is divided into two rock-fabric flow layers, mud-dominated dolostone and grain-dominated dolostone (figs. 21b and 22b). There are three rock fabrics within each silt-based cycle, a silty dolostone, a mud-dominated dolostone, and a grain-dominated dolopackstone. The silty and mud-dominated dolostones are combined in the model because they both tend to be dense. The middle Clear Fork reservoir is divided into 42 flow layers, and the lower Clear Fork reservoir also into 42 flow layers. This strategy is used in order to maintain the high-porosity character of the grain-dominated fabrics and the low-porosity character of the mud-dominated fabrics when the reservoir model is converted into a flow-simulation model.

Permeability values in carbonate rocks are highly variable, and a judgment must be made concerning their spatial correlation when grouping the values. Porosity and, by association, permeability vary widely within each flow layer. Engineers and geologists tend to define each fluctuation as a bed having lateral continuity. However, data gathered from the Permian outcrop analogs in the Guadalupe and Sierra Diablo Mountains, New Mexico and Texas, have shown that permeability varies by several orders of magnitude on the scale of feet and has a near-random distribution at this scale (Jennings and others, 2000). This observation suggests that the vertical variability observed in Clear Fork well logs does not represent beds. The “beds” in this reservoir are the rock-fabric layers that correlate from well to well. Within these rock-fabric flow layers permeability can vary one or two orders of magnitude at the scale of feet and have little spatial correlation. Therefore, HFC’s are the basic geologic units, and rock-fabric layers are the basic petrophysical elements for constructing a reservoir model. To complete the model, petrophysical properties must be interpolated or distributed geostatistically within the flow layers between wells.

A series of cross sections showing HFC’s and rock-fabric flow layers were prepared for the middle and lower reservoirs. Porosity, permeability, and water saturation values calculated from wireline logs together with HFC and flow-layer tops were entered into a database for use in fluid-flow simulation. This database is available from the Bureau of Economic Geology.

Two examples of these cross sections are illustrated in figures 23 and 24 and located in figure 20. A north-south cross section of the lower Clear Fork reservoir is presented in figure 23.

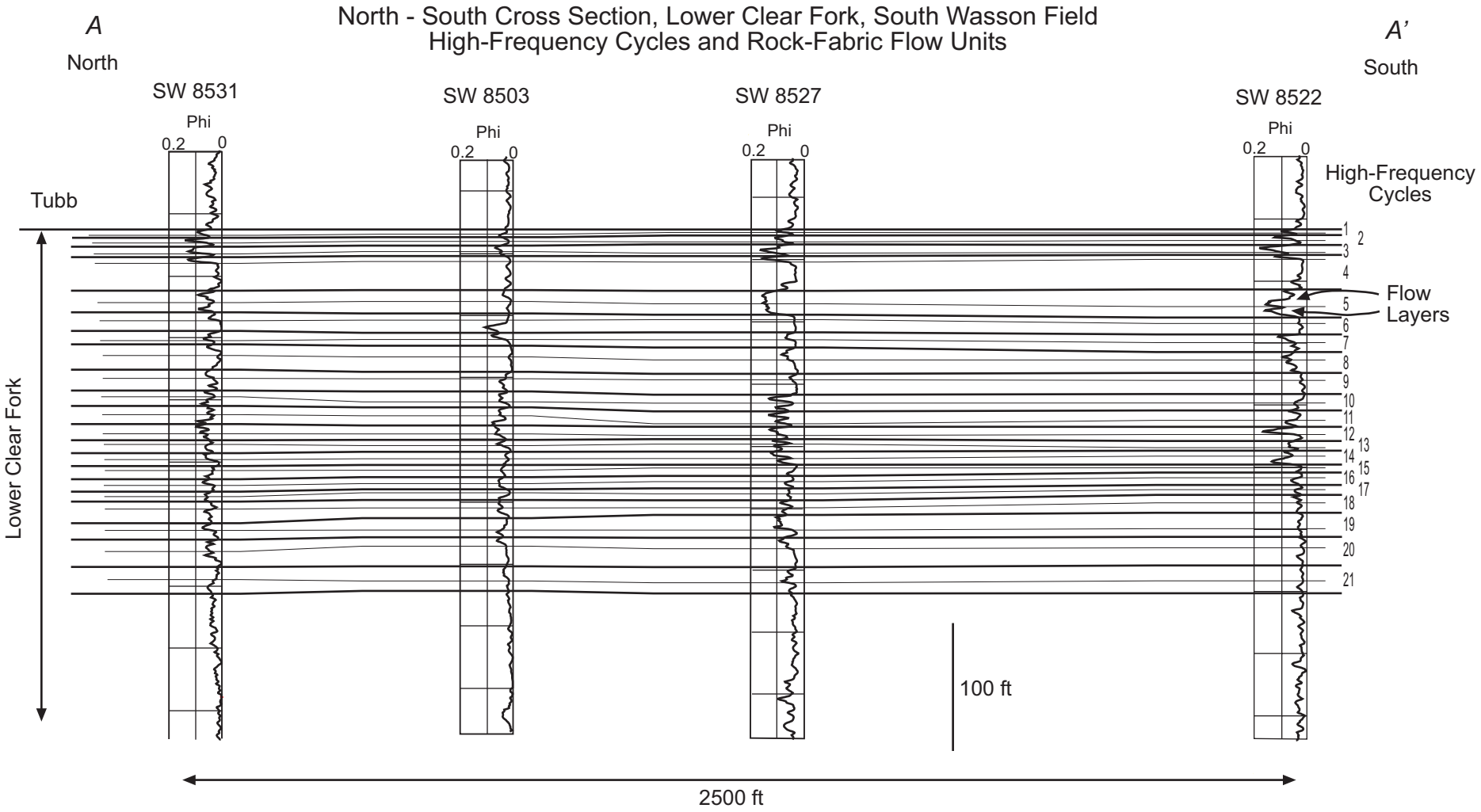

Figure 23. Cross section illustrating an example of the layer model for the lower Clear Fork reservoir showing 21 HFC's and 21 rock-fabric flow layers. (See fig. 20 for location of cross section.)

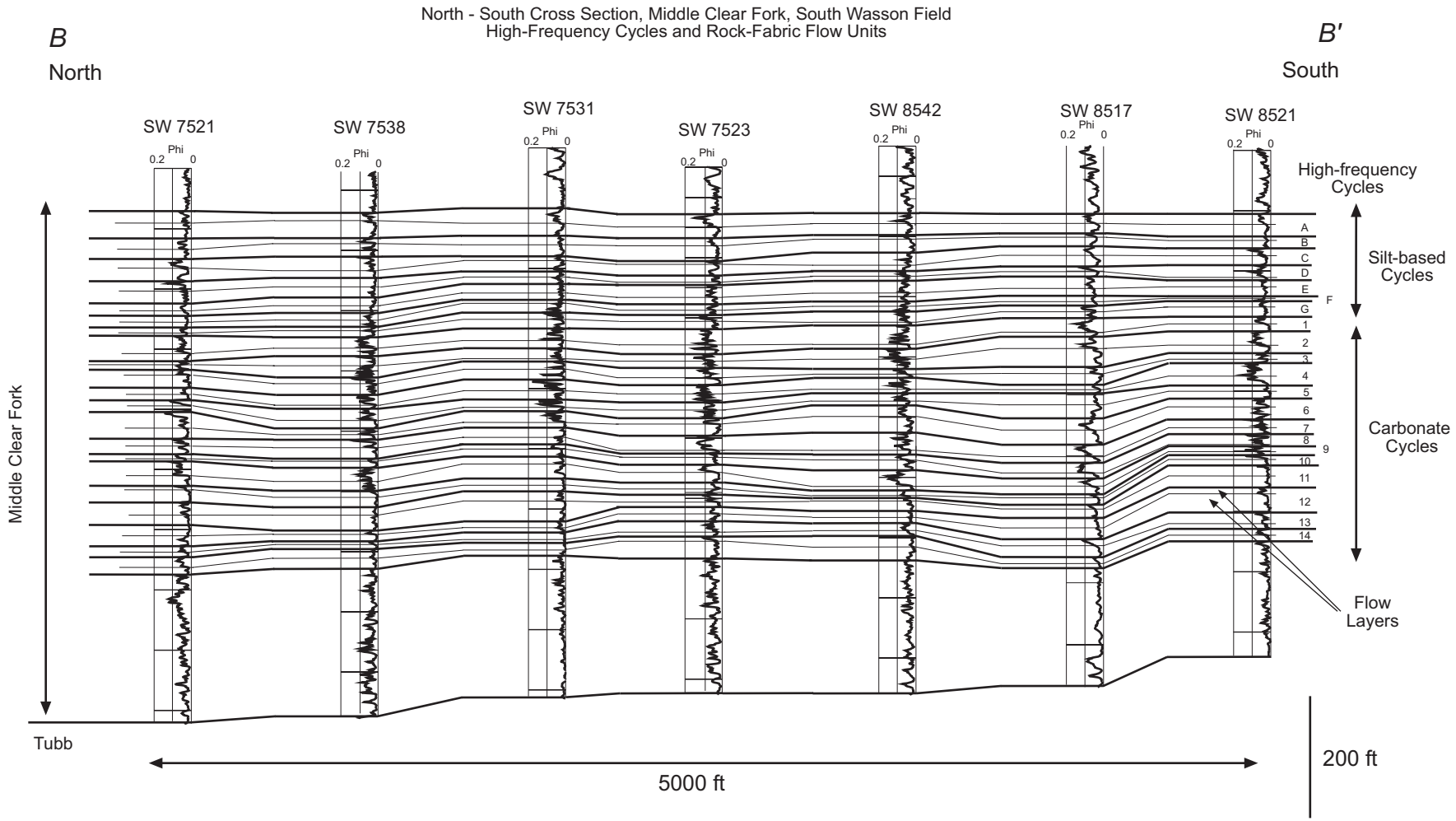

Figure 24. Cross section illustrating an example of the layer model for the middle Clear Fork reservoir showing seven silt-based cycles labeled A–G, 14 carbonate cycles, and 21 rock-fabric flow layers. (See fig. 20 for location of cross section.)

The lower Clear Fork reservoir interval contains 21 subtidal carbonate cycles and 42 flow layers. The cycles have an average thickness of 14 ft and a range from 7 to 26 ft. Ruppel and Ariza (this report) report cycles that average 6 ft in thickness and range from 2 to 15 ft. This difference is probably due to lumping thin beds with thicker beds. The flow layers average 7 ft in thickness and range from 3 to 21 ft. The upper cycles are well defined by porosity logs. The lower cycles, however, are poorly defined because porosity decreases with depth and many wells have cycles with little or no porosity.

A north-south cross section of the middle Clear Fork reservoir is presented in figure 24. The middle Clear Fork thins from north to south over the crest of the structure and contains 21 cycles and 42 flow layers, coincidentally the same number as defined in the lower Clear Fork. Cycles were not defined in the lower measures of the middle Clear Fork because the low porosity suggests little contribution to production (fig. 2). The cycles vary in thickness with no systematic pattern and have an average thickness of 28 ft, ranging from 16 to 40 ft. Again, these cycles are much thicker than those reported by Ruppel and Ariza (this report), probably because of lumping thin and thick beds. The flow layers average 14 ft in thickness and range from 8 to 24 ft. By coincidence, the middle Clear Fork cycles and flow layers are exactly twice the thickness of those in the lower Clear Fork

Seven silt-based cycles are found in the upper 150 ft labeled A through G, which vary in thickness from 16 to 40 ft. Some silt is also found locally at the base of carbonate cycles 1 and 2 (fig. 25). Characteristically the highest porosity is located at the top of these cycles, which is consistent with the cycles being capped with grain-dominated fabrics. The silt beds are generally dense and are flow barriers in this reservoir. Detailed maps show that most of the beds are not continuous over the study area and that they become more continuous vertically (fig. 25)

The flow-layer tops and permeability values were imported into Stratamodel, and a cross section of the permeability model is presented in figure 26. In this model, permeability is interpolated between wells at every foot parallel to the flow layers. The layered structure of the reservoir is captured in the permeability model as well as the lateral changes in permeability at the well-spacing scale. Smaller scale variability is incorporated into the model using geostatistical methods for waterflood simulations reported by Jennings in this report. The rock-fabric layers and the vertical profiles of porosity, permeability, and water saturation are the basic hard data used for constructing the simulation model.

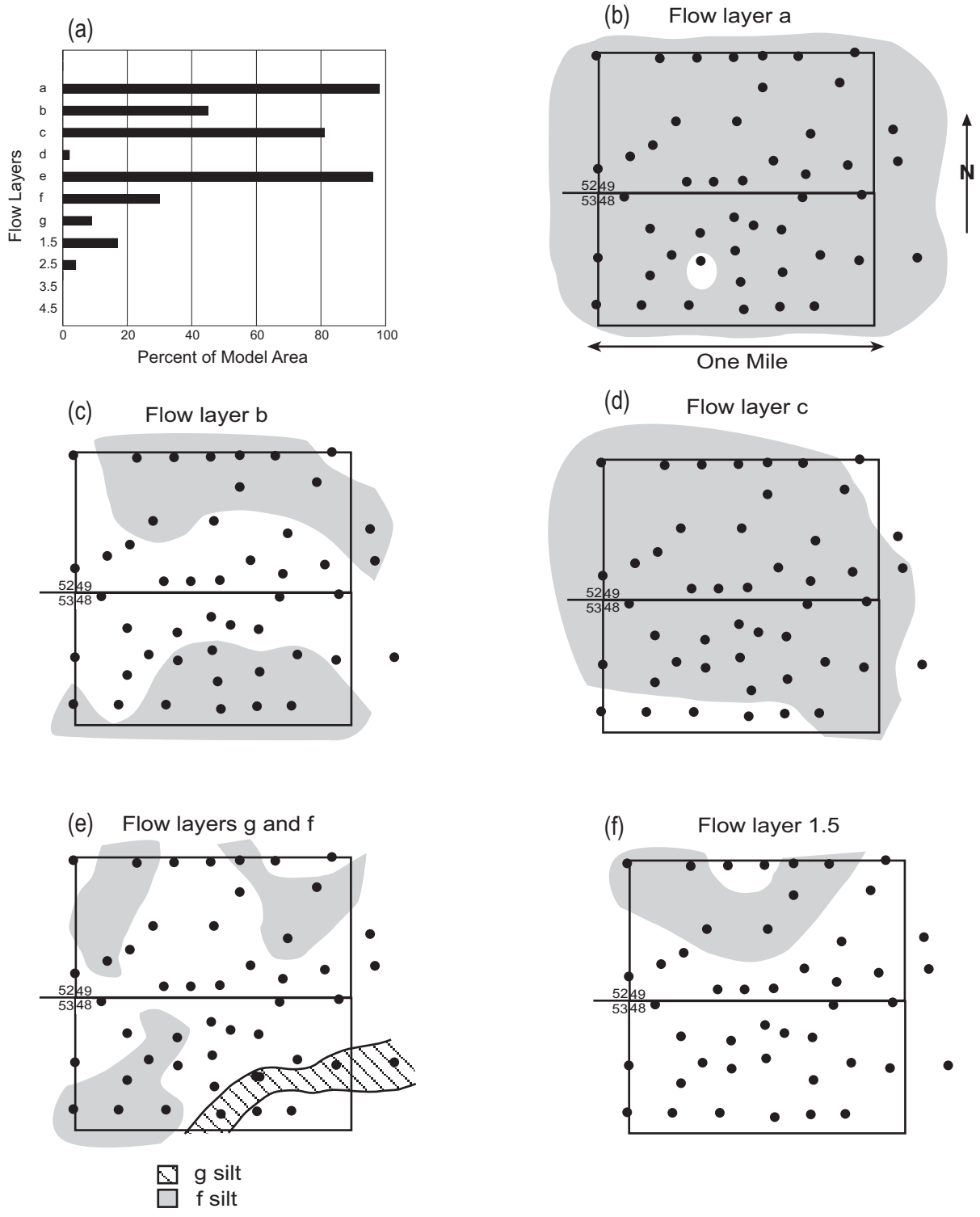

Figure 25. Illustration showing the distribution of silt beds in the study area. (a) Graph showing the areal coverage of silts. Note that some silt is found in cycles 1 and 2 as well as in the silt-based cycles. (b–f) Maps of various HFC's showing well control and the distribution of silt (gray).

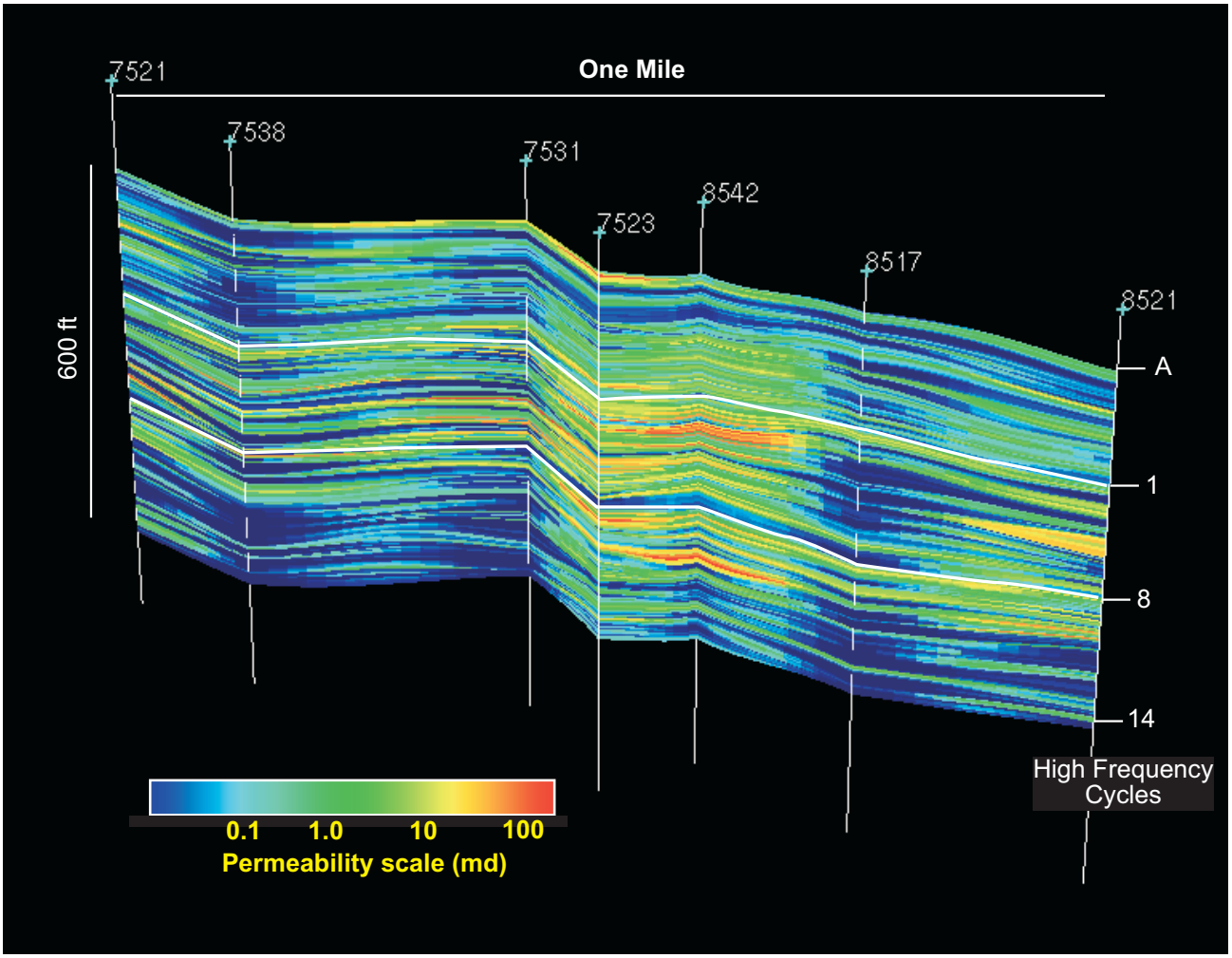

Figure 26. North-to-south Stratamodel cross section of the middle Clear Fork reservoir showing permeability distribution.

CONCLUSIONS

The South Wasson Clear Fork reservoir is composed of anhydritic dolostone and siltstone. The dominant rock fabrics are grain-dominated dolopackstones, mud-dominated dolopackstones, and dolowackestones. Many of the grain-dominated dolopackstones have grains more than 500 μm in diameter, and these dolopackstones are classified as class 1 along with a few samples of dolograinstone. Fabrics having dolomite crystal size greater than 100 μm are also classified as class 1. The remaining fabrics are classified as class 2 because the dolomite crystal size is between 20 and 100 μm. Only a few class 3 fine crystalline mud-dominated dolostones have been described. There is very little vuggy porosity because most of the grain molds and fractures are filled with anhydrite.

Perhaps the most surprising result of this study is that a single porosity-permeability transform and a single saturation, porosity, and reservoir-height equation can be used to characterize this reservoir despite the robust variety of rock fabrics. Cross plots of porosity and permeability demonstrate that all the fabrics tend to plot in the petrophysical class 1 field, whether classified as class 1 or 2. Class 2 fabrics plot in the class 1 field because of the unusually large volumes of poikilotopic and pore-filling anhydrite. The anhydrite patches have no porosity and occupy an average of 20 percent of the rock, creating a nonuniform patchwork of porous and dense rock. Conceptually, adding the patches of anhydrite reduces the porosity, but the pore sizes remain constant. Therefore, as the porosity is reduced, the permeability is reduced less than would be expected if the porosity had been reduced evenly throughout the sample. This results in samples moving laterally from a higher petrophysical class to a lower class instead of moving within a petrophysical class. The resulting porosity-permeability transform is

$$k(md) = (4.6442*10^{6}) * \varphi_f^{5.526} \quad r = 0.95$$

Water saturation can also be modeled with a single equation. Like the permeability relationships, the capillary-pressure curves are similar to the class 1 curves described by Lucia (1995). A model that relates water saturation to porosity and reservoir height was developed by multivariant analysis of the mercury capillary-pressure curves. The resulting model is

$$Sw = [1 - A*\ln(B/Pc)]^{\wedge} (-\lambda/A)$$

where,

Pc = Capillary pressure, and

λLambda = $C*(D + \ln\phi)$.

Constants are given as

A = 0.98

B = 22.7

C = 0.91

D = 4.2

On the basis of core descriptions, there are two types of HFC's in this reservoir, silt-based cycles that are capped by grain-dominated dolopackstone and carbonate cycles that typically have bases composed of mud-dominated fabrics and caps of grain-dominated dolopackstone. The gamma-ray log could not be calibrated with the HFC's because of the large amount of diagenetic uranium in the Clear Fork. Cross plots of porosity and water saturation are of little use because the fabrics group into one petrophysical class. The acoustic and porosity logs were used to identify silt beds and silt-based cycles. A statistical study of porosity and rock fabrics shows that on average the mud-dominated fabrics have lower porosity than do grain-dominated fabrics. Therefore, vertical increases in porosity were interpreted to mean a change from mud- to grain-dominated fabrics. This approach was used to pick and map HFC's.

In order to maintain high and low permeability in the flow model, each HFC was divided into a lower, low-permeability mud-dominated layer and an upper, high-permeability grain-dominated packstone layer. The layers are referred to as rock-fabric flow layers and are the basic elements in the construction of a flow model. The flow model has 42 flow layers in the middle Clear Fork and 42 flow layers in the lower Clear Fork. These layers together with porosity, permeability, and water saturation are the hard data for input into a flow simulator.

ACKNOWLEDGMENTS

This research was funded by the U.S. Department of Energy under contract no. DE-AC26-98BC15105 and by the sponsors of the Reservoir Characterization Research Laboratory: Altura, Amerada Hess, Anadarko, Aramco, ARCO, BP International, Chevron, Elf Aquitaine, ExxonMobil, Great Western Drilling, Japan National Oil Corporation, Kinder Morgan, Marathon, Oxy, Pan Canadian, Pennzoil, Petroleum Development Oman, Shell International, Statoil, South Western Energy, Texaco, and TOTAL. Able assistance was provided by Fatma Akyurek, who described most of the thin sections. We are particularly appreciative Oxy Permian, the current operator of the South Wasson Clear Fork field, who provided us with field data and encouragement. Figures were prepared by the Bureau of Economic Geology graphics department under the direction of Joel L. Lardon.

REFERENCES

Bebout, D. G., Lucia, F. J., Hocott, C. R., Fogg, G. E., and Vander Stoep, G. W., 1987, Characterization of the Grayburg Reservoir, University Lands Dune field, Crane County, Texas: The University of Texas at Austin, Bureau of Economic Geology Report of Investigations No. 168, 98 p.

Cruz, W. M., 1997, Study of Albian carbonate analogs: Cedar Park Quarry, Texas, USA, and Santos Basin reservoir, southeast offshore Brazil: The University of Texas at Austin, Ph.D. dissertation, 213 p.

Grotsch, Jurgen, and Mercadier, Christophe, 1999, Integrated 3-D reservoir modeling based on 3-D seismic: the Tertiary Malampaya and Camago buildups, offshore Palawan, Philippines: American Association of Petroleum Geologists Bulletin, v. 83, no. 11, p. 1703–1728.

Jennings, J. W., Jr., and Lucia, F. J., 2001, Predicting permeability from well logs in carbonates with a link to geology for interwell permeability mapping: Society of Petroleum Engineers SPE paper no. 71336, 16 p.

Jennings, J. W., Jr., Ruppel, S. C., and Ward, W. B., 2000, Geostatistical analysis of permeability data and modeling of fluid flow effects in carbonate outcrops: Society of Petroleum Engineers Reservoir Evaluation and Engineering, v. 3, no. 4, p. 292–304.

Kerans, Charles, and Tinker, S. W., 1997, Sequence stratigraphy and characterization of carbonate reservoirs: Society of Economic Paleontologists and Mineralogists Short Course Notes, no. 40, 130 p.

Kolodzie, S., 1980, Analysis of pore throat size and use of the Maxman-Smits equation to determine OOP in Spindle field, Colorado: Society of Petroleum Engineers SPE paper no. 9382, 10 p.

Lucia, F. J., 1995, Rock-fabric/petrophysical classification of carbonate pore space for reservoir characterization: American Association of Petroleum Geologists Bulletin, v. 79, no. 9, p. 1275–1300.

Lucia, F. J., 1999, Carbonate reservoir characterization: New York, Springer-Verlag, 226 p.

Lucia, F. J., 2000, Petrophysical characterization and distribution of remaining mobile oil: South Cowden Grayburg reservoir, Ector County, Texas: The University of Texas at Austin, Bureau of Economic Geology Report of Investigations No. 260, 54 p.

Lucia, F. J., Jennings, J. W., Jr., and Rahnis, Michael, 2001, Permeability and rock fabric from wireline logs, Arab-D reservoir, Ghawar field, Saudi Arabia: GeoArabia, v. 6, no. 4, p. 619–645.

Lucia, F. J., Kerans, Charles, and Wang, F. P., 1995, Fluid-flow characterization of dolomitized carbonate-ramp reservoirs: San Andres Formation (Permian) of Seminole field and Algerita Escarpment, Permian Basin, Texas and New Mexico, *in* Stoudt, E. L., and Harris, P. M., eds., Hydrocarbon reservoir characterization: geologic framework and flow unit modeling: SEPM (Society for Sedimentary Geology), SEPM Short Course No. 34, p. 129–153.

Martin, A. J., Solomon, S. T., and Hartmann, D. J., 1999, Characterization of petrophysical flow units in carbonate reservoirs: Reply: American Association of Petroleum Geologists Bulletin, v. 83, no. 7, p. 1164–1173.

Neo, Sadafumi, Asada, Jiro, Fujita, Nozomi, Mohammed, Salman, and Arab Hani, 1998, Geological framework modeling and rock type optimization for a giant oil field, offshore Abu Dhabi Society of Petroleum Engineers, SPE paper no. 49447, 17 p.

Pittman, E. C., 1992, Relationship of porosity and permeability to various parameters derived from mercury injection capillary pressure curves for sandstone: American Association of Petroleum Geologists Bulletin, v. 72, no. 2, p. 191–198.

3-D MODELING OF STRATIGRAPHICALLY CONTROLLED PETROPHYSICAL VARIABILITY IN THE SOUTH WASSON CLEAR FORK RESERVOIR

James W. Jennings, Jr.

Bureau of Economic Geology
John A. and Katherine G. Jackson School of Geosciences
The University of Texas at Austin

TABLE OF CONTENTS

LIST OF FIGURES

ABSTRACT

Petrophysical heterogeneity in the South Wasson Clear Fork (SWCF) reservoir and other shallow-water platform carbonates in the Permian Basin and elsewhere is composed of a large-scale stratigraphically controlled component and a small-scale poorly correlated component. The large-scale variability exists as a flow-unit scale petrophysical layering that is laterally persistent at interwell scales and produces highly stratified reservoir behavior. Modeling these large-scale heterogeneities as trends using moving averages within a high-resolution sequence-stratigraphic framework reduced the requirement for arbitrary k_v/k_h adjustments to inhibit cross-flow in waterflood simulations. Carefully controlled power-averaging effectively captured the rate-enhancing effect of the small-scale variability.

INTRODUCTION

Petrophysical properties in Permian dolomitized shallow-water platform carbonates of West Texas and New Mexico exhibit a high degree of spatial variability over a wide range of scales. These spatial variabilities are organized into rock-fabric flow units that in turn compose the laterally continuous high-frequency cycles of a sequence-stratigraphic framework. Most of the petrophysical variability occurs at scales within the rock-fabric flow units and exhibits weak spatial correlations (Lucia and others, 1992; Senger and others, 1993; Kerans and others, 1994; Jennings, 2000). The larger scale heterogeneities are spatially controlled by the stratigraphy. These heterogeneities have a smaller variance and are easily obscured by the small-scale variability in data analysis; nevertheless, they exert a dominant control on large-scale sweep patterns in moderate mobility ratio displacements (Jennings and others, 2000). Therefore, it is critically important to identify and model the larger scale features for waterflood reservoir performance prediction.

The small-scale variabilities contribute to smearing of displacement fronts but do not otherwise affect sweep patterns in moderate mobility ratio displacements (Jennings and others, 2000). Displacements with highly adverse mobility ratios may be more dependent on small-scale variability. However, regardless of the mobility ratio, the small-scale heterogeneities do have important effects on displacement rate (Grant and others, 1994). These rate effects must be

accounted for in flow modeling with effective permeabilities because the variabilities are usually much smaller than the grid blocks of a reservoir performance simulation.

In this report a new approach is presented for the construction of 3-D reservoir flow simulation models with a superior representation of stratigraphically controlled petrophysical variability. Using the SWCF reservoir as an example, and well logs as a primary source of subsurface data, a method of model construction is illustrated that links high-resolution sequence-stratigraphic frameworks, porosity-permeability relationships from core data, outcrop-derived models of small-scale spatial statistics, and a practical approach to porosity-permeability scaleup.

In the proposed methodology spatial moving averages are used with geostatistical stochastic simulation in a sequence-stratigraphic framework to detect and model the larger scale variabilities. The resulting model exhibits stratification and stacking patterns typical of shallow-water platform carbonates in the Permian Basin and elsewhere, and it has a reduced requirement for arbitrary k_v/k_h reductions to inhibit cross-flow in waterflood simulations. Carefully controlled power-averaging effectively captures the rate-enhancing effect of the small-scale variability.

The following eight sections of this chapter describe the statistical analysis and modeling methodology employed in this study of the SWCF reservoir. The first two sections describe the less familiar statistical spatial analysis and modeling tools used in the study and establish a terminology for the various levels of scaleup encountered. The next section summarizes the spatial statistics of the outcrop analog petrophysical data. This section is followed by a section on quantification of petrophysical layering and two sections on porosity and permeability grid construction. The final two sections present the results of flow simulation using the improved SWCF model and summarize the conclusions of the modeling study.

SPATIAL ANALYSIS AND MODELING TOOLS

In addition to the familiar statistical and geostatistical tools generally used in reservoir modeling three additional tools are useful for spatial data analysis and modeling of stratigraphically controlled petrophysical variability: stratigraphic coordinate transformations, moving averages and standard deviations for trend modeling, and analysis of residuals. Although these three tools are simple, they are perhaps less familiar than standard statistical and

geostatistical methods, and they play a key role in the proposed methodology. The three additional tools are described in this section of the chapter.

Stratigraphic coordinate transformation

The spatial patterns of petrophysical data in shallow-water platform carbonates are stratigraphically controlled. These spatial variabilities occur at the scale of rock-fabric objects, high-frequency cycles, and the larger scale sequence-stratigraphic units they compose. These stratigraphically controlled variabilities have important effects on fluid flow, but they are easily obscured by the higher variance, smaller scale, and nearly uncorrelated variabilities within rock-fabric objects. Nevertheless, the stratigraphic patterns can be extracted from well data by averaging measurements at equivalent stratigraphic locations from multiple wells.

This stratigraphic averaging, as well as other statistical analyses conducted within a sequence-stratigraphic framework, can be conveniently carried out by first moving the data to a stratigraphically flattened coordinate system. The idea is similar to the familiar concept of "hanging" well logs from a datum to remove structure, except that it is generalized to flatten *every* correlated sequence-stratigraphic surface simultaneously, rather that just one (fig. 1). The measurements and their x and y coordinates are unchanged, but a new vertical coordinate, z, is defined such that data at the same z are at an equivalent stratigraphic position in the subsurface. Any horizontal plane in the transformed coordinate system corresponds to an approximate stratigraphic surface in the original coordinate system.

Some commercial reservoir modeling packages will perform stratigraphic coordinate transformations transparently as a part of their data analysis routines, but these packages may not have the flexibility to perform all the trend and residual modeling steps to be described later. Data analysis and modeling in this study were performed with a combination of standard plotting and spreadsheet applications, specially developed software for computing moving statistics, and a commercial geostatistical package (Geovariances, 2001). None of these have a stratigraphic coordinate transformation capability, so this step was performed separately. However, even if built-in coordinate transformations were available, it would be worthwhile to perform this step separately to ensure consistency between the various analysis and display operations.

This stratigraphic coordinate transformation can be computed with various degrees of sophistication, but for unfaulted reservoirs with vertical wells, like SWCF, a simple table lookup

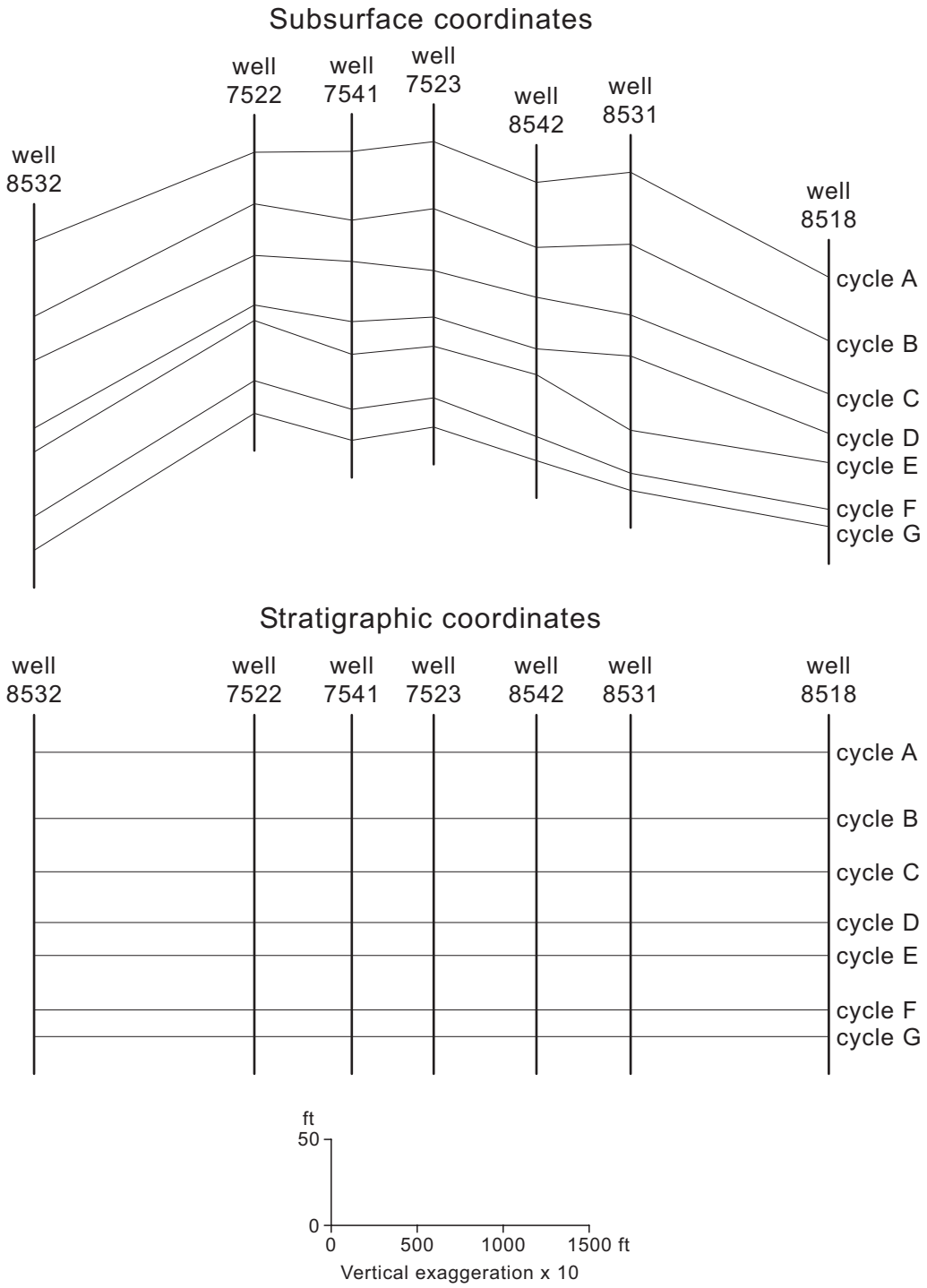

Figure 1. East-west cross section through the SWCF study area showing the top five cycles of the middle Clear Fork and illustrating subsurface (top) and stratigraphic (bottom) coordinate systems.

with piecewise linear interpolation is adequate (fig. 2). The node points for the interpolation are the depths to the geologically interpreted stratigraphic surfaces in each well, and a corresponding list of "stratigraphic depths" below the top of the reservoir computed by accumulating the average thicknesses of each interval. Thus, interval thicknesses in the transformed coordinate system are constant and equal to the corresponding average thicknesses before transformation. Transformed depths for the measurement points in a well are computed by finding the appropriate table interval between the interpreted surface depths for that well, then interpolating a corresponding stratigraphic depth, z.

If geological surface interpretations are missing from the bottom of some wells because the wells were not drilled or logged to the bottom of the reservoir, then the missing surfaces must be estimated, or the data below the last surface must be ignored. The latter approach was used in this study. Similar approaches can be applied if surfaces are missing at the top of the reservoir owing to ambiguities in geological interpretation. Missing interior surfaces can be dealt with by performing the linear interpolation between the nearest existing surfaces. This process is equivalent to assuming that the stratigraphic positions of the missing surfaces are the same as their average stratigraphic positions in the other wells. This may not always be a good assumption, so it is preferable that the stratigraphers always provide at least a guess for every surface at every well in the logged reservoir interval. In this study an interpretation was provided for the top and bottom of every flow unit in the two reservoir intervals studied and every well in the study area, except for one well that was not logged in the lower Clear Fork (well 8502).

Moving averages and standard deviations

Moving averages are useful for filtering small-scale variability from a data set, thus aiding in the identification and modeling of larger scale trends. The simplest kind of moving average is computed by finding all the data within a given distance of a target point, then assigning the resulting average to that point. The resulting "averaging window" is an interval of constant length in 1-D, a circle of constant radius in 2-D, and a sphere of constant radius in 3-D, with weights of 1 for data inside and 0 for data outside the window. The target points may be any list of points, not necessarily coinciding with the data locations, and neither the data nor the target points need be on a regular grid.

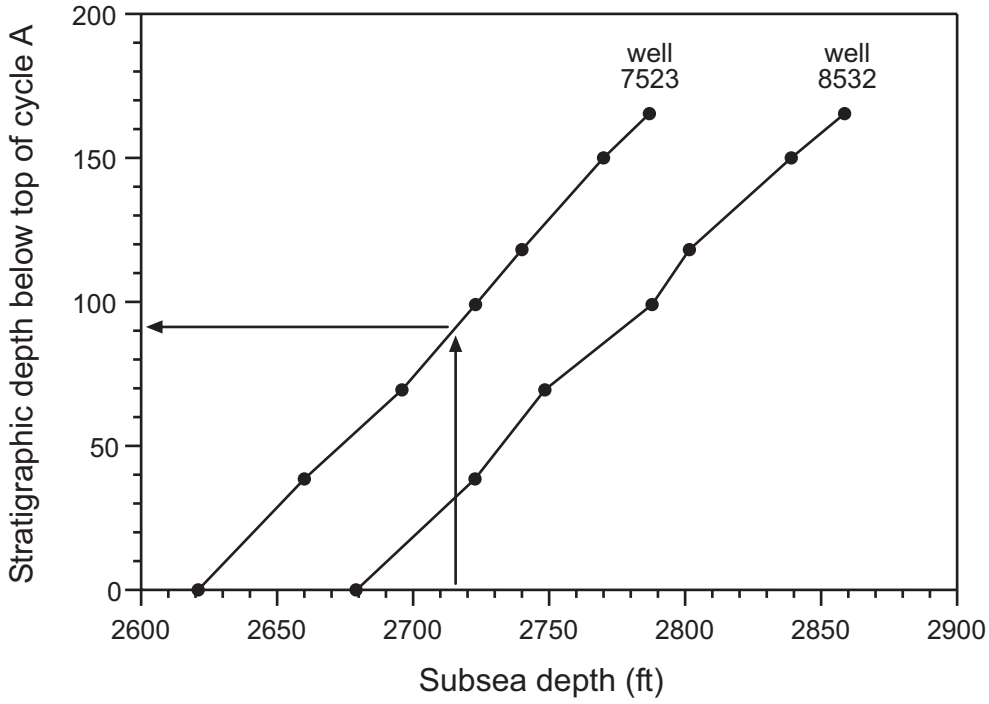

Figure 2. Stratigraphic depth transformations for individual well-log points are computed by piecewise linear interpolation of stratigraphic depths at individual wells. For example, a subsea depth of 2,716 ft at SWCF well 7523 becomes 92 (no units) in the stratigraphic coordinate system.

Simple and useful generalizations to this calculation include (1) ellipsoidal rather than spherical window geometries, (2) continuous tapered weight functions rather than binary ones and zeros changing abruptly on the window boundary, and (3) variable weights for the data to accommodate different degrees of confidence in different measurements. These generalizations may be accomplished with

$$\bar{v}(x,y,z)=\frac{\sum_{i}^{n} w_i v_i}{\sum_{i}^{n} w_i}, \tag{1}$$

where $\bar{v}$ is the moving average at a target point with coordinates (x, y, z), v_i is a petrophysical datum value, and n is the total number of data values. Each weight, w_i, is a product of a variable weight assigned to each data point, w_i^d, and an ellipsoidal moving spatial weight function, w_i^f, dependent on the datum and target point locations:

$$w_i = w_i^d w_i^f(x,y,z), \tag{2}$$

where

$$w_i^f(x,y,z)=f\left(\sqrt{\left(\frac{x_i-x}{d_x}\right)^2+\left(\frac{y_i-y}{d_y}\right)^2+\left(\frac{z_i-z}{d_z}\right)^2}\right). \tag{3}$$

Equation 3 may be equivalently expressed:

$$w_i^f(x,y,z)=f(h_i(x,y,z)), \tag{4}$$

where

$$h_i(x,y,z)=\sqrt{\left(\frac{x_i-x}{d_x}\right)^2+\left(\frac{y_i-y}{d_y}\right)^2+\left(\frac{z_i-z}{d_z}\right)^2} \tag{5}$$

is the scaled distance from the target point to the datum i, (x_i, y_i, z_i) are the coordinates of the datum i, and (d_x, d_y, d_z) are the dimensions of an ellipsoid aligned with the coordinate axes. A variety of effects may be obtained by carefully choosing the function f, but for this study an exponential function was used:

$$f(h)=\exp\left(-h^{\alpha}\right), \tag{6}$$

where α is an exponent usually set to 1 for an exponential decay or 2 for a Gaussian decay. With this weight function every datum value is used in the moving average at each target point, but with weights that decay with distance from the target.

A moving standard deviation required for the analysis of residuals may be computed with

$$s(x,y,z)=\sqrt{\frac{\left(\sum_i^n w_i\right)\left(\sum_i^n w_i v_i^2\right)-\left(\sum_i^n w_i\right)^2 \bar{v}^2(x,y,z)}{\left(\sum_i^n w_i\right)^2-\sum_i^n w_i^2}}. \tag{7}$$

This formula produces an unbiased estimate of the moving standard deviation, s, for any set of weights and regardless of the number of data.

Although every datum value is used for the moving statistics at each target point, some are used with much less weight than others, and it is useful to compute an effective n,

$$n_{eff}(x,y,z)=\frac{\left(\sum_i^n w_i\right)^2}{\sum_i^n w_i^2}. \tag{8}$$

The moving averages, moving standard deviations, and n_{eff} should be computed with a consistent set of weights.

Analysis of residuals

When modeling petrophysical variability in shallow-water platform carbonates it is helpful to separate the large-scale stratigraphically controlled heterogeneities, which will be termed "trends," from the small-scale variability, which will be termed "residuals." The advantages to this approach are flexibility, simplicity, the ability to easily deal with nonstationarity of the mean and variance, and convenience in accommodating different fluid-flow effects at different scales.

An important advantage is flexibility; after the trends and residuals have been separated, entirely different methods may be selected for their most appropriate modeling. In shallow-water platform carbonates the trends are usually stratigraphically controlled variations with abrupt vertical contrasts at rock-fabric flow unit boundaries and gradational lateral transitions that can be mapped from well data at typical West Texas well spacings. It is appropriate to regard these variabilities as deterministic features to be mapped, rather than stochastic heterogeneities to be simulated. The residuals, on the other hand, are much smaller scale features with a very different style of spatial correlation. They cannot be mapped between wells; they must be stochastically simulated. Separating the trends from the residuals makes it possible to employ different analysis and modeling methods for these two very different types of heterogeneity. In this study, moving averages and variances were used to model the trends, and standard geostatistical methods were used to stochastically simulate the residuals.

It is a very simple matter to separate the trends and residuals using

$$r_i = \frac{v_i - \bar{v}_i}{s_i}, \tag{9}$$

where r_i, v_i, $\bar{v}_i$, and s_i are the residual, the petrophysical datum value, and the trends for the average and standard deviation, respectively, all evaluated at the datum location i. Thus, the residual is a normalized variable with a variance of 1 and a mean of 0. After the trends and residuals have been modeled on a grid, a grid of petrophysical values may be constructed with

$$v_g = r_g s_g + \bar{v}_g \quad , \tag{10}$$

where r_g, v_g, $\bar{v}_g$, and s_g are the residual, the petrophysical grid value, and the trends for the average and standard deviation, respectively, all evaluated at the grid point location g.

Geostatistical analysis and stochastic simulation of the residuals are easier than working with the petrophysical data directly, because the mean and variance of the residuals are automatically stationary at the same scale with which variations in the trends have been modeled. This produces several simplifications. First, interpretation and modeling of the experimental semivariograms are easier in the absence of long-range features. Second, if the petrophysical data are not Gaussian the residuals are frequently closer to a Gaussian distribution, placing less of a burden on Gaussian transformation methods. Last, although various methods have been proposed for direct stochastic simulation of a nonstationary variable (for example, sequential Gaussian simulation with an external drift, Deutsch and Journel, 1998) these methods are more complex, and most do not allow for nonstationarity of the variance. Stochastic simulation of residuals defined by equation 9 will still imply an assumption that the semivariogram of the residuals is stationary. This in turn implies an assumption that the normalized semivariogram *shape* of the original petrophysical variable is stationary, but not necessarily its *sill*. This assumption appears to be a good one in carbonates (Jennings, 2000; Jennings and others, 2000).

The trends and residuals tend to have different effects on fluid flow. An additional advantage to modeling them separately is convenience in focusing on the special aspects of each that will be most important in reservoir performance prediction. The trends have important effects on large-scale sweep patterns. Special attention should be paid to their detection, quantification, modeling, and comparison with geological insight. The residuals, on the other hand, have important effects on displacement rate that must be accommodated with scaleup methods because of their small scale. In this study the trends were modeled within a high-resolution sequence-stratigraphic framework, capturing flow-unit-scale petrophysical layering and systematic lateral trends consistent with the geological models. The effects of the residuals on displacement rate were incorporated with scaleup methods involving carefully controlled power averaging of small-scale permeability variations.

SCALEUP LEVEL TERMINOLOGY

The SWCF model construction process involved several explicit or implied levels of scaleup. Discussion of the modeling steps can be clarified by establishing a terminology for the scaleup levels:

Level 0 will refer to petrophysical heterogeneity at scales smaller than the volume of investigation of the well-log porosity measurements. Measurements on core plugs are included in level 0.

Level 1 will refer to heterogeneity scaled up to the porosity-log investigation volume. Scaleup to level 1 is implied by the use of well-log data as the basis of statistical analysis and modeling. Because the porosity logs are presumed to be accurately calibrated arithmetic averages of the level 0 heterogeneity, this scaleup level for porosity modeling is automatically provided by the log data itself. However, careful consideration of the effects of level 0 heterogeneity in level 1 effective permeabilities is required because effective permeabilities are not arithmetic averages.

Level 2 will refer to well-log data scaled up to flow-unit thicknesses, but with the lateral scale unchanged. For porosity modeling at SWCF this scaleup level was obtained by a simple arithmetic average of the well-log porosity data within each flow unit at each well. For permeability modeling a nonarithmetic average was required.

Level 3 will refer to level 2 data scaled up laterally to the grid blocks of the reservoir flow model. In the SWCF model each flow unit was represented by one layer of grid cells, so scaleup from level 2 to level 3 did not involve any vertical scale change. As with the previous scaleup levels, porosity scaleup was accomplished with a simple arithmetic average, but permeability scaleup required a carefully controlled nonarithmetic averaging procedure.

The scaleup level numbers will be used as subscripts in various mathematical symbols to simplify notation. Thus, core-plug permeability data will be denoted by k_0, individual well-log porosity measurements by ϕ_1, average flow-unit porosities at each well by ϕ_2, grid-block effective permeabilities by k_3, and so on.

ANALYSIS OF OUTCROP PETROPHYSICAL DATA

Permeability data were obtained from 414 1-inch-diameter samples drilled along a 2,740-ft horizontal transect at 5-ft spacing in a single high-frequency cycle in the Victorio Peak (a Clear Fork equivalent) outcrop at Apache Canyon (Jennings and others, 2000; Ruppel and Ariza, this volume). The samples were cut into 696 1-inch-long plugs, allowing semivariogram computation at a 1-inch lag as well as multiples of 5-ft lags (fig. 3).

This semivariogram exhibits a small-scale variance concentration typical of petrophysical spatial statistics in carbonates. At scales of 5 ft and above, the spatial correlations exhibit the usual shallow-slope power-law behavior, but the 1-inch separation point indicates a steepening at scales less than 5 ft. A 180-ft periodicity is also present in both porosity and permeability, but it does not correspond to changes in facies, texture, or rock fabric from either outcrop observations or characterization of 122 thin sections from every fourth sample location (Jennings, 2000).

The outcrop semivariogram can be approximated with a "gamma" model (Geovariances, 2001),

$$\gamma(l) = c\left(1 - \frac{1}{(1 + l/p)^{\beta}}\right), \tag{11}$$

where l is the separation distance, or "lag," $c = 1.03$ is the "sill" parameter, $p = 0.0625$ ft is the "range" parameter, and $\beta = 0.2$ is a shape parameter. The 180-ft periodicity was not modeled.

QUANTIFICATION OF PETROPHYSICAL LAYERING

Flow-unit-scale petrophysical layering in SWCF and other shallow-water platform carbonate reservoirs is a key heterogeneity in the modeling of fluid displacement. Quantification and modeling of these layers from well-log data involve the interrelated issues of flow-unit identification, flow-unit correlation, lateral-trend modeling, and layer-geometry modeling. These aspects of data analysis and model construction are discussed from a statistical point of view in this section of the chapter.

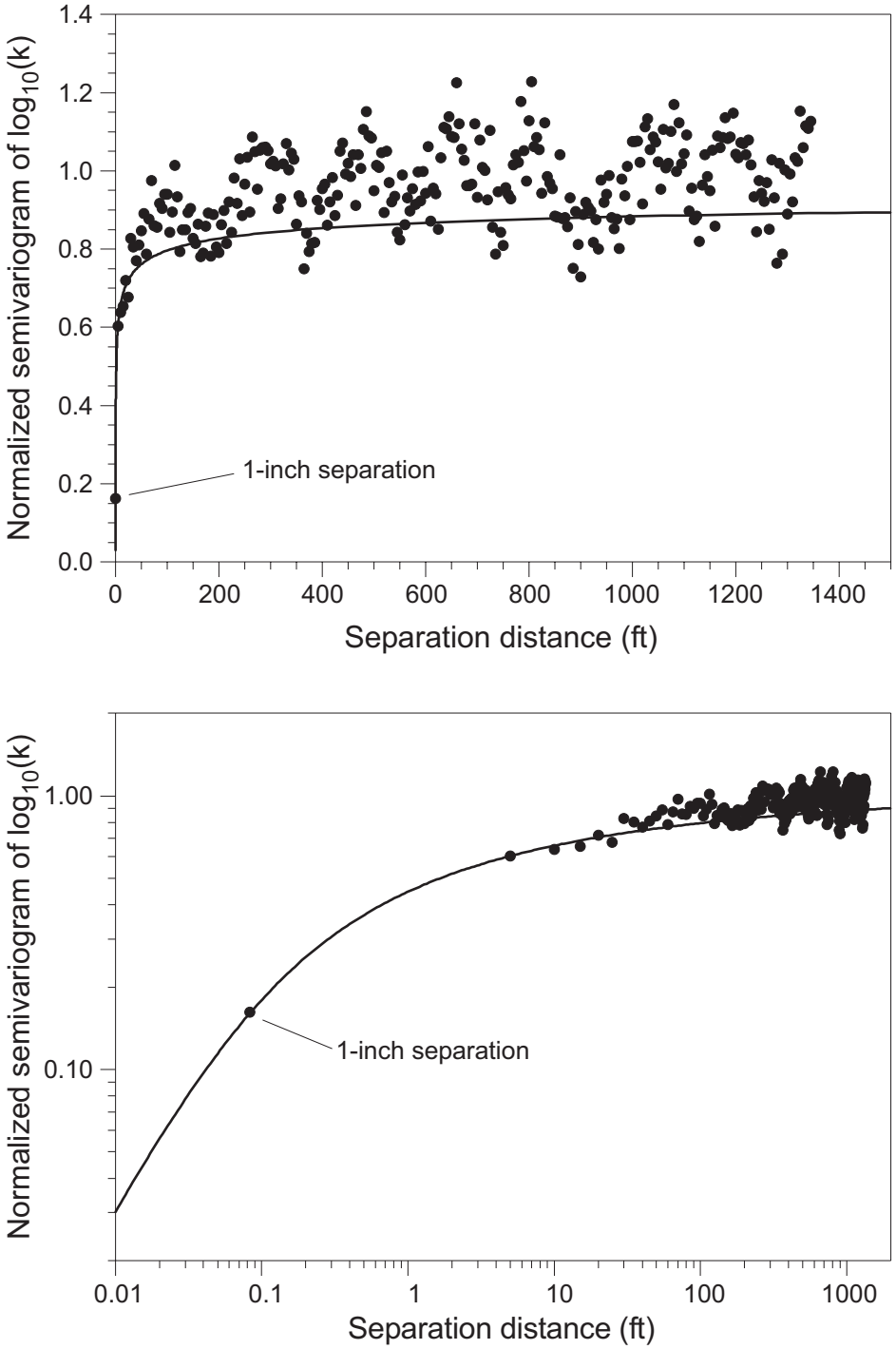

Figure 3. Normalized semivariogram of permeability data from a horizontal transect at Apache Canyon (points) and a gamma semivariogram model used in subsurface modeling (curve) plotted on Cartesian coordinates (top) and logarithmic coordinates (bottom).

Flow-unit identification

As shown by Lucia and Jennings (this report), different rock-fabric flow units at SWCF exhibit significant contrasts in petrophysical properties. These contrasts are illustrated in figure 4b showing well-log porosity data from wells in the study area plotted as a function of the stratigraphic depth. A 1-D vertical moving average of these data shows a strong porosity alternation between cycle tops and cycle bottoms in the middle Clear Fork, and several thin higher porosity intervals in the lower Clear Fork, both of which correlate laterally across the entire study area. This flow-unit-scale layering is probably the most important heterogeneity controlling reservoir-scale waterflood sweep patterns. Therefore, it is reasonable to model the reservoir intervals with one grid layer per flow unit, producing 84 active model layers. Additional vertical resolution would allow for the modeling of vertical trends within the flow units, but these trends are likely to be less important for modeling reservoir behavior.

The average porosities for the 84 active layers range from 0.9 to 7.9 percent with an average of 3.5 percent and a variance of 2 percent squared. However, the individual well-log porosities in the same 84 layers range from 0 to 23 percent with a variance of 8 percent squared. Thus, the variation in layer averages accounts for only one-quarter of the total variance of the well-log data. Three-quarters of the total variance is smaller scale variability within the rock-fabric flow units. This dominance of small-scale variability in the total variance is typical of carbonate petrophysical properties (Jennings, 2000; Jennings and others, 2000) and has a number of important consequences for reservoir characterization and modeling.

One of the consequences of the dominance of small-scale variability is the fact that although different rock-fabric flow units may have significantly different average petrophysical properties, identification of the flow units from petrophysical measurements alone will be unreliable. This effect is illustrated in figure 5 showing histogram models of core-plug and well-log porosity from well 7531. Data from middle Clear Fork cycles G through 9 (10 cycles) (see Lucia and Jennings, this report) were used for this comparison because they have similar statistics in the study area, allowing the data to be reasonably lumped into two histograms, one for cycle tops and the other for cycle bottoms. Although the contrast between average log porosity in the cycle tops and bottoms is statistically significant, the histograms substantially overlap, making flow-unit identification from porosity alone difficult.

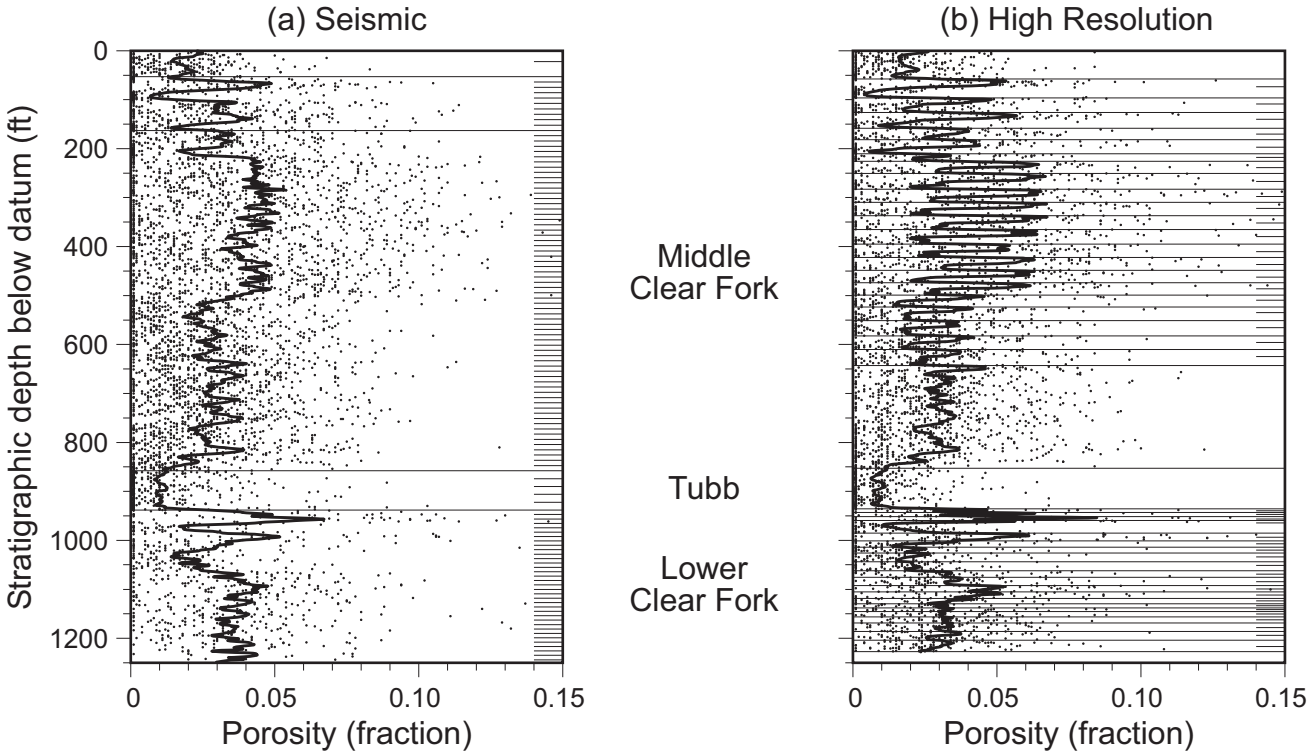

Figure 4. Well-log porosity data from wells in the SWCF study area (points) and vertical moving averages (curves) computed in a seismic-based coordinate system (a) and a high-resolution sequence-stratigraphic coordinate system (b). Only every fifth point is plotted for clarity. The datum is an interpreted surface about 50 ft above the top of cycle A. The seismic coordinate system was constructed from six surfaces (long horizontal lines, two not shown) with proportional subdivision (short horizontal lines). The high-resolution sequence-stratigraphic coordinate system was constructed from detailed high-frequency cycle interpretations (long horizontal lines) and rock-fabric flow unit interpretations (short horizontal lines). The moving averages were computed with $\alpha = 1$ and $dz = 1$ ft.

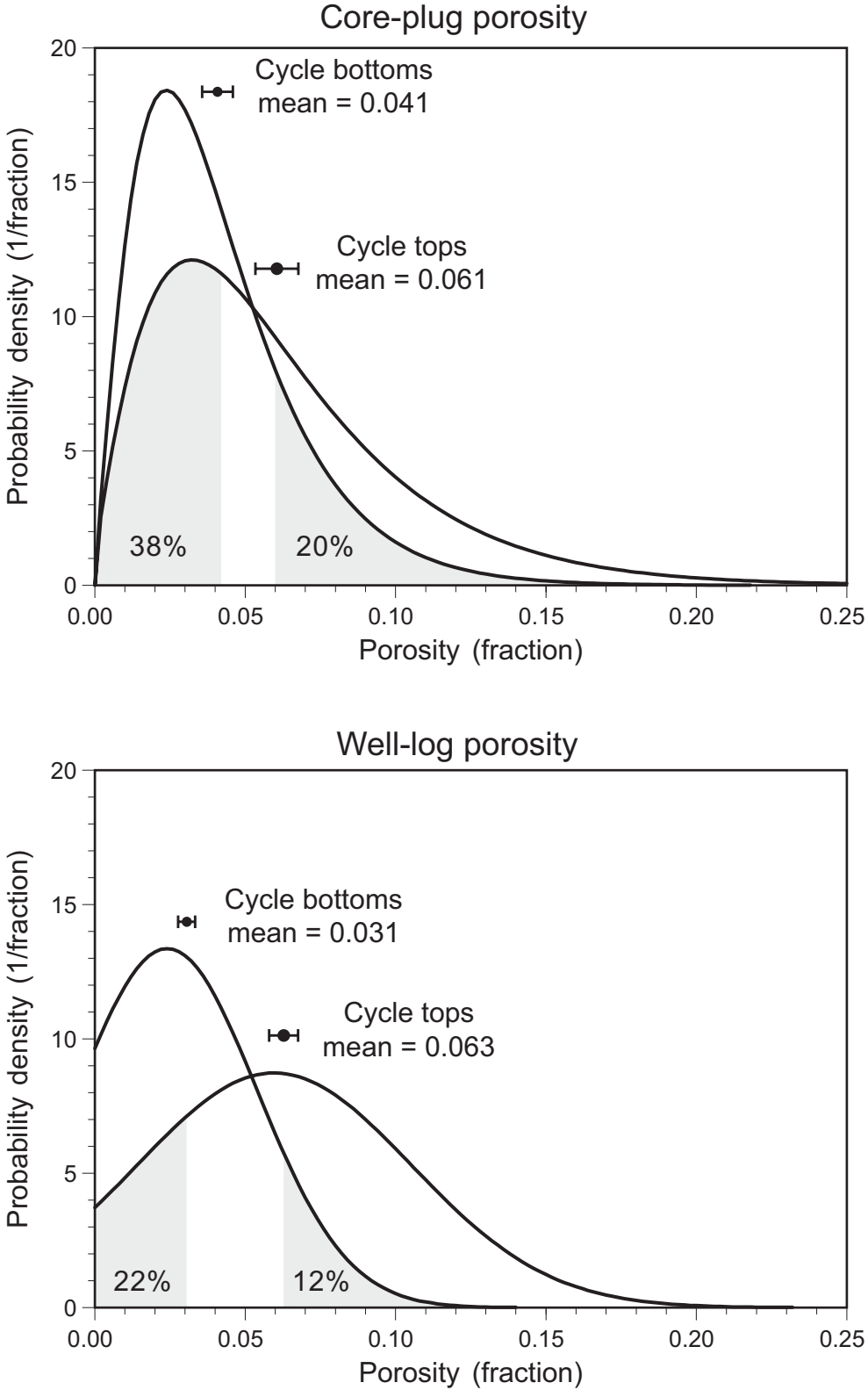

Figure 5. SWCF well 7532 core-plug (top) and well-log (bottom) porosity histograms for middle Clear Fork cycles G through 9. In the cycle tops 38 percent of core-plug porosities are smaller than the cycle-bottom average, and in the cycle bottoms 20 percent are larger than the cycle-top average. In the cycle tops 22 percent of well-log porosities are smaller than the cycle-bottom average, and in the cycle bottoms 12 percent are larger than the cycle-top average.

The effect of small-scale variability is further illustrated in figure 6 showing the expected spatial heterogeneity within two adjacent flow units. This stochastic simulation of plug-scale porosity variability was constructed with core-plug histogram models from well 7531 (fig. 5), an outcrop derived horizontal semivariogram (fig. 3), and a vertical semivariogram from well 7531 plug-porosity data (not shown). Although the simulation was constructed with a sharp contrast in average porosity between the two flow units, the small-scale variability with its much larger range of porosities visually dominates the image.

If a porosity cutoff halfway between the cycle top and bottom averages were used for flow-unit identification, 35 percent of the log measurements in cycle tops would be misidentified as cycle bottoms, and 28 percent of the cycle bottoms would be misidentified as cycle tops because of the significant overlap between the log-porosity histograms (fig. 5). Indeed, 22 percent of the log porosities in the cycle tops are *smaller* than the average porosity of the cycle bottoms, and 12 percent in the cycle bottoms are *larger* than the average porosity of the cycle tops. The situation is somewhat worse when using plug data because the measurement scale is smaller and the small-scale variance is even larger. A plug porosity cutoff halfway between the cycle top and bottom averages would misidentify 41 percent of the cycle-top plugs and 38 percent of the cycle-bottom plugs. The problem is similar when considering other petrophysical properties such as permeability, pore-throat radius and, by implication, capillary properties in general, and a derived petrophysical property known as the "flow-zone indicator" (Amaefule and others, 1993). All of these properties are highly variable within rock-fabric flow units (Jennings and Lucia, 2001). The practical consequence of this property of carbonate rocks is that flow-units cannot be identified from petrophysical data alone. Geological interpretation is required.

Flow-unit correlation

The flow-unit-scale layering is an important heterogeneity controlling reservoir-scale waterflood sweep patterns at SWCF because the layer properties are laterally persistent at interwell distances. This lateral persistence is indicative of a highly stratified reservoir that will display rapid waterflood sweep in the larger-permeability layers, bypassing of the smaller-permeability layers, minimal cross-flow between layers, and early water breakthrough. Nevertheless, detecting this lateral persistence in petrophysical data is surprisingly difficult using spatial statistical analysis alone. This difficulty exists because standard statistical analyses are

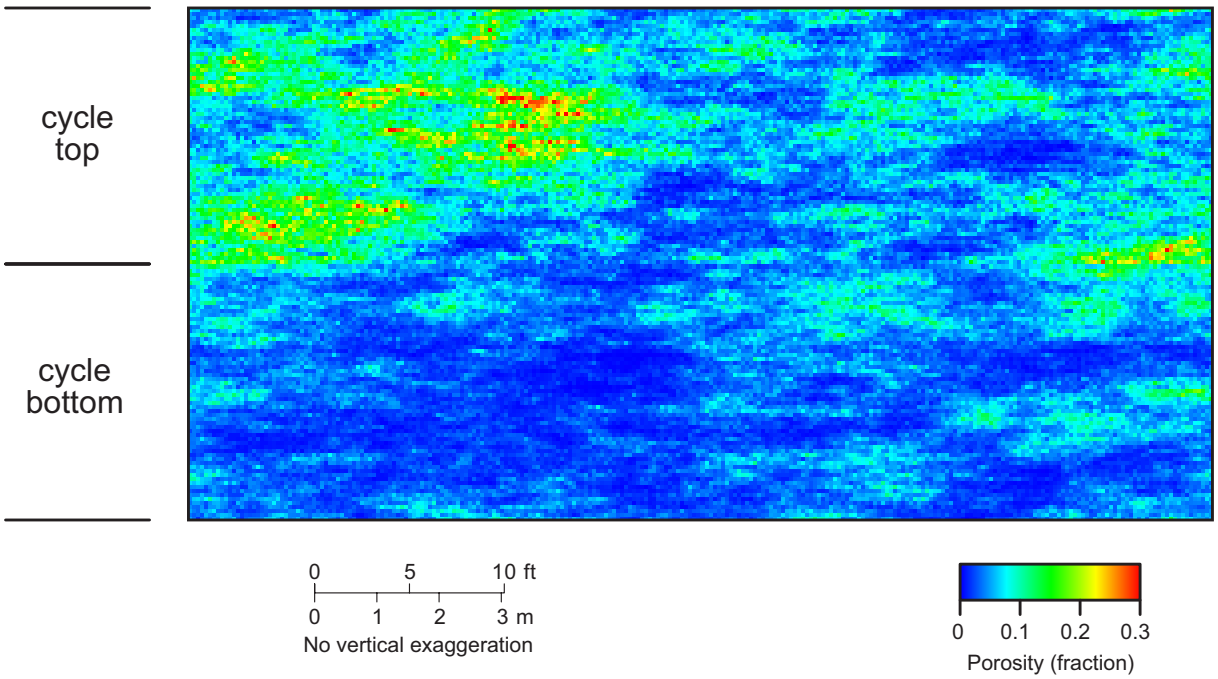

Figure 6. Stochastic simulation of core-plug scale porosity in a cross section of a typical middle Clear Fork high-frequency cycle near SWCF well 7531.

only capable of quantifying spatial correlation within a given geometrical framework; they cannot determine if a proposed *geometrical* framework is a reasonable *sequence-stratigraphic* framework. Spatial statistical analysis cannot substitute for geological knowledge. Geological interpretation is required not only in flow-unit identification at individual wells; it is also required in determining how flow units are connected between wells.

The importance of having a high-resolution sequence stratigraphic framework for the quantification of petrophysical layering is illustrated in figure 4 comparing the effect of two different stratigraphic coordinate systems on the analysis of porosity layering in the SWCF study area. Figure 4a was constructed from a stratigraphic framework based upon six surfaces interpreted from seismic data. Two of these seismic surfaces are outside of the modeled reservoir intervals, one above and one below, and are not shown on the figure. The seismic resolution is insufficient to resolve individual high-frequency cycles and flow units, but the reservoir interval was proportionally subdivided into 86 active layers for flow model construction. Figure 4b was constructed from a high-resolution sequence-stratigraphic framework based upon 88 surfaces resolving individual high-frequency cycles and flow units from well-log data (see Lucia and Jennings, this report).

The most important difference between the quantifications of porosity layering in these two different stratigraphic frameworks is that the strong porosity alternation between adjacent flow units in the middle Clear Fork is almost entirely missed in the lower resolution seismic-based framework. There is better agreement in lower Clear Fork porosity layering, presumably because those flow units are better approximated by a proportional geometry. It is important to point out that the same basic well-log data and exactly the same statistical analysis were used to evaluate porosity layering in these two different coordinate systems. The only difference is between the coordinate systems themselves. Furthermore, the statistical analysis, in this case a moving average, can only tell us that the middle Clear Fork porosity alternation is present in one coordinate system, but not in the other. There is nothing in the moving average per se, nor is there likely to be in any other spatial statistical analysis, that can tell us if the porosity alternation is *real*. For that determination geological knowledge is required. The high-resolution sequence-stratigraphic framework in this study is preferred for SWCF modeling because the reservoir stratification it illuminates is similar to that observed in other shallow-water platform carbonates in general and other Clear Fork reservoirs and outcrops in particular.

Lateral trend modeling

Although the laterally persistent contrasts between the average properties of different rock-fabric flow units at SWCF are very important for modeling reservoir behavior, it would not be adequate to model the reservoir as if the layers were homogeneous having no lateral variation. Because the reservoir model has only one layer of grid cells per rock-fabric flow unit, it is appropriate to perform spatial statistical analysis and modeling at scaleup level 2 using well-log data vertically averaged at the wells through each layer. These 3,829 porosity averages (84 active layers in 47 wells less 119 layers missing from 3 of the wells), denoted by ϕ_2, range from 0 to 14 percent with a variance of 5.4 percent^2. The variance of the 84 overall layer averages is 2.0 percent^2, so about one-third of the total variance of the condensed data set is explained by porosity contrasts between the layers. The remaining two-thirds of the variance is lateral variability within the layers.

A horizontal semivariogram indicates that most of the ϕ_2 lateral variability within layers occurs at distances smaller than the well spacing (fig. 7). This component should be stochastically simulated. The remaining lateral variabilities were modeled as trends using 2-D lateral moving averages and standard deviations in each layer with $\alpha = 2$, $d_x = d_y = 4000$ ft, and

$$w_i^d = \sqrt{n_i} \quad , \tag{12}$$

where n_i is the number of well-log measurements in a given flow unit at a given well. Equation 12 produces data weights approximately inversely proportional to the standard error in estimating ϕ_2 at a given location from n_i well-log measurements. The resulting moving averages and standard deviations are denoted $\overline{\phi}_2$ and $s_{\phi 2}$ respectively.

The lateral trends in ϕ_2 are subtle and barely distinguishable from homogeneous layers in a visual display because this component of variability is small compared with the contrast between the layers (fig. 8). The lateral trends are more easily visualized by subtracting the 84 homogeneous layer averages, revealing a systematic north-to-south porosity increase throughout the reservoir (fig. 9). This systematic porosity trend is small, resulting in a north-to-south

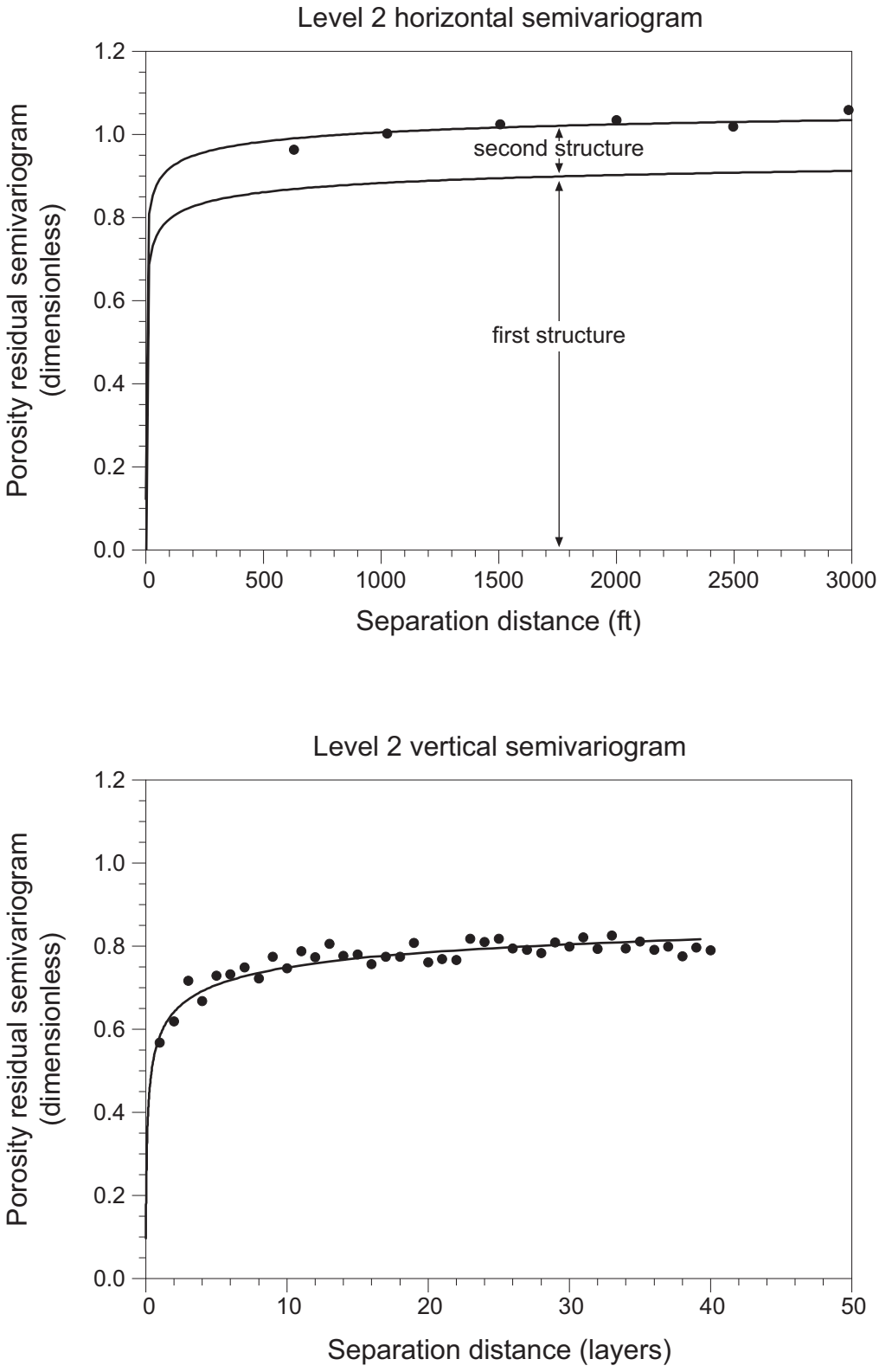

Figure 7. Horizontal (top) and vertical (bottom) measured semivariograms (points) and semivariogram models (curves) for SWCF well-log level 2 porosity residuals.

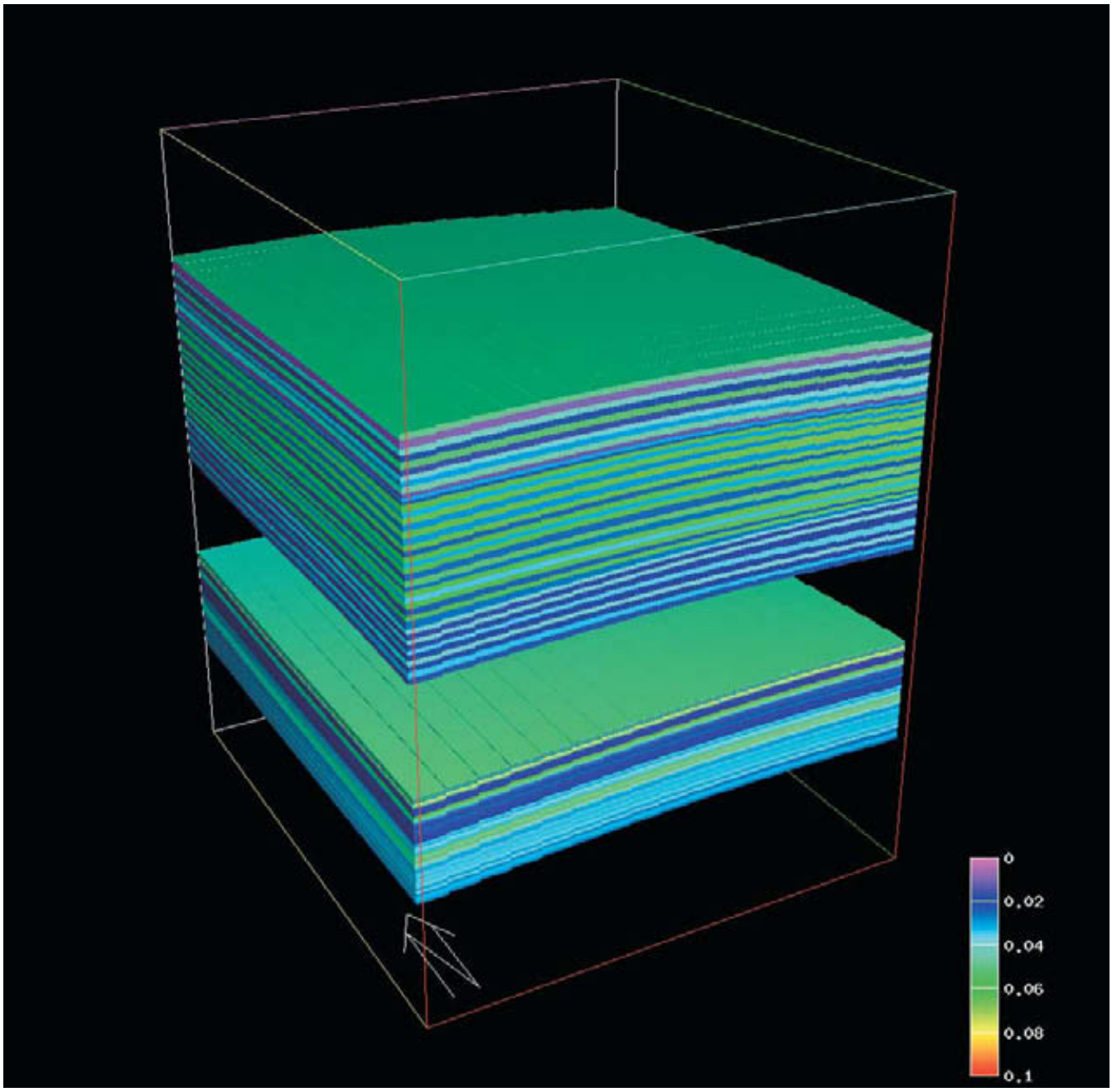

Figure 8. SWCF lateral level 2 porosity trends for each of the 84 active model layers.

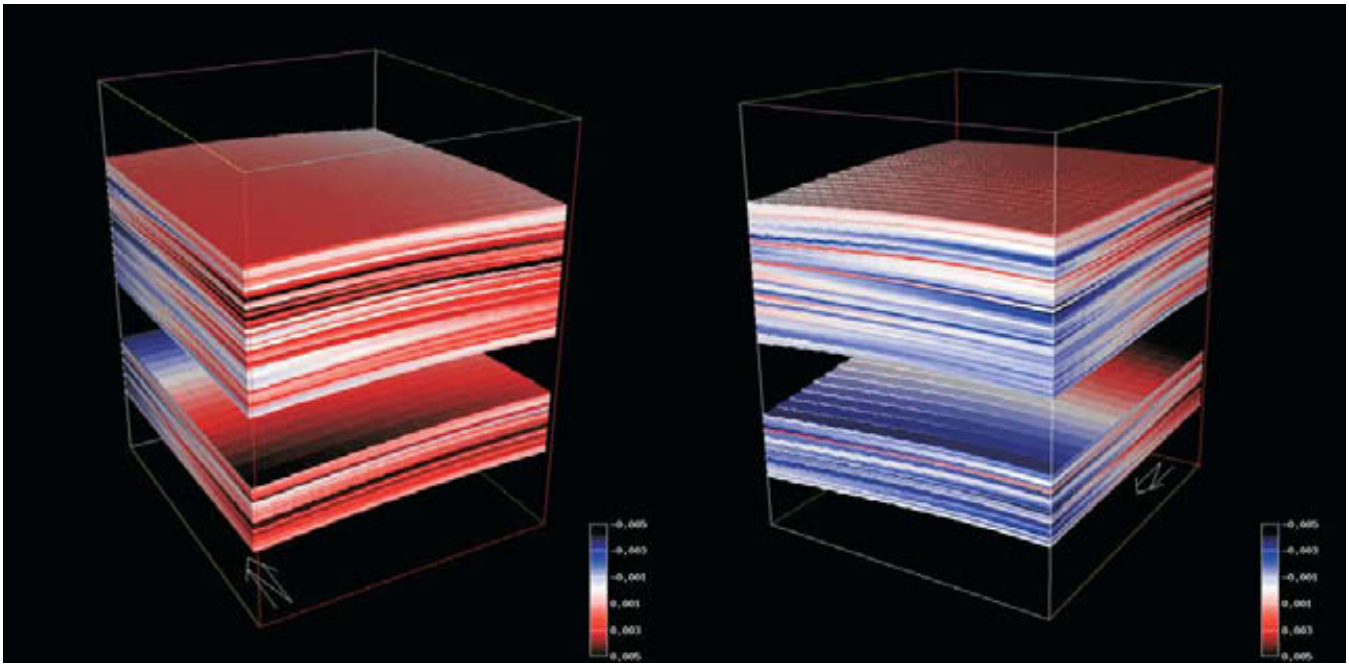

Figure 9. Differences between the SWCF lateral level 2 porosity trends and homogeneous porosity averages for each of the 84 active model layers, viewed from the south (left) and from the north (right).

porosity change of only 1 percent of the bulk volume on the average, but it is consistent with the geological model of more seaward higher energy deposits to the south.

Layer geometry modeling

Layer geometry modeling is required for displays such as figures 8 and 9, and for constructing flow-model layer thicknesses. However, flow-model grid geometries and grid properties, such as porosity and permeability, can be constructed independent of each other. Although it is important that accurate flow-unit correlations be used when transforming well-log data to a stratigraphic coordinate system for quantifying petrophysical layering, it is not necessary for the resulting grid layers to be modeled at exactly the same set of depths. Indeed, it may be desirable for the grid geometry to be smoother than the interpreted flow-unit surfaces if significant surface fluctuations represent errors in depth measurement, errors in surface interpretation, or true surface irregularities at a scale smaller than the grid blocks.

A detailed investigation of the surface fluctuations in SWCF has not been conducted. Nevertheless, it was decided to model the layer geometries with 2-D lateral moving averages for each surface with $\alpha = 2$, $d_x = d_y = 1000$ ft, and $w_i^d = 1$. The resulting surfaces were used to construct the grid geometries used for flow modeling and for the 3-D displays in figures 8 and 9, and similar displays elsewhere in this chapter.

POROSITY GRID CONSTRUCTION

Porosity grid construction for the SWCF model involved trend modeling and spatial statistical analysis of the residuals conducted using the level 2 flow-unit porosity averages, followed by stochastic simulation and scaleup to the level 3 porosity grid. The trend modeling was described in the previous section of this chapter; the remaining steps are described in this section.

Analysis of residuals

The residuals were computed from equation 9 applied to ϕ_2,

$$r_{\phi 2i} = \frac{\phi_{2i} - \overline{\phi}_{2i}}{s_{\phi 2i}} \quad . \tag{13}$$

The residuals were transformed to a Gaussian distribution with a mean of 0 and a variance of 1, then vertical and omnidirectional lateral semivariograms were computed in the stratigraphic coordinate system using layer number as the vertical coordinate (fig. 7). The semivariograms were modeled with a sum of two structures,

$$\gamma_\phi(l_x, l_y, l_z) = \gamma_{\phi a}(l_a) + \gamma_{\phi b}(l_b) \quad , \tag{14}$$

where γ_ϕ is the porosity residual semivariogram, $\gamma_{\phi a}$ and $\gamma_{\phi b}$ are its two component structures, and (l_x,l_y,l_z) is a lag vector. The scaled separation distance l_a is defined by

$$l_a = \sqrt{\left(\frac{l_x}{p_{xa}}\right)^2 + \left(\frac{l_y}{p_{ya}}\right)^2 + \left(\frac{l_z}{p_{za}}\right)^2} \quad , \tag{15}$$

where p_{xa}, p_{ya}, and p_{za} are range parameters for the three coordinate directions. An analogous definition was used for l_b. These definitions for l_a and l_b establish independent geometric models of anisotropy for the two different semivariogram structures (Isaaks and Srivastava, 1989).

The primary semivariogram structure, $\gamma_{\phi a}$, was approximated with a "gamma" model to match the semivariogram observed at the outcrop analog,

$$\gamma_{\phi a}(l_a) = c_a\left(1 - \frac{1}{(1 + l_a)^\beta}\right) \quad , \tag{16}$$

where $c_a = 1.03$ is the sill parameter, and $\beta = 0.2$ is a shape factor. The anisotropic correlation range was modeled with $p_{xa} = p_{ya} = 0.0625$ ft and $p_{za} = 0.0156$ layers. The second semivariogram structure, $\gamma_{\phi b}$, was modeled with a more familiar exponential semivariogram,

$$\gamma_{\phi b}(l_b) = c_b\left(1 - \exp(-l_b)\right) \quad , \tag{17}$$

where $c_b = 0.122$ is the sill parameter. The anisotropy was modeled with $p_{xa} = p_{ya} = 0$ and $p_{za} =$ infinity. This second structure can be thought of as an "anisotropic nugget," contributing nothing to the semivariogram in the vertical direction and a constant $c_b = 0.122$ in lateral directions (Zimmerman, 1993). The second structure was required to model a component of the variability, about 10 percent of the total variance, which exists in lateral but not vertical directions. This component of the variance was assumed to be due to errors in well-log calibration, which varied randomly between wells but were constant for any single well.

Stochastic simulation and scaleup

Construction of a porosity grid can be easily accomplished by (1) conditional stochastic simulation of the Gaussian transformed residuals using the semivariogram model described above, followed by (2) reverse application of the Gaussian transform to obtain a conditional simulation of $r_{\phi 2}$, which is in turn followed by (3) replacement of the trends to obtain a conditional simulation of ϕ_2 using

$$\phi_{2g} = r_{\phi 2g} s_{\phi 2g} + \overline{\phi}_{2g} \quad . \tag{18}$$

However, this simulation of ϕ_2 should not be used directly in flow modeling for two reasons. The first reason is that what is required for flow modeling is porosity at scaleup level 3, the grid cells, not scaleup level 2, the vertical flow-unit averages of well-log scale data. Although ϕ_2 can be easily simulated on the grid centers, and each grid block may be filled with the corresponding constant value for display purposes (fig. 10), the values do not actually represent grid-block averages. Each grid-block porosity obtained in this manner represents a single sample of a level 2 porosity average from the center of the block. Level 2 porosities are averages over much smaller volumes than the required level 3 grid-block averages; therefore, the variance of ϕ_2 is too large.

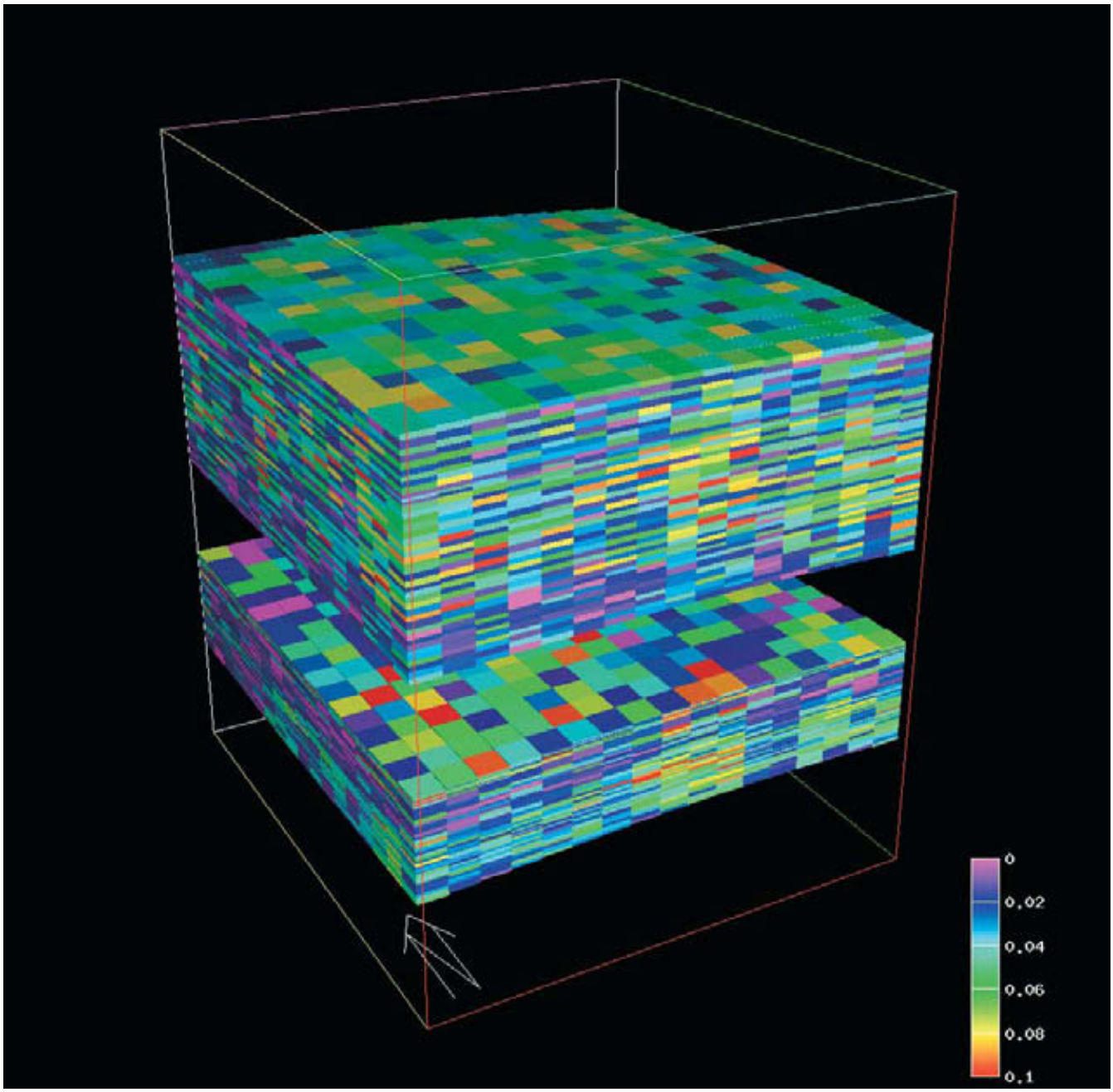

Figure 10. Conditional stochastic simulation of SWCF level 2 porosity at grid-block centers.

The second problem with using a simulation of ϕ_2 directly in SWCF flow modeling is that it contains a component of variability generated from the second structure in the semivariogram model. This component of ϕ_2 is not an artifact of the stochastic simulation. It is an actual spatial property of the well-log data set, but it represents random errors in well-log calibration that are not thought to be present in the reservoir itself.

Scaleup from level 2 to level 3 and removal of the second semivariogram structure can be accomplished in a single step by performing the stochastic simulation on a refined grid followed by averaging within each grid block. The level 2 porosity data already represents a vertical flow-unit average, so refinement is only required in the two lateral directions. This refinement was accomplished with a 10 by 10 subdivision of each grid block. The averaging was performed more conveniently using $r_{\phi 2}$ rather than ϕ_2 because the geostatistical software can compute the block averages of the stochastically simulated variable automatically producing a conditional block stochastic simulation of $r_{\phi 3}$. The conditional simulation of ϕ_3 was obtained from

$$\phi_{3g} = r_{\phi 3g} s_{\phi 3g} + \overline{\phi}_{3g} \quad , \tag{19}$$

using $s_{\phi 2}$ and $\overline{\phi}_2$ as approximations for the trends $s_{\phi 3}$ and $\overline{\phi}_3$. Strictly speaking, the block averaging should be performed using ϕ_2 computed from equation 18, but the result is nearly the same because the trends $s_{\phi 2}$ and $\overline{\phi}_2$ do not change very much within any given grid block.

A resulting conditional block stochastic simulation of ϕ_3 is illustrated in figure 11. The lateral averaging involved in the scaleup from level 2 to level 3 removed most of the small-scale variability within the grid blocks, but it did not remove the larger scale variability modeled by the trends. Thus, the flow-unit stratification represents a larger fraction of the total variance in ϕ_3 than it does in ϕ_2, and the petrophysical layering is more visually apparent in figure 11 than in figure 10.

A porosity grid previously constructed with a more traditional geostatistical approach is shown in figure 12. This modeling method used the geometrical framework shown in figure 4a with direct spatial analysis and modeling of well-log porosities, but trend modeling and residual analysis were not employed. Unlike the SWCF model developed in this study, the model shown in figure 12 included seismic data via stochastic seismic inversion, which probably aided

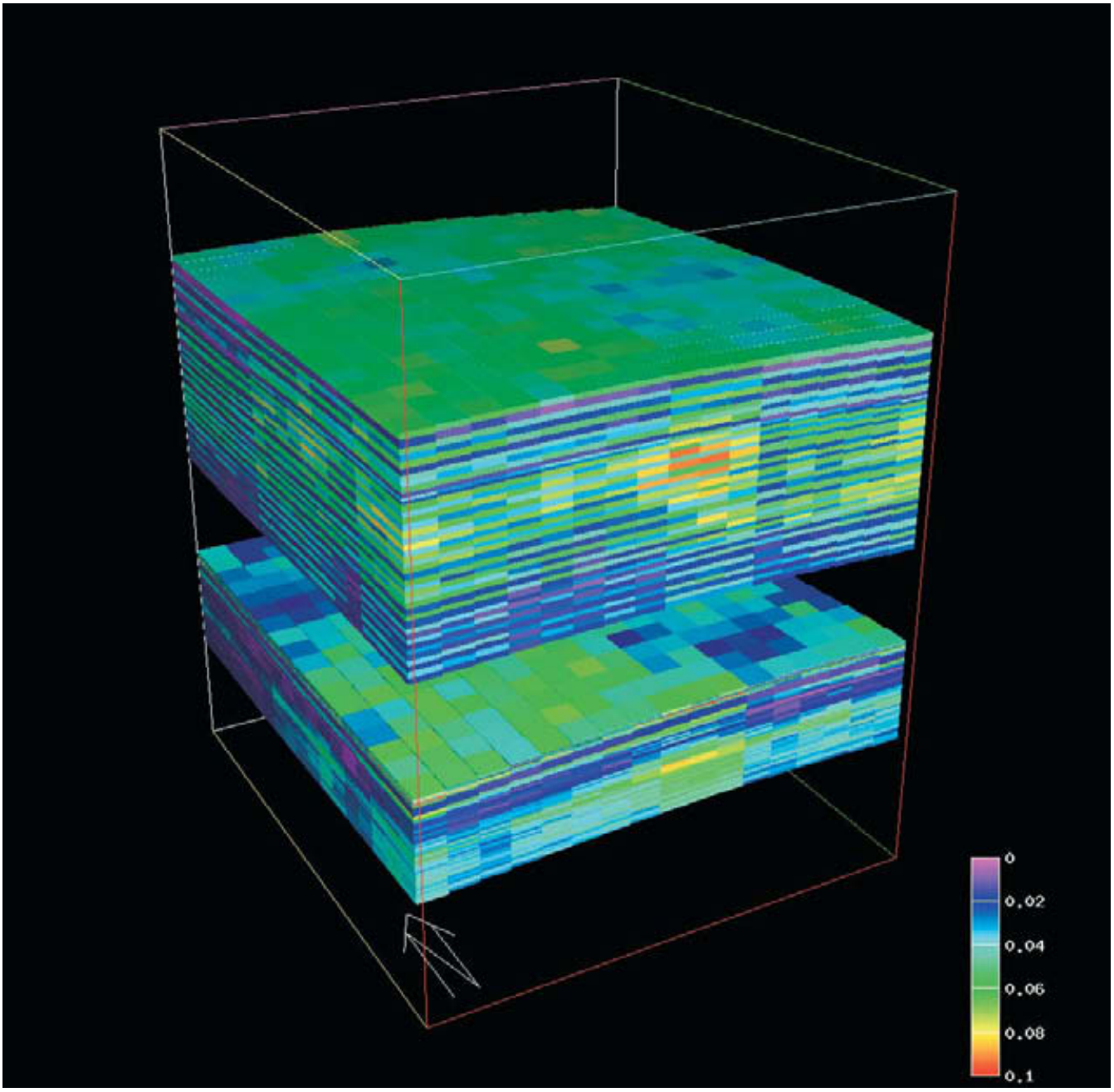

Figure 11. Conditional stochastic simulation of SWCF level 3 grid-block averaged porosity.

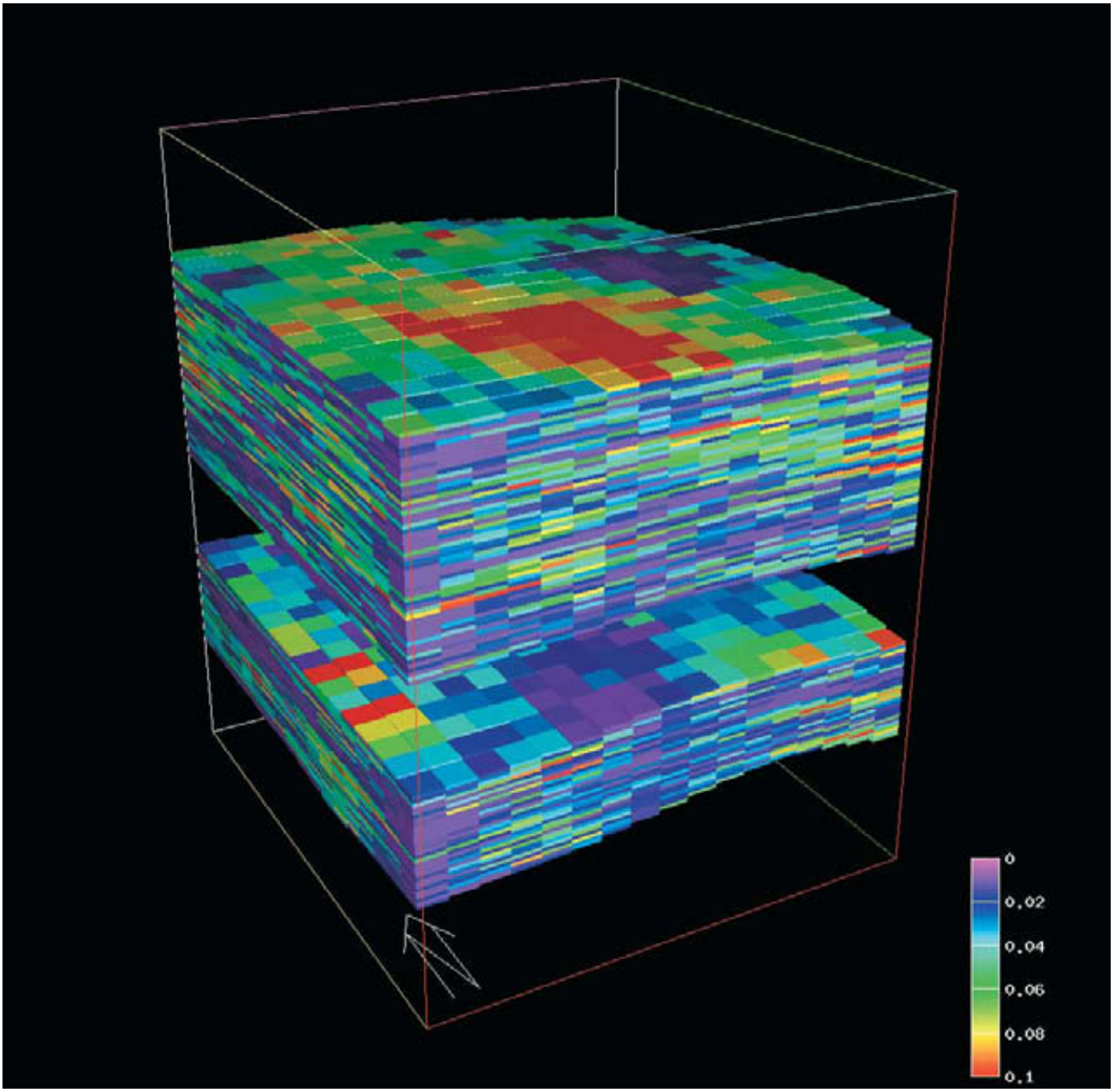

Figure 12. Traditional geostatistical simulation of SWCF porosity from a previous study.

modeling of lateral trends at an interwell scale not accessible from well-log data alone. However, the seismic information did not help to resolve the important flow-unit-scale petrophysical layering apparent in figure 11. Quantification and modeling of the petrophysical layering requires a high-resolution sequence-stratigraphic framework and careful modeling of lateral trends at the flow-unit scale.

PERMEABILITY GRID CONSTRUCTION

If effective permeabilities were accurately represented by arithmetic averages, then a permeability grid could be constructed with exactly the same procedure as was used to construct the porosity grid. Unfortunately, permeability modeling and scaleup are not so simple. However, considerable simplification of permeability modeling in carbonates is obtained from the observation that effective permeabilities within flow units are generally well approximated by a one-third power average,

$$k_{eff} = \left(\frac{\sum k_i^{1/3}}{n} \right)^3 , \qquad (20)$$

where k_{eff} is the effective permeability for a volume of rock, k_i is the permeability of a small-scale sample within the volume, and n is the number of such samples. The one-third power average for effective permeability is a theoretical result that applies in three dimensions when the small-scale permeabilities are log-normally distributed, are isotropic, and have isotropic spatial correlations whose correlation ranges are small compared with the size of the averaging volume (Hristopulos and Christakos, 1999). These conditions are well approximated by the small-scale permeabilities within most carbonate flow units where the spatial correlations are weak, most of the variance is concentrated at small scales, and the correlation ranges are only moderately anisotropic (Jennings, 2000; Jennings and others, 2000). In addition, most core-scale permeability data from carbonate outcrops and subsurface reservoirs are approximately log-normally distributed with only moderate directional permeability anisotropy. The validity of a one-third power average for approximating effective permeabilities within a carbonate flow unit has been experimentally verified (Noetinger and Jacquin, 1991).

The use of power averaging greatly simplifies permeability grid construction and scaleup because k_{eff} as expressed in equation 20 may be viewed as the cube of an arithmetic average of permeabilities raised to an exponent of 1/3. Thus, a grid of effective permeabilities at scaleup level 3 may be constructed from well-log-based permeability estimates at level 1 by (1) raising the level 1 data to an exponent of 1/3, (2) applying the same modeling procedure as was used for porosity, and (3) raising the resulting grid values to an exponent of 3.

For this approach to work correctly the well-log-based permeability estimates must themselves represent effective permeabilities at scaleup level 1. However, the porosity-permeability transform used in this study was developed with a regression on the logarithms of core-plug measurements at scaleup level 0 that predicts the geometric average of permeability for a given porosity (Lucia and Jennings, this volume). This geometric average can be corrected to provide an approximate one-third power average of plug permeabilities within the well-log investigation volume with the following formula (Aitchison and Brown, 1969):

$$k_{eff} = k_g \exp\left(\frac{\sigma^2}{6}\right), \qquad (21)$$

where k_g is a geometric average obtained by applying the porosity-permeability transform to a well-log porosity measurement, and σ^2 is the variance of the natural logarithms of the plug-scale permeabilities within the well-log investigation volume. The formula is approximate in that the plug-scale permeabilities are assumed to be log-normally distributed within any well-log measurement volume. The second term on the right-hand side of this formula can be regarded as a simple multiplicative correction to the porosity-permeability transform. For SWCF modeling σ^2 was estimated as the fraction of the variance of the logarithms of the core-plug permeabilities from well 7531 that was not explained by a regression with the corresponding well-log porosities. Application of this variance in equation 21 produces a multiplicative correction, $k_{eff} = 2.22\ k_g$, that was assumed to be constant throughout the reservoir (fig. 13).

These resulting well-log effective permeability estimates were used for modeling and scaleup using the procedure described above. The trends and residuals of $k^{1/3}$ were modeled with the same procedures applied to porosity. The $k^{1/3}$ residuals after Gaussian transformation had very nearly the same semivariogram as porosity. Cross plots of the simulated permeability and porosity for each scaleup level indicate a systematic effective permeability increase with each

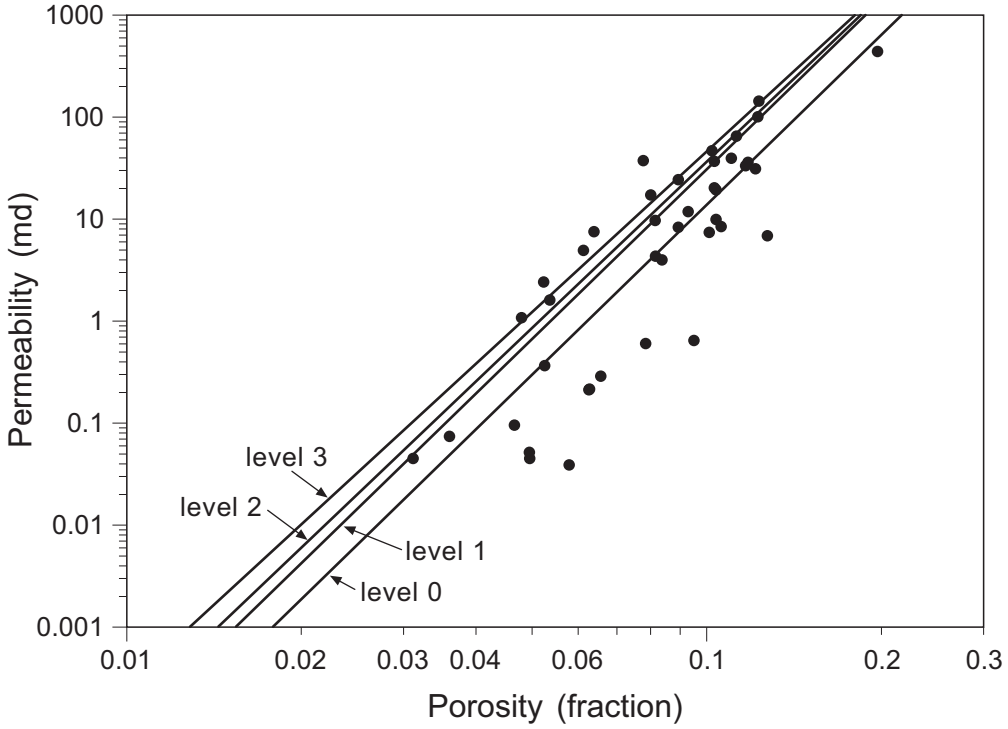

Figure 13. Core-plug porosity and permeability data from SWCF well 7531 (points) and power-law porosity-permeability correlations at scaleup levels 0, 1, 2, and 3.

scaleup step (fig. 13). The largest permeability increase was produced at the smallest scale, scaling up from core-plug permeabilities to well-log effective permeabilities.

Equation 21 is not only useful in approximate scaleup calculations, it also summarizes nicely the dependence of flow rate on small-scale permeability heterogeneity and helps in understanding the observations from figure 13. In three dimensions the effective permeability is dependent not only on the average of the permeability logarithms, but also on the variance of the permeability logarithms. Effective permeability increases systematically with increasing variance for a given geometric average, and we should expect effective permeabilities to increase with scale as additional variance is incorporated. Furthermore, in carbonates we should expect the largest increases to occur at the smallest scales because that is where most of the spatial variance is concentrated. Therefore, the plug-to-well-log scaleup step is likely to be the most important, but neglecting any component of permeability variance in scaleup calculations will produce a scaleup estimate that is too small, leading to a corresponding flow-rate underestimate in reservoir performance predictions.

FLUID-FLOW MODELING

Fluid-flow simulation was conducted to assess the benefits to reservoir performance prediction provided by the improved SWCF model. However, detailed waterflood simulation and history matching were not required to achieve this objective. For the purposes of this study it was sufficient to compare the behavior of the model when running simplified reservoir fluid-flow cases with the behavior of a previously history matched model running the same cases. The model chosen for this comparison is illustrated in figure 12. Although this model incorporated seismic information, it was constructed without a high-resolution sequence-stratigraphic framework, trend modeling, or residual analysis, and will be referred to as the “traditional model.” The model developed in this study will be referred to as the “improved model.”

The areal grid of the improved model was chosen to coincide exactly with that of the traditional model. The layering is different in the two models, but a subset of 86 active layers from the traditional model was selected to coincide approximately with the 84 active layers of the improved model. The total bulk volumes of the selected layers in the two models agree to within

1 percent. The same set of well-log data was used for the construction of both models, and the pore volumes agree to within 5 percent; the improved model has the smaller pore volume.

Although the details of well completion histories and injection schedules are usually important for meaningful reservoir behavior modeling, it was sufficient for this study to compare the two models running the same simplified set of well controls. Twenty of the SWCF wells were modeled as vertical wells at their approximate areal locations in the grid. All the wells were completed in every active layer at the same time with fluid injection or production controlled by a constant bottom-hole pressure. The SWCF historical injection data showed that five of these wells were injectors for at least some of their operational history. These 5 wells were modeled as injectors throughout the simulation runs; the remaining 15 wells were modeled as producers.

Injectivity and sweep were the aspects of reservoir performance addressed in this study. Meaningful comparison of the injectivity and sweep predictions of the two models was achieved by conducting single-phase tracer injection simulations, avoiding the additional complications of waterflood modeling. Thus, no initial saturation, residual saturation, or relative permeability modeling was required. The single-phase fluid was modeled as an incompressible liquid having a constant viscosity.

Detailed waterflood matching of the traditional model to historical SWCF performance was conducted in a previous study. A good history match was obtained by applying a k_v/k_h multiplier of 0.0002 to reduce cross-flow between the layers and by increasing the horizontal permeabilities by a factor of 2 to match reservoir pressure behavior. In this study the improved model was matched to the traditional model, with both models running the same simplified incompressible tracer displacement case, by adjusting the same two parameters.

The k_v/k_h multiplier in the improved model was adjusted to obtain the same sweep at one pore volume injection (fig. 14). However, the k_v/k_h multiplier required to achieve this match was 0.02, two orders of magnitude larger than that required in the traditional model and much closer to the moderate flow-unit scale k_v/k_h ratio expected from typical whole-core data in carbonates. This improvement in performance modeling was produced by the improved representation of petrophysical layering in the model.

The tracer sweep patterns at one pore volume injection in the improved model are stratigraphically organized into alternating high- and low-permeability flow units in the middle Clear Fork, and thin higher permeability flow units near the top of the lower Clear Fork (fig. 15).

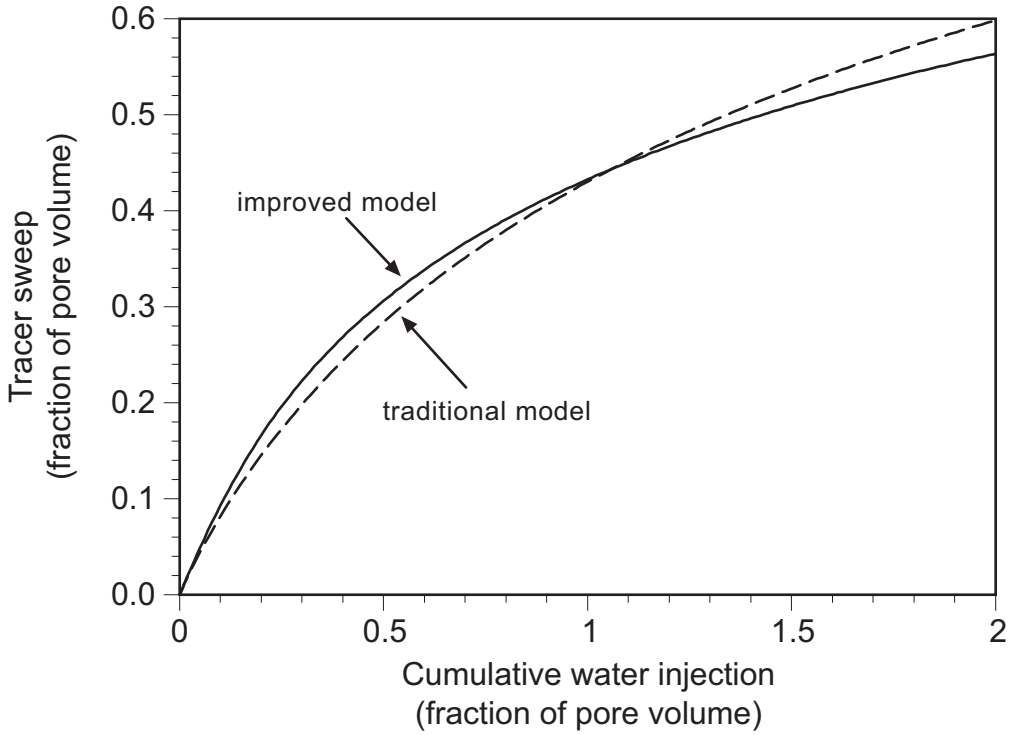

Figure 14. Tracer sweep predictions from the traditional model with a k_v/k_h of 0.0002 to match SWCF waterflood history, and the improved model with a k_v/k_h of 0.02 to match the tracer sweep of the traditional model at one pore volume injection.

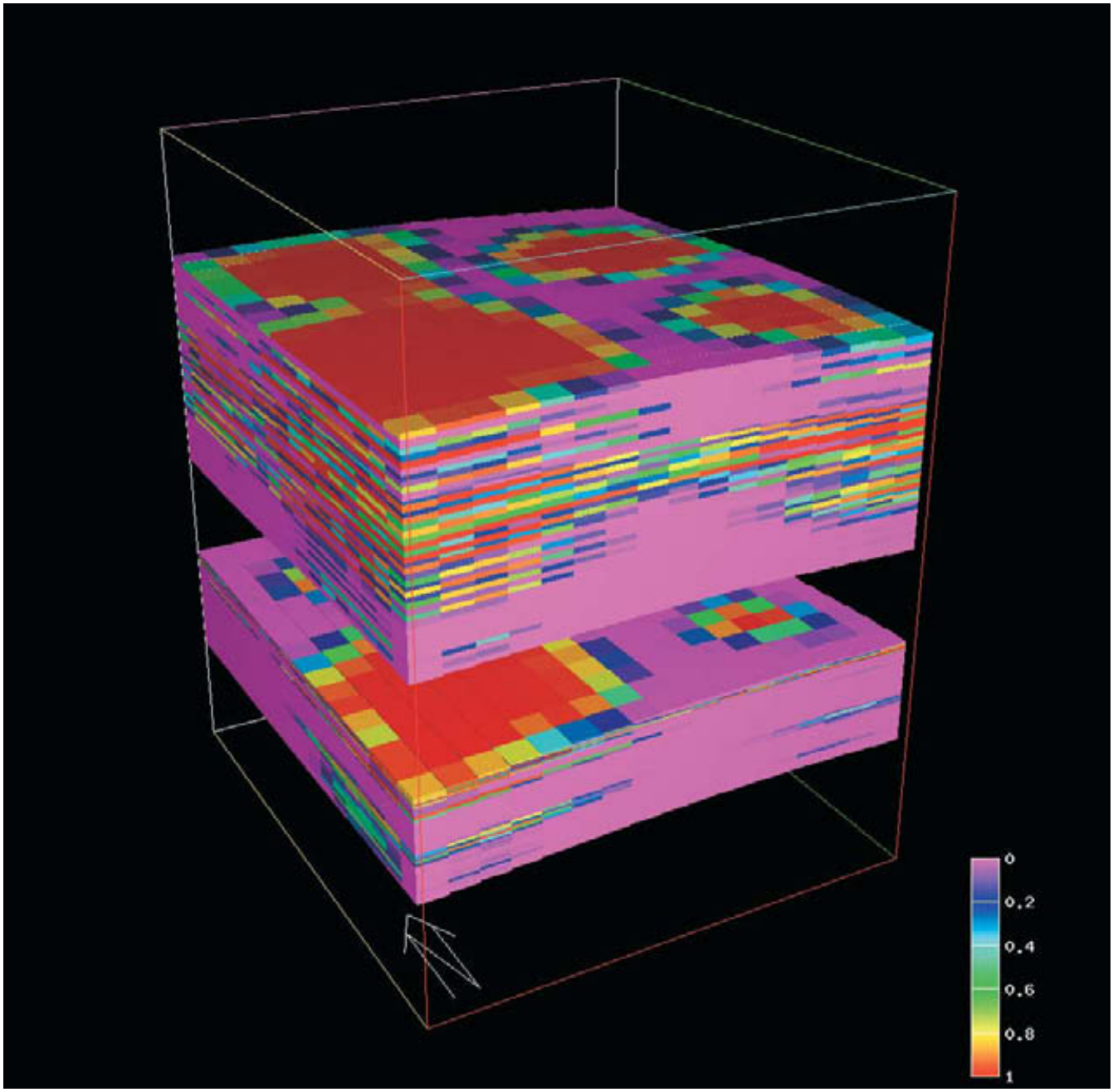

Figure 15. Tracer sweep pattern in the improved model at one pore volume injection.

These sweep patterns were produced by the stratigraphically organized petrophysical layering. The corresponding sweep patterns in the traditional model are more random (fig. 16). The improved model also predicts more injection in the southern portion of the model, relative to the injection predicted by the traditional model, because of the subtle north-to-south porosity increase detected by the trend modeling portion of this study. Careful comparison with reservoir performance data, outside of the scope of this study, would be required to demonstrate that these sweep patterns in the improved model constitute a superior representation of reservoir behavior. Nevertheless, the sweep patterns are consistent with the SWCF geological interpretation and are thus more satisfying.

Direct comparison of injectivity predictions from the two models is complicated by the use of different plug-scale porosity-permeability transforms. To better understand the differences in behavior the traditional model was run twice, once with its original permeability grid and a second time with permeabilities recomputed from the original porosity grid and the plug-scale porosity-permeability transform developed in this study. The improved model with a k_h multiplier of 1 has nearly the same injectivity as the traditional model with a k_h multiplier of 2, when the two models are compared using the same porosity-permeability transform. This comparison indicates that the scaleup calculations of the improved model have reduced the requirement for arbitrary simulator permeability enhancements to match reservoir injectivity.

Nevertheless, the porosity-permeability transform developed in this study reduces injectivity in the traditional model by a factor of 2 relative to that obtained with the original permeability grid. Therefore, the improved model would also require a k_h multiplier of 2 for detailed waterflood matching of historical SWCF performance. This factor of 2 is most likely within the uncertainty of the plug-scale porosity-permeability transform. It is unclear if the discrepancy between the reservoir and model injectivity is caused by an error in the porosity-permeability transform, a remaining inadequacy of the scaleup calculation, or other unaccounted for factors, such as natural fractures (Philip and others, this volume), but whatever its cause the discrepancy is easily corrected and not large enough to destroy confidence in the resulting reservoir performance predictions.

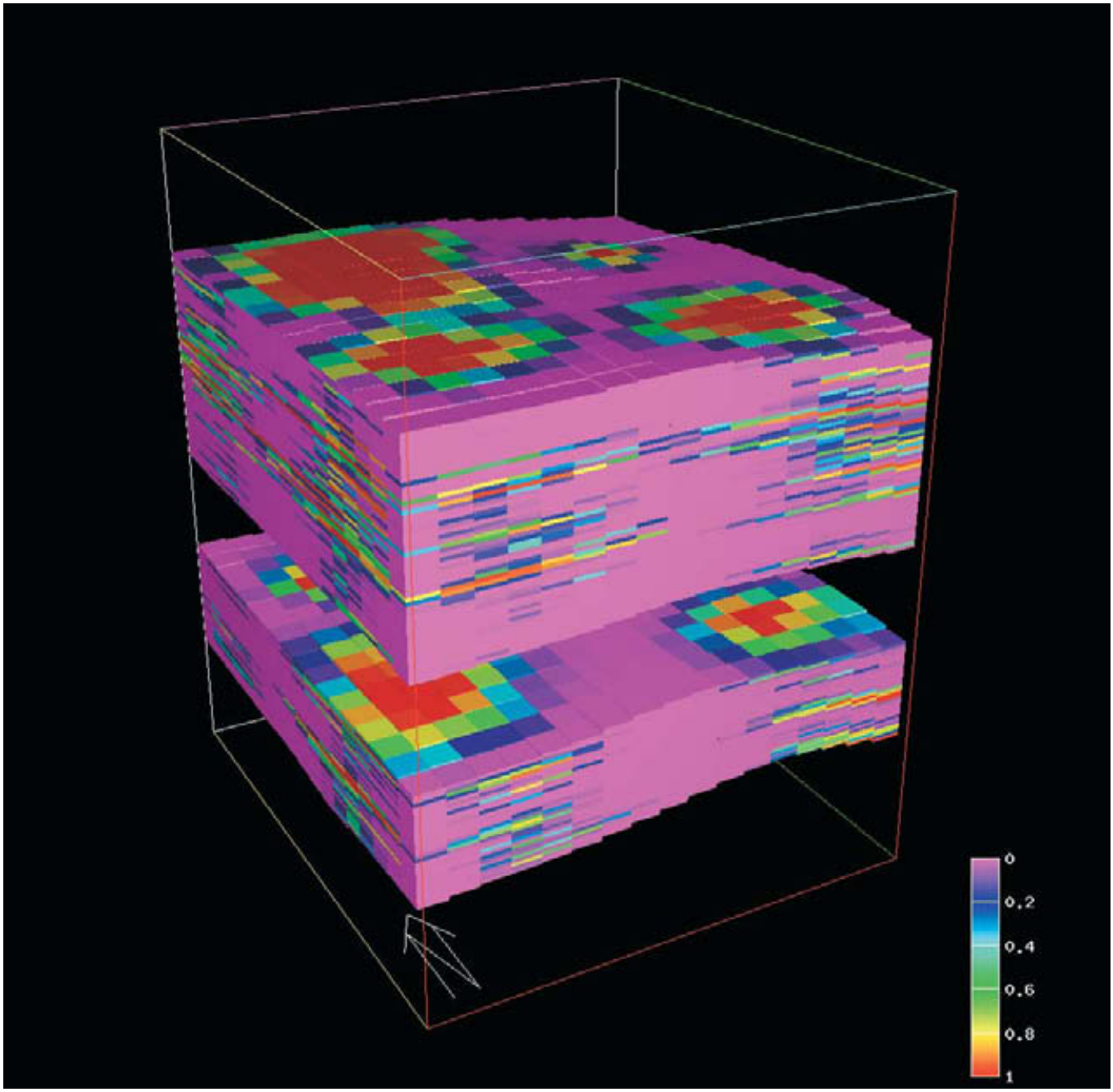

Figure 16. Tracer sweep pattern in the traditional model at one pore volume injection.

SUMMARY AND CONCLUSIONS

Petrophysical variability in Permian dolomitized shallow-water platform carbonates of West Texas and New Mexico is composed of a large-scale stratigraphically controlled component and a small-scale poorly correlated component. These two very different types of heterogeneity have different effects on fluid flow and are best modeled separately. At SWCF the large-scale variabilities were modeled as deterministic trends using moving averages and standard deviations, whereas the small-scale variabilities were modeled as stochastic heterogeneities using standard geostatistical methods.

The large-scale component of petrophysical variability is spatially organized into rock-fabric flow units, high-frequency cycles, and the larger scale sequence-stratigraphic units they compose, with abrupt vertical contrasts at flow-unit boundaries and gradual lateral transitions. At SWCF and other shallow-water platform carbonates this stratigraphic control produces a flow-unit-scale petrophysical layering that is laterally persistent at interwell scales, leading to highly stratified reservoir behavior with rapid waterflood sweep in the larger permeability layers, bypassing of the smaller permeability layers, minimal cross-flow between layers, and early water breakthrough. Identification and modeling of this petrophysical layering are critical for waterflood performance prediction.

The flow units cannot be reliably identified in individual wells, nor can their lateral correlation between wells be determined from statistical analysis of well-log data alone. However, the petrophysical layering can be quantified from well-log data by moving averages and standard deviations within a high-resolution stratigraphic framework provided by geological interpretation. At SWCF this high-resolution stratigraphic analysis revealed a strong flow-unit-scale petrophysical alternation in the middle Clear Fork that correlates across the entire study area, several thin higher porosity intervals in the lower Clear Fork that also correlate across the study area, and a subtle but systematic north-to-south porosity trend consistent with the geological model. Careful modeling of these stratified trends produced a 100-fold reduction in the requirement for arbitrary k_v/k_h reductions to inhibit cross-flow in waterflood simulations and match historical waterflood performance.

The small-scale component of petrophysical variability usually dominates the petrophysical variance in carbonate systems and obscures the larger scale trends. This small-scale but relatively large magnitude petrophysical variance contributes to the difficulty in identifying flow units from well-log data alone and creates the necessity for the averaging of data from multiple wells in the quantification of petrophysical layering. Although this small-scale heterogeneity has little effect on sweep patterns in moderate mobility ratio displacements, it does have an important effect on effective permeability and displacement rate. Larger permeability variances within an averaging volume produce larger effective permeabilities for a given geometric average. The biggest effect typically occurs at the smallest scale, plug-scale heterogeneities within a well-log volume of investigation, because that is where most of the petrophysical variance is concentrated.

Fortunately, effective permeabilities within carbonate flow units can be well approximated with one-third power averages, greatly simplifying modeling and scaleup. Application of this approach in the SWCF model systematically increased the grid-block effective permeabilities and reduced, but did not eliminate, the requirement for arbitrary permeability adjustments to match historical injectivity.

ACKNOWLEDGMENTS

This research was funded by the U.S. Department of Energy under contract no. DE-AC26-98BC15105 and by the sponsors of the Reservoir Characterization Research Laboratory: Altura, Amerada Hess, Anadarko, Aramco, ARCO, BP International, Chevron, Elf Aquitaine, ExxonMobil, Great Western Drilling, Japan National Oil Corporation, Kinder Morgan, Marathon, Oxy, Pan Canadian, Pennzoil, Petroleum Development Oman, Shell International, Statoil, South Western Energy, Texaco, and TOTAL. We are grateful to Oxy Permian, the current operator of the South Wasson Clear Fork field, who provided us with field data and encouragement. Oxy Permian staff Jeff F. Simmons and Raul Valdez were particularly helpful with reservoir fluid-flow modeling issues and provided a history matched traditional SWCF model for comparison purposes. Geostatistical, fluid-flow modeling, and 3-D display software was provided by Geovariances, Schlumberger Geoquest, and Roxar. The figures were prepared by the Bureau of Economic Geology graphics department under the direction of Joel L. Lardon. The manuscript was edited by Susann V. Doenges.

REFERENCES

Aitchison, J., and Brown, J. A. C., 1969, The lognormal distribution: Cambridge, Cambridge University Press.

Amaefule, J. O., Altunbay, M., Tiab, D., and Kersey, D. G., 1993, Enhanced reservoir description using core and log data to identify hydraulic (flow) units and predict permeability in uncored intervals/wells: Society of Petroleum Engineers, Paper SPE 26436, 16 p.

Deutsch, C. V., and Journel, A. G., 1998, GSLIB, Geostatistical Software Library and User's Guide: New York, Oxford University Press, p. 145–146.

Geovariances, 2001, ISATIS reference guide: Avon, France, 531 p.

Grant, C. W., Goggin, D. J., and Harris, P. M., 1994, Outcrop analog for cyclic-shelf reservoirs, San Andres formation of Permian Basin: stratigraphic framework, permeability distribution, geostatistics, and fluid-flow modeling: American Association of Petroleum Geologists Bulletin, v. 78, no. 1, p. 23–54.

Hristopulos, D. T., and Christakos, G., 1999, Renormalization group analysis of permeability upscaling: Stochastic Environmental Research and Risk Assessment, v. 13, p. 131–160.

Isaaks, E. H., and Srivastava, R. M., 1989, An introduction to applied geostatistics: New York, Oxford University Press, 561 p.

Jennings, J. W., 2000, Spatial statistics of permeability data from carbonate outcrops of West Texas and New Mexico: implications for improved reservoir modeling: The University of Texas at Austin, Bureau of Economic Geology Report of Investigations No. 258, 50 p.

Jennings, J. W., Jr., and Lucia, F. J., 2001, Predicting permeability from well logs in carbonates with a link to geology for interwell permeability mapping: Society of Petroleum Engineers, Paper SPE 71336, 16 p. and featured synopsis: Journal of Petroleum Technology, v. 53, no. 11, p. 42–43.

Jennings, J. W., Jr., Ruppel, S. C., and Ward, W. B., 2000, Geostatistical analysis of permeability data and modeling of fluid-flow effects in carbonate outcrops: Society of Petroleum Engineers Reservoir Evaluation and Engineering, v. 3, no. 4, p. 292–303.

Kerans, C., Lucia, F. J., and Senger, R. K., 1994, Integrated characterization of carbonate ramp reservoirs using outcrop analogs: American Association of Petroleum Geologists Bulletin, v. 78, no. 2, p. 181–216.

Lucia, F. J., Kerans, C., and Senger, R. K., 1992, Defining flow units in dolomitized carbonate-ramp reservoirs: Society of Petroleum Engineers Annual Meeting, Washington, D. C., SPE 24702, p. 399–406.

Noetinger, B., and Jacquin, C. G., 1991, Experimental tests of a simple permeability composition formula: Society of Petroleum Engineers, Paper SPE 22841, 8 p.

Senger, R. K., Lucia, F. J., Kerans, C., Fogg, G. E., and Ferris, M. A., 1993, Dominant control on reservoir-flow behavior in carbonate reservoirs as determined from outcrop studies, *in* Linville, W., ed., Reservior Characterization III: Proceedings, Third International Research Characterization Conference, Tulsa, Oklahama, p. 107–150.

Zimmerman, D. L., 1993, Another look at anisotropy in geostatistics, Mathematical Geology, v. 25, no. 4, p. 453–470.

NOMENCLATURE

Variables

c	=	semivariogram-model sill parameter
d_x, d_y, d_z	=	moving average weight function ellipsoid dimensions
f	=	moving average 1-D weight function
h	=	scaled distance from moving average target to datum location
k	=	permeability
k_{eff}	=	effective permeability
k_g	=	geometric average permeability
k_h	=	horizontal permeability
k_v/k_h	=	vertical-horizontal permeability ratio
l	=	semivariogram separation distance or “lag”
n	=	number of data values for a moving average
n_{eff}	=	effective number of data values for moving statistics
n_i	=	number of well-log measurements in a flow-unit at a well
p	=	semivariogram-model range parameter
r	=	residual
s	=	moving standard deviation
v	=	a petrophysical variable
$\bar{v}$	=	moving average of v
w	=	moving average weight
w^d	=	moving average individual datum weight
w^f	=	moving average spatial weight function
x, y	=	map coordinates
z	=	stratigraphic vertical coordinate
α	=	moving average weight function exponent
β	=	“gamma” semivariogram model shape parameter
γ	=	semivariogram
ϕ	=	porosity
$\bar{\phi}$	=	moving average of porosity
σ^2	=	variance

Subscripts

0, 1, 2, 3	=	scaleup levels
a, b	=	first and second semivariogram model structures
g	=	grid point index
i	=	datum index
x, y, z	=	coordinate directions
ϕ	=	porosity

FRACTURE ANALYSIS OF CLEAR FORK OUTCROPS IN APACHE CANYON AND CORES FROM SOUTH WASSON CLEAR FORK FIELD

J. F. W. Gale, S. E. Laubach, R. M. Reed, J. G. Moros Otero, and L. Gomez

Bureau of Economic Geology
John A. and Katherine G. Jackson School of Geosciences
The University of Texas at Austin

TABLE OF CONTENTS

LIST OF FIGURES

LIST OF TABLES

ABSTRACT

Opening-mode fractures were characterized in Clear Fork Formation outcrops at Apache Canyon in the Sierra Diablo Mountains, and in cores from South Wasson Clear Fork field well 7531. Fractures are steeply inclined with respect to bedding, and most samples contain at least two sets of fractures. Fracture aperture sizes from sets in core and outcrop follow similar power-law distributions, indicating that outcrops are a good analog for the subsurface with respect to aperture-size distribution. Fracture spacing in outcrop follows negative exponential distributions. Fracture aperture-length relationships are power law, although correlation coefficients for these relationships are low. Strain associated with fracture extension, which was measured for outcrop examples, is typically around 0.007.

Fractures were observed using standard petrography and new SEM-based cathodoluminescence imaging techniques, and range from open to sealed. Cements in core fractures include dolomite and anhydrite, and cements in outcrop include dolomite and calcite. The calcite is most likely a late pedogenic deposit and thus unrelated to fracture attributes in the subsurface. This is an example of the importance of distinguishing-features in outcrops that may not be a direct analog for the subsurface from those that may be used successfully. In the subsurface, two processes control fracture pore-space preservation. The first is precipitation of authigenic dolomite on the fracture walls, which may seal fractures below the size emergent threshold and reduce the apertures and lengths of those fractures above the emergent threshold. The second is precipitation of authigenic anhydrite, which, because this cement is heterogeneously distributed, may leave open, partly seal, or completely seal fractures. The timing and distribution of different phases of dolomite and anhydrite precipitation with respect to fracturing are not yet fully understood.

INTRODUCTION

Fracture analysis of Clear Fork Formation outcrops and core samples is an important part of the wider project covered in this report, because fluid flow in the reservoir is affected by fracture systems (Philip and Jennings, this report). The intensity, spatial architecture, and openness of fracture sets, and the relationship between fracture sets and the diagenetic history of

the rock have been characterized. The approach of this study was to use outcrop data to better understand the subsurface. The use of outcrop fracture systems as subsurface analog is valid only when (1) fractures formed in the subsurface and are not related to uplift, exhumation, or weathering; (2) it is appreciated that the diagenetic and structural history of outcrops is different from that in the subsurface region of interest. Outcrops that have had similar histories to subsurface rocks until uplift—for example, in maximum burial depth—should provide the closest match to the subsurface. In this outcrop study we used fractures that are filled or partly filled with cements that in part match those found in core. Fracture patterns in the outcrop are thus probably reasonably good analogs for those in the subsurface.

GENERAL FRACTURE OBSERVATIONS

The fractures we analyzed in both core and outcrop are opening mode, or extension, fractures. They are mostly inclined at close to right angles to bedding, so that they are nearly vertical in flat-lying beds. In outcrop, sets are marked by consistent preferred orientations and several fracture sets, but we did not study orientation patterns in outcrop, and we did not have access to oriented core. It is likely, on the basis of observation of unoriented core, that more than one fracture set is present. Faults may also be present in outcrop, but these were not examined.

Extension fractures in both core and outcrop have a range of sizes, in terms of height, length, and aperture. However, most of the fractures we measured in outcrop have height and length dimensions of centimeters, and outcrop and core fractures have kinematic apertures of millimeters or less. Length cannot be measured effectively in core, and some height measurements in core are affected by truncation, as fractures pass out of the core. Thus, most of the fractures we examined are relatively small.

Fractures in both outcrop and core range from open to sealed. Cements in fractures in core include dolomite and anhydrite. Cements in fractures in outcrop include dolomite and calcite. At lease some of the calcite in fractures in outcrop appears to be a near-surface, late pedogenic deposit and thus unrelated to fracture attributes to be expected in the reservoir.

FRACTURE SCALING ANALYSIS—SIERRA DIABLO, APACHE CANYON OUTCROP

Extension fractures are known to exist at a range of scales in many rocks, and it has been shown that aperture size distributions of fracture populations follow power laws (Marrett and others, 1999). The value of this relationship is that it allows prediction of fracture intensity at scales not measured in a given sample. In using outcrop data to represent the subsurface we have an opportunity to collect data over much larger scales than is possible from cores. Outcrop data may be compared with data from core sample thin sections to calibrate results from the outcrop against the subsurface and to establish how representative the outcrop data are of fracture systems in the subsurface. In many situations, however, suitable outcrop analogs may not be available, and extrapolation of microfracture data collected from core samples may be the only source of fracture information. This study provides a means for validating the scaling approach because both core and outcrop are accessible.

Aperture-Size Distributions

The Apache Canyon outcrop in the Sierra Diablo Mountains (see Ruppel and others, this report) contains numerous fractures. We have collected fracture spacing and aperture values from four scanlines, constructed normal to the trend of the dominant fracture set. Only those fractures having partial or complete mineral fill were included in the study. The results show power-law scaling in fracture aperture-size distribution for scanlines 1, 3, and 4. Data from scanline 2 are best fit to an exponential function (fig. 1). The steeply negative slope (exponent of –1.94 in a power law), which is inconsistent with results from a scanline, its irregularity, and the fact that it spans less than one order of aperture magnitude, suggests that the sample is too small to provide a reliable distribution function. If the three largest aperture data points, which contribute to a censoring bias, are removed, the data may be fit to a power law with coefficient and exponent similar to the other scanline data. Scanlines 1, 3, and 4 indicate a consistent power law from different parts of the outcrops.

Fracture apertures are plotted against the position of each fracture along the four scanlines, to give a picture of the fracture distribution (fig. 2). Spacing between fractures was measured in each of the four scanlines, and the spacing size was plotted against cumulative

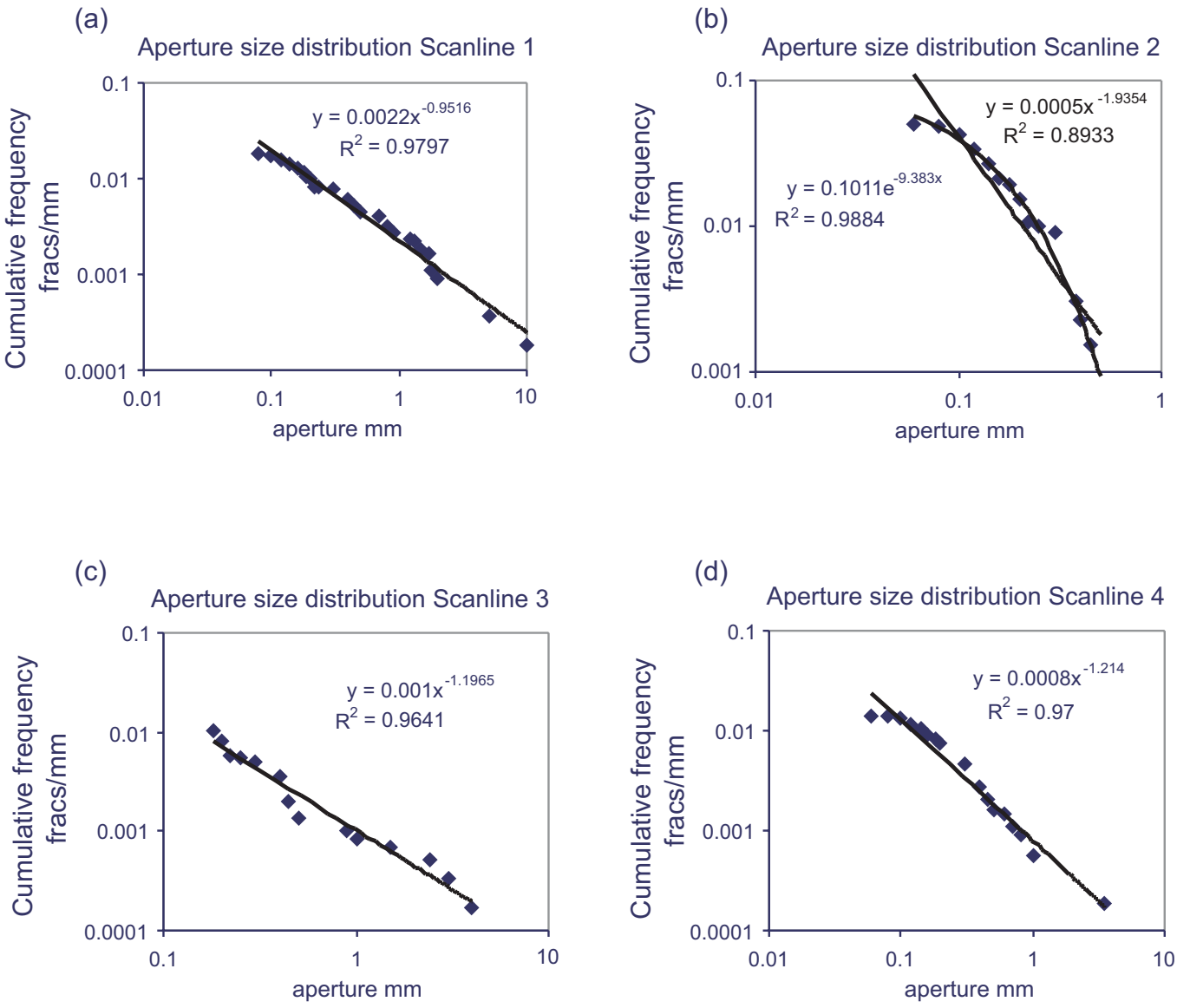

Figure 1. Aperture size distribution plots for scanlines 1–4 from Apache Canyon outcrops, Sierra Diablo. Diamonds represent data points, straight lines are power-law best fits to data. Power-law equations and correlation coefficients are given for each best fit. For scanline 2 the curve represents the exponential curve best fit, and the equation and correlation coefficient for this curve are also given.

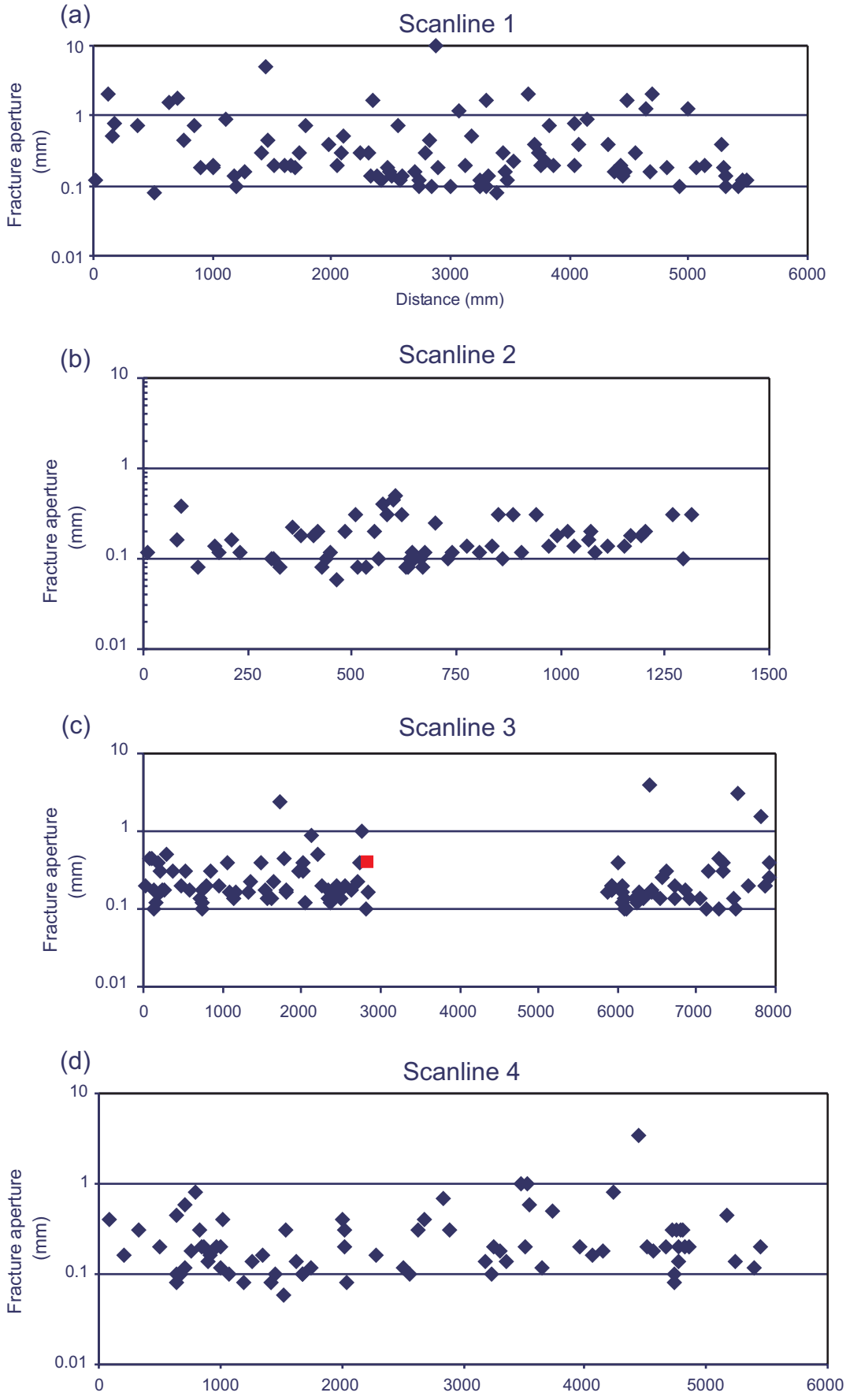

Figure 2. Plots of aperture size against position along the scanline for scanlines 1–4 from Apache Canyon outcrops, Sierra Diablo. The break in scanline 3 represents two subsets of data, collected along this line.

number. Fracture spacing size distributions for fractures in the Apache Canyon scanlines are best fit to negative exponential functions (fig. 3).

Fracture Connectivity

Fracture connectivity was addressed by comparing independent fracture length and aperture measurements. Such a relation would permit length estimates to be made from aperture measurements in boreholes (where fracture lengths cannot be determined directly because they exceed the borehole diameters). The possibility of overlapping fractures linking in en echelon arrays is enhanced with longer fractures. Fracture length affects fluid-flow pathways because longer fractures are more likely to overlap with other fractures, minimizing flow through unfractured host rock.

As part of a wider study, Moros (1999) examined variation in fracture aperture along fracture length by measuring the kinematic aperture of the fracture at centimeter intervals along the fracture length. Fractures in Clear Fork dolostone were divided into three categories, isolated, en echelon, and linked. Most isolated fractures were found to have aperture profiles with a flat but irregular plateau along most of the fracture length with sharp aperture gradients near the tips (fig. 4a). Some isolated fractures have a distinct maximum aperture near one fracture tip. Fractures with a symmetrical profile where the maximum aperture is close to the fracture center were the least common and were not found in outcrop. For en echelon fracture arrays Moros (1999) analyzed the profiles as separate fractures and then amalgamated the apertures in the overlapping zone. The results using amalgamated apertures were that the overlapping zone was a flat, irregular plateau, with sharp gradients at the array ends (fig. 4b). Fewer fractures had asymmetrical profiles, and very few had symmetric profiles with a distinct maximum. The linked fractures showed a similar range of profiles to the en echelon arrays.

SEM-Based Cathodoluminescence Imaging

Samples collected from the Apache Canyon outcrop were made into polished sections and were carbon coated in preparation for SEM-based cathodoluminescence (SEM-CL or scanned CL). The objectives of this stage of the study were (1) to examine the fracture fill and wall rock for more detailed information on relative timing of fracturing and different cements

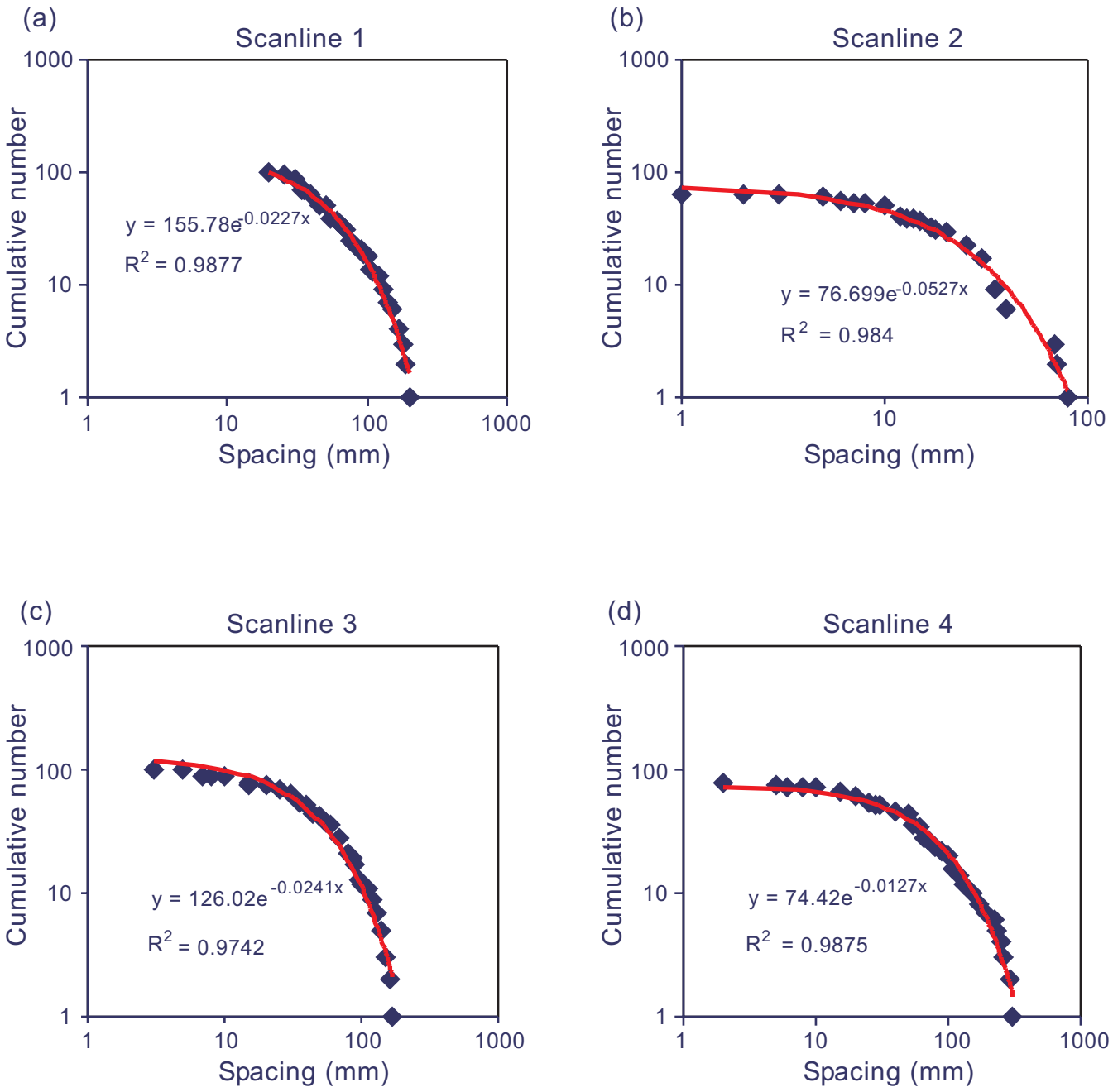

Figure 3. Fracture spacing size distribution plots for scanlines 1–4 from Apache Canyon outcrops, Sierra Diablo. Diamonds represent data points, curves are best-fit negative exponential functions. Equations and correlation coefficients are given for each curve.

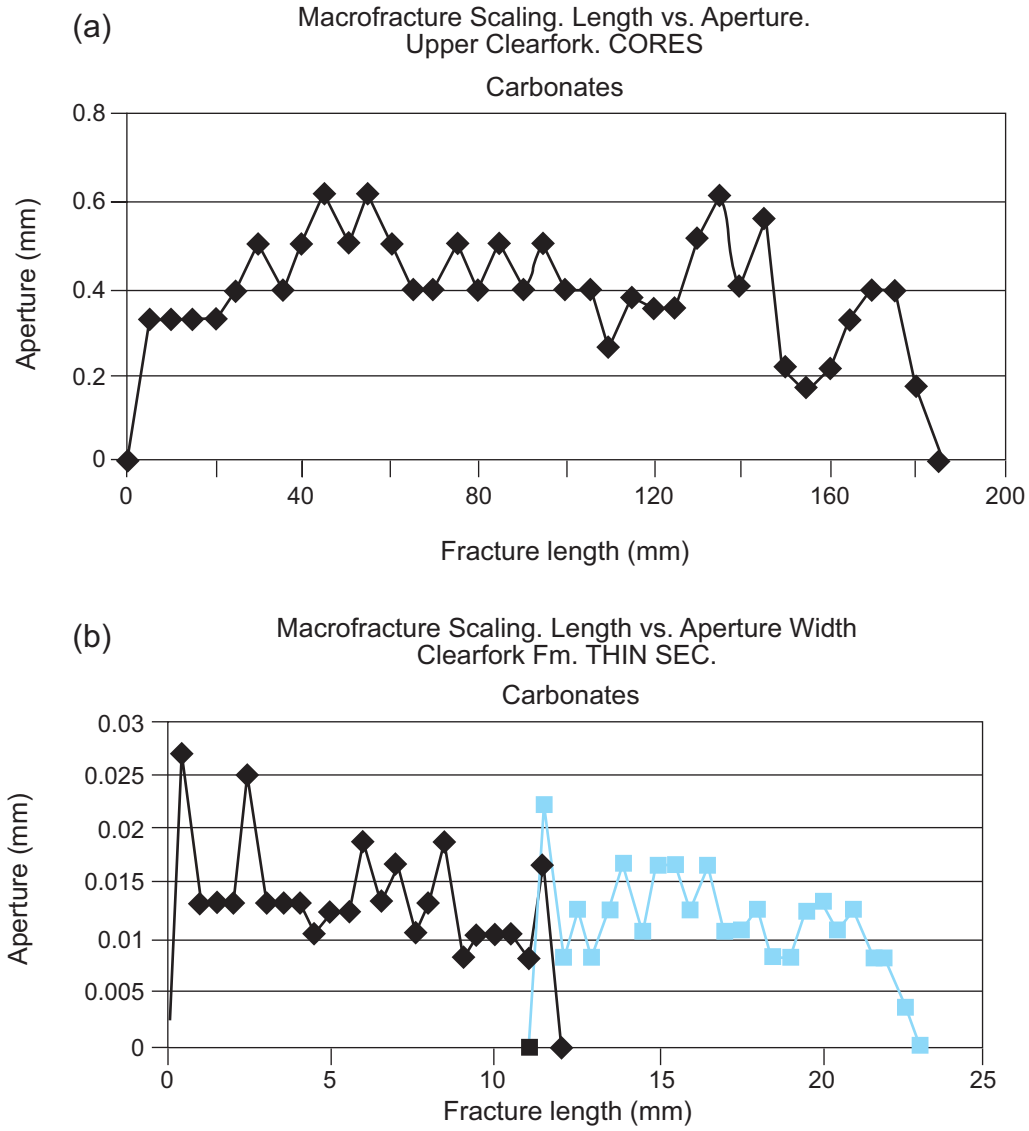

Figure 4. Variation of aperture along fracture length from Apache Canyon. (a) Typical aperture profile for a single segment fracture showing a "plateau" of aperture sizes in the fracture center, with rapid decreases in aperture at each tip. (b) Two segments of an en echelon fracture pair. Individually, the segments behave as for (a), but when summed the overlapping region has a total aperture similar to that of the central portions of each segment, implying opening strain is "shared" between the two fractures.

within the fractures and the host rock and (2) to detect microfractures not observed using conventional petrography. Both objectives rely on the different cement phases having different luminescence properties in order for the fracture relationships to be clear. Many microfractures are not apparent using conventional imaging methods but can be quantified using SEM-CL (Milliken and Laubach, 2000). New imaging methods are being applied and tested to push the size of microfracture that can be accurately measured to smaller sizes. As part of this study we discovered that the use of certain filter combinations in SEM-CL imaging permits features to be observed that are not apparent by any other CL method for certain carbonate rocks (Reed and Milliken, in prep.). However, these advances have not overcome all of the challenges of imaging microstructures in carbonate rocks, and microstructures in Clear Fork dolostone mostly cannot be delineated clearly.

CL observation of dolomite cement lining fracture porosity along macroscopic fracture walls in Clear Fork dolostone reveals cements that have luminescence signatures that are close to that of the authigenic dolomite cement of the rock mass. Owing to a tendency for smaller microfractures to be entirely sealed with the same cements that line large fractures, this observation shows that microfractures, if present, will have luminescence that is very similar to that of the host rock. Much of the dolomite from the Apache Canyon samples thus has very few features visible under SEM-CL, although a few partly open microfractures were observed (fig. 5, sample AC-62-1645).

Crack seal is a deformation mechanism where small increments of extension repeatedly occur across a planar discontinuity, followed by repeated sealing by cement. Crack-seal texture records fracture opening history marked by progressive reopening and filling of breaks within fill as fractures grow. Crack-seal texture is compatible with cement precipitation that is broadly episodic or essentially continuous. No clear evidence of crack seal was observed, but in a few cases, evidence of different phases of dolomite cement was observed by comparing the CL image with a secondary electron image (SEI) (fig. 6a, b). Zoned cements in crystals growing on the original fracture wall have distinctly darker luminescence than the paler dolomite in the fracture walls and the dolomite growing into the center of the fracture as euhedral crystals. Fracture porosity clearly shows up in the SEI as dark areas, whereas in the CL image it is difficult to distinguish low luminescence from porosity.

(a)

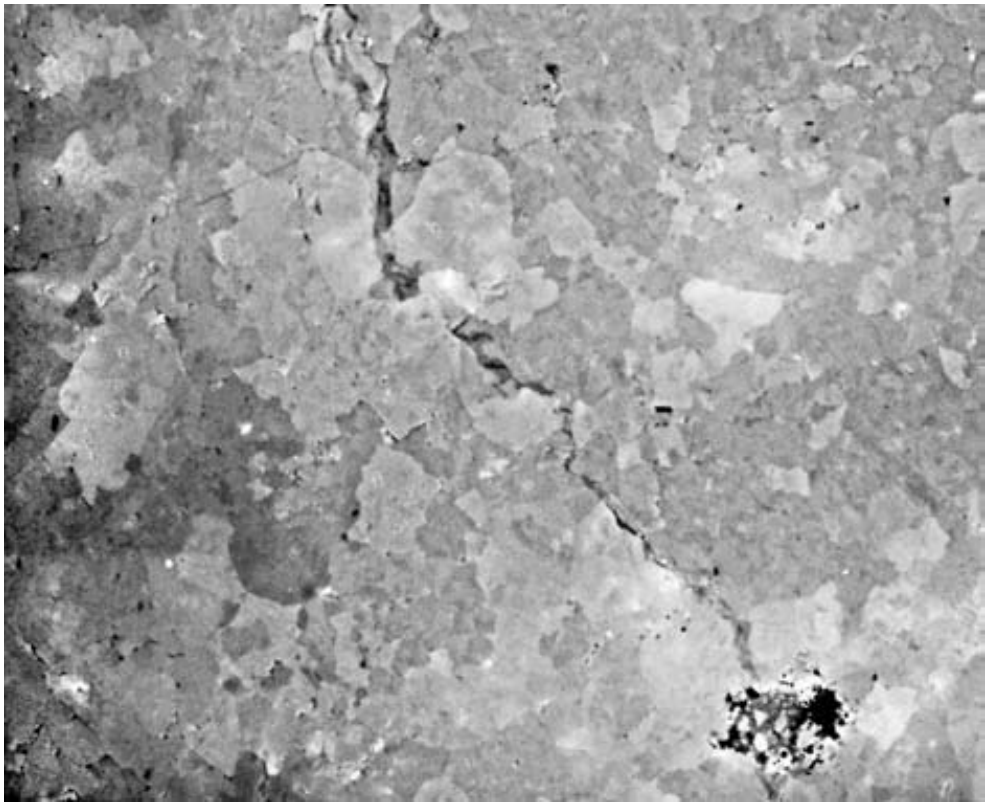

(b)

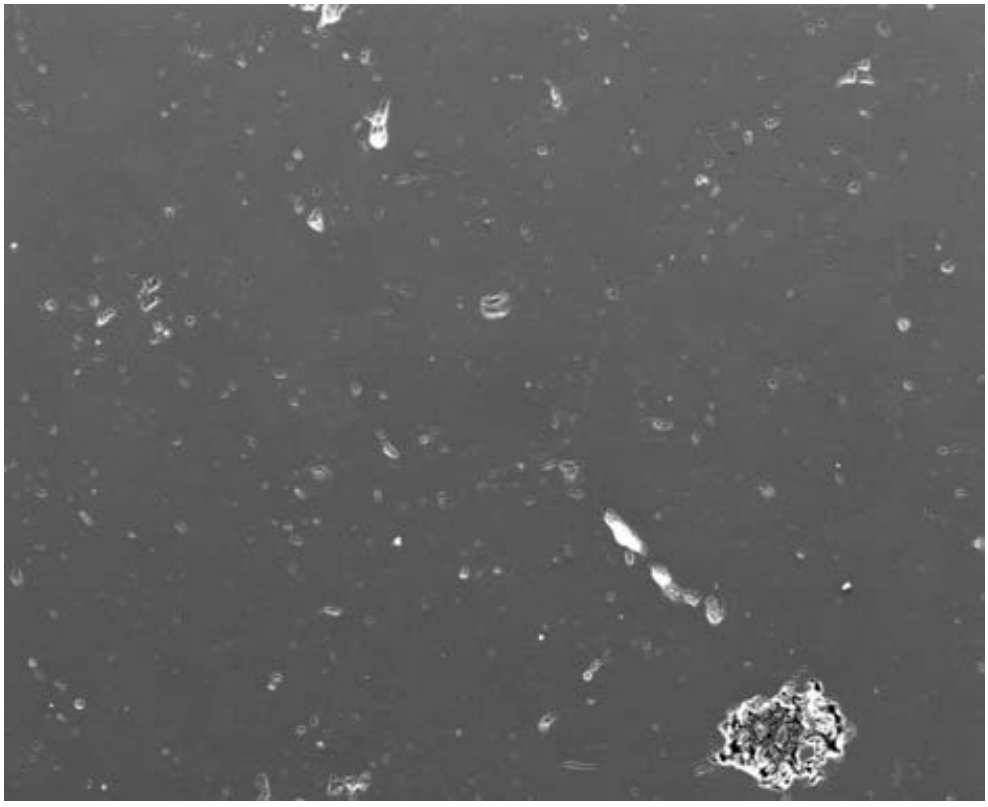

Figure 5. (a) SEM-CL image of sample AC-62-1645 from Apache Canyon, showing two approximately orthogonal fractures. (b) Secondary electron image (SEI) of the same field of view as the image in (a). The SEI shows the areas of porosity (elongate white areas). If the two images are compared it can be seen that the majority of the larger fractures and all of the smaller fractures are filled with cement. Width of images is ≈0.7 mm.

(a)

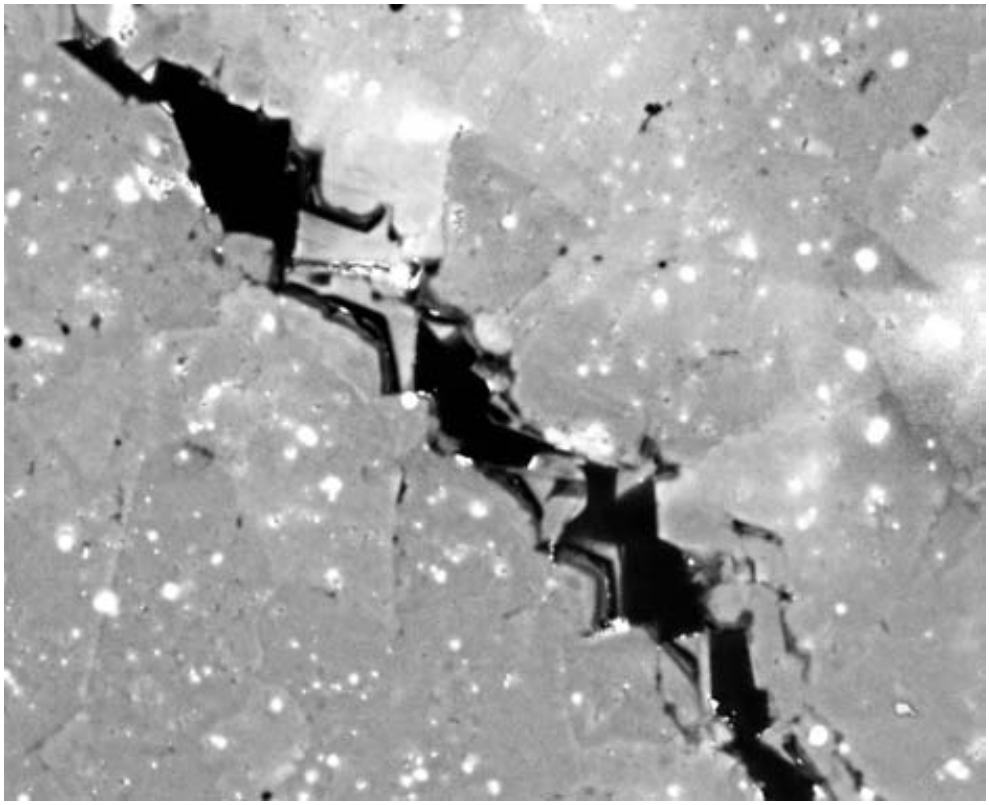

(b)

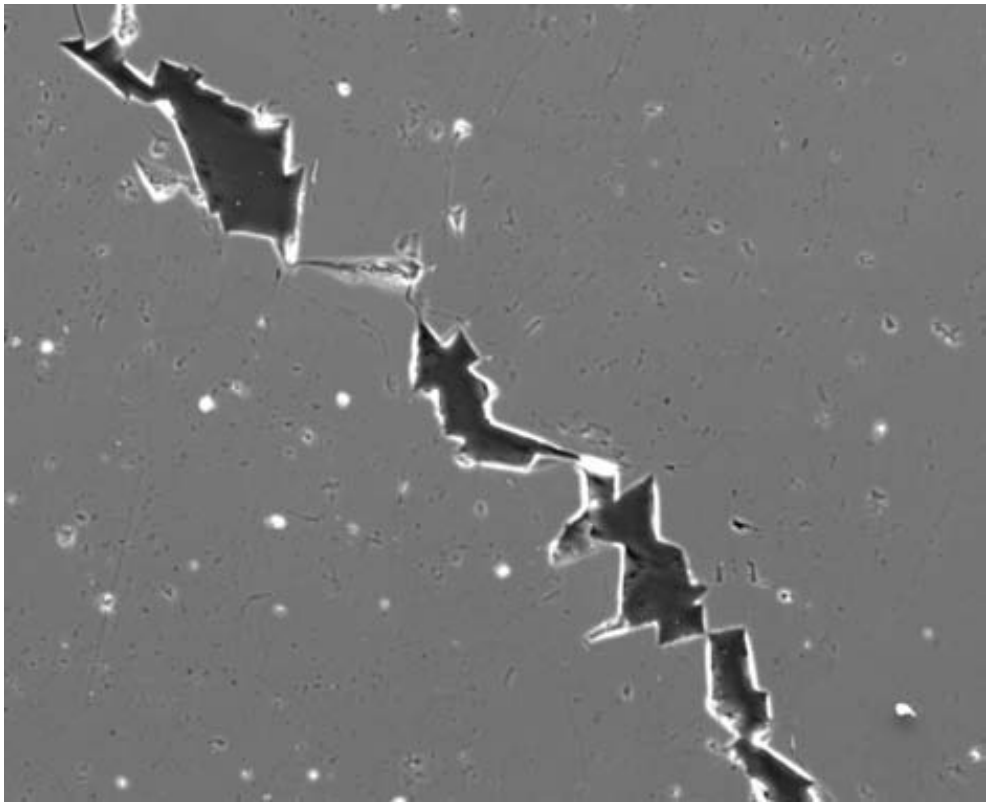

Figure 6. Microfracture in sample AC-62-6951 from Apache Canyon. (a) SEM-CL image showing zoned cement in euhedral crystals growing into the fracture. (b) SEI of the same field of view as (a) showing the remaining fracture porosity (gray areas). Width of images is ≈0.7 mm.

Cement spans some fractures, forming mineral bridges that range from isolated, narrow pillars to wide, semicontinuous masses having contact areas on fracture walls of tens of square millimeters or more. Bridges mark mineral growth sufficient, locally, to connect opposite fracture walls. Intact bridges are evidence of cessation of fracture widening; more fracture growth would have broken the bridge. In general, bridges in fractures result from incomplete cement fill in static fractures because of cement precipitation in opening fractures.

FRACTURE SCALING ANALYSIS—SOUTH WASSON CLEAR FORK FIELD

An extensive data set was collected from South Wasson Clear Fork (SWCF) well 7531 core (tables 1 and 2). Thin sections from SWCF well 7531 were examined using standard petrographic techniques to establish lithologies and determine whether macrofractures and microfractures are present. Selected samples were then examined using SEM-based cathodoluminescence, to look for microfractures not visible with conventional light microscopy, and to determine details of fracture fill and dissolution relative to diagenetic events. The number of fracture sets at each depth; their relative timing, degree, and type of mineral fill were determined. If sufficient numbers of microfractures were present a fracture scaling analysis was attempted to calculate fracture intensity across a range of aperture sizes. A detailed structural-diagenetic history was established for the samples, and pre-, syn- and postkinematic cements were identified. Samples were point-counted with a view to calculating a measure of the amount of postkinematic cement available to seal open fractures, the "degradation index ." Degradation index work is reported separately in the section Fracture Quality. The SWCF field is mostly dolostone with a few beds of dolomitic siltstone.

South Wasson Clear Fork Dolostone

Dolostones from well 7531 are mud-dominated dolopackstones, grain-dominated dolopackstones, dolograinstones, and dolowackestones. Many of the sections have macrofractures, with apertures as wide as 0.5 mm, visible using conventional light microscopy. Fractures are lined with authigenic dolomite. Some fractures are partly or wholly filled with anhydrite cement (fig. 7a, sample 6350), whereas others are open and lack anhydrite. Typically, the open part of these fractures varies with the composition of the wall grains, being wider where

Table 1. Thin-section analysis spreadsheet for samples from the South Wasson Clear Fork well 7531.

WELL	DEPTH	DOLOMITE		CALCITE	SULFATE		QUARTZ		TEXTURE	PARTSIZE	%IP	Psv		Ptv	Class	DEGRADATION	
	ft	%	Size	%	%Anh	Type	%	Size	Name			%Psv	Type	Type			
7531	5908.16	97.3	25	0.7	2	PO			MDP	25	2.5	1.2	MO	FR	2	35.1	
7531	5911.50	95	30		5	PO			MDP	30	2.5	0.6	MO	FR	2	61.7	
7531	5929.20	98.8	30		1.2	PO			GDP	180	4	1.7	MO		2	17.4	
7531	5956.20	90	30		10	PO			MDP	30	4	0.5	MO	FR	2	69.0	
7531	5972.30	88	40		12	PO			W	40	1.5	0.6	MO	FR	2	85.1	
7531	6024.00	82.8	25		17	PO-FB	0.2	70	GDP/MDP	200	4.5	0.5	MO-IG	FR	2	77.3	
7531	6042.80	95	40		5	PO			MDP	40	2	0.3	MO	FR	2	68.5	
7531	6048.90	86.7	25		13	PO	0.3	40	GDP/MDP	120-25	5	0.8	MO-IG	FR	2	69.1	
7531	6091.10	92	60		8	PO			GDP	>600	3.5	2.5	IG	FR	2	57.1	
7531	6107.80	85	20		15	PO			GDP	180	5	1.2	MO	FR	2	70.8	
7531	6159.50	88	20		5	PO	7	45	W	20				FR	3	100.0	
7531	6120.60	62	30		35	PO	3		W	30	0.5			FR	2	98.6	
7531	6134.70	8			2	PO	90	80	Siltstone	80						100.0	
7531	6141.70	76	40		18	PO	6	60	MDP	40	4.5			FR	2	80.0	
7531	6155.70	43.5	35		55	PO-FB	1.5	60	MDP	35					2	100.0	
7531	6112.30	95	35		5	PO			GDP	210	6	0.3	MO		2	44.2	
7531	6180.30	94	40		6	PO			MDP	40	3	1.5	MO		2	57.1	
7531	6184.50	61.5	45		37	PO	1.5	50	MDP	45	1.5	1	MO		2	93.7	
7531	6208.11	94	40-10		5	PO-FB	1	60	MDP	40-10	3.5	1	MO	FR	2	52.6	
7531	6219.10	76.2	40		23	PO	0.8	50	GDP/MDP	40	5.5	1.5	MO-IG			76.7	
7531	6237.40	93.5	35		6	PO	0.5	60	GDP	240	9	1.6	MO-IG		2	36.1	
7531	6243.20	71	35		29	PO-FB			GDP/MDP	240-35	5	0.5	IG	FR	2	84.1	
7531	6251.80	92.5	30		6	PO	1.5	50	W	30	3	1.6	MO	FR	2	56.6	
7531	6257.70	87.5	30		12	PO-FB	0.5	50	W	30	2.5	1	MO	FR	2	77.4	
7531	6260.10	61.4	50		38	PO-IF	0.6	50	GDP	>600	1.8	0.5	IG	FR	2	94.3	
7531	6273.70	94.5	25		5	PO	0.5	50	GDP	180	6	2	MO-IG	FR	2	38.5	
7531	6279.20	96	45		4	PO			W	45	2.5	2.5	MO	FR	2	44.4	
7531	6306.50	99.4	50		0.6	PO-IF			GDP	>600	6	3.5	IF	FR	2	5.9	
7531	6313.80	94.5	35		5	PO	0.5	50	GDP	20	7	1.5	MO-IF		2	37.0	
7531	6318.10	93	45		6	PO	1	50	W	45	2.5	1.2	MO	FR	2	61.9	
7531	6332.80	83.5	60		15	PO	1.5	50	MDP	60	4.5	2	MO	FR	2	69.8	
7531	6350.10	92.5	40		6.5	PO	1	50	W	40	2.5	0.8	MO	FR	2	66.3	
7531	6378.11	76.5	40		23	PO	0.5	40	GDP	200	10	1.2	IG		2	67.3	
7531	6401.20	72	100		28	PO-FB			GDP	350	7.5	3.5	IF-MO	FR	1	71.8	
7531	6405.50	84.5	80		15	PO	0.5	50	GDP	400	9	1.5	MO	FR	2	58.8	
7531	6430.30	91	40		9	PO-FB			W	40	2	1.5	MO	FR	2	72.0	
7531	6440.10	65	80		35	PO			MDP	80	5.5	2	IF-MO		2	82.4	
7531	6461.30	98	80		2	PO			W	80	2	0.6	MO	FR	2	43.5	
7531	6486.10	97	100		3	PO			GDP	240	16	1.2	MO-IG		1	14.9	
7531	6489.10	97	120		3	PO			GDP	120	15	1	MO		1	15.8	
7531	6505.60	99	70		1	PO			MM	70	0.8	0.6	MO	FR	2	41.7	
7531	6529.20	92	50		8	PO			MDP	50	2.5	0.8	IX	FR	2	70.8	
7531	6546.20	85	100		15	PO			GDP	500	13	2	IF	FR	1	50.0	
7531	6577.3	100	130						W	130	3	1.2	MO	FR	1		
7531	6607.6	85	>100		15	PO			MDP	>100	7	1	MO	FR	1	65.2	
7531	6870.7	98	110		2	PO			M	110	1.5			FR	1	57.1	
7531	6885.5	90.5	90		9	PO	0.5		W	90	3.5	3	MO	FR	2	58.1	
7531	6926.2	97.5	120		2.5	PO			M	120				FR	1		
7531	7088.1	64	25		36	PO-IF			G	250	18	10	MO-OMO		1	56.3	
7531	7127.3	50	25		50	FB			MDP	50		3.5	MO-IF		2	93.5	
7531	7190.4	96	60		3	PO	0.7	50	MDP	60	4	4	IF-MO	FR	2	27.3	

Table 2. Point-count data summary for samples from the South Wasson Clear Fork well 7531.

CLEAR FORK FM. - SOUTH WASSON
WELL # 7531
POINT COUNT SUMMARY

SAMPLE	WELL	DEPTH ft	DOLOMITE %	ANHYDRITE %	QUARTZ %	POROSITY %	OTHER %	CLASS	DEGRADATION
1	7531	5908.16	70	6.5	0.5	19	0	2	25.49
2	7531	5920.00	78.5	9.5	0	11	1	2	46.34
3	7531	5929.20	64	18.5	0	17.5	0	2	51.39
4	7531	5956.20	70.5	8	1	17	1	2	32.00
5	7531	5972.30	67	29.5	0	3.5	0	2	89.39
6	7531	6024.00	77	9	7.5	6.5	0	2	58.06
7	7531	6042.80	83.5	13	1.5	1.5	0.5	2	89.66
8	7531	6048.90	76.5	10.5	0	12	1	2	46.67
9	7531	6091.10	72.5	10	1.5	14.5	1.5	2	40.82
10	7531	6107.80	72.5	16.5	0	11	0	2	60.00
11	7531	6120.60	52.5	44.5	0	3	0	2	93.68
12	7531	6134.70	10	6	81.5	2.5	0	2	70.59
13	7531	6141.70	60.5	19	5.5	14	1	2	57.58
14	7531	6155.70	58	39.5	1	1.5	0	2	96.34
15	7531	6159.50	83.00	8.5	8.5	0	0	3	100.00
16	7531	6112.30	76	9	0	15	0	2	37.50
17	7531	6180.30	81	7.5	0	11.5	0	2	39.47
18	7531	6184.50	49	45	0	6	0	2	88.24
19	7531	6208.11	75.5	9	0	15.5	0	2	36.73
20	7531	6219.10	70.5	17	0	12.5	0	2	57.63
21	7531	6237.40	70.5	8	1.5	20	0	2	28.57
22	7531	6243.20	52.5	38.5	1	8	0	2	82.80
23	7531	6251.80	91.5	5	1	2.5	0	2	66.67
24	7531	6257.70	76.5	18	0.5	5	0	2	78.26
25	7531	6260.10	55.5	42.5	0.5	1.5	0	2	96.59
26	7531	6273.70	64.5	8	1.5	26	0	2	23.53
27	7531	6279.20	83	13.5	0	3.5	0	2	79.41
28	7531	6306.50	63	28	0.5	8	0.5	2	77.78
29	7531	6313.80	65.5	12.5	0	22	0	2	36.23
30	7531	6318.10	88.5	7	1	3	0.5	2	70.00
31	7531	6332.80	64.5	26.5	1.5	7.5	0	2	77.94
32	7531	6350.10	77	9.5	1	11.5	1	2	45.24
33	7531	6378.11	43.5	43	0	13.5	0	2	76.11
34	7531	6401.20	53	31.5	1	14.5	0	1	68.48
35	7531	6405.50	65.5	21.5	0	13	0	2	62.32
36	7531	6430.30	81	15	0	3.5	0.5	2	81.08
37	7531	6440.10	64.5	28.5	0	6.5	0.5	2	81.43
38	7531	6461.30	91	5	0	4	0	2	55.56
39	7531	6486.10	79.5	2	0	18.5	0	1	9.76
40	7531	6489.10	82	0.5	0	17.5	0	1	2.78
41	7531	6505.60	97.5	1	0	1.5	0	2	40.00
42	7531	6529.20	80.5	11	0	8.5	0	2	56.41
43	7531	6546.20	69.5	20	0.5	10	0	1	66.67
44	7531	6577.3	89.5	7	0	3.5	0	1	66.67
45	7531	6607.6	85.5	7.5	1	6	0	1	55.56
46	7531	6870.7	95.5	3	0	1.5	0	1	66.67
47	7531	6885.5	93	5	1	1	0	2	83.33
48	7531	6926.2	95.5	2.5	0	2	0	1	55.56
49	7531	7088.1	38.5	49	0	12.5	0	1	79.67
50	7531	7127.3	57.5	22	0	19.5	1	2	53.01
51	7531	7190.4	96	2	0	2	0	2	50.00

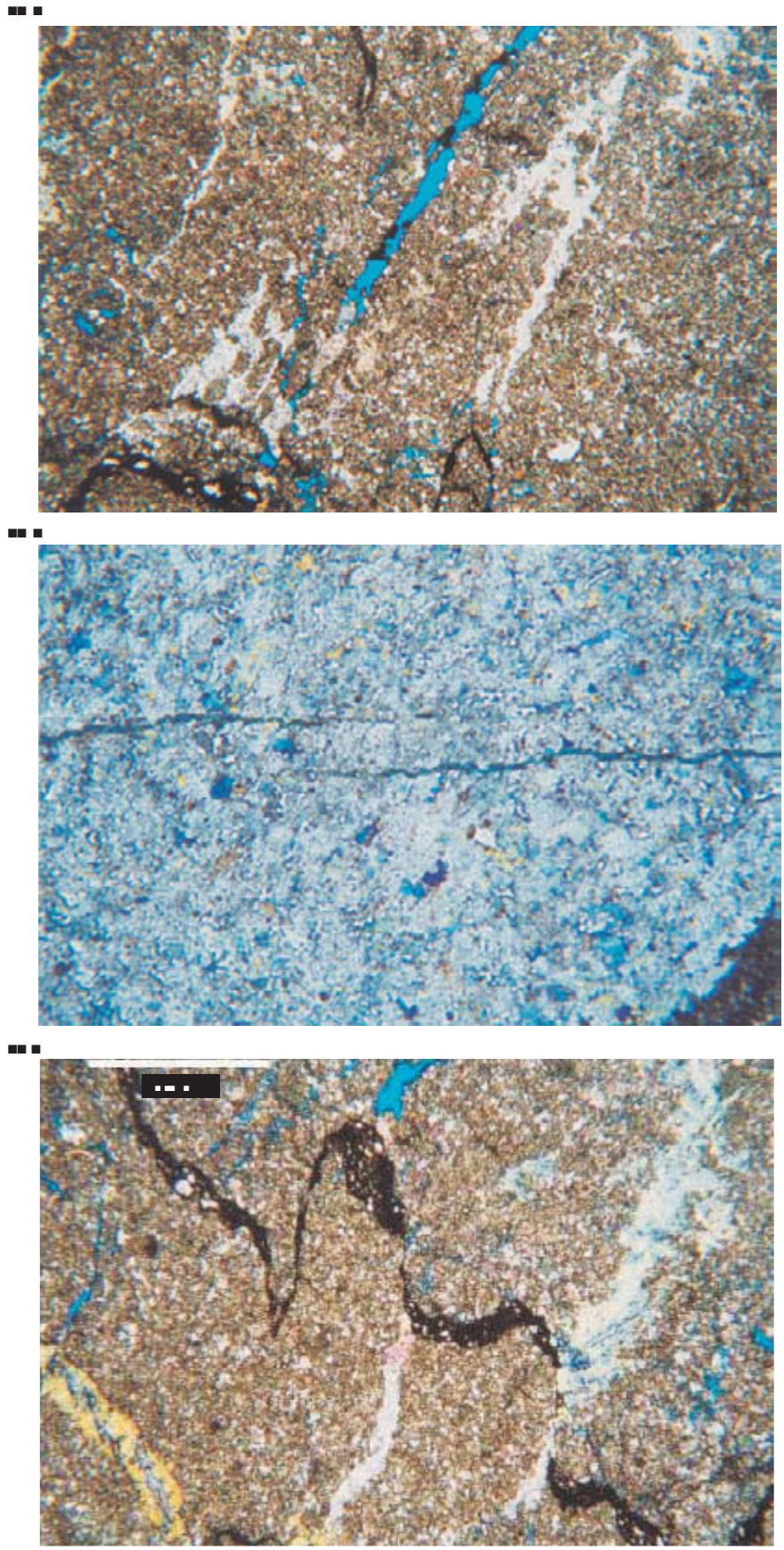

Figure 7. Photomicrographs of fractures from South Wasson Clear Fork field well 7531. (a) Sample 6350, fractures are partly or wholly filled with anhydrite cement, whereas others are open and lack anhydrite. (b) Sample 6024, a second fracture set, which has much less mineral fill, postdates anhydrite-filled fractures. Here, two en echelon fractures cut across poikilotopic anhydrite. (c) Sample 6350.1, anhydrite-filled fractures terminate or are displaced at a prominent stylolite. Scales for all photomicrographs as for (c).

the fracture cuts dolomite grains and narrower where the fracture cuts anhydrite grains (for example, sample 6430.3. Other fractures, which have much less mineral fill, appear to postdate the anhydrite-filled fractures (fig. 7b, sample 6024). Some fractures in this second set, F_2, have isolated euhedral-subhedral crystals of anhydrite growing in the fracture pore space.

In samples 6350.1 and 5956.2 there is considerable porosity in the rock, even though fractures are anhydrite filled. Fracture fill varies along the length of individual fractures. Fracture walls are poorly defined in the anhydrite-filled set. Poikilotopic anhydrite extends across the fracture-wallrock interface. Anhydrite-filled fractures also commonly terminate at stylolites, and opaque material is locally present in the fracture at or near stylolites (fig. 7c, sample 6350.1). Large anhydrite patches occur in sample 6024, and are broken by a series of en echelon, open fractures that track twin and cleavage planes in these crystals. In sample 5908.16 some fractures are dolomite lined and have anhydrite and dolomite bridges. These fractures are partly filled with postkinematic calcite.

The samples were not oriented, so although the relative timing and general characteristics of fractures could be established, there was no possibility of determining the orientation of the different fracture sets. Each thin section contains just a few macrofractures.

Unfortunately, unlike several other dolostones we have studied, dolostones in the Clear Fork Formation of the SWCF well 7531 appear to be largely indistinguishable in SEM-CL, and detailed observations of fracture relationships were limited. Some fractures are filled with anhydrite (section 4.1.1), but anhydrite is difficult to work with in SEM-CL because it takes a very poor polish and is commonly plucked. Anhydrite in the samples in this study has very high luminescence compared with dolomite but is otherwise featureless. Measurement of microfracture population size distributions in the dolostone samples was not possible using SEM-CL because of the sparse numbers of microfractures observed. It is possible that this is because microfracture intensities are low but equally likely that they could not be distinguished from the host rock they cut because of similarities in rock and fracture-fill luminescence.

South Wasson Clear Fork Siltstone

Although the microfractures could not be imaged in the dolostones, microfractures were found in a dolomite-cemented siltstone in sample 6138. This sample was selected for further

microfracture analysis. Previous work has shown that quartz-filled microfractures, which cut quartz grains, are readily imaged using SEM-based cathodoluminescence (SEM-CL). Difficulties in distinguishing fracture-filling dolomite from the host-rock dolomite in dolostone samples from this well meant that microfractures were not measurable in sufficient numbers to obtain population information. The siltstone sample provided an opportunity to obtain such information. Although fracture populations in the siltstone are not necessarily similar to fracture populations in adjacent dolostone units, they may be important locally for fluid flow. Results from the study are compared with scaling analysis results from dolostone outcrop samples.

Microfractures in sample CF2-38 from 6138 ft were imaged successfully in SEM-CL. A mosaic of images allowed a 2-D analysis of the fractures in a 3.4108-mm^2 area of the sample (fig. 8). Fractures were categorized according to the Laubach (1997) scheme, which distinguishes tectonic fractures (category I) from compaction-related and inherited fractures. These fractures were marked on the SEM-CL mosaic; 76 category I fractures were used for the fracture characterization. Fracture tips were picked on the digital image, and apertures and lengths were automatically recorded from these data. Fracture orientations, relative to the sample notch, which was unoriented, were plotted on a length-weighted rose diagram (fig. 9). The plot shows two orientation maxima—one with trends ranging from 320º to 360° "NNW" (in an arbitrary reference frame owing to the core not being oriented) and the other with trends ranging from 070º to 090° "ENE". Most microfractures in this sample are confined to single grains, and very few exhibit crosscutting relationships. Where two fractures do intersect, the relationships are mostly ambiguous, although there is one good example of a fracture in the "ENE" set that postdates a fracture trending "NE" (Fig. 8b). Fractures in the 'NNW' set are most abundant, 24 falling into this category, with just 5 fractures trending "ENE". There are relatively few fractures in other orientations.

Apertures of the 24 "NNW"-trending fractures were plotted on an aperture size distribution plot (fig. 10). The data were fitted to a curve that models a power-law "backbone" and two sampling bias errors at either end of the size spectrum, a truncation effect at the small aperture size range and a censoring effect at the large aperture size range. The best-fit curve provides a model power law for the population. This power law can then be used to predict the frequency of fractures having apertures larger than those measured. For sample CF2-38 this power law is

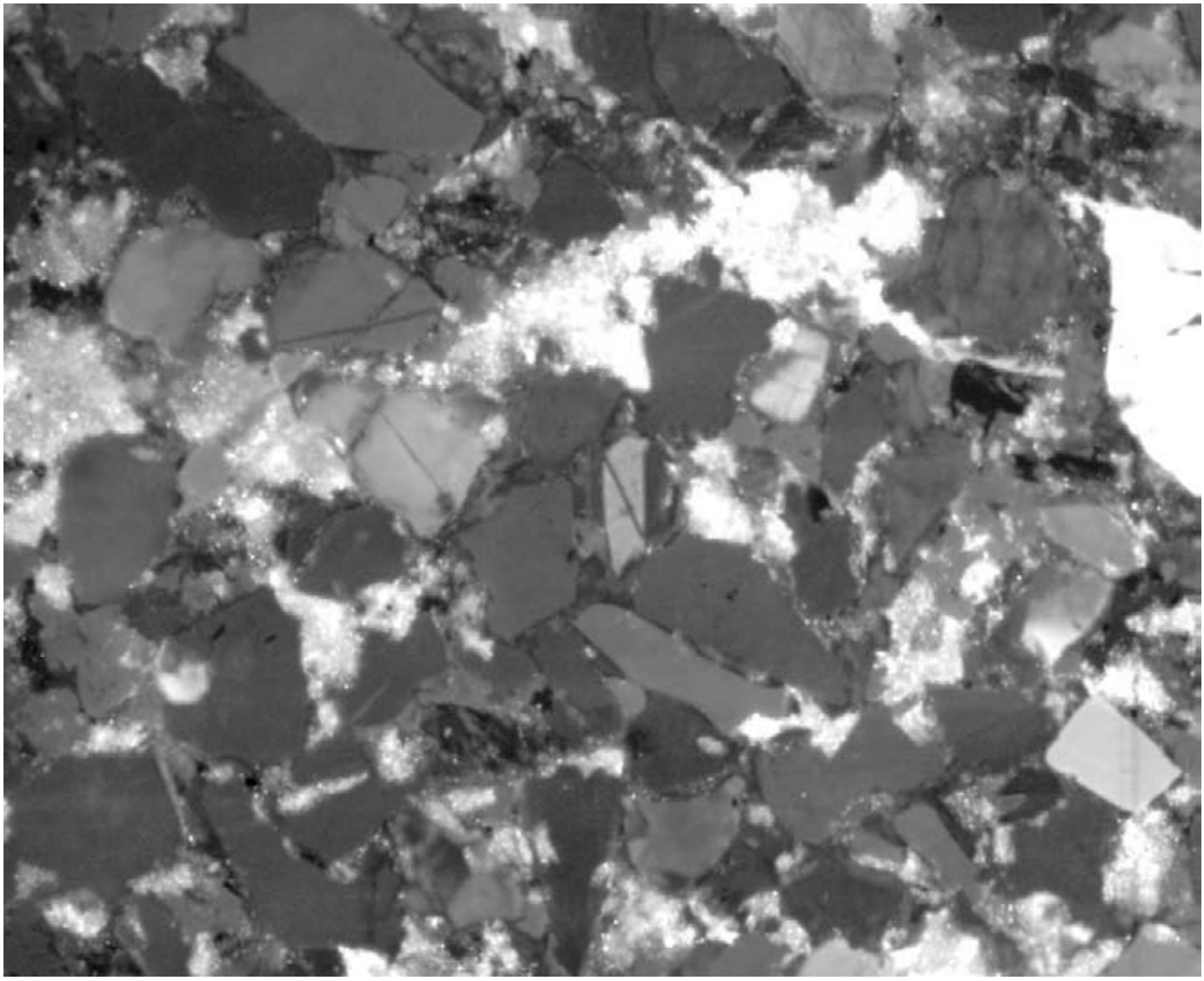

Figure 8. SEM-CL of siltstone sample CF2-38 from the South Wasson Clear Fork well 7531 showing crosscutting microfractures in quartz grains. A fracture trending “ENE” clearly crosscuts a fracture trending “NE”.

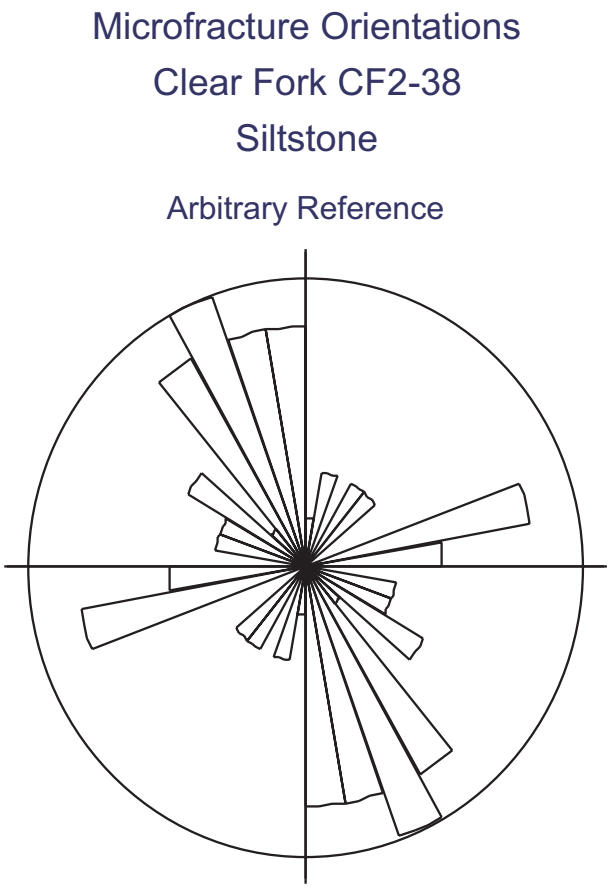

Figure 9. Rose diagram of category I fractures from siltstone sample CF2-38 , South Wasson Clear Fork well 7531. Orientations are with reference to an arbitrary direction, but the plot shows two clear maxima, one in the “NNW” direction and another in an “ENE” direction.

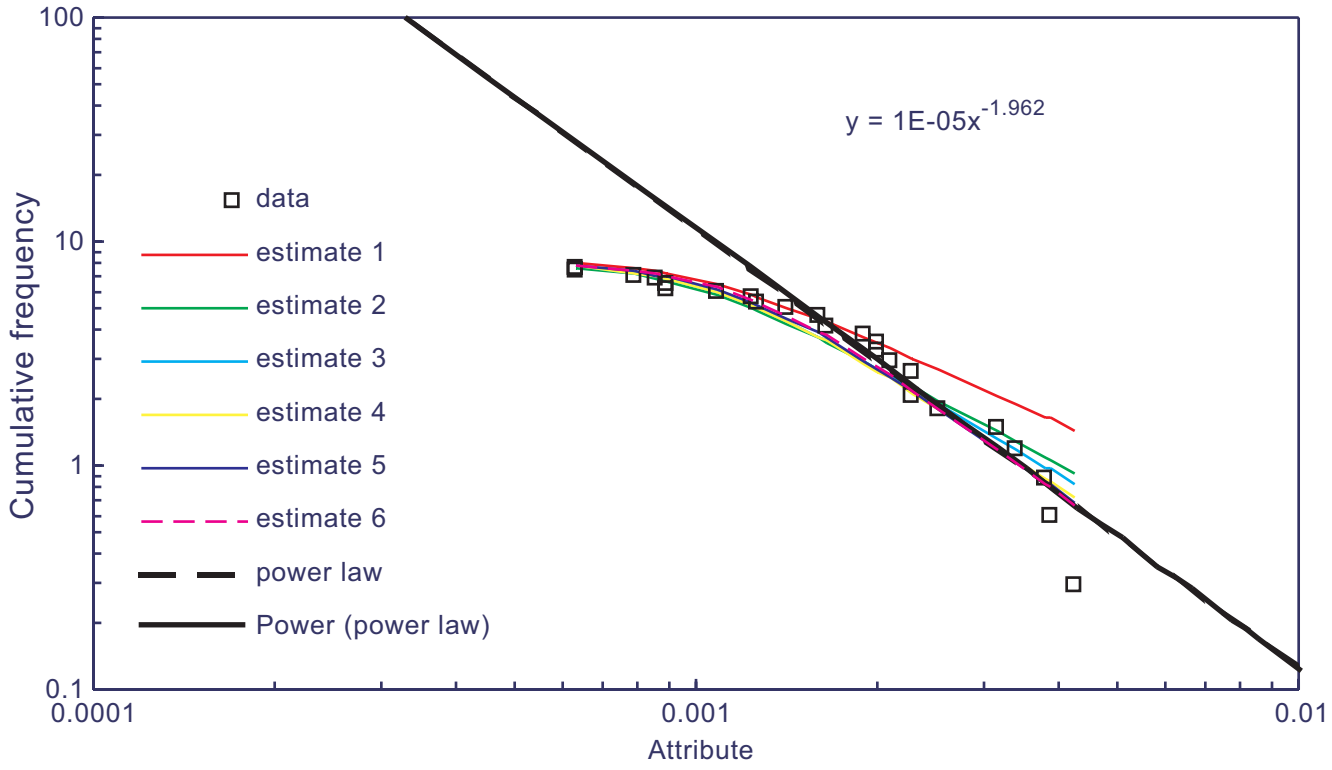

Figure 10. Aperture size distribution for fractures in the "NNW"-trending set from siltstone sample CF2-38, South Wasson Clear Fork well 7531. The curves are a bias regression model, with a power-law backbone, of the data. The equation for the power-law backbone is shown.

Frequency of fractures (fracs/mm2) = 1.49 × 10-5 aperture –1.962

For example, for fractures of aperture 1 mm and above, there would be 1.49×10^{-5} fractures/mm^2 or approximately 15 fractures/m^2. In order to compare the 2-D analysis above with the 1-D analysis, using scanlines, of the outcrops at Apache Canyon, the 2-D power-law must be converted to its 1-D equivalent. This involves conversion of both the coefficient and the exponent in the equation, according to the conversions described by Marrett (1996).

The exponent conversion requires a relationship between the length and apertures of the fractures. Length data are collected routinely as part of the microfracture analysis of SEM-CL images and can be utilized here. The length-aperture relationships of the "NNW" set of 24 fractures are shown in figure 11, with a power-law as follows:

$$\text{Aperture (mm)} = 0.0079 \text{ length (mm)}^{0.5193}$$

The correlation coefficient for the power-law best-fit function is very low at 0.1564. Using the exponent of this aperture-length relationship will give a poor conversion between topologies:

Following Marrett (1996)

$$|c_s| + 1/m = |c_T| + 2/m \qquad (1)$$

where c_s is the 2-D exponent of the frequency-aperture power law and c_T is its 1-D equivalent and m is the exponent of the aperture-length power law. Substituting the measured values for c_s and m into equation 1, c_T may be determined.

$$1.962 + 1/0.5193 - 2/0.5193 = 0.036$$

This is a very low positive value that is atypical of any scanline measurements we have obtained in other studies. It is likely that the aperture-length relationship is invalid. Fractures in other parts of the well 7531 show a tendency toward power-law relationships between length and aperture for fractures, although some of the correlations are rather poor (fig. 12). The majority of

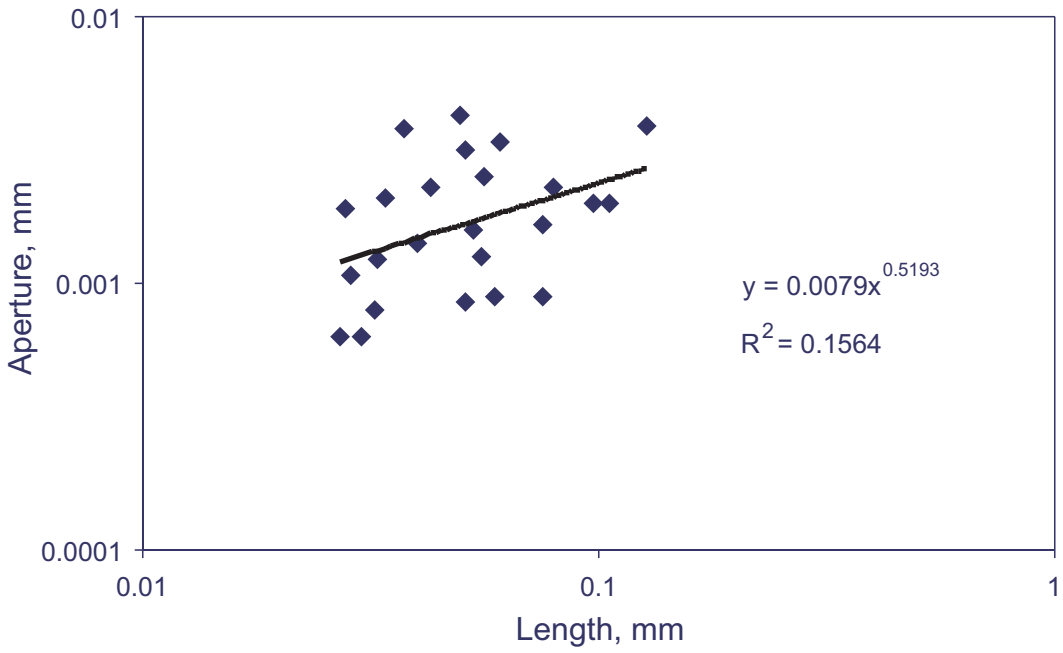

Figure 11. Length-aperture plot for fractures in the "NNW"-trending set from siltstone sample CF2-38, South Wasson Clear Fork well 7531. Data are shown as diamonds, the line is a best-fit power-law regression. The correlation coefficient is very low for this best fit.

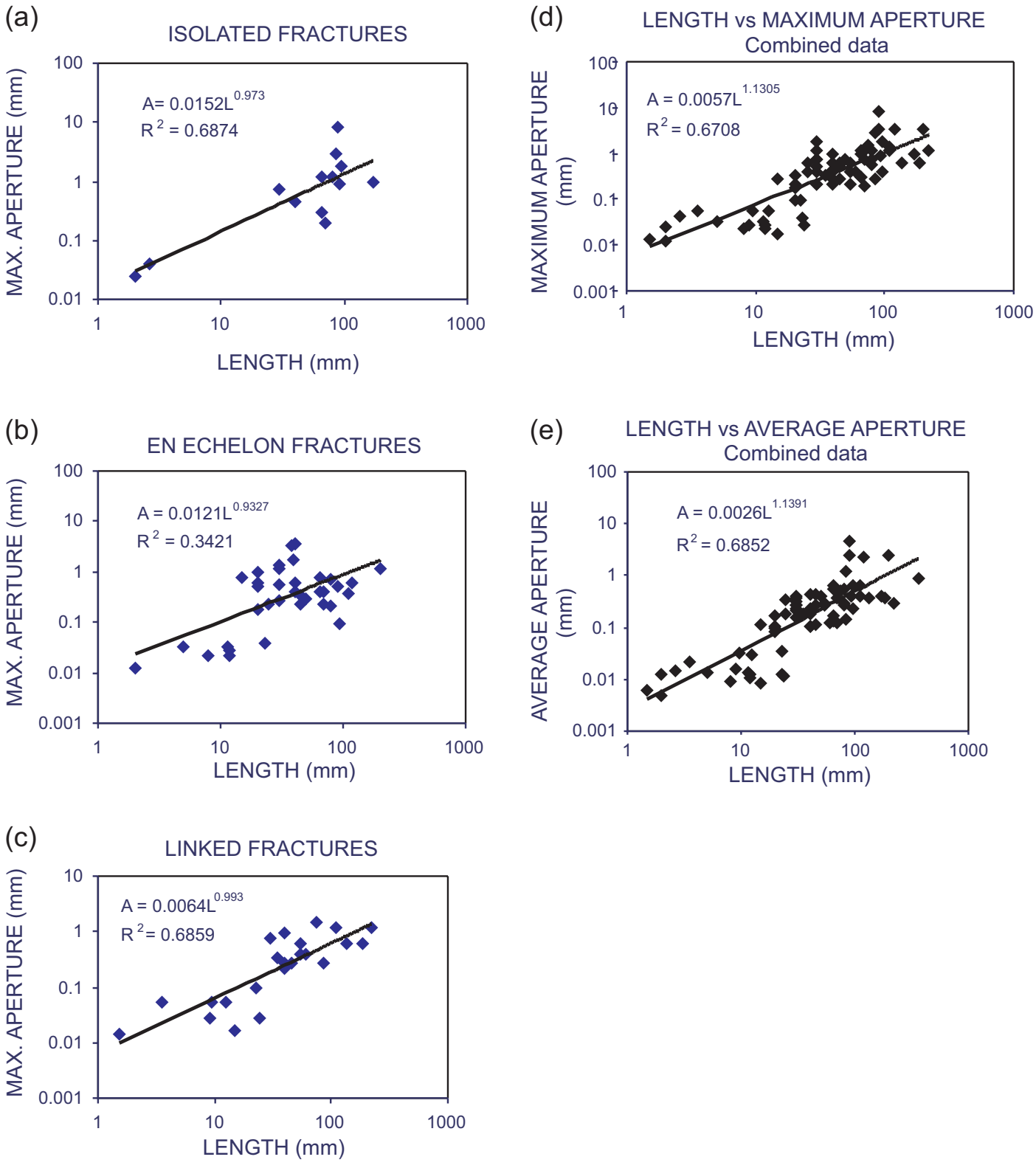

Figure 12. Length-aperture plots for fractures from core samples from South Wasson Clear Fork well 7531. (a), (b), and (c) are for individual fracture segments, en echelon sets, and linked systems, respectively. (d), (e) combined data showing power-law best fits for maximum aperture length and average aperture-length, respectively.

these plots indicate an exponent of approximately 1 for the power-law relationship, irrespective of whether fractures are present as individual segments, en echelon sets, or linked systems (fig. 12a, b, c). The power laws for maximum aperture versus length and mean aperture versus length are similar (fig. 12d, e). If we use an exponent of m = 1 for the aperture-length power law,

$$|c_T| = |c_s| - 1$$

so that 0.962 = 1.962 -1 and c_T would then be –0.962, which is close to many measured exponents.

Conversion of the coefficient is more problematic in that it requires knowledge of the fracture ellipticity; data not available in this case. If we assume a penny-shaped fracture, where ellipticity = 1, then the coefficient conversion is as follows:

$$a_s |c_s| g^{1/m} = 4\, a_T |c_T| g^{2/m} / \pi \qquad (2)$$

where a_s is the 2-D coefficient for the frequency-aperture power law and a_T is its 1D equivalent and g is the coefficient of the aperture-length power law. If we assume m = 1 then

$$\frac{(1.49\times10^{-5})(1.962)(7.9\times10^{-3})\pi}{(4)(0.962)(7.9\times10^{-3})^2} = a_T = 3.021 \times 10^{-3}$$

Thus the 1-D frequency-aperture power law would become

$$\text{Frequency (fractures/mm)} = 3.021 \times 10^{-3}\ \text{aperture (mm)}^{-0.962}$$

Fracture Quality

A critical observation is the timing between fracture formation and fracture- and pore-filling cements. Cements are classified with reference to the timing of cement precipitation relative to fracture opening; prekinematic, synkinematic, postkinematic cements, respectively, predate, are contemporaneous with, and postdate fracture opening. The width of fractures that are lined with synkinematic cement but that preserve fracture porosity with respect to synkinematic

cement is referred to as the "emergent threshold" (Laubach, in prep.). Dolomite appears to be the synkinematic cement in the SWCF, and the emergent threshold is about 100 microns. The main postfracture (postkinematic) cement is anhydrite.

Fracture quality is a measure of the extent to which large fractures have retained pore space. Microfractures are typically readily sealed owing to their small volumes relative to fracture surface area, but large fractures are more resistant to sealing. Although large fractures in Clear Fork dolostone are lined with authigenic dolomite, where these large fractures are sealed it is mainly by anhydrite. Because large fractures are sparse owing to inherent sampling limitations dictated by sampling vertical fractures using vertical wellbores, we used an indirect method or surrogate to infer fracture quality systematically throughout the core interval (Laubach, in prep.).

The quality of the fractures observed in SWCF cores is predicted by comparing the amount of postkinematic cements (anhydrite) with the amount of porosity plus postkinematic cement in the rock mass. This surrogate for fracture quality is called the degradation index (Laubach, in prep.). This index has been calculated for 49 samples, of which 8 had open fractures, 12 had partly filled fractures, 16 had filled fractures, and 13 had no fractures (fig. 13). Low degradation implies that large fractures or networks of fractures are open and capable of transmitting fluids.

Inspection of figure 13 shows that there is a range of degradation index values. Many of the samples having an index of less than 50 percent (high quality) have no fractures and therefore do not provide a test of the degradation index predictions, and there is no clear separation between open, partly open, and closed fractures. This is partly a reflection of two other factors. First, the fractures span a range of sizes, and the degree of postkinematic fracture fill is size-dependant. Second, crosscutting relations suggest that at least two sets of fractures are present. Moreover, crosscutting relations indicate that multiple generations of anhydrite precipitation have occurred. Some fractures transect (crosscut) anhydrite, whereas elsewhere the same fracture may contain anhydrite. This is consistent with previous diagenetic analysis of the Clear Fork that suggest that numerous episodes of sulfate precipitation and dissolution may have occurred (Lucia, pers. comm.). Unfortunately, these various generations of anhydrite can only be separated into a time sequence relative to fractures where they are in contact with the fractures, greatly reducing the efficacy of the surrogate.

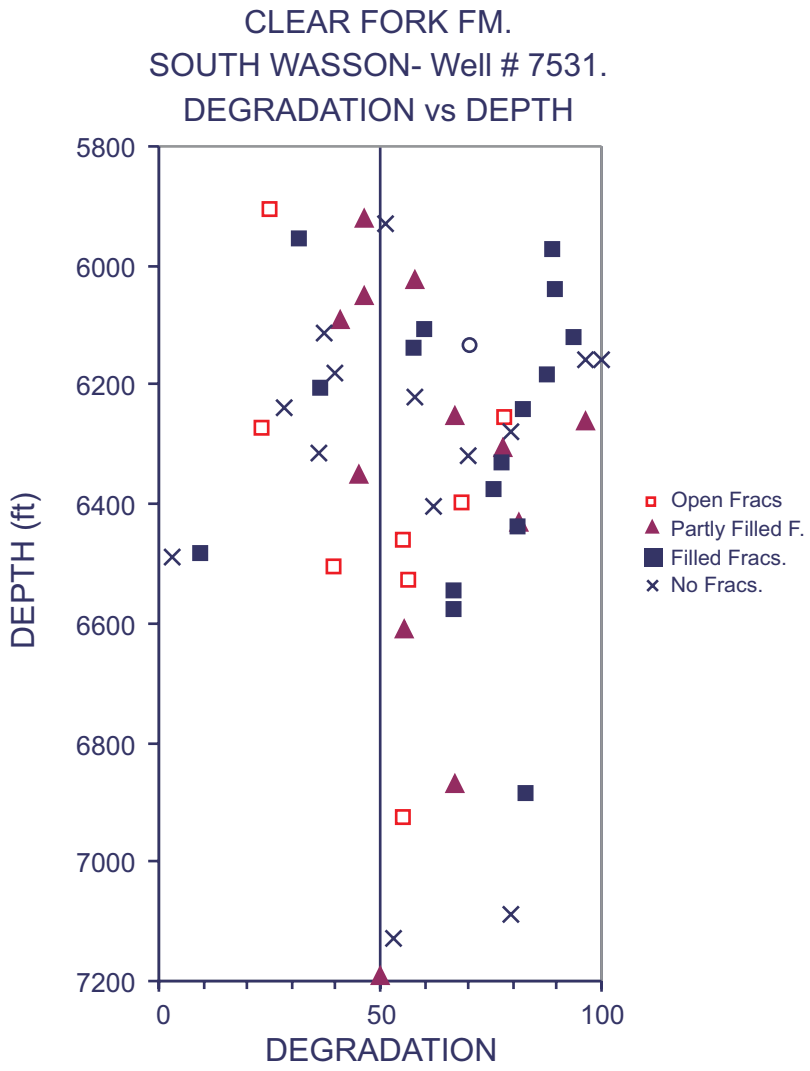

Figure 13. Depth plot of the degradation index from core samples of South Wasson Clear Fork well 7531. Degradation index is the ratio of postkinematic cement (anhydrite) to postkinematic cement plus pore space.

From the fracture analysis we conclude that where the fractures are filled, most fractures in the SWCF reservoirs are filled with anhydrite. Extensive networks of open to partly open fractures may exist in these rocks, but it is also likely that in some areas fracture networks have been damaged, and possibly completely sealed, by postkinematic anhydrite.

Thus, two diagenetic factors have acted to reduce fracture pore space, constricting apertures and reducing length. The first is precipitation of authigenic dolomite. This has probably affected all fractures to some extent, sealing microfractures that are below the emergent threshold size, and diminishing the apertures and lengths of fractures above the threshold size in a systematic way. The second is precipitation (and reprecipitation) of authigenic anhydrite. Core observations show that this phase is very heterogeneously developed, in some cases sealing some fractures but not others on a millimeter scale. Because pre- and postkinematic anhydrite cannot at this time be distinguished effectively in rocks lacking macroscopic fractures, surrogates like the degradation index are not effective in mapping areas having open versus sealed macrofractures. We infer from high anhydrite content in the rock mass that postkinematic anhydrite locally probably has a deleterious effect on fracture porosity retention.

DISCUSSION OF FRACTURE ANALYSIS RESULTS

Fracture Architecture

Opening-mode fractures observed in Clear Fork outcrops and cores have aperture sizes spanning up to two orders of magnitude in an individual data set. Aperture-size distributions are best described by power laws, and we submit that these power laws may be used to predict fracture intensities for fracture aperture sizes larger than those observed. The power laws for the Clear Fork outcrop examples may be compared with the frequency-aperture power laws obtained from outcrop 1-D scanlines, measured at Apache Canyon, and other carbonate formations (table 3; fig. 14). The power-law exponent and coefficient for the siltstone CF2-38 fracture aperture size distribution fall within the range measured for Apache Canyon dolostone samples. Fracture intensities at all scales are similar for these samples. The intensities lie in the mid-range of intensities measured for other fractured carbonate formations, although the extrapolations for fractures at the large-aperture-size range fall to the low end of the spectrum (fig. 14). This means

Table 3. Comparison of power-law exponents and coefficients from the outcrop study at Apache Canyon (dolostones) and the siltstone CF2-38 from the South Wasson Clear Fork well 7531, depth 6,138 ft. Figures for the latter were converted from 2-D measurements to 1-D so that comparisons could be made.

Sample	**Lithology**	**Extensional strain**	**Exponent**	**Coefficient**
Scanline 1 Apache Canyon	dolomite	0.0104	-0.9516	2.2×10^{-3}
Scanline 2 Apache Canyon (Censoring bias data removed)	dolomite	0.0086	Exponential (-1.2405)	Exponential (2.1×10^{-3})
Scanline 3 Apache Canyon	dolomite	0.0069	-1.1965	1×10^{-3}
Scanline 4 Apache Canyon	dolomite	0.0035	-1.214	8×10^{-4}
South Wasson #7531 6138 ft	siltstone	--------	-0.962	3.021×10^{-3}

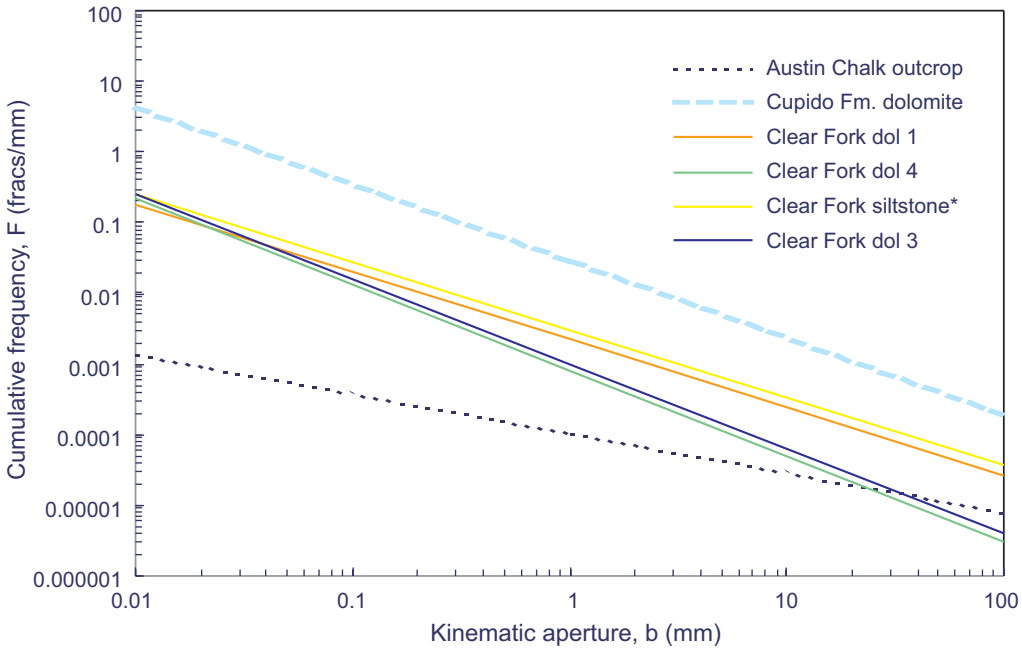

Figure 14. Summary fracture aperture size distribution power laws, comparing curves for the Clear Fork dolostones and the siltstone from this study with curves for fracture populations from outcrops of Austin Chalk and Cupido Formation dolostone.

that large fractures are relatively less abundant in the Clear Fork Formation than for the Austin Chalk (Stowell, 2000) and Cupido Formation dolomites (Ortega and Marrett, 2001).

Extensional strain, relating solely to deformation associated with the fractures, was calculated for individual scanlines and is given in table 3. The mean of these results gives a strain of 0.00734. A strain of 0.00725, which is consistent with these results, was used to condition the geomechanical model to generate a fracture pattern to use in the flow simulation part of this project (Philip and Jennings, Section 2.2, this volume).

Exponential spacing size distributions have been linked by some workers (for example, Rives and others, 1992; Gillespie and others, 1993) to random distributions of fracture positions. Aperture size, however, is not linked to spacing in their interpretations, so there is no indication of how large fractures are distributed with respect to small fractures. The fracture arrays shown in figure 2 indicate a weak fracture clustering, which could be consistent with a random array. There is no consistent relationship between the location of large fractures and fracture clusters.

Fracture Quality

The timing of dolomite formation relative to fracture formation is a key issue in our efforts to predict fracture permeability in the SWCF reservoir. Although synkinematic dolomite has been observed, developing criteria to identifying synkinematic dolomite in the matrix remains a challenge. The SWCF reservoir is completely dolomitized, and there are most likely multiple periods of dolomitization or authigenic dolomite precipitation. Methods for distinguishing the various periods of dolomitization have not yet been established. However, phases of dolomite cement have been successfully distinguished in other dolostone reservoirs using conventional CL (Ruppel and Cander, 1988a, b), so the prospects are good for successfully unraveling these relations using the more powerful imaging methods now available. Observed emergent threshold values, which are the result of authigenic dolomite precipitation, were used to modify modeled fracture patterns (Philip and Jennings, this volume).

The timing of anhydrite formation relative to fracture formation is also a key issue in predicting fracture permeability in the SWCF reservoir. Anhydrite is a diagenetic mineral like dolomite, and, although it fills fractures, it is widespread but not ubiquitous in the matrix as well as in the fractures. The diagenetic history of anhydrite might be complicated, and techniques for

unraveling the history have not yet been developed. It is likely that some anhydrite was originally the hydrous form gypsum. It is clear that some calcium sulfate minerals are penecontemporaneous with early dolomite formation and that others formed later. We cannot assume that all the anhydrite is postkinematic (some is clearly prekinematic), and methods for distinguishing various phases of anhydrite emplacement need to be developed before an accurate accounting of postkinematic anhydrite cement can be made for areas where large fractures have not been sampled.

REFERENCES

Gillespie, P. A., Howard, C. B., Walsh, J. J., and Watterson, J., 1993, Measurement and characterization of spatial distributions of fractures: Tectonophysics, v. 226, p. 114–141.

Laubach, S. E., 1997, A method to detect natural fracture strike in sandstone: American Association of Petroleum Geologists Bulletin 81, p. 604–623.

Laubach, S. E., in preparation, Practical approaches to identifying sealed and open fractures.

Marrett, R., 1996, Aggregate properties of fracture populations: Journal of Structural Geology, v. 18, p.169–178.

Marrett, R., Ortega, O. J., and Kelsey, C. M., 1999, Extent of power-law scaling for natural fractures in rock: Geology, v. 27, p. 799–802.

Milliken, K. L., and Laubach, S. E., 2000, Brittle deformation in sandstone diagenesis as revealed by cathodoluminescence imaging with application to characterization of fractured reservoirs, Chapter 9: *in* Pagel, M., Barbin, V., Blanc, P., and Ohnenstetter, D., eds., Cathodoluminescence in Geosciences: Springer-Verlag, p. 225–244.

Moros Otero, J. G., 1999, Relationship between fracture aperture and length in sedimentary rocks. The University of Texas at Austin, unpublished Master's thesis.

Ortega , O., and Marrett, R. A., 2001, Stratigraphic controls on fracture intensity in Barremian-Aptian carbonates, Northeastern Mexico, *in* Marrett, R. A., ed., Genesis and controls of reservoir-scale carbonate deformation, Monterrey Salient, Mexico: The University of Texas at Austin, Bureau of Economic Geology Guidebook 28, p. 57–82.

Reed, R. M., and Milliken, K. L., submitted, How to overcome imaging problems associated with carbonate minerals on SEM-based cathodoluminescence systems, Journal of Sedimentary Petrology.

Rives, T., Razack, M., Petit, J.-P., and Rawnsley, K. D., 1992, Joint spacing: analogue and numerical simulations: Journal of Structural Geology, v. 14, p. 925–937.

Ruppel, S. C., and Cander, H. S., 1988a, Effects of facies and diagenesis on reservoir heterogeneity: Emma San Andres field, West Texas: The University of Texas at Austin, Bureau of Economic Geology Report of Investigations No. 178, 67 p.

Ruppel, S. C., and Cander, H. S., 1988b, Dolomitization of shallow-water platform carbonates by sea water and seawater-derived brines: San Andres Formation (Guadalupian), West Texas, *in* Sedimentology and geochemistry of dolostones: Society of Economic Paleontologists and Mineralogists, Special Publication No. 43, p. 245–262.

Stowell, J. F. W., 2000, Specifying lengths of horizontal wells in fractured reservoirs: Proceedings of the 2000 SPE/CIM International Conference on Horizontal Well Technology, Calgary, 6-8 Nov. 2000, SPE 65458.

MODELING COUPLED FRACTURE-MATRIX FLUID FLOW IN GEOMECHANICALLY SIMULATED FRACTURE PATTERNS

A CASE STUDY OF THE SOUTH WASSON CLEAR FORK RESERVOIR

Zeno G. Philip, James W. Jennings, Jr., Jon E. Olson, and Jon Holder

Bureau of Economic Geology
John A. and Katherine G. Jackson School of Geosciences
The University of Texas at Austin

TABLE OF CONTENTS

LIST OF FIGURES

LIST OF TABLES

ABSTRACT

Subcritical crack growth parameters were measured from representative rock samples of the South Wasson Clear Fork reservoir. These measurements along with other inferred parameters such as the strain and Young's modulus were used with a geomechanical crack growth simulator to generate fracture patterns at a series of increasing strain levels. The resulting fracture patterns exhibited total fracture lengths, mean fracture lengths, and cluster spacing dependent on strain level, bed height, and subcritical crack index. Fluid-flow simulations were conducted to estimate effective permeability in the simulated fracture patterns using two different approaches representing fractures (1) explicitly with high-permeability grid cells and (2) indirectly with nonneighbor connections between matrix grid cells.

The ratio of effective permeability to matrix permeability, R_k, was found to increase with strain level, total fracture length, and mean fracture length. For a given strain level R_k depended on the subcritical crack index and bed height. Fracture aperture, however did not affect R_k. The reduction of effective permeability by the filling of fractures with diagenetic cements was also studied.

INTRODUCTION

In conventional reservoir simulation, grid-block permeabilities must frequently be assigned values systematically larger than those observed in core measurements or inferred from well logs in order to obtain reasonable history matches. Even then, accuracy with regard to some aspects of the performance such as water or gas cuts, breakthrough times, and sweep efficiencies may be inadequate. This could be due to a substantial part of the flow taking place through fractures not accounted for in the simulation.

High-permeability fracture networks in a matrix system can create high-conductivity channels for the flow of fluids through a reservoir, producing larger flow rates and larger apparent permeabilities than those in the matrix alone. The presence of fractures can also lead to poorer sweep efficiencies for flooding operations with large portions of the reservoir remaining untouched by the displacing fluid. A better understanding of reservoir performance may be obtained by including the physics of fluid flow in fractures in reservoir flow modeling.

It is impossible to accurately quantify interwell fracture network geometries in sufficient detail to directly model their effect on reservoir behavior. Most modeling approaches have been statistical, using data from outcrop and well-bore observations to determine distributions for fracture attributes such as fracture length, spacing, and aperture to randomly populate a field. Sometimes observed data can also be used to establish interdependence between fracture characteristics to constrain the distributions used in the statistical study. These approaches, although useful, are limited by the quality and quantity of data available. Data from well bores are sparse and often altered by drilling processes. Data from outcrops could be subject to weathering influences. Moreover, in many instances, plant growth and terrain inaccessibility hampers the obtaining of data from available outcrops.

An alternative approach to statistical modeling is a geomechanics-based approach where a physical understanding of the fracturing process is used in predicting fracture characteristics. Fracture initiation in rock is often nonlinear because of inelastic deformation on the grain scale prior to macroscopic fracture formation (Ingraffea, 1987). However, linear elastic fracture mechanics is appropriate when the fracture length is large relative to the inelastic process zone at the fracture tip (Olson, 1993). Previous studies have shown that microfractures in many types of rock act as nucleation points for macrofractures (Olsson and Peng, 1976; Tapponier and Brace, 1976; Wang and Heard, 1985).

Opening-mode (mode I) fractures propagate in the direction perpendicular to the least compressive stress. Such fractures propagate when the fluid pressure inside them exceeds the local least compressive stress or when the local stress becomes tensile. However, this is a necessary condition but not sufficient. The parameter that determines fracture propagation from an existing flaw is the stress intensity factor, B_I. In the rock mechanics literature this quantity is conventionally given the symbol K_I, but we will use B_I to avoid confusion with permeability, k.

The mode I stress intensity factor, B_I, for a uniformly loaded isolated crack of length 2c is defined by

$$B_I = \Delta\sigma_I \sqrt{\pi c} \quad ,$$

and

$$\Delta\sigma_I = P_p - \sigma_{min} \quad ,$$

where $\Delta\sigma_I$ is the driving stress, P_p is the pore pressure in the rock, and σ_{min} is the in situ least compressive stress.

Material failure typically occurs when the stress intensity factor is greater than a quantity defined as the critical stress intensity factor, B_{IC}, also known as the fracture toughness. In such cases, the fracture propagation velocity is usually one-quarter to one-third the elastic wave speed in the solid media (Renshaw, 1996). This is called critical crack propagation. However, in cases of long-term loading in corrosive or liquid-saturated environments, cracks have been known to propagate at stress intensities much below the critical stress intensity. This type of fracture propagation, called subcritical crack (SCC) growth, is thought to be representative of most natural fracturing processes in subsurface rocks (Atkinson, 1984; Atkinson and Meredith, 1987). The velocity of SCC propagation is much slower than that for critical crack propagation and has been observed to follow an empirical power law:

$$V = V_{\max}\left(\frac{B_I}{B_{IC}}\right)^s \quad ,$$

where V_{max} is the maximum propagation velocity at $B_I = B_{IC}$, and s is the SCC growth index. The conditions for crack propagation can be determined by computing the stress intensity factor at the crack tip for an applied load and comparing it with the material's critical stress intensity factor, B_{IC}. Critical crack growth will occur if the crack-tip stress intensity factor exceeds the critical stress intensity factor. SCC growth will initiate at a much lower threshold stress intensity, B^*_I.

For a single crack in a homogeneous medium subcritical and critical growth will produce the same crack geometry, but at different rates. However, for multiple cracks subcritical and critical growth will yield different results. In critical growth the stresses will be large enough that the stress intensities at almost all the crack tips will be above the critical stress intensity factor. The cracks will then grow at the critical velocity, which is large enough to make crack interaction effects negligible. In SCC growth the velocities of crack propagation are small enough that the interaction among these cracks could affect individual crack propagations differently. For example, when a particular crack tip approaches another in an en echelon manner the stress intensity at both tips increases, but when the tips pass one another the stress intensity at the overlapping tips decreases because of the stress shadow around the cracks. In SCC growth the

velocity of crack propagation is determined by the subcritical index. Therefore, with the same set of initial flaws, different fracture patterns can be obtained with different subcritical crack indices because of differences in crack velocities and interaction among cracks (Olson, 1993).

GEOMECHANICAL SIMULATION

Simulation Methodology

A linear elastic fracture mechanics-based crack growth simulator based on the boundary element method has been developed by Olson (1991). This simulator has been used in our present study. A bed of rock with mechanical properties representative of the reservoir is populated with random starter flaws and is subjected to a constant displacement rate (strain rate). The starter flaws are each composed of two patches of fixed length. When the reservoir bed is subjected to a tensile strain the stress intensities at most of the flaw tips are increased. A lower limit for crack initiation of $B_I^* = B_{IC}/10$ is assumed. Thus for subcritical crack growth,

$$B_I^* \le B_I < B_{IC} \quad .$$

Individual crack tip stress intensities are computed on the basis of the applied strain, interaction with other cracks, and an effective Young's modulus, E^*, computed from (Olson, 1993):

$$E^* = \frac{E}{1 + 2\pi\left(1 - \nu^2\right)\rho} \quad ,$$

where E is the Young's modulus, and ν is the Poisson's ratio. The areal fracture density, ρ, is given by

$$\rho = \frac{1}{D}\sum_{j=1}^{N} c_j^2 \quad ,$$

where c_j is the half-length of fracture j, D is the area of the representative fractured region, and N is the number of fractures.

Those flaws for which the stress intensity is above the stress-intensity threshold but below the critical stress intensity factor grow at a velocity determined by the SCC index. The crack grows by the addition of a new patch to the tip of an existing one. The crack growth simulation is stopped when the prescribed strain is reached.

Simulation Parameters: South Wasson Clear Fork Case Study

The SCC index has been measured with the dual-torsion-beam apparatus (Williams and Evans, 1973; Pletka and others, 1979) for samples from six representative layers of the South Wasson Clear Fork reservoir (Holder and others, 2001). The results are presented in table 1.

Table 1. Mean values of the SCC index for six South Wasson Clear Fork samples.

Sample depth (ft)	Type of test	No. of tests	Average SCC index
6,091 Grain-dominated dolopackstone	Dry	7	43
	Wet	5	37
6,138 Dolomitic siltstone	Dry	11	40
	Wet	3	34
6,367 Grain-dominated dolopackstone	Dry	6	60
	Wet	12	53
6,385 Dolowackestone	Dry	6	81
	Wet	3	70
6,484 Grain-dominated dolopackstone	Dry	5	43
	Wet	1	37
6,520 Grain-dominated dolopackstone	Dry	8	38
	Wet	10	30

In these measurements the SCC index ranges from 40 to 80. We have used these two extreme values as our case study scenarios. A Young's modulus of 40,000 MPa for this formation was estimated from a typical porosity of 10 percent using a published correlation for dolomites. A strain of 0.00725 was inferred from fracture-aperture measurements at an outcrop of the Victorio Peak Formation (a Clear Fork equivalent), Apache Canyon, West Texas (Gale and others, this volume). The geometric mean of the apertures observed from the outcrop is 0.212 mm. A typical thickness for rock-fabric flow layers in the South Wasson Clear Fork field is 5 m

and for high-frequency cycles is 10 m (see Lucia and Jennings, this report). These thicknesses were used in the crack simulation. Owing to crack simulation limitations the inferred strain of 0.00725 could not be applied. Therefore a value of strain was applied such that the resultant geometric mean aperture obtained was fairly close to that observed in the outcrop. The input data used to generate fracture patterns are given in table 2.

Table 2. Input data to the crack growth simulator.

Parameter	Value
Area of study	50 × 50 m
Young's modulus, E	40,000 MPa
Critical stress intensity factor	1.5 MPa(m)$^{1/2}$
Threshold stress intensity factor	0.15 MPa(m)$^{1/2}$
Displacement increment	0.00005 m
No. of increments	83
Total strain	7.33E-5
Time	19.7 million years
Strain rate	2.30E-19 1/s
No. of initial flaws	2,000

Four case scenarios were studied combining two bed heights, 5 and 10 m, and two SCC indices, 40 and 80. Other geomechanical simulation parameters were obtained from table 2. For each case, seven different realizations were studied, each realization with a different set of random starter cracks. Thus, a total of 28 different geomechanical simulations were performed.

A sample set of fracture patterns obtained for each of the four cases (realization 3) is shown in figures 1 through 4. For all other parameters remaining constant, the subcritical index, *s*, of 80 produces a fracture pattern with a larger number of smaller fractures as compared with the subcritical index of 40. Further, for everything else remaining constant, we see that the bed height of 5 m causes fracture patterns in which the fracture clusters are more closely spaced than when the bed height is 10 m.

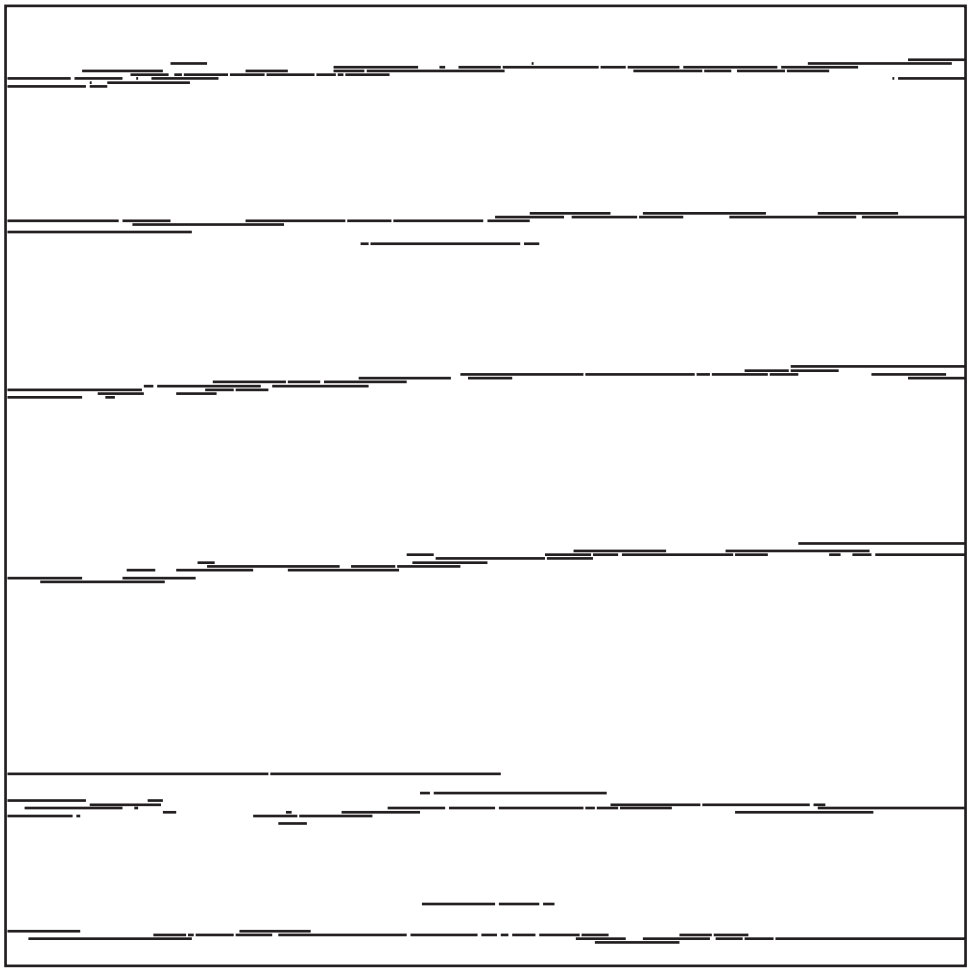

Figure 1. SWCF simulated fracture pattern (realization 3) with a bed height of 10 m and SCC index of 40.

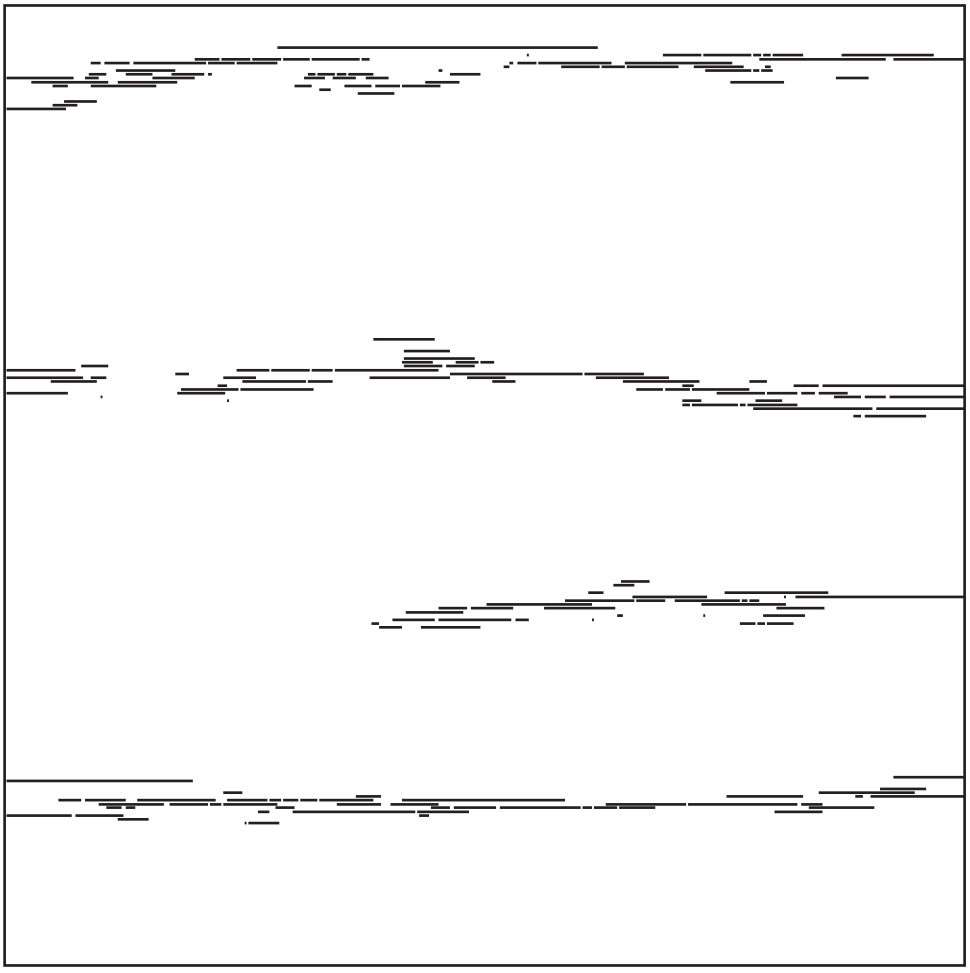

Figure 2. SWCF simulated fracture pattern (realization 3) with a bed height of 10 m and SCC index of 80.

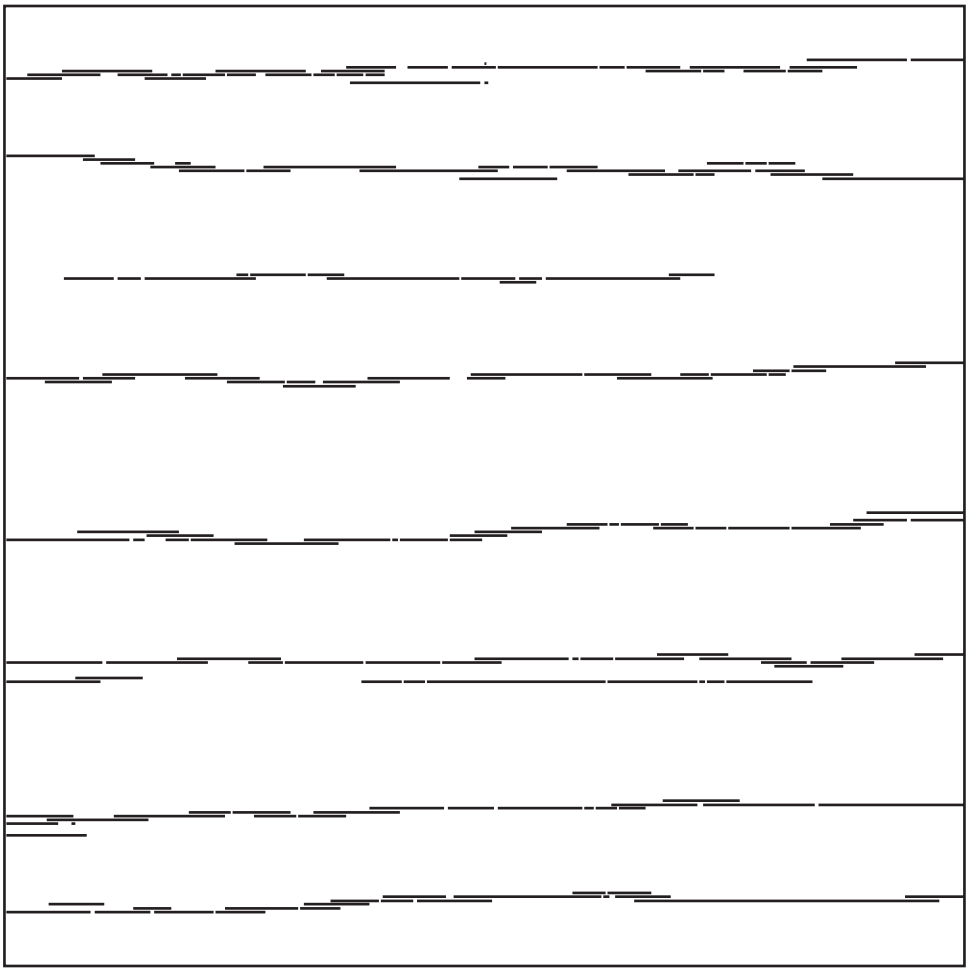

Figure 3. SWCF simulated fracture pattern (realization 3) with a bed height of 5 m and SCC index of 40.

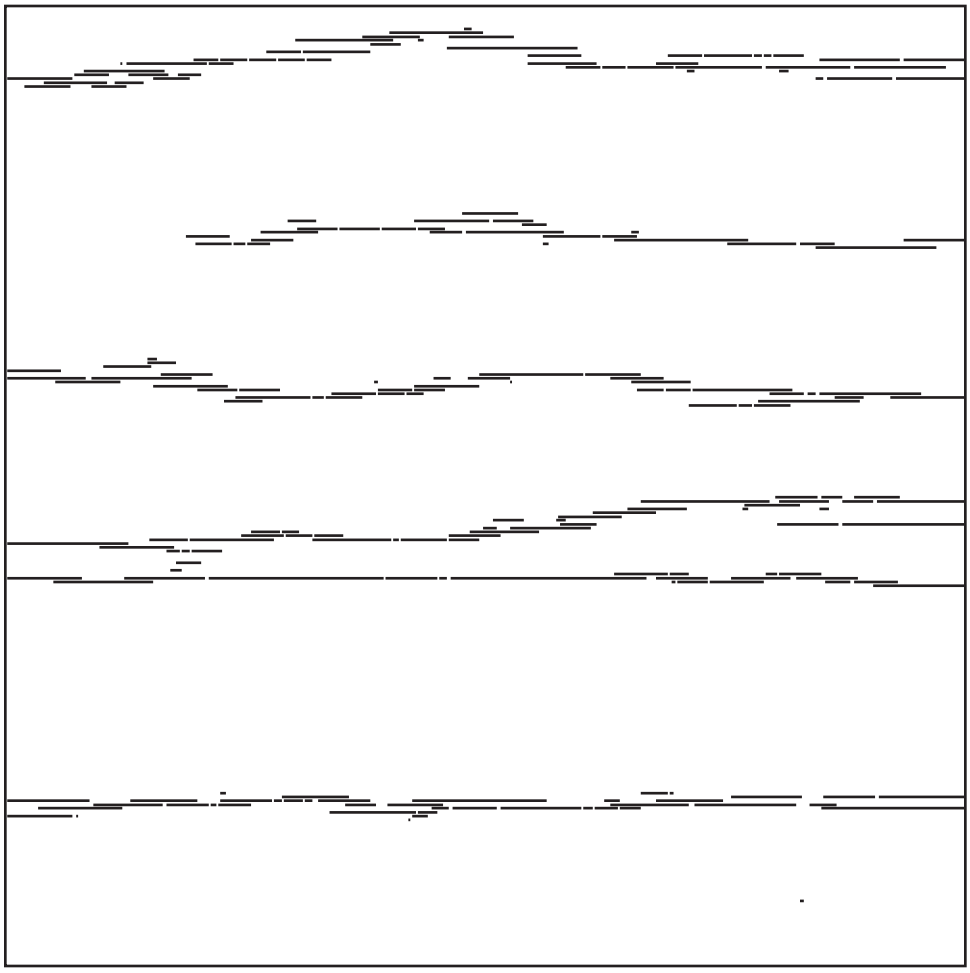

Figure 4. SWCF simulated fracture pattern (realization 3) with a bed height of 5 m and SCC index of 80.

FLOW MODELING

Explicit Fracture Representation

The geomechanical simulation produces a list of patches with location and aperture information. Each fracture is made up of a series of patches lying end to end. The greater the number of patches associated with a particular crack the greater is the length of that particular crack. Thus a fracture can have varying apertures along its length.

For a flow simulation, the flow area is gridded to the same resolution as the geomechanical simulation. In this study the geomechanical simulation area was 50 × 50 m square, and the patches were 0.1 m in length. Therefore, the flow simulations were performed on the same 50 × 50 m area with 500 × 500 = 250,000 cells of equal x and y dimension (0.1 m). This ensures that each patch can be represented by one cell in the flow simulation. The z direction cell size was 0.5 m.

The permeability of a fracture patch, k_{frac}, with uniform aperture w (fig. 5), can be computed using (Halihan and others, 1999)

$$k_{frac} = \frac{w^2}{12} \quad .$$

The permeability of a cell in the flow simulation containing a patch can be computed using

$$k_{cell} = \frac{\left(k_{frac} w + k_{mat}\left(\Delta y - w\right)\right)}{\Delta y} \quad ,$$

where k_{cell} is the permeability of a flow simulation cell containing a fracture patch, and k_{mat} is the matrix permeability. The width of the simulation cell perpendicular to the flow direction is Δy. *A matrix permeability of 1 md was used for all flow simulations.* However, this value is much lower than the matrix permeability in the South Wasson Clear Fork reservoir (see Lucia and Jennings, this report).

Figure 5. Grid cell representation of a fracture patch, showing the cell dimension and fracture aperture.

Each cell in the flow simulation was assigned a unique permeability on the basis of the location and aperture of the patches. The *y* and *z* direction permeabilities were unchanged because the geomechanical simulations were constrained to produce fractures only in the *x* direction. A Fortran program was written to create lists of cell permeabilities from the patch coordinates and aperture information obtained from the geomechanical simulations.

Nonneighbor Connections

Flow through fractures can also be modeled using nonneighbor connections (NNC) in a traditional finite-difference simulator (Hearn and others, 1997). In this approach the fractures are assumed to have infinite conductivity, making fracture aperture information irrelevant. The fracture patterns are gridded such that the fractures lie at the boundaries between grid cells.

The matrix flow transmissibility between any two grid cells is

$$T_{x(mat)} = \frac{k_x A_x}{\Delta x} \quad ,$$

where A_x is the area perpendicular to flow in the *x* direction, $\Delta y \Delta z$, and k_x is the permeability in the *x* direction (fig. 6). If there is a fracture between the cells as shown in figure 7, an additional transmissibility for fracture flow can be assigned using

$$T_{x(frac)} = \frac{k_y A_y}{2\left(\Delta y \big/ 2\right)} = \frac{k_y A_y}{\Delta y} \quad ,$$

where A_y is the area perpendicular to flow in the *y* direction, $\Delta x \Delta z$, and k_y is the permeability in the *y* direction. The total *x* direction transmissibility, accounting for both matrix and fracture flow, is

$$\begin{aligned} T_{x(total)} &= T_{x(mat)} + T_{x(frac)} \\ &= \frac{k_x A_x}{\Delta x} + \frac{k_y A_y}{\Delta y} \quad . \end{aligned}$$

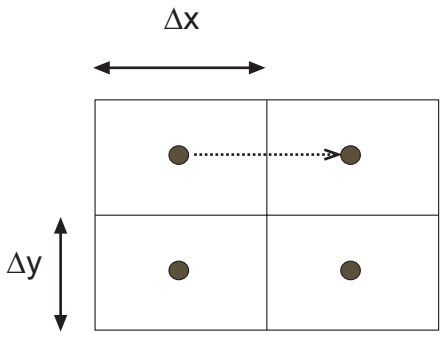

Figure 6. Schematic of grid, depicting cell dimensions and x direction permeability

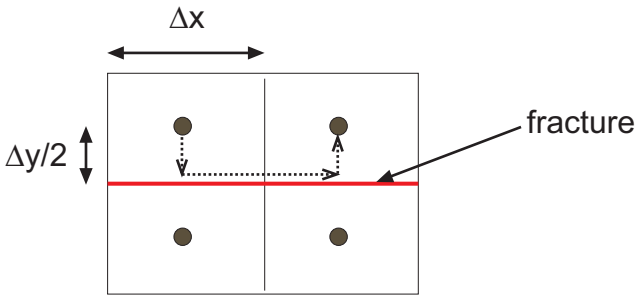

Figure 7. Schematic of grid, depicting the location of, and x direction permeability due to, a fracture.

The transmissibility between adjacent cells due to matrix flow is computed automatically by the simulator, connecting cell *i* to cells *i*-1 and *i*+1. The transmissibility between cells due to fracture flow can be entered explicitly using NNC, connecting cell *i* to cells *i*-1 and *i*+1 as well as to all other cells on that same fracture. The NNC between cell *i* and its neighbors *i*-1 and *i*+1 is in addition to that due to matrix flow. Thus, a fracture extending between cells 1 and *n* connects cell 1 to cells 2 through *n*, cell 2 to cells 3 through *n*, and so on (fig. 8). The total number of NNC per fracture is

$$\left(\frac{n(n-1)}{2}\right)2 = n(n-1) \quad .$$

The multiplication by 2 accounts for cells on both sides of the fracture. A Fortran program was written to create a list of NNC transmissibilities from the endpoint locations of fractures in a fracture pattern simulation. A fracture between rows 1 and 2 extending from cells 1 to *n* results in the following nonneighbor transmissibilities for connections between cell 1 and the others in row 1:

$$T_{1,2}, T_{1,3}, ..., T_{1,n(frac)} = \frac{k_y(\Delta x \Delta z)}{\Delta y} \quad .$$

Likewise the nonneighbor transmissibilities between cell 2 and cells 3 through *n* are

$$T_{2,3}, T_{2,4}, ..., T_{2,n(frac)} = \frac{k_y(\Delta x \Delta z)}{\Delta y} \quad ,$$

and so on, for cells 3 through *n*. The transmissibilities for cell connections in row 2 are computed similarly. The corresponding matrix transmissibilities are computed automatically by the simulator.

Flow Simulation Methodology

A finite difference simulator, Eclipse 100, (Schlumberger, 1995, 1997) was used to perform 2-D, single-phase flow simulations. Constant pressure boundaries were maintained on

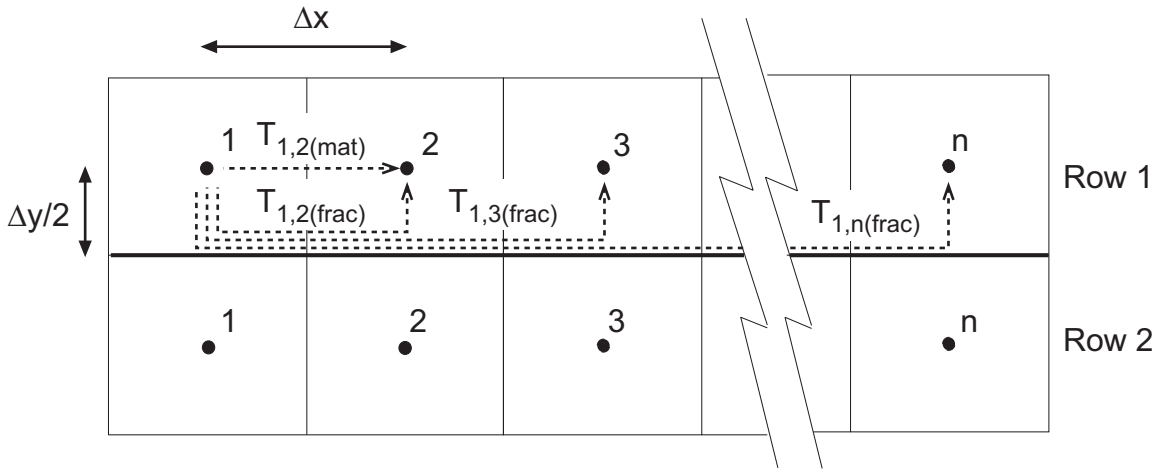

Figure 8. Schematic of grid, depicting NNC between cells, to model flow due to a fracture.

two opposing sides while the other two sides were no-flow boundaries. Constant pressure was maintained by assigning to each of the cells on a particular side producing wells on pressure control, and to each of the cells on the opposing side injector wells on pressure control. Thus the number of producers and injectors was each equal to the number of rows in the flow grid.

Water was used as the flowing phase, both with and without tracer. Tracers were used only for flow visualization and do not otherwise affect the simulation. The flow simulation was performed till a steady-state flow rate, q, was obtained. Knowing q, the pressures at both the ends, P_1 and P_2, the distance between the constant pressure conditions, L - (2(Δx)/2), and the fluid properties, one can obtain an effective permeability for the fractured grid as follows,

$$k_{eff} = \frac{q\mu(L - \Delta x)}{A(P_1 - P_2)} \quad ,$$

where is μ is the fluid viscosity, and A, the area perpendicular to flow, is the product of Δy, Δz, and the number of cells in the y direction.

VERIFICATION

Effective permeability estimates from flow simulations using explicit fracture representations and NNC were verified by comparison with analytical solutions for (1) a single finite aperture fracture extending across the entire simulation grid, and (2) the Chirlin solution for a staggered periodic array of infinite-conductivity fractures (Chirlin, 1985; Nakashima and others, 2000).

Single-Fracture Analytical Solution

The analytical solution for the effective permeability of a rectangle with a single fracture extending across the entire area is (fig. 9)

$$k_{anal} = \frac{k_{frac} w_{frac} + k_{mat} w_{mat}}{w_{grid}} \quad .$$

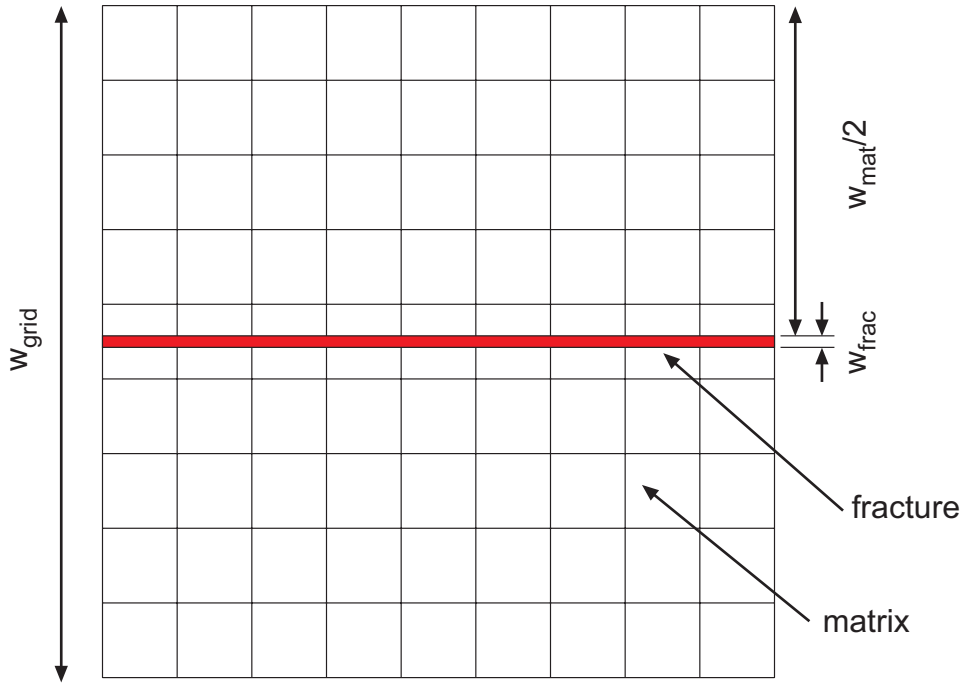

Figure 9. Plot showing an embedded fracture extending from end to end in a simulation grid.

Flow simulations were conducted using the explicit fracture method for two different grid cell sizes of 0.5 m and 0.05 m and a series of fracture widths ranging from 1 to 10,000 microns. The effective permeabilities obtained from the flow simulations agreed to within 0.5 percent of the effective permeabilities obtained using the analytical solution for all fracture apertures studied and for both grid sizes.

The NNC method does not give a good match with the analytical solution for the case of a fracture extending across the entire simulation grid. The reason for this is that in the flow simulation the boundary conditions are established with constant pressures and fluid injection or production at the midpoints of the left and right columns of grid cells. However, in the NNC approach the fractures are assumed to lie in between the grid cells, and the flow resistance from the midpoint of a boundary cell to its edge at both ends of the fracture is sufficient to cause a substantial discrepancy between the simulated and analytical effective permeabilities. This problem does not occur in the explicit fracture approach because the constant pressure boundaries can be applied directly to both ends of the fracture.

Chirlin Solution

An analytical solution for the effective permeability in a staggered periodic array (fig. 10) of infinite conductivity fractures gives the effective permeability ratio R_k as follows:

$$R_k = \frac{k_{eff}}{k_{mat}} = \frac{2WG(r)}{hG\left(\sqrt{1-r^2}\right)} \quad ,$$

where $G(r)$ is the complete elliptic integral of the first kind. In the mathematical literature the symbol $K(r)$ is usually used for this function, but $G(r)$ will be used here to avoid confusion with permeability, k. The modulus, r , of the elliptic integral is given by

$$\frac{1}{r} = \frac{2m(P-1)^2}{(mP+1)^2} + 1 + \sqrt{\left[\frac{2m(P-1)^2}{(mP+1)^2} + 1\right]^2 - 1} \quad ,$$

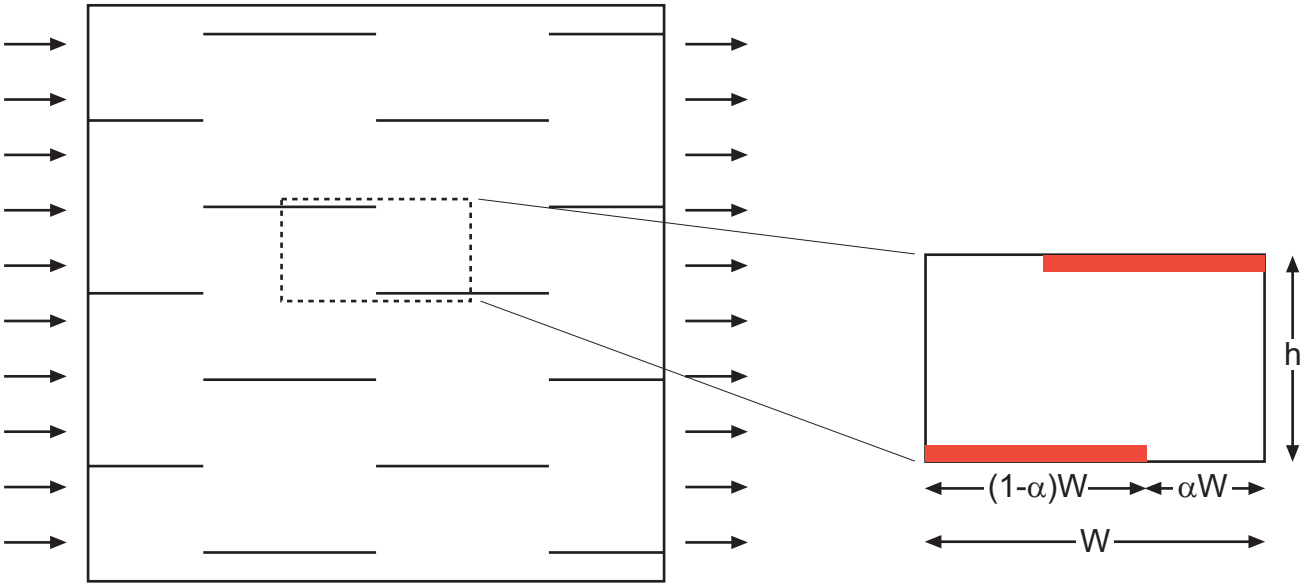

Figure 10. Periodic staggered array of fractures depicting parameters used in the Chirlin solution.

where

$$\frac{1}{P} = dn\left[\alpha G\left(\sqrt{1-m^2}\right), \sqrt{1-m^2}\right] \quad ,$$

dn is a Jacobian elliptic function, and *m* is the modulus of elliptic integral, obtained by solving

$$\frac{G\left(\sqrt{1-m^2}\right)}{G(m)} = \frac{2W}{h} \quad .$$

These equations have been implemented in Mathematica (Wolfram, 1999), and the solution is plotted in figure 11.

Flow simulations for this arrangement of fractures were run until steady-state flow conditions were achieved and the resulting values of R_k were compared with those obtained from the analytical solution. For the explicit-fracture-representation case we studied an array with four fractures—two on the edge and two completely embedded in the grid (fig. 12). This ensured that the north and south edges were no-flow boundaries, whereas the east and west edges were constant-pressure boundaries. We used a width W of 4.5 ft, a fracture spacing h of 1.5 ft, and an α value of 1/3, giving $2W/h = 6$ and an analytical solution for the effective permeability ratio $R_k = 5.8404$. The results for two different grid cell sizes of 0.05 ft and 0.025 ft are as shown in the tables 3 and 4. The effective permeability ratios obtained from the flow simulations approach the Chirlin solution for infinite conductivity fractures as the fracture aperture increases. The accuracy improves with grid refinement.

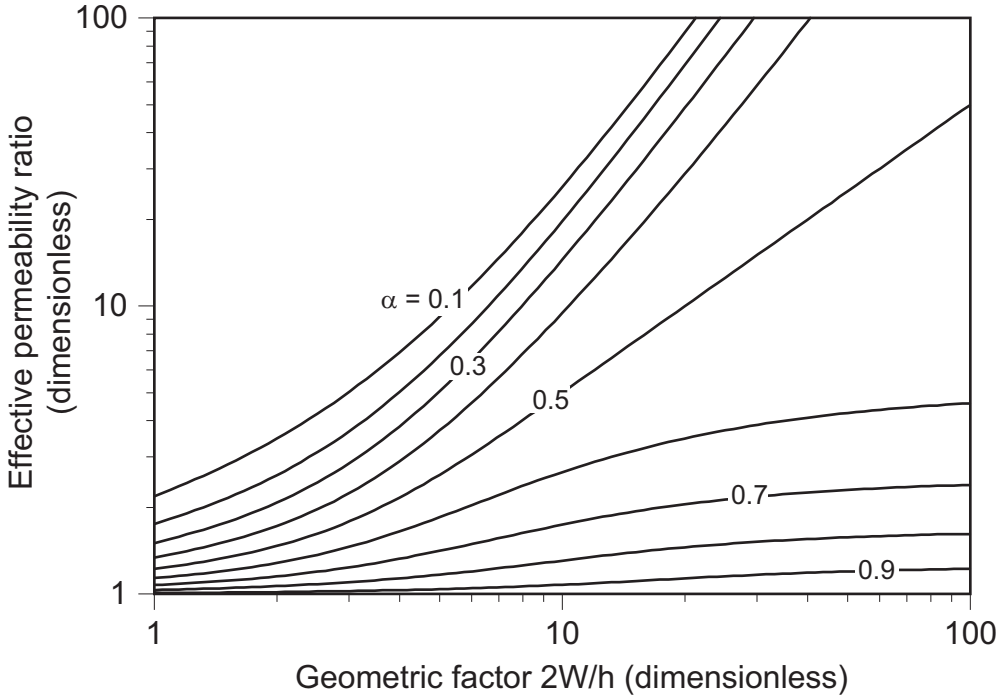

Figure 11. The Chirlin solution for effective permeability ratio, *R*

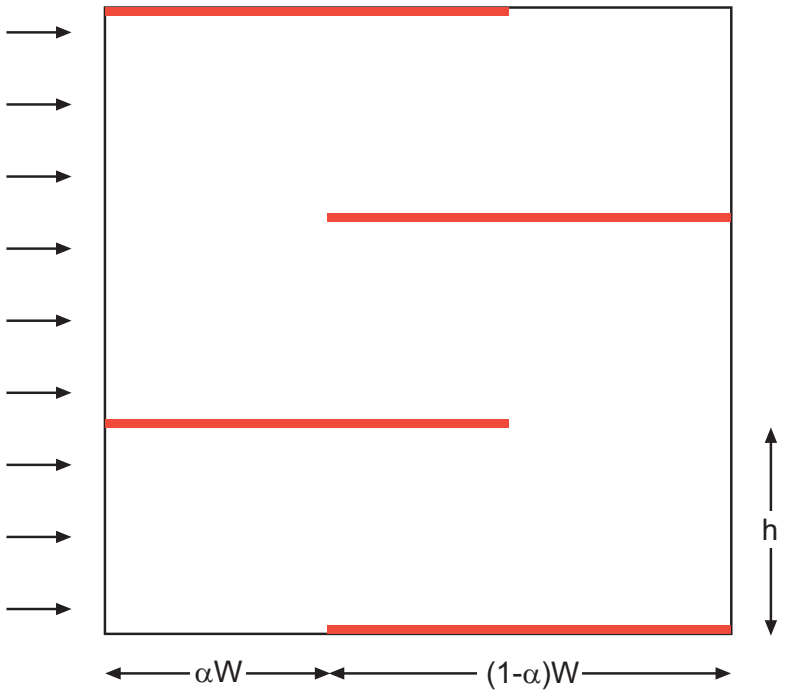

Figure 12. Chirlin layout for the explicit fracture representation study.

Table 3. Simulation results using the explicit fracture-representation method and a cell size of 0.05 ft for a staggered array of four fractures.

Fracture aperture (microns)	Fracture permeability (md)	Grid effective k ratio (R_k)
1	8.44E+01	1.0055
10	8.44E+03	1.0991
100	8.44E+05	4.7088
1,000	8.44E+07	4.8399
10,000	8.44E+09	4.8399

Table 4. Simulation results using the explicit fracture-representation method and a cell size of 0.025 ft for a staggered array of four fractures.

Fracture aperture (microns)	Fracture permeability (md)	Grid effective k ratio (R_k)
1	8.44E+01	1.0109
10	8.44E+03	1.1096
100	8.44E+05	5.1643
1,000	8.44E+07	5.3290
10,000	8.44E+09	5.3290

We applied the NNC method to two periodic fracture cases. For the first case, we used a width, W, of 4.5 ft, a fracture spacing, h, of 4.5 ft, and an α of 1/3 (fig. 13), giving $2W/h = 2$ and an analytical solution of $R_k = 1.947$ (fig. 11). As the grid becomes finer in resolution, the effective permeability obtained by the flow simulation gets closer to the analytical solution (fig. 14).

For the second test we had multiple fractures inside the gridded region (fig. 15). The dimensions were the same as for the previous case, with a width, W, of 4.5 ft and an αW of 1.5 ft,

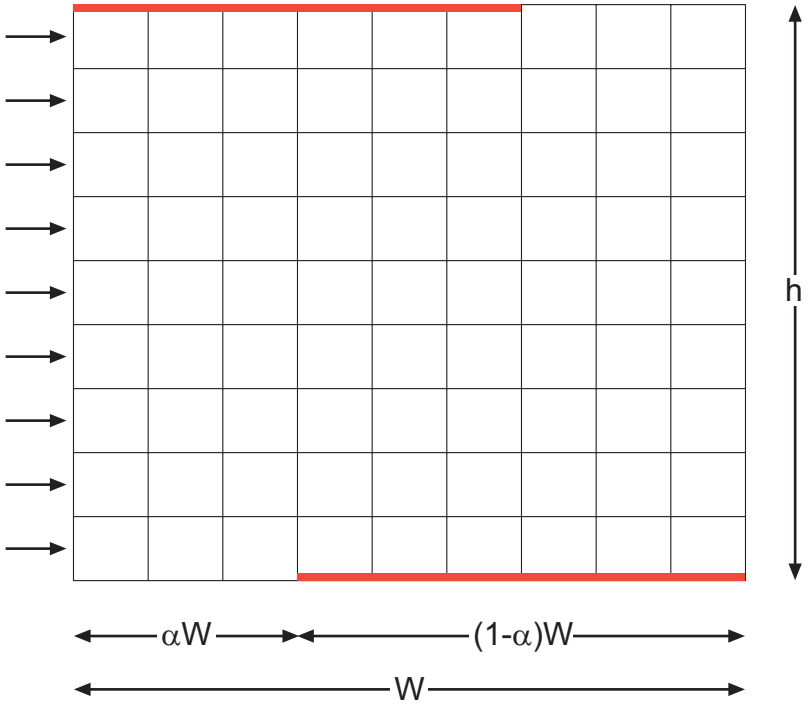

Figure 13. Gridded 9 × 9 array with two edge fractures.

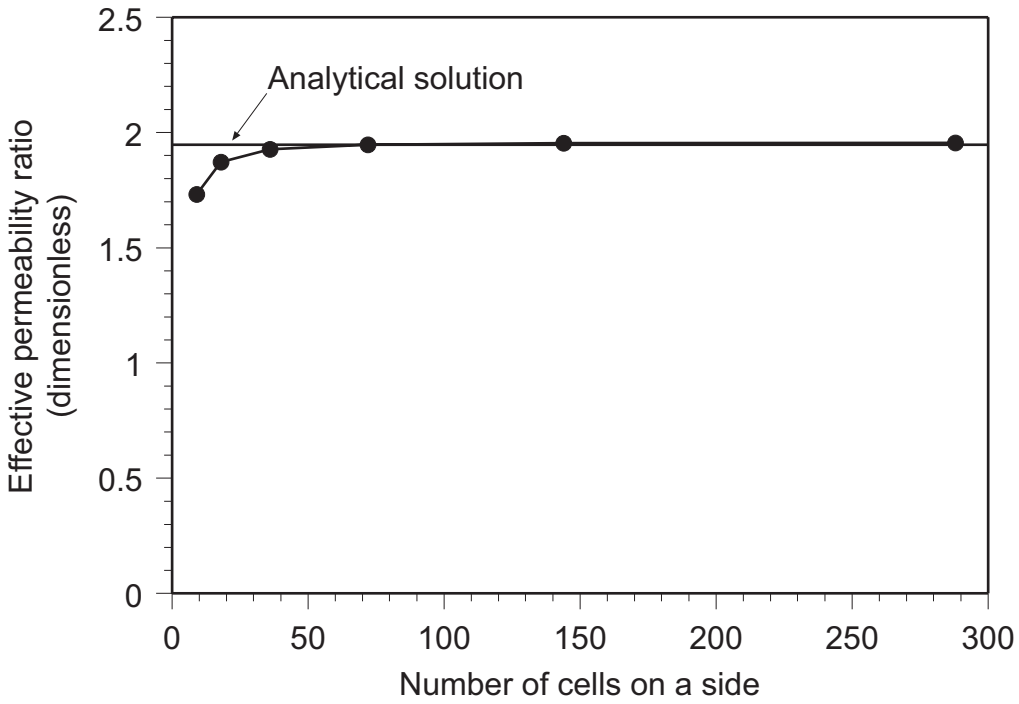

Figure 14. Comparison of analytical solution and NNC simulation for the effective permeability of a periodic array of fractures with two fractures on the edge of the grid.

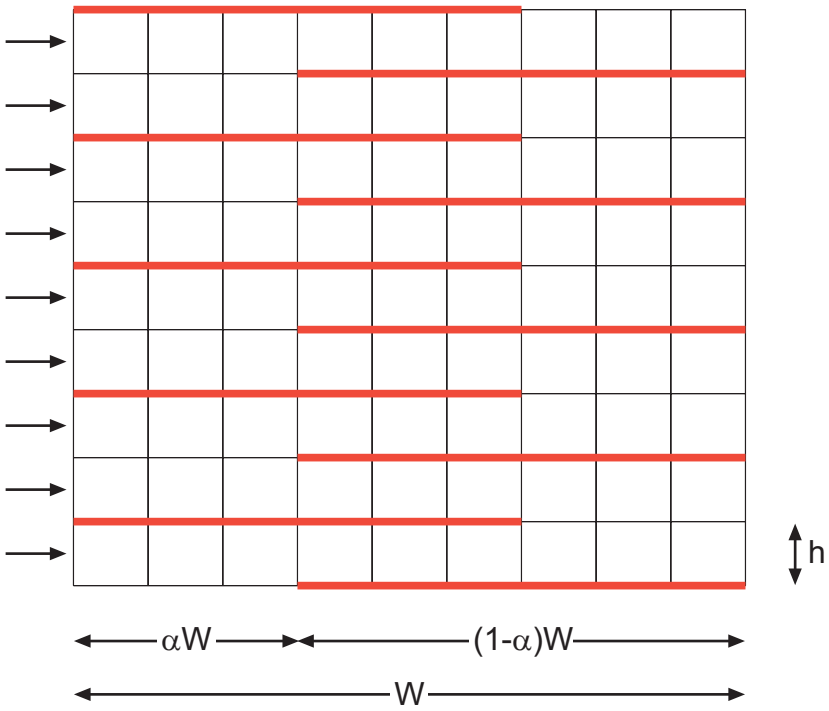

Figure 15. Gridded 9 × 9 array with multiple fractures.

giving an α of 1/3. The fracture spacing, h, however, varied depending on the number of fractures. We studied this scenario for two values of h. For the first case the number of fractures was 4, giving a value of 1.5 for h, and for the second case the number of fractures was 10, giving a value of 0.5 for h. For a given α and W, as h decreases the effective k ratio increases. Thus, for $h = 1.5$ the analytical solution is $R_k = 5.8402$, and for h=0.5 the analytical solution is $R_k = 34.944$ (fig. 11). We modeled both these cases with six gridding schemes increasing grid resolution from 9×9 to 288×288 numbers of cells.

The simulation results for both cases are shown in figures 16 and 17. With increasing grid resolution the effective permeability ratio, R_k, obtained from the simulation gets very close to the analytical solution. One gets to within 5 percent of the analytical solution if there are 12 cells between fractures and to within 2 percent of the analytical solution if there are 24 cells between fractures. The difficulty with the NNC approach that occurred when simulating a single fracture extending across the entire simulation grid did not occur when simulating a periodic array of fractures because the fractures extend only two-thirds of the way across the simulation grid. The additional resistance due to an extra half-matrix cell at one end of each fracture is small compared with the resistance due to the unfractured matrix beyond the other end of each fracture.

FLOW MODELING OF SIMULATED FRACTURE PATTERNS

A fracture pattern was obtained for each run of the fracture simulation and each displacement increment. From these patterns the cell permeabilities for input to the eclipse simulator were computed. The total fracture length, mean fracture length, and geometric mean fracture aperture were also computed. For each strain level, steady-state flow simulations were performed and the effective k ratio, R_k, was computed. Thus, for each of the four cases of a particular combination of bed height and subcritical index and for each strain level the average R_k of seven realizations was obtained. This procedure was repeated for increasing values of strain.

Explicit Fracture Representation

Values of R_k vs. strain obtained for each of the runs and for the individual bed heights of 5 m and 10 m are plotted in figures 18 and 19. The R_k values depend on both the bed height and the subcritical index with a large degree of variability between the different realizations. The

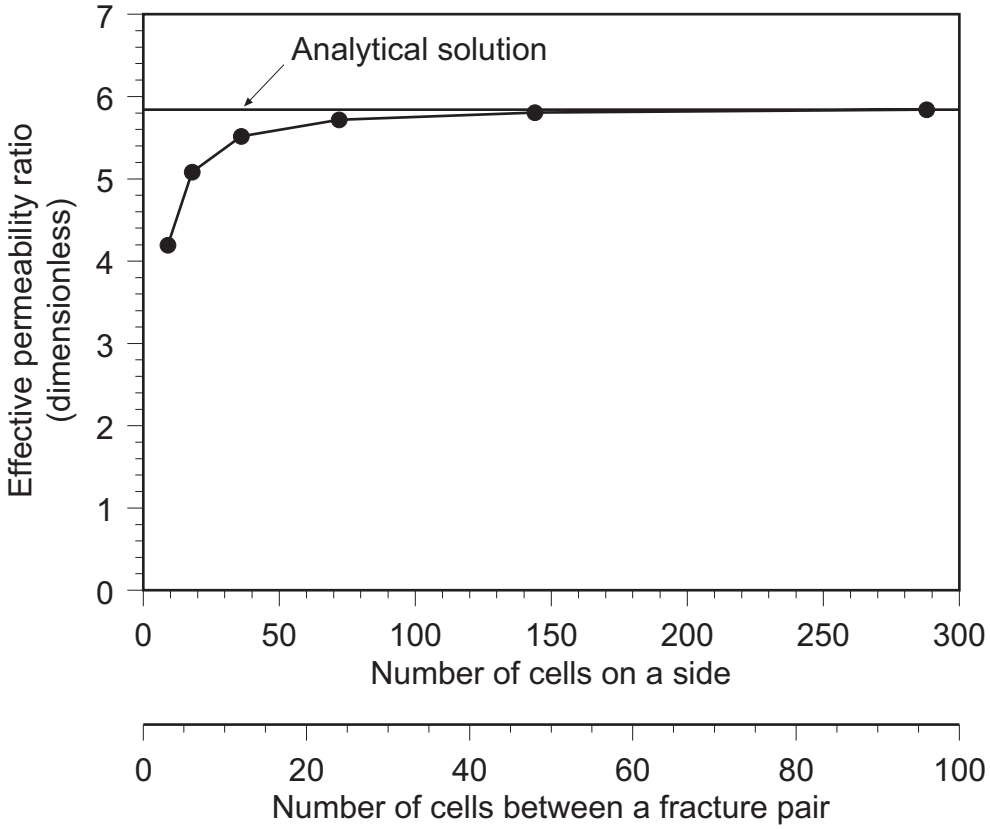

Figure 16. Comparison of analytical solution and NNC simulation for the effective permeability of a periodic array of fractures with multiple fractures in the grid. (h = 1.5).

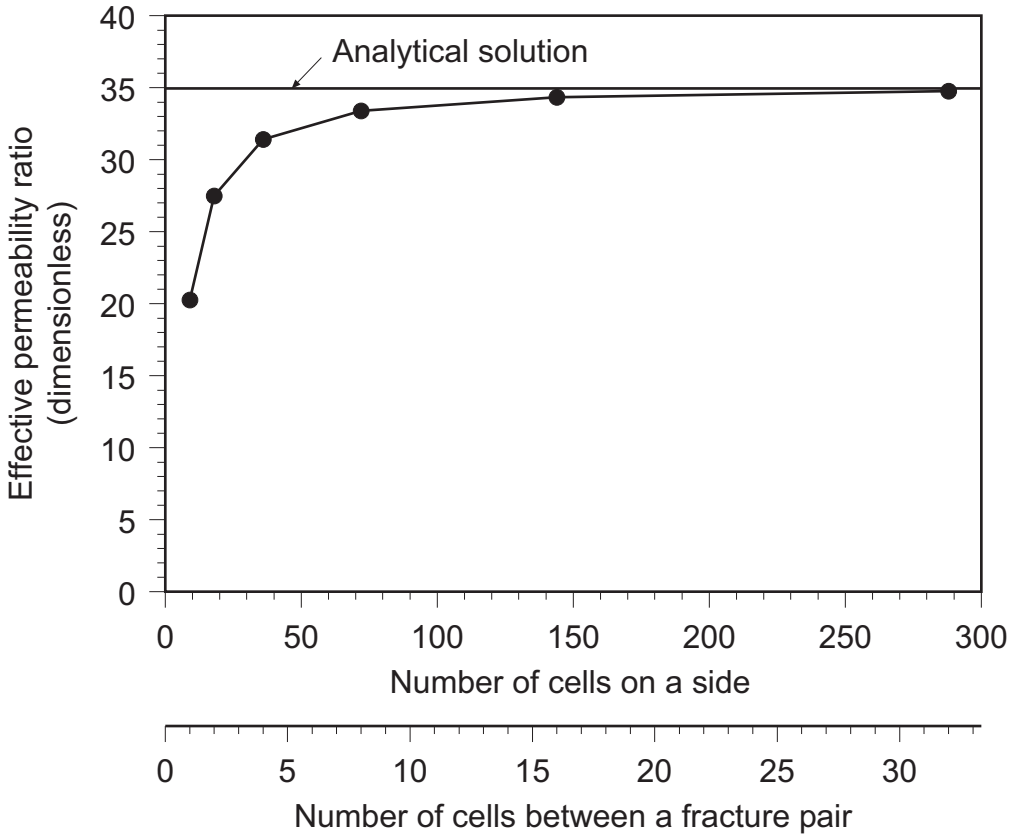

Figure 17. Comparison of analytical solution and NNC simulation for the effective permeability of a periodic array of fractures with multiple fractures in the grid. (h = 0.5).

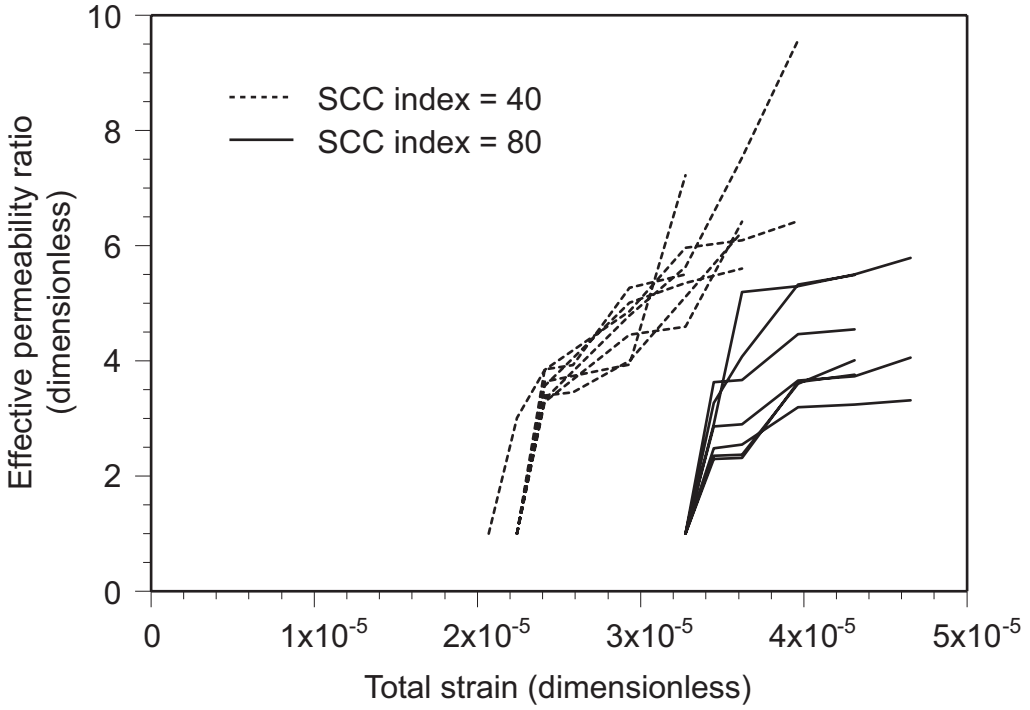

Figure 18. Values of R vs. strain for all seven realizations and a bed height of 10 m.

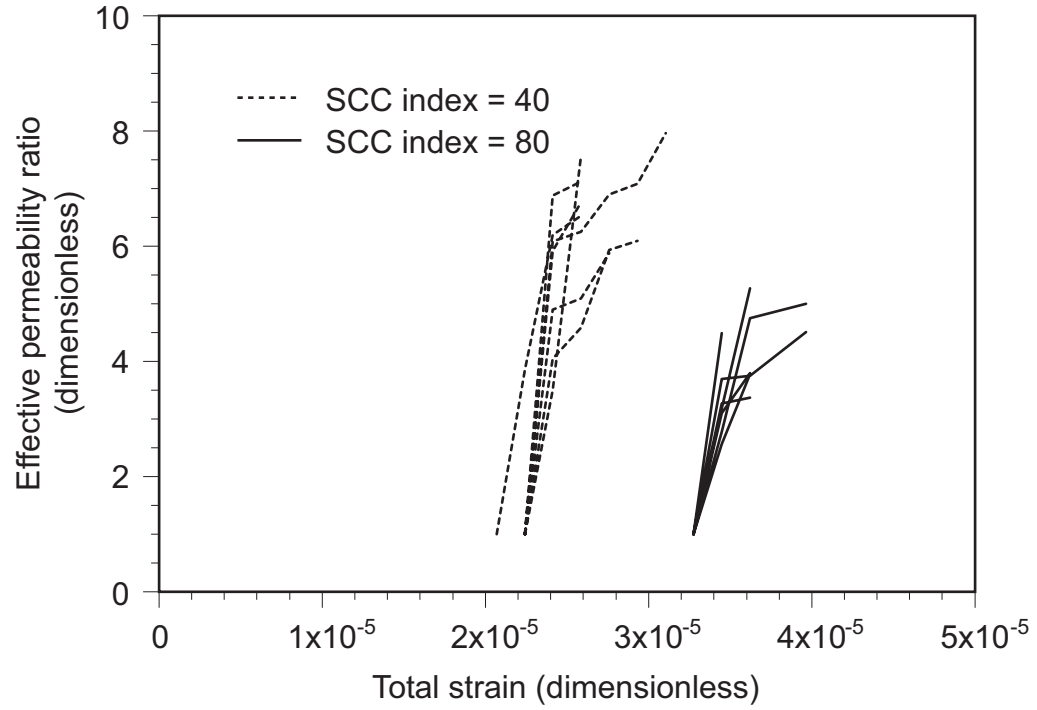

Figure 19. Values of R_k vs. strain for all seven realizations and a bed height of 5 m.

means and standard deviations of R_k from the seven realizations for each of the four combinations of bed height and subcritical index are shown in figures 20 and 21. In subsequent analysis and figures, we shall be referring to only the average of the seven realizations.

In figures 20 and 21 we can see the effect of strain on the effective permeability ratio, R_k. As expected, an increase in the strain causes an increase in R_k. The first significant fractures appear at a strain 2.0E-5 for the index of 40, but at a larger strain of 3.2E-5 for the index of 80 because the larger SCC index produces a smaller crack propagation velocity. Furthermore, for a given strain the total fracture length and the R_k is larger for the lower index.

It is also evident from figures 20 and 21 that for a given index, the rate of increase in R_k is larger for the bed height of 5 m compared with the bed height of 10 m. This is because for the smaller bed height at a particular strain, a larger number of starter flaws develop into fractures, leading to a larger total fracture length. The smaller bed height also causes a closer spacing in the fracture clusters (figs. 1 through 4), but that factor probably does not by itself cause an increase in R_k.

For each combination of bed height and index for each strain level, the average total fracture length of seven realizations was computed. As expected, the total fracture length increases with the strain; therefore, the effective *k* ratio, R_k, also increases with the strain (fig. 22). For the same total length, the case with the index of 40 has a higher R_k than that with an index of 80. This is because an index of 40 in the geomechanical simulations leads to fracture patterns with a smaller number of larger fractures compared with cases with an index of 80.

Further, we see in this figure that there is no strong dependence of R_k on the bed height. There is a slight dependence for the lower index value of 40 but no dependence for the index of 80. The larger R_k for a lower bed height (figs. 20 and 21) was due to the larger fracture length at the same strain.

Similarly, for each strain level, the average mean length of seven realizations was also computed. The effective *k* ratio, R_k, increases with an increase in the fracture mean length (fig. 23). For the initial part of the curve, that is, for values of mean length below about 2.5 m, there is no difference in the R_k values obtained for the different indices or bed heights. However, toward the end of the crack growth simulation, the index of 40 does produce fractures with an average mean length (~3.5 m) larger than that produced by the index of 80 (~2.5 m).

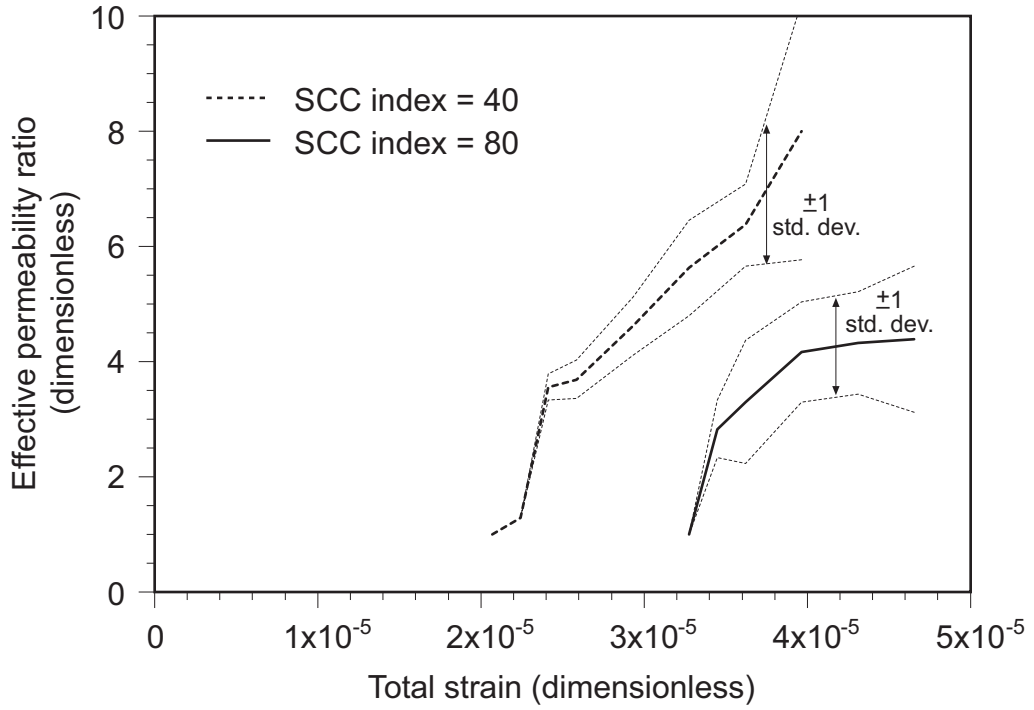

Figure 20. Mean and standard deviation of the effective permeability ratios for a bed height of 10 m.

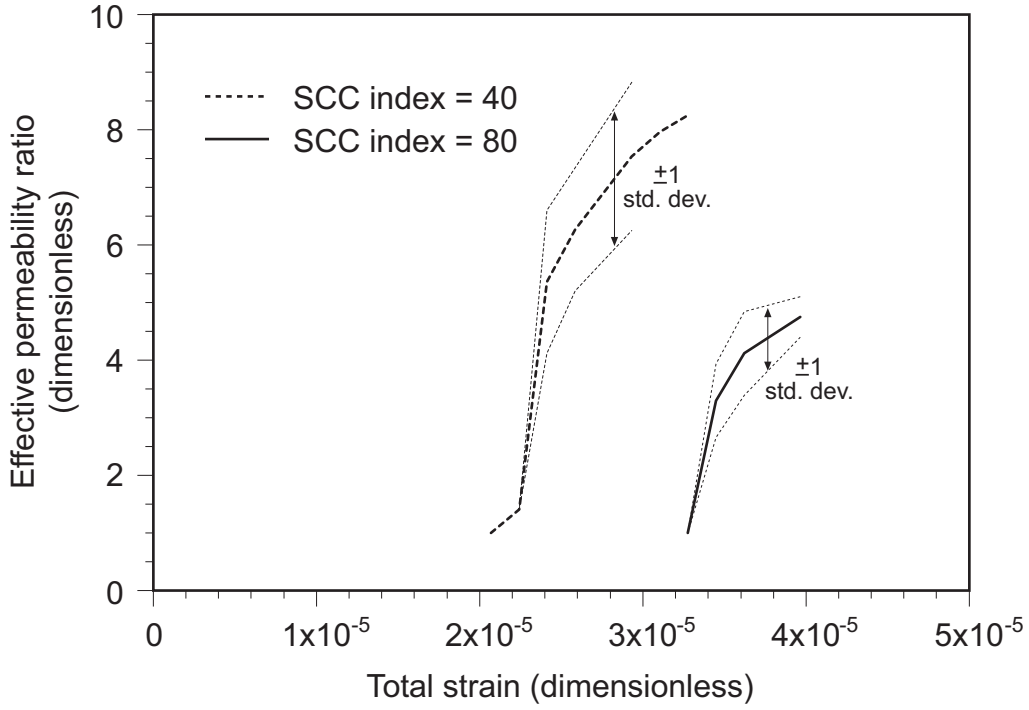

Figure 21. Mean and standard deviation of the effective permeability ratios for a bed height of 5 m

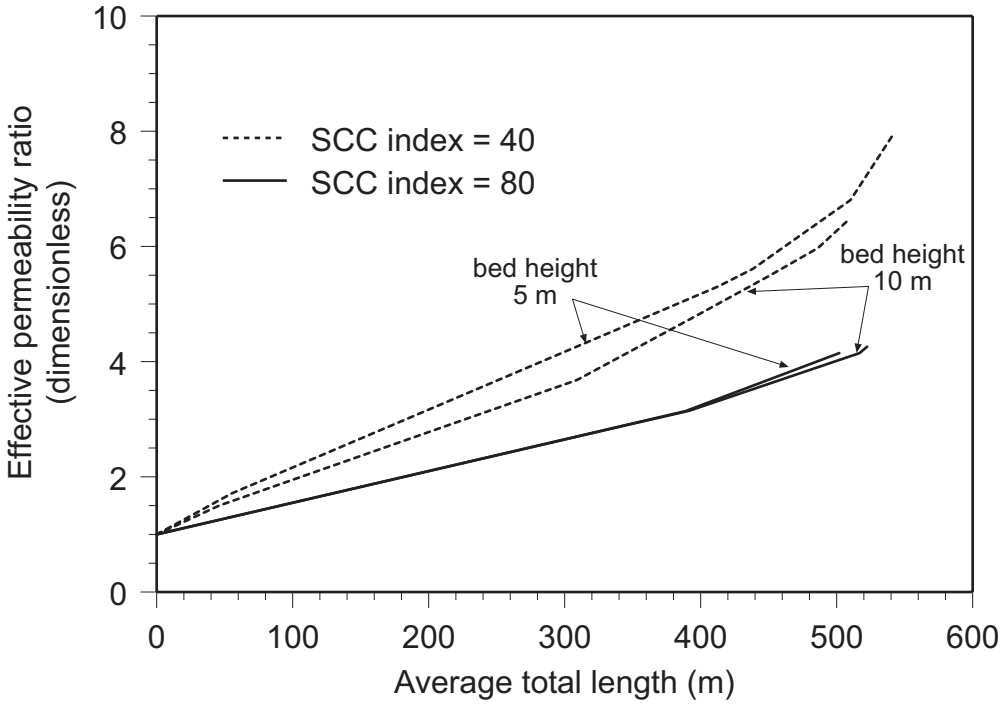

Figure 22. Average R_k vs. average total length (average of seven realizations).

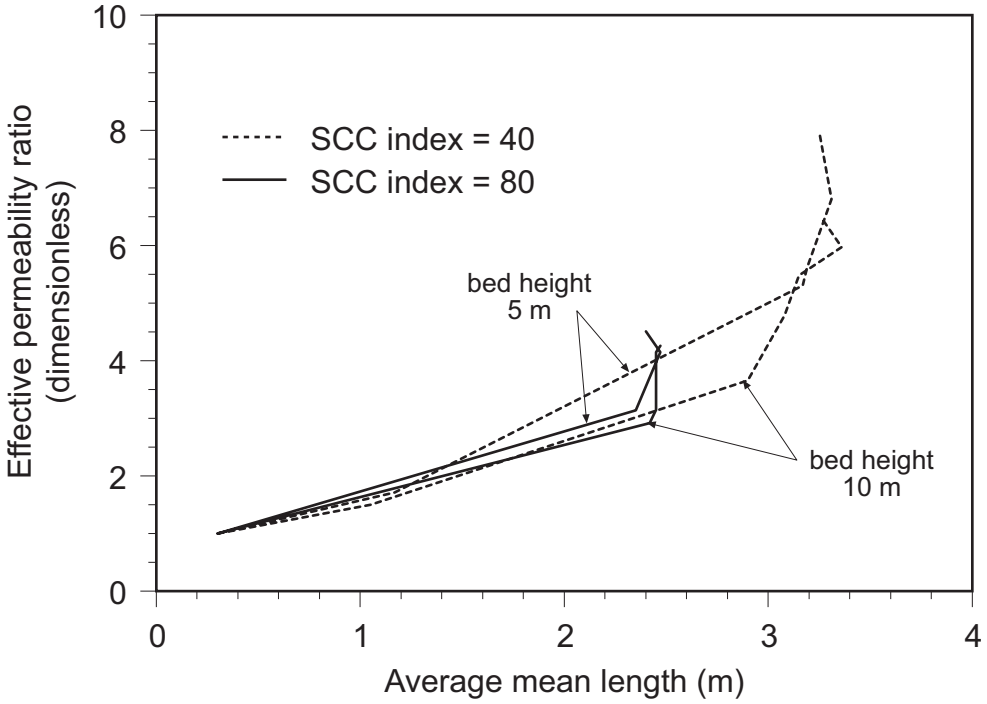

Figure 23. Average R_k vs. average mean length (average of seven realizations).

In figure 23, the sharp increase in the R_k values at the end of the simulations for both the indices of 40 and 80 is due to the increase in the number of fractures of the same mean length. There is not much of a dependence on bed height. The previous observation of R_k dependence on bed height (figs. 20 and 21) at a given strain is due to differences in fracture total length and fracture mean length and not due to the closer spacing between fracture clusters. The spacing between the fracture clusters does not appear to have an effect on R_k.

A plot of the effective k ratio, R_k, vs. average mean aperture is shown on figure 24. At first glance, it appears that R_k does increase with the average mean aperture. However, it is to be noted that each marker point represents a different strain level. Therefore, with a change in the mean aperture, the total length and mean length are also changing. The apparent increase in R_k with the mean aperture for the index of 40 is probably due to an increase in the fracture total length and/or mean length.

Further, for seven realizations of one of the cases (bed height 10 m and index 40) the fracture cell permeabilities were increased by a factor of 10 and the flow simulations repeated. The resultant grid permeabilities, however, went up only 6 percent. Thus, the effective permeability ratio is not very sensitive to the fracture aperture when the fracture permeabilities are much larger than the matrix permeability.

Nonneighbor Connection Fracture Representation

Flow simulations for one set of runs (realization 1) for both bed heights (5 m and 10 m) and both indices (40 and 80) were repeated using the NNC approach. The effective permeabilities are similar to those obtained using explicit fracture representations except that in the NNC approach the R_ks are bigger by about 30 percent because the fractures are assumed to be infinitely conductive. Nevertheless, the similarity of results from the two methods indicates that effective permeability is more sensitive to the fracture pattern than fracture conductivity.

The fluid-flow simulations were performed using the fully implicit method. The memory and run-time requirements for the NNC approach depend on the number of fractures and were much higher than that required for the explicit fracture representation method. The memory required ranged from about 1.5 to 3 times that of the explicit fracture representation method, whereas the CPU run time ranged from about 15 to 30 times that of the explicit fracture representation method.

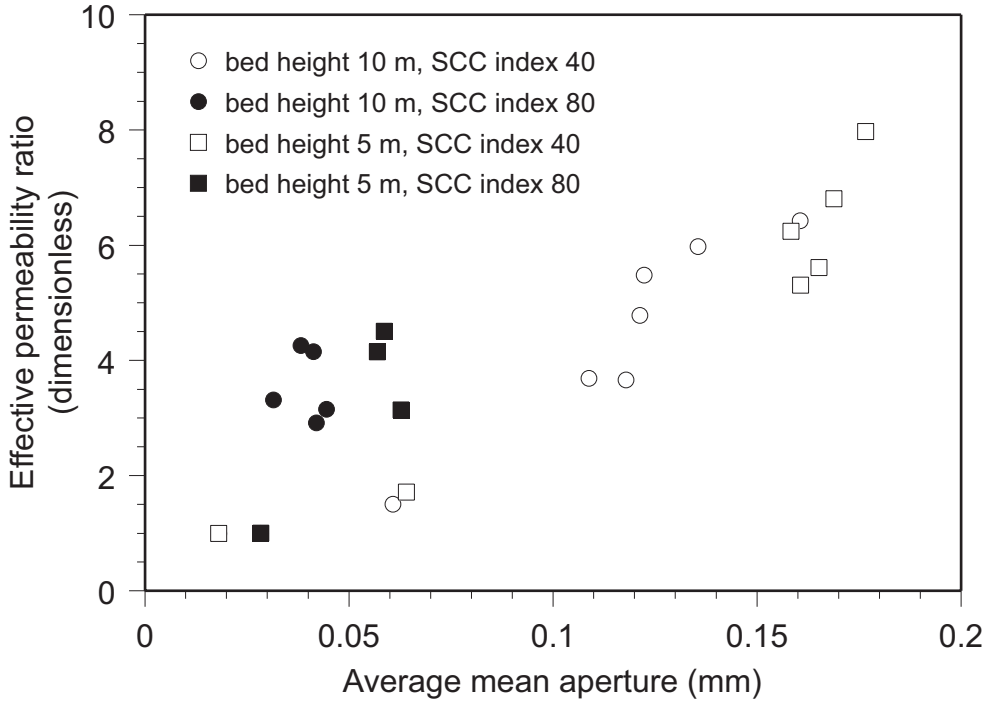

Figure 24. Average R_k vs. average mean aperture (average of seven realizations).

OTHER FACTORS AFFECTING FRACTURE PERMEABILITY

Synkinematic Cement

In some cases cement is precipitated on the walls of the fracture as the fractures form, thus reducing the fracture aperture everywhere by a constant amount. Cement that is precipitated in conjunction with fracture propagation is called synkinematic cement. The constant amount by which the aperture is reduced is defined as the emergent threshold, e_t (Laubach and others, 2000). In the South Wasson Clear Fork reservoir the emergent threshold is estimated at 100 μm (see Gale and others, this report). To examine the effect of the partial filling of fractures by cement, we define an emergent threshold ratio, e_r , such that

$$e_r = \frac{e_t}{w_{gm}} \quad ,$$

where w_{gm} is the geometric mean of the simulated apertures.

Fractures, or portions of them, that have apertures less than the emergent threshold are completely filled in. The effect of the emergent threshold was studied on a sample run (realization 4) with a bed height of 10 m and SCC index of 40. The emergent threshold ratio was varied from 0 (that is, no reduction in aperture) to 2. The effective k ratio, R_k, was computed for each of the cases studied. We see that as the emergent threshold increases, R_k decreases (fig. 25).

However, this decrease in R_k is not so much due to the decrease in the fracture apertures as to the change in the fracture pattern and interconnectivity. Fracture patterns for an emergent threshold ratio, e_r, of 0 and 2 are shown in figures 26 and 27. All the fractures in figure 27 with an aperture less than the e_r of 2 are filled, causing a change in the fracture pattern.

Further, because the permeability of the grid cells containing fractures is much higher (on the order of hundreds of Darcys) than the permeability of the matrix cells (1 md), a reduction of the aperture by even a fairly large amount would still result in fracture grid cells having a high permeability. Only if the fractures are completely filled in would the permeability of the fracture grid cells drop to the matrix permeability.

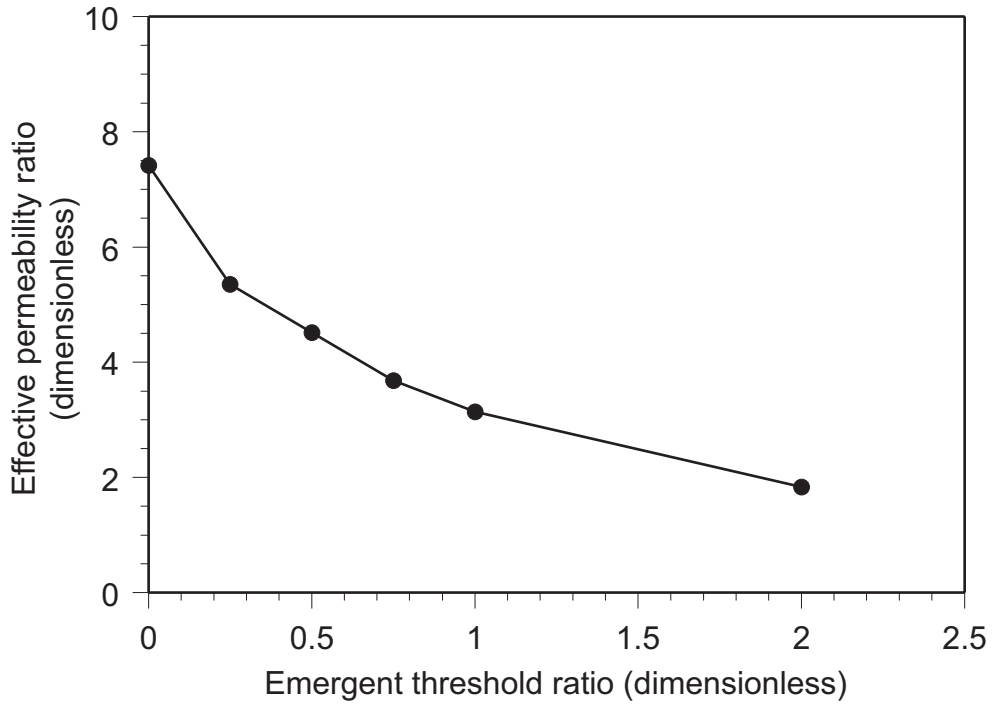

Figure 25 The effect of synkinematic cement on effective permeability for a SWCF simulated fracture pattern (realization 4) with a bed height of 10 m and SCC index of 40.

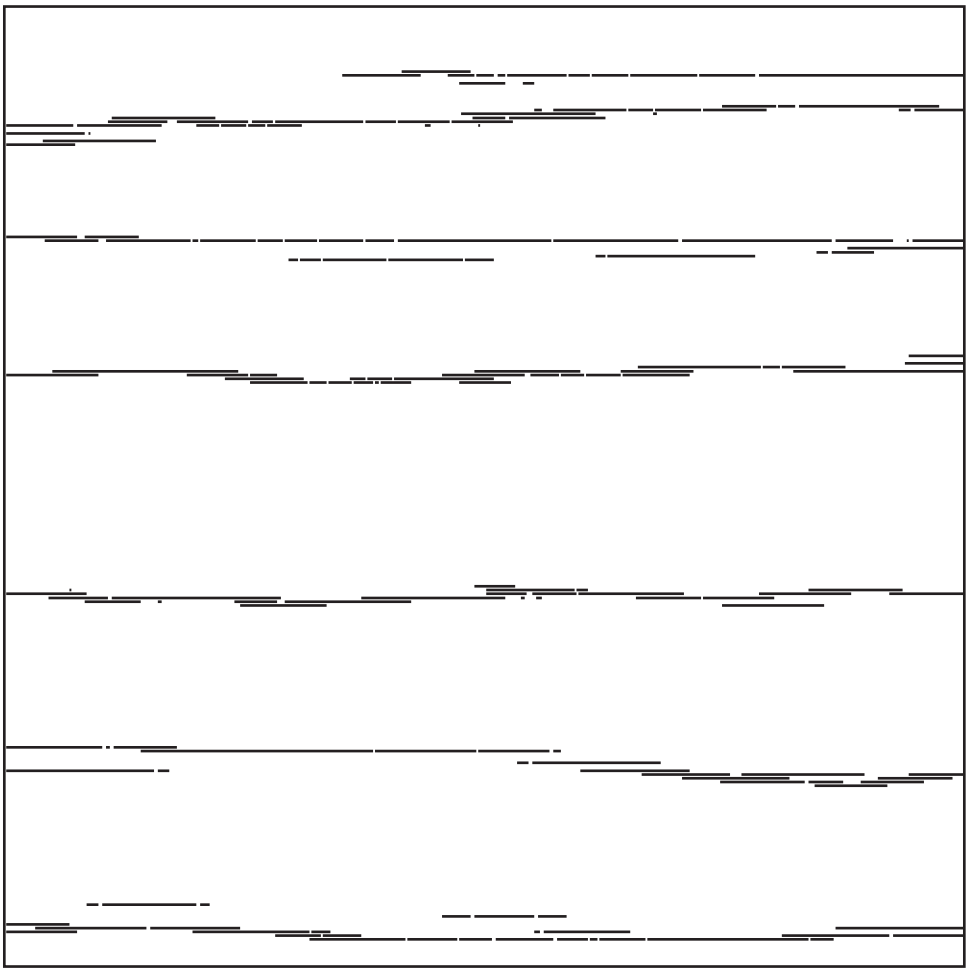

Figure 26. SWCF simulated fracture pattern (realization 4) with a bed height of 10 m and SCC index of 40 with an emergent threshold ratio of 0 and no degradation.

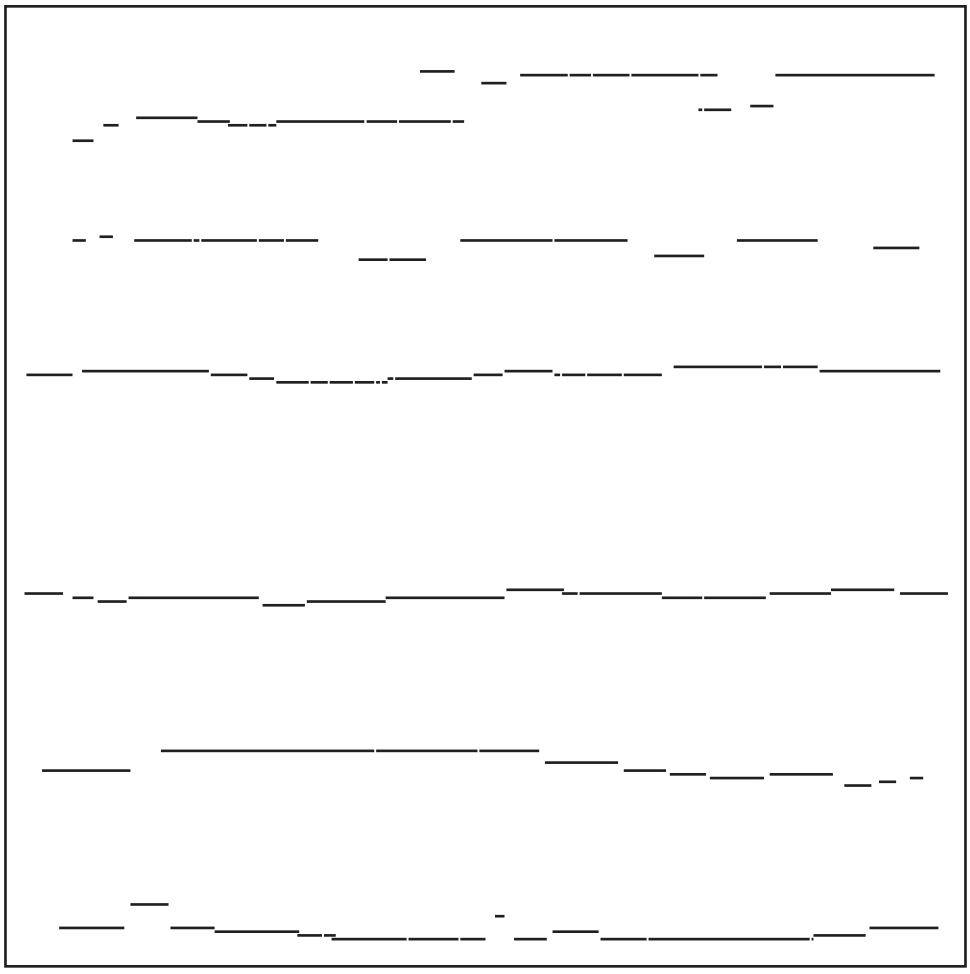

Figure 27. SWCF simulated fracture pattern (realization 4) with a bed height of 10 m and SCC index of 40 with an emergent threshold ratio of 2.

Postkinematic Cement

In some cases, cement is precipitated after fractures are formed. This cement randomly fills in all kinds of porosity including fracture porosity. Cement that is precipitated after fracture propagation is called postkinematic cement. Unlike synkinematic cement, where there is a constant reduction in fracture aperture, postkinematic cement causes some fractures to be completely filled at random, regardless of their aperture. The effect of varying values of postkinematic cement was also studied on a sample run (realization 4) with a bed height of 10 m and an SCC index of 40 by randomly eliminating some of the fractures independent of their length.

It is possible from point-count data of thin sections to obtain the fraction of pore-space filled in with cement, termed the degradation index. This often correlates well with the percentage of fractures filled in microfracture observations and hence is frequently used to predict the amount of filled macrofractures (Laubach and others, 2000). However, in the South Wasson Clear Fork reservoir, the percentage of microfractures filled did not correlate well with the degradation index (Gale and others, this volume). Therefore, instead of a degradation index we have used the extent of microfracture filling obtained directly from thin-section analysis (see table 5, Gale and others, this volume). The partly filled fractures were treated as fully open in case 1 and as fully closed in case 2.

Table 5. Microcrack observations from South Wasson Clear Fork thin sections

Open fractures	8
Partly filled fractures	12
Filled fractures	16
Total fracture observations	36

Case 1: Percent of fractures filled = 16/36 = 44%

Case 2: Percent of fractures filled = (16+12)/36 = 78%

The fracture pattern with no filled fractures is shown in figure 26. The final fracture patterns obtained for both cases are shown in figures 28 and 29. It is evident that fracture filling

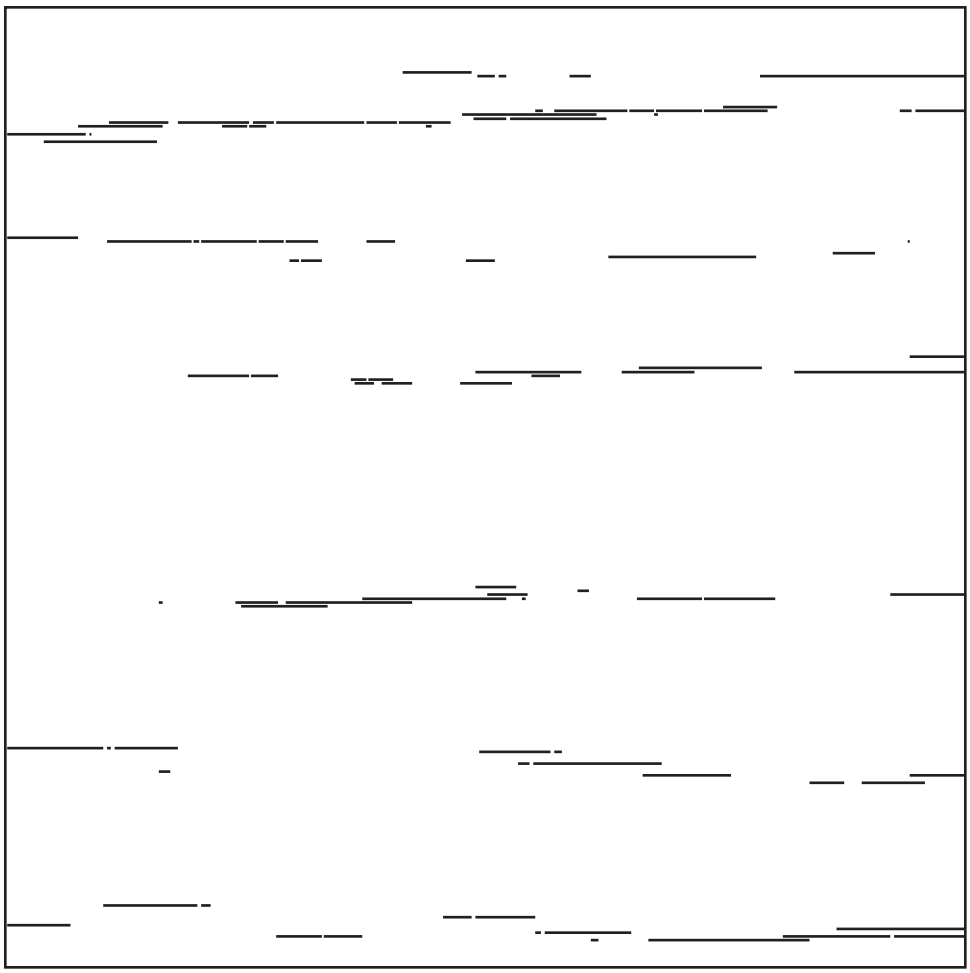

Figure 28. SWCF simulated fracture pattern (realization 4) with a bed height of 10 m and SCC index of 40 with a degradation index of 44 percent.

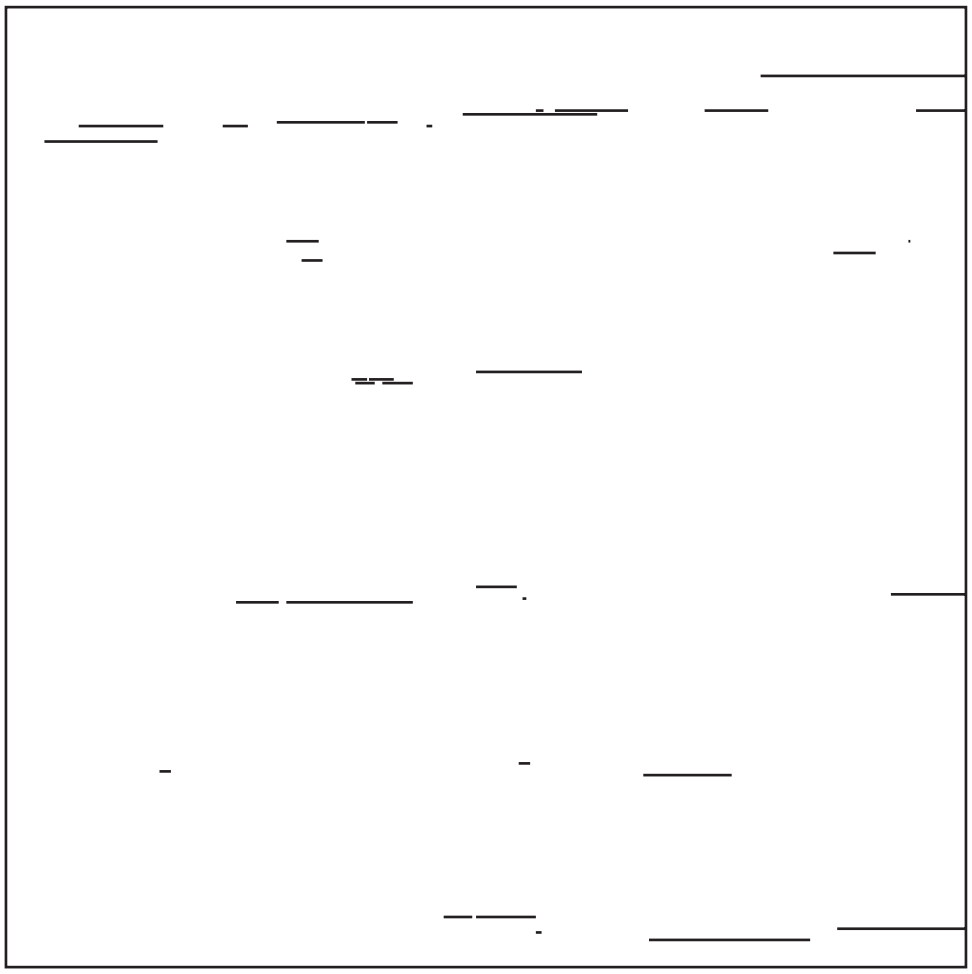

Figure 29. SWCF simulated fracture pattern (realization 4) with a bed height of 10 m and SCC index of 40 with a degradation index of 78 percent.

with postkinematic cement also changes the fracture pattern. Higher filling reduces fracture total length and interconnectivity. The effective k ratio, R_k, was computed for each case. As expected the permeability decreases with increasing fracture filling (fig. 30).

CONCLUSIONS

Traditional models of the South Wasson Clear Fork reservoir underpredict injectivity. An improved model removes some of the discrepancy by using a carefully controlled power-averaging scale-up method (Jennings, this volume), but there is still a shortfall in the observed permeability by a factor of 2. One reason for this could be the presence of fractures, which are known to exist in carbonate reservoirs. This study indicates that the effective grid permeability due to the presence of fractures is enhanced by a factor of between 2 and 10. This is substantially lower than the 1,000- or 10,000-fold increase that one would expect by simply computing the fracture permeability, but it is more than enough to explain the discrepancy between the observed and modeled injectivity.

In future studies, careful measurements that include detailed mapping of fractures with a particular emphasis on fracture connectivity are needed to meaningfully include the presence of fractures in reservoir modeling. Aperture information is not critical, except for modeling fracture filling by synkinematic cement. Further, for flooding operations, breakthrough times and sweep efficiencies could probably be better understood by the incorporation of fractures into the flow analysis.

The simulation studies done for this study have demonstrated improved fracture modeling methods and provided guidance for future research in fractured reservoir studies. It is possible to include fractures in reservoir simulation both explicitly and using NNC. Both methods give reasonable results with the accuracy of the solution improving with grid refinement. However, the NNC approach cannot be reliably used for fractures that extend across a simulation grid. Further, the NNC approach assumes that the fractures are infinitely conductive, whereas in explicit fracture representation, fracture width and hence fracture permeability information can be incorporated. The NNC approach also requires much higher CPU time and memory compared with the explicit fracture representation.

Although fracture permeability is highly sensitive to fracture aperture, the resultant effective permeability is not unless the fracture network is completely connected. It is more

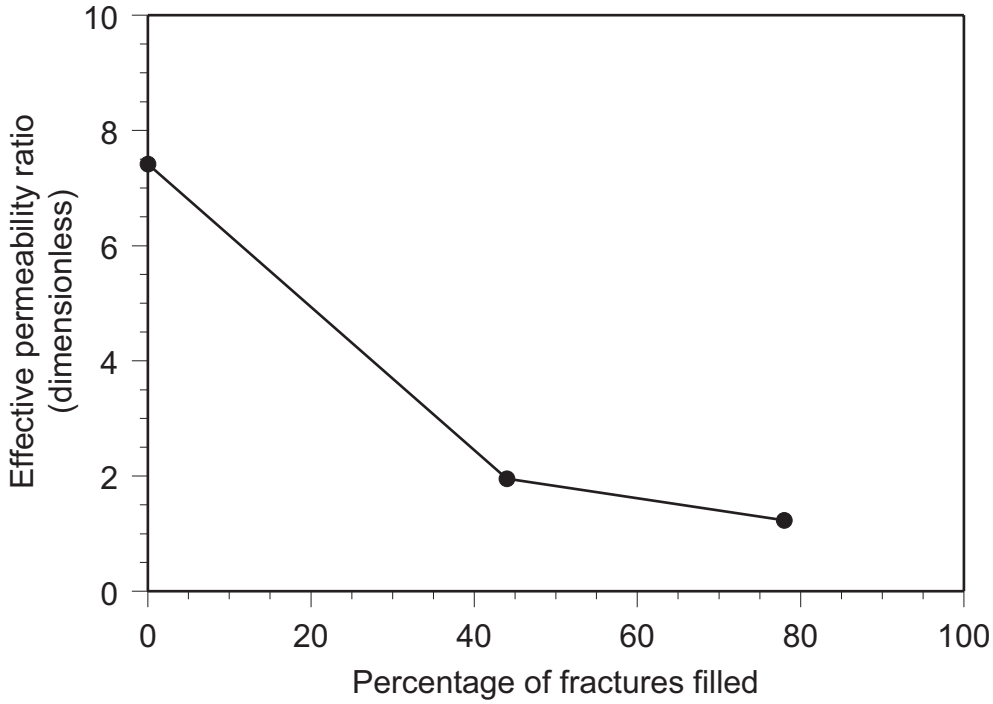

Figure 30. The effect of postkinematic cement on effective permeability for a SWCF simulated fracture pattern (realization 4) with a bed height of 10 m and SCC index of 40.

sensitive to fracture pattern and connectivity. The reason for this is that fracture permeability is usually so much larger (on the order of hundreds of Darcys) than the matrix permeability (on the order of millidarcys) that an increase in the fracture aperture does not produce an equivalent increase in the grid effective permeability. The matrix portions of the grid act as "bottlenecks," reducing the flow. This observation is supported by the fact that the NNC approach yields effective permeability ratios that are only 30 percent higher than those obtained using the explicit-fracture representation.

The effective permeability ratio increases with total fracture length and mean fracture length. An increase in the fracture length decreases the matrix portion of the grid, thereby reducing the "bottlenecks". The rate of increase of the effective permeability ratio increases as the fracture length or mean length increased. This is because as the fracture length increases the probability that two fractures link up or become very close to one another increases.

Beds having a higher subcritical index tend to have a lower effective permeability than those having lower indices because they tend to have fractures with smaller mean lengths. This is because a higher index has a lower velocity of subcritical crack propagation. Therefore, visible crack growth is delayed, and the stresses are also released at a lower rate for the higher index. When cracks eventually do start to form, more cracks tend to grow at the same time, leading to a lower mean length.

Grid effective permeability is highly sensitive to fracture filling by synkinematic and postkinematic cements. Both types of cement close a portion of the fracture network and reduce the effective permeability. It is to be emphasized that both types of cement lower the effective permeability by changing the fracture pattern and reducing fracture interconnectivity.

REFERENCES

Atkinson, B. K., 1984, Subcritical crack growth in geological materials: Journal of Geophysical Research, v. 89, no. B6, p. 4077–4114.

Atkinson, B. K., and Meredith, P. G., 1987, The theory of subcritical crack growth with applications to minerals and rocks, in Atkinson, B. K., ed., Fracture mechanics of rock: San Diego, Calif., Academic, p. 111–166.

Chirlin, G. R., 1985, Flow through a porous medium with periodic barriers or fractures: SPEJ, p. 358–362.

Halihan, Todd, Sharp, J. M., Jr., and Mace, R. E., 1999, Interpreting flow using permeability at multiple scales, in Palmer, A. R., Palmer, M. V., and Sasowsky, I. D., eds., Karst modeling: Karst Waters Institute Special Publication No. 5, Charlottesville, Va., p. 82–96.

Hearn, C. L., SPE, Occidental Petroleum of Qatar Ltd., Al-Emadi, Ismail A. Abdulla, SPE, Qatar General Petroleum Corp., Worley, Paul L. H., and Taylor, R. D., SPE, Occidental Petroleum of Qatar, Ltd., 1997, Improved oil recovery in a tight reservoir with conductive faults, ISND Shuiaba, Qatar: presented at the 1997 SPE Annual Technical Conference and Exhibition, San-Antonio, Tex., USA, October 5–8, SPE 38908.

Holder, Jon, Olson, J. E., and Philip, Zeno, 2001, Experimental determination of subcritical crack growth parameters in sedimentary rock: Geophysical Research letters, v. 28, no. 4, p. 599–602.

Ingraffea, A. R., 1987, Theory of crack initiation and propagation in rock, in Atkinson, B. K., Fracture mechanics of rock: Academic, San Diego, Calif., p. 71–110.

Laubach, Steve, Marrett, Randy, and Olson, Jon, 2000, New directions in fracture characterization: The Leading Edge, July.

Nakashima, T., SPE, Waseda University, Sato, K., SPE, The University of Tokyo, Arihara, N., SPE, Waseda University, and Yazawa, N., SPE, JNOC, 2000, Effective permeability estimation for simulation of naturally fractured reservoirs: presented at the SPE Asia Pacific Oil and Gas Conference and Exhibition held in Brisbane, Australia, October 16–18, SPE 64286.

Olson, J. E., 1991, Fracture mechanics analysis of joints and veins: Stanford University, Stanford, Calif., Ph.D. dissertation, 174 p.

Olson, J. E., 1993, Joint pattern development: effects of subcritical crack growth and mechanical crack interaction: Journal of Geophysical Research, v. 98, no. B7, p. 12251–12265.

Olson, J. E., Qiu, Yuan, Holder, Jon, and Rijken, Peggy, 2001, Constraining the spatial distribution of fracture networks in naturally fractured reservoirs using fracture mechanics and core measurements: presented at the 2001 SPE Annual Technical Conference and Exhibition held in New Orleans, Louisiana, September 30–October 3.

Olsson, W. A., and Peng, S. S., 1976, Micro-crack nucleation in marble: International Journal of Rock Mechanics and Mining Science, v. 13, p. 53–59.

Pletka, B. J., Fuller, E. R., Jr., and Koepke, B. G., 1979, An evaluation of double-torsion testing—experimental, in Freiman, S. W., ed., Fracture mechanics applied to brittle materials: American Society for Testing and Materials, ASTM STP 678, p. 19–37.

Renshaw, C. E., 1996, Influence of subcritical fracture growth on the connectivity of fracture networks: Water Resources Research, v. 32, no. 6, p. 1519–1530.

Schlumberger, 1995, The Eclipse 100 reference manual, 96A.

Schlumberger, 1997, The Eclipse 100 technical description, 97A.

Tapponier, P., and Brace, W. F, 1976, Development of stress induced micro-cracks in Westerly granite: International Journal of Rock Mechanics and Mining Science, v. 13, p. 102–112.

Williams, D. P., and Evans, A. G., 1973, A simple method for studying slow crack growth: Journal of Testing and Evaluation, v. 1, no. 4, p. 264–270.

Wang H. F., and Heard, H. C., 1985, Prediction of elastic moduli via crack density in pressurized and thermally stressed rock: Journal of Geophysical Research, v. 90, p. 10342–10350.

Wolfram, Stephen, 1999, The Mathematica book (4th ed.): New York, Cambridge University Press, 1470 p.

NOMENCLATURE

Variables

B_I = mode 1 stress intensity factor
B_{IC} = mode 1 critical stress intensity factor or material fracture toughness
B^*_I = mode 1 threshold stress intensity factor
$\Delta\sigma$ = driving stress, differential
P = pressure
σ = compressive stress
V = velocity of crack propagation
s = subcritical crack growth index
n = number of matrix cells in a row touching a particular fracture
E = Young's modulus
E^* = Effective Young's modulus
ν = Poisson's ratio
ρ = areal fracture density
c = half length of fracture
D = plan area of fractured region
k = permeability
R_k = effective permeability ratio
G = complete elliptic integral of the first kind
T = transmissibility between two matrix cells
w = fracture aperture
e_t = emergent threshold
e_r = emergent threshold ratio

W = width of simulation grid
h = perpendicular distance between two fractures
A = area perpendicular to flow
dn = Jacobian elliptic function
Δx = dimension of grid cell in x direction
Δy = dimension of grid cell in y direction
Δz = dimension of grid cell in z direction
ΔP = pressure drop
m, r = modulus of elliptic integral
N = number of fractures

Subscripts

i = cell index
j = fracture index
$frac$ = fracture
mat = matrix
eff = effective
gm = geometric mean
x = x direction
y = y direction
z = z direction
p = pore
max = maximum
min = minimum
$cell$ = fracture cell
$anal$ = analytical
sim = simulated